Ollscoil na hÉireann, Corcaigh

National University of Ireland, Cork

Synthesis and Characterisation of Aurivillius Phase Materials

Thesis presented by

Jennifer Halpin, BSc, MSc

orcid.org/0000-0002-4839-2395

for the degree of

Doctor of Philosophy

University College Cork

School of Chemistry

Head of School: Dr Humphrey Moynihan

Supervisors: Dr Lynette Keeney

Prof. Martyn Pemble

Dr Ian Povey

2021

Table of Contents

Declaration

This is to clarify that the work I am submitting is my own and has not been submitted for another degree, either at University College Cork or elsewhere. All external references and sources are clearly acknowledged and identified within the contents. I have read and understood the regulations of University College Cork concerning plagiarism.

31-05-22

Jennifer Halpin | Date

Acknowledgments

This thesis would not have been possible without the help and support of many people. Firstly, I would like to thank my supervisors Lynette, Martyn, and Ian for allowing me the opportunity to pursue this research project and for providing valuable guidance and expertise throughout.

Thanks also to the staff of the School of Chemistry in UCC particularly Ian and Simon for the chance to demonstrate undergraduate labs. Also, Trevor for facilitating outreach trips to secondary schools with SIAS.

I would like to thank the maintenance team, particularly Vince, for his help and patience with fixing the kit.

I would like to acknowledge the current and former members of AMSG, particularly Jan and Catherine who set the standard for a good PhD research student and a thank you to Tyndall National Institute in general for provide a welcoming and safe work environment.

A special thanks to the engineers who surrounded me in the office, Brendan, Andrija and Yash. Both the in-person and virtual gatherings during lockdown were invaluable for keeping spirits up.

My thanks to the UCC Karate club for providing an outlet twice a week for all PhD frustrations.

Massive thanks to Shóna for being a great friend throughout ten years and counting of studying chemistry.

And finally, the invaluable support of my family without which I would never have gotten far.

Abstract

Multiferroic materials, which are materials that exhibit two or more 'ferro' orders in a single phase, such as both ferroelectricity and ferromagnetism in the same phase, are an attractive area of research due to their novel properties and potential uses. Emerging areas of research for multiferroic materials include the biomedical, photocatalytic and photovoltaic areas, four state memory devices and multiferroic tunnel junctions.

Despite the increasing research interest there is currently a lack of genuine single-phase multiferroic materials. Ferroelectricity and ferromagnetism arise from fundamentally different conditions, where ferroelectricity requires ions with empty orbitals to accept electron density donation and ferromagnetism requires partially filled orbitals to allow unpaired electrons to align to give net spin. It is therefore necessary to have materials capable of supporting different types of ions to provide the conditions necessary for both ferroelectricity and ferromagnetism.

The Aurivillius phase materials ($Bi_2O_2(A_{m-1}B_mO_{3m+1})$ m = 1-9) have a naturally layered structure capable of accommodating a range of ions at the A and B-sites of the perovskite units. The Aurivillius materials are well known ferroelectrics with the electrical polarisation originating from polar distortions (rigid shifts of the Bi_2O_2 layers, displacements of the *A*-site / *B*-site cations) and tilts and rotations of the BO_6 unit. Substitution of magnetic ions such as iron and manganese at the *B*-sites has been shown to produce room temperature multiferroic materials.

Magnetic coupling between ions requires proximity between the magnetic ions. The work presented in this thesis involves an investigation into two approaches for improving the magnetic behaviour of the Aurivillius phase materials. The first approach used is to increase the concentration of magnetic ions in the material, which should increase the likelihood that the magnetic ions will be located close to each other within the crystal lattice. The second approach used is to locally concentrate the magnetic ions within the structure without the need to increase the total concentration of the ions.

To increase the concentration of magnetic ions in the *m* = 4 Aurivillius material a method known as aliovalent substitution was employed. The co-substitution of Fe^{3+} and Nb^{5+} for Ti^{4+} was performed to maintain a material with a net neutral charge. For the material $Bi_5Ti_{3-2x}Fe_{1+x}Nb_xO_{15}$ (x = 0, 0.1, 0.2, 0.3 and 0.4) a solubility limit of x = 0.1 was found before the appearance of secondary impurity phases became apparent. The increased iron content resulted in an increased absorption in the visible light region of the solar spectrum. It was found that there is generally a larger piezoelectric response for materials with more iron due to the increased distortion of the perovskite unit due to the substitution of the larger ions. Magnetic measurement of the x = 0.1 material demonstrated ferromagnetic behaviour with remnant magnetisation of M_R = 1.5 emu/cm^3 at 300 K. Previous work of the $Bi_6Ti_{2.8}Fe_{1.52}Mn_{0.68}O_{18}$ material deposited using a very similar process exhibited a magnetic response of M_R = 0.18 emu/cm^3 [1].

A systematic study into the *m* = 5 $Bi_6Ti_xFe_yMn_zO_{18}$ Aurivillius materials established a threshold of 52 % Ti occupancy at the *B*-site of the perovskite unit below which the structure undergoes rearrangement to the higher *m* = 6 phase. The driving force behind this change is the net charge that results from the substitution of Fe^{3+} and Mn^{3+} for Ti^{4+}. It is proposed that the structure responds with oxidation of Mn^{3+} to Mn^{4+} and rearrangement to the higher '*m*' phase to accommodate a charge-balanced material. Detailed transmission electron microscopy analysis confirms the presence of mixed Aurivillius phases.

To examine the second approach outlined above, a modified direct liquid injection chemical vapour deposition (DLI-CVD) method called sequential DLI-CVD was employed. With this method, gaseous precursors enter the reaction chamber in the order that mimics the Aurivillius structure. In this way it was hoped to impose order on the location of the ions in the structure. Using this method, $Bi_5Ti_{2.9}Fe_{1.1}O_{15}$ (BTFO) and $Bi_5Ti_{2.8}Fe_{1.1}Mn_{0.1}O_{15}$ (BTFMO) films were deposited on epitaxial substrates (LSAT and STO) at 710 °C. The as-deposited crystalline thin films displayed a magnetic response despite the relatively low concentration of magnetic ions in the material (30 % Fe and Mn in BTFMO compared to 44 % of Fe and Mn in previous B6TFMO room

temperature multiferroic material [2]). The influence of the strain applied by the substrate was examined for its effect on the structure and magnetic behaviour of the materials. A larger magnetic response was observed for materials deposited on STO than on LSAT substrates (at 20 K, BTFMO on STO M_R = 3.51 emu/cm^3 and BTFMO on LSAT M_R = 1.50 emu/cm^3).

Further work found that crystalline Aurivillius structures were formed on epitaxial substrates at temperatures as low at 610 °C. A further modification of the sequential DLI CVD recipe was introduced which was found to help maintain the levels of bismuth within the materials throughout the growth process. Narrower FWHM of the peaks obtained during XRD analysis suggest that fewer dislocations due to the formation of different '*m*' phases were occurring using the method. This modified sequential DLI-CVD method involved an injection of the bismuth precursor accompanying each precursor injection during the deposition. Finally, the work presented here is summarised and some suggestion for future work are presented.

The work presented in this thesis has advanced the understating of the Aurivillius phase materials and their potential as multiferroic materials. In particular, the in-depth analysis of their structural response to changing chemical composition and the development of experimental techniques to locally concentrate magnetic ions within the Aurivillius structure will be critical to their future use in the area of multiferroic research.

References

[1] L. Keeney et al., "Magnetic Field-Induced Ferroelectric Switching in Multiferroic Aurivillius Phase Thin Films at Room Temperature," Journal of the American Ceramic Society, vol. 96, no. 8, pp. 2339-2357, 2013/08/01 2013, doi: 10.1111/jace.12467.

[2] L. Keeney, C. Downing, M. Schmidt, M. E. Pemble, V. Nicolosi, and R. W. Whatmore, "Direct atomic scale determination of magnetic ion partition in a room

temperature multiferroic material," Scientific Reports, vol. 7, May 2017, Art no. 1737, doi: 10.1038/s41598-017-01902-1.

List of publications

Published works:

1. J. C. Halpin, M. Schmidt, T. Maity, M. E. Pemble and L. Keeney, "Compositional tuning of the Aurivillius phase material Bi5Ti3-2xFe1+xNbxO15 (0≤x≤0.4) grown by chemical solution deposition and its influence on the structural, magnetic and optical properties of the material," in IEEE Transactions on Ultrasonics, Ferroelectrics, and Frequency Control, doi: 10.1109/TUFFC.2020.2997406
2. J. Halpin and L. Keeney, OAJ materials and Devices, vol 5(1) – chap No7 in “Perovskites and other Framework Structure Crystalline Materials”, p 233 (Coll. Acad. 2021) DOI:10.23647/ca.md20202905

In preparation:

J. C. Halpin, M. Schmidt, M. E. Pemble and L. Keeney "Structural reorganisation and charge compensation in Aurivillius-phase $Bi_6Ti_xFe_yMn_zO_{18}$ compositions prepared by chemical solution deposition."

List of abbreviations

AFM: Atomic Force Microscopy

ALD: Atomic Layer Deposition

CVD: Chemical Vapor Deposition

CSD: Chemical Solution Deposition

DART-PFM: Dual AC Resonance Tracking Piezo Force Microscopy

EDX: Energy Dispersive X –Ray Spectroscopy

FeRAM: Ferroelectric Random Access Memory

FWHM: Full Width, Half Maximum

UV: Ultraviolet

UV-vis: Ultra violet visible

MRAM: Magnetic Random Access Memory

NN: Nearest Neighbours

NNN: Next Nearest Neighbours

PFM: Piezo Force Microscopy

PXRD: Powder X – Ray Diffraction

RMS: Root Mean Square

SEM: Scanning Electron Microscopy

SQUID: Superconducting Quantum Interference Device

XPS – x-ray photon spectroscopy

XRD – x-ray diffraction

TEM: Transmission Electron Microscopy

ZFC-FC: Zero Field Cooled – Field Cooled

Comments on my contributions

A majority of this work was carried out at Tyndall National Institute, Cork. Funding was secured by Martyn E. Pemble. My contributions to the previous publications included the design of experiment, synthesis of samples, characterisation and analysis of materials, interpretation of data and manuscript preparation. The planning and monitoring of the project was conducted by L. Keeney and M. Pemble. All authors of the final publications contributed to the final manuscript. The specific contribution of each co-authors is outlined below

Chapter 3: M. Schmidt preformed transmission electron microscopy and aided in the interpretation of that analysis. T. Maity performed magnetic measurements and aided in the interpretation of that analysis.

Chapter 4: M. Schmidt preformed transmission electron microscopy and aided in the interpretation of that analysis. L. Keeney, H. Neill and M. Rouzies synthesised the materials.

Chapter 5: B. K. Shaw conducted magnetic analysis and the collaboration was facilitated by T. Maity. M. Conroy performed STEM analysis.

Chapter 6: M. Conroy performed STEM analysis. J. Alaria performed out-of-plane and rocking curve X-ray diffraction analysis.

Chapter 1

1. Introduction

1.1. Ferroelectricity

1.1.1. Overview and definitions

Materials can be classified into different categories of metals, semiconductors and insulators based on the electron band structure of the materials. In metals, the conduction and valence energy bands overlap, in semiconductors there is a small band gap of 0 to 3 eV between the energy levels and in insulating materials there is a larger band gap (>3 eV) between the conduction and valence energy levels [1].

Insulating materials that can be polarised through the application of an electric field are known as dielectrics. The inhomogeneous distribution of electron density in a material may originate in solid materials through either ionic or polar bonding between atoms. In ionic solids, electron transfer occurs between two atoms forming a positive cation and negative anion which then form an ionic bond. In polar solids electrons are shared between atoms resulting in the formation of polar bonds between atoms with different electronegativities. The dipole moment of a material is the extent of separation between the positive and negative charges in the material.

In 1880, it was observed by Pierre and Jacques Curie that polarisation could be induced in a material through the application of mechanical stress or load [2]. This phenomenon was termed piezoelectricity from the greek 'piezo' meaning pressure. Piezoelectric materials are defined as materials where the molecular dipole moment can be changed through the application of mechanical stress [1].

The piezoelectric effect can be divided into two types, the direct and the converse piezoelectric effect. In the direct piezoelectric effect, the application of mechanical stress to a material produces a proportional electrical charge in the material. In the converse piezoelectric effect, the crystal structure is changed through the application of an electric field [1] (the piezoelectric effect is discussed in more detail in section 2.2.3).

The origin of piezoelectricity stems from the non-centrosymmetric nature of the crystal structure of polar materials. Of the 32 crystallographic point groups, 21 are

non-centrosymmetric of which 20 are classified as piezoelectric (note that for point group 432, the combination of symmetry elements eliminates piezoelectricity). A subsection of piezoelectric materials are experimentally determined to be ferroelectric who possess a spontaneous polarisation which can be reoriented by application of an applied electric field. This polarisation remains even when the applied field is removed.

Ferroelectricity was first proposed and examined throughout the 1920s and 1930s. In the 1920's ferroelectric behaviour was first studied in Rochelle salt ($NaKC_4H_4O_6.4H_2O$) by Joseph Valasek [3]. The name "ferroelectric" for this phenomenon was coined due to its similarity to ferromagnetic behaviour. The theory of ferromagnetism was well understood by this time and the hysteresis nature of applied magnetic field and magnetic moment was analogous to an applied electrical field and net polarisation. Further analysis by Valasek determined the presence of two Curie points in Rochelle salt [4].

In the 1930's, materials based upon KH_2PO_4 [5] which exhibited ferroelectricity were examined. The simple crystal structure of these materials compared to Rochelle salt led to the development of a theory of ferroelectric transitions in 1940s with the Slater model of ferroelectricity [6]. Macroscopic level understanding of ferroelectricity was developed from Landau's theory for solid state phase transitions. This theory was applied to ferroelectric materials by Ginzburg [7] and Devonshire [8]. This became the Landau-Ginzburg-Devonshire (LGD) thermodynamic theory of ferroelectric phase transitions [1]. In the 1950's, Kittle added theory explaining antiferroelectric behaviour [9] and in the 1960's a microscopic level understanding of ferroelectricity was developed by Anderson [10] and Cochran [11] with the 'rattling' ion soft modes.

1.1.2. Origins of ferroelectricity

A ferroelectric material is defined as a material where a net polarisation, caused by the alignment of electrical dipole moments, can be induced through the application of an electric field. This net polarisation is maintained when the applied field is

removed and the polarisation vector can be reversed or switched through the application of an electric field [1].

The polar crystal structure of ferroelectrics can be spontaneously polarised and switched through the application of an electric field. Above a certain temperature, known as the ferroelectric Curie point (T_C), a ferroelectric material exists in a high symmetry paraelectric state. Below T_C the material adopts a non-centrosymmetric polarised state. Barium titanate, $BaTiO_3$, is a well-studied ferroelectric material. $BaTiO_3$ has a perfect perovskite cubic structure above 120 °C but below that temperature it adopts the lower symmetry tetragonal structure where the displacement of Ti^{4+} ions causes spontaneous polarisation of the material [1]. The Jahn-Teller distortion describes the distortion of the crystal lattice in order to remove degenerate energy levels and so lowers the energy of the system making it more stable. This results in the distorted structure being a lower energy state than the symmetric structure below the Curie point. Most perovskite ferroelectrics stabilise their structure through hybridisation of empty *d* orbital (e.g. for Ti^{4+}) with the O 2*p* orbitals [12]. Another origin of polarisation is lone pair electron displacement (e.g. for stereochemically active Bi^{3+}, Pb^{2+}) leading to ferroelectricity [13].

Landau theory can be used to describe the macroscopic behaviour of ferroelectric materials. The Landau potential, described as the free energy potential vs polarisation of a ferroelectric material, forms a double well potential when below the Curie temperature. For a second order ferroelectric transition, at and above the Curie temperature there is only one minima, corresponding to the centrosymmetric nonpolar phase. The two minima that occur when the material is below its Curie temperature represent the two ferroelectric polarisation states with opposite orientations [14]. Most ferroelectrics are weakly first order, in first order transitions two local minima occur below the Curie temperature but the behaviour shows a discontinuity at T_C not observed in second order transitions (figure 1) [14].

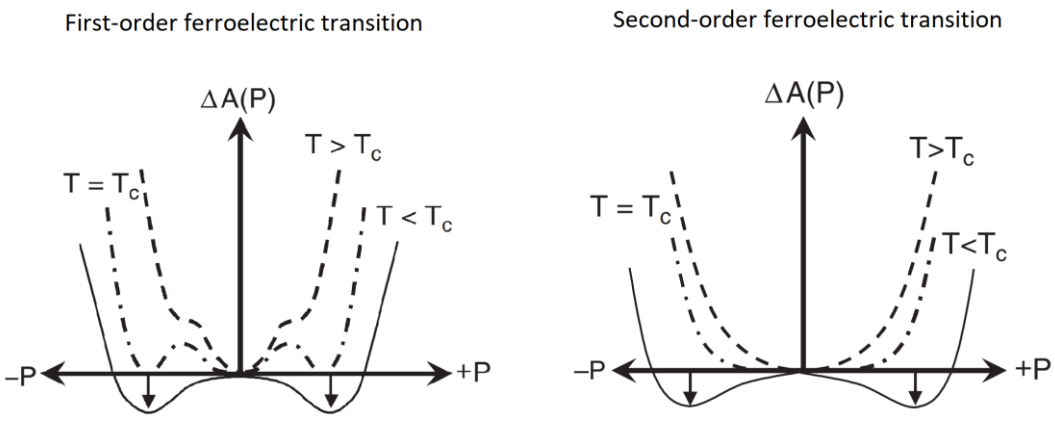

Figure 1: The energy potential vs polarisation of a ferroelectric material for First (left) and Second (right) order ferroelectric transitions. Image adapted from [14].

Perhaps the defining feature of ferroelectrics is the ability to switch the electrical polarisation vector or dipoles through the application of an electric field. The dipoles will align along the direction of the applied electric field. An idealised ferroelectric hysteresis loop of the polarisation (P) vs. electric field (E) is presented in figure 2. An ideal hysteresis loop is symmetrical and the values for the positive and negative coercive field and remanent polarisation are equal [15]. Factors which can affect the shape of the hysteresis loop include the sample thickness, mechanical stress, preparation conditions and thermal treatment [15]. An ideal ferroelectric material which has not been subjected to an electric field will possess zero net polarisation due to the random orientation of polarisation vectors. On initial application of an electric field, a wake up cycle or poling is performed on the materials figure 2 (a). The polarisation vectors will align along the direction of the applied electrical field producing a non-linear increase in net polarisation. The point called the saturated polarisation (P_S) is reached when all available polarisation vectors have the same orientation figure 2 (b). When the applied field is removed, some polarisation vectors may switch back, but a majority retain their orientation and the net polarisation at zero applied field is called the remanent polarisation (P_R) of the material (figure 2 (c)). If an electrical field is applied in the opposite direction, polarisation vectors will

switch their orientation to align along this opposite field. The point at which the net polarisation is zero (d) due to an equal magnitude of polarisation vectors being orientated in opposite directions is called the coercive field ($-E_C$). A continued increase in the negative electrical field will reach the saturation polarisation ($-P_S$) (e).

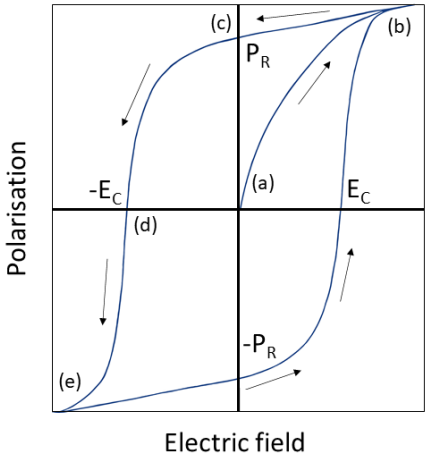

Figure 2: Idealised ferroelectric hysteresis loop, electric field vs polarisation, (a) wake up cycle, (b) saturation polarisation, (c) remanent polarisation (P_R), (d) coercive field (E_C) and (e) saturated polarisation ($-P_R$).

In ferroelectric materials, areas of uniform polarisation minimise electrical and elastic energy by forming domains separated by domain walls. Domains are regions where dipoles or polarisation vectors align along the same direction [15].

1.2. Ferromagnetism

1.2.1. Origins of magnetic moments

Magnetism has been observed since Greek Antiquity and the practical use of iron oxide (Fe_3O_4) as navigational aids began in the late 11^{th} century in China [12]. The modern study of magnetism began in earnest in the 1600s with the publication of *De Magnete* by William Gilbert which proposed the existence of magnetic poles on the Earth. In the late 1700s to early 1800s the developing theory of electromagnetism

and the work of Michael Faraday and James Clerk Maxwell lead to the modern era of research into magnetism [12].

The origins of magnetism at the atomic scale were examined by Pierre Weiss in the early 20th century who introduced the theory of the ferromagnetic molecular field concept, or later understood as quantum mechanical exchange energy. This states that electrons with parallel spins will have lower energy than electrons with antiparallel spins [16]. In 1928, Heisenberg developed the spin-dependent model of exchange interaction [17] and in 1932, Louise Néel put forward a theory explaining antiferromagnetic behaviour [18]. The Stoner theory sought to account for the deviation from the Cuire Weiss law observed. The Stoner theory proposes that while the exchange energy is minimised if all electrons have the same spin, this is opposed by the increasing band energy for moving electrons from low energy bands to higher energy bands [19].

Magnetic behaviour arises out of the orbital movements and the spins of electrons. The spin of an electron can be thought of as a small bar magnet with a north (N) and south (S) orientation. Two electrons can only occupy the same orbital if the spins align with the opposite spin orientation to each other, one N-S and the other S-N (Pauli exclusion principle). The net atomic magnetic moment is the sum of all moments form all electrons. If there is a greater alignment of electron spins along one direction (due to the presence of unpaired electrons) then a net magnetic moment exists. Orbital movements can also produce solenoid like magnetic behaviour due to the movement of the electrons around the nucleus [20].

Degeneracy refers to the different physical arrangement of a system which has the same energy. In the absence of an applied magnetic field, the orientation of the spin of the electron is degenerate, i.e. N-S has the same energy as S-N. With the application of a magnetic field, spin degeneracy can be removed due to the different interactions that the N-S and S-N spin orientations will have with the applied field. Orbital degeneracy can also be removed with the application of an external magnetic field.

There are different types of magnetic behaviour. Diamagnetism is a very weak form of magnetism that is non-permanent. It occurs when the electron density of the paired electrons is disturbed by the application of a magnetic field creating a small electrical current. The induced magnetic field is in the opposite direction to the applied field meaning that a diamagnetic material will be repulsed by the magnetic field. This has the effect of the material weighing less when weighed in the presence of a magnetic field.

Paramagnetism occurs only with the application of an external field. Unpaired electrons align along the direction of the applied field. It is lost when the external field is removed. In complexes that contain both paired and unpaired electron both diamagnetic and paramagnetic behaviour may occur. The contribution of diamagnetism is much weaker than paramagnetism and can be easily accounted for when the empirical formula of the complex is known.

Ferromagnetism is a spontaneous magnetisation that persists after the removal of an applied field. The magnetic moments align along the direction of the applied field. In antiferromagnetic materials the adjacent magnetic moments align antiparallel to each other resulting in a net zero magnetic moment at zero field. Ferrimagnetism is where a majority of magnetic moments align along the direction of the applied field but a minority are aligned antiparallel to the net magnetic moment. Canted magnetism arises when the antiferromagnetic magnetic moments are deflected out of plane resulting in weak ferromagnetism (figure 3).

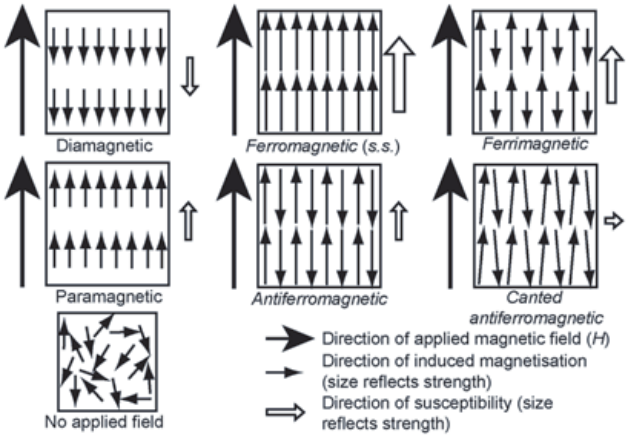

Figure 3: different types of magnetic behaviour. Image taken from O'Driscoll *et al.* [21].

The movement of electrons around the nucleus creates a solenoid-like magnetic behaviour. The angular momentum contribution is said to be quenched when it is lost due to environmental effects such as chemical bonding or crystal field splitting. Assuming the contribution of the orbital degeneracy has been fully quenched allows the use of the spin-only equation (1.1) to calculated the effective magnetic moment μ_{eff}.

$$\mu_{eff} = \sqrt{n(n+2)} \qquad (1.1)$$

Where n is the number of unpaired electrons. The spin-only equation can be used reliably to calculate the magnetic moment for the first row transition metal elements. It is unsuitable for the second and third row elements as the spin-orbital coupling is much stronger.

Magnetism is observed in materials with unpaired electrons in the *d* orbitals or more rarely in the *f* orbitals [1]. The *d* orbitals in an uncoordinated transition element are degenerate with the same energy. When that transition elements exists in a complex, it will interact with the ligands and the different orbitals will have different energies. This is known as crystal field splitting. In octahedral systems such as the *B*-site ion in perovskite structures (discussed in section 1.4) the interaction between orbitals and ligands will result in energy level splitting. The ligands lie along the x, y and z axis and so the d_{xy}, d_{xz} and d_{yz} levels will be lower in energy (t_{2g}) and the d_z^2 and d_x^2 - $_y^2$ levels will be higher in energy (e_g) (figure 4).

A further splitting of the energy levels in the form of the Jahn Teller effect may occur to remove degeneracy if there is more than one arrangement of the electrons possible. This usually happens through the elongation of bonds along the z-axis. Energy levels with a z component are now lower in energy (d_z^2 , d_{xz}, d_{yz}).

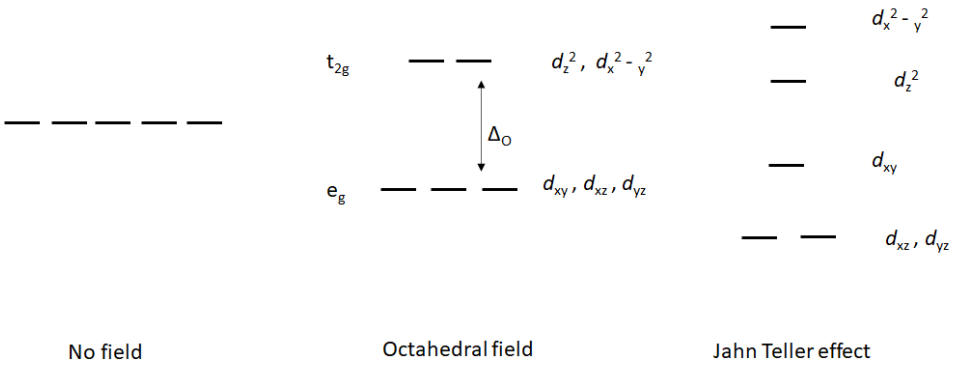

Figure 4: Degenerate energy levels in the absence of any field. Degeneracy is removed through Crystal Field splitting in the octahedral complex. Degeneracy is further removed through Jahn-Teller distortion.

1.2.2. Magnetic exchange interactions

A direct exchange of electrons between atoms with overlapping orbitals is quite rare in magnetic materials. More common in transition metal oxides are the superexchange and double exchange mechanisms. The superexchange mechanism involves the coupling of electrons between cations through an intermediate non-metallic anion (oxygen). Due to the Pauli exclusion principle (electrons with the same spin orientation cannot occupy the same orbital) the type of magnetic behaviour resulting from this mechanism is usually antiferromagnetic (figure 5 (a)). It can result in ferromagnetic behaviour if the cations are connected at 90° to each other as opposed to 180° or when virtual electron transfer is from a half-filled orbital to an empty orbital, for example between a half-filled e_g orbital in high-spin Fe^{3+} and an empty e_g orbital in Mn^{4+}.

The Double exchange mechanism involves a two-step process where the electrons are delocalised along the cation - non-metallic anion - cation bond (figure 5 (b)). The neighbouring magnetic ions must retain their spin orientation resulting in a parallel alignment of spins in the material producing ferromagnetism [12]. This exchange mechanism occurs between cations with different oxidation state i.e. Mn^{3+} – O – Mn^{4+}.

Dzyaloshinskii–Moriya interaction or antisymmetric exchange is a form spin canted ferromagnetism in an antiferromagnetic system leading to a net magnetisation [22]. The antiparallel spins are canted off centre leading to a weak ferromagnetism occurring usually at low temperatures.

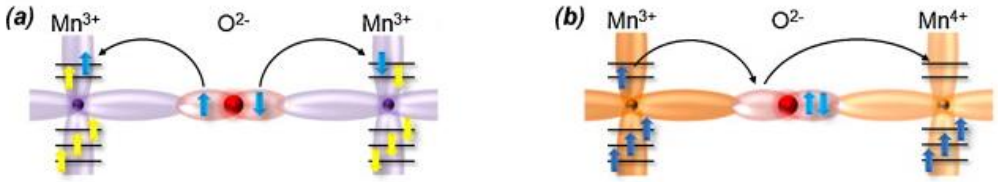

Figure 5: Image depicting electron exchange mechanisms, (a) superexchange and (b) double exchange. Image modified from Martin *et al.* [12].

The Goodenough- Kanamori rules [23-25] are a reliable guideline for predicting the type of magnetism which may be present in a material based on the oxidation state of the ions. The guidelines state that virtual electron exchange from an ion with filled orbitals to an ion with partially filled orbital will result in ferromagnetic behaviour and exchange between ions both with partially filled orbitals will result in antiferromagnetic behaviour.

1.2.3. Ferromagnetic behaviour

Ferromagnets are characterised by a hysteresis loop where the net magnetisation (B) does not follow a linear relationship to the applied magnetic field (H). In figure 6 an idealised ferromagnetic hysteresis loop is presented. At the initial application of an external magnetic field (a) the magnetisation increases as the unpaired electrons align themselves along the direction of the applied field. When all the available electrons are aligned along the same direction, the system has reached its magnetic saturation point (b). When the field is reversed, most of the magnetisation is maintained and the point at zero applied field (c) represents the remanent magnetisation (B_r). Further decreasing of the field decreases the net magnetisation

as electrons reorientate along the opposite direction. At the net zero magnetisation, the orientation of the spins in both direction is equal, this is known as the coercive point ($-H_C$). At (e) the saturated magnetisation in the opposite direction is achieved ($-B_r$).

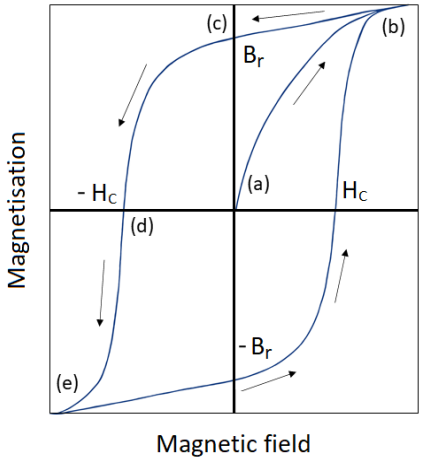

Figure 6: Idealised ferromagnetism hysteresis loop. (a) initial application of a magnetic field, (b) saturated magnetisation, (c) remanent magnetisation, (d) coercive field and (e) negative saturated magnetisation.

Magnetic domains are regions in a material where all of the magnetic moments are aligned in the same direction. Domain walls exist between domain regions with different magnetic moment orientations. Domain walls are areas where the magnetic moment orientation gradually changes.

The temperature at which the transition occurs between the paramagnetic phase and the ferromagnetic/ferrimagnetic phase is known as the magnetic Curie temperature (T_C). On decreasing temperature, the Néel temperature (T_N) marks a sharp decrease in magnetic susceptibility in antiferromagnetic materials [1].

1.3. Multiferroism

1.3.1. Overview and definitions

The term multiferroism was coined [26] to describe materials which have two or more of the 'ferroic' orders. Multiferroic materials are materials which exhibit two or more of the following order parameters: ferroelectricity, ferromagnetism, ferroelasticity and/or ferrotoroidicity. The term multiferroic encompasses a range of materials, which can lead to confusion. For example materials with ferroelectric and antiferromagnetic behaviour are also referred to as multiferroic. Another distinction can be made between single phase and composite multiferroic materials. To illustrate the complexity, figure 7 shown the four 'roots' of ferroelectricity and ferromagnetism and the various branches formed from different combinations leading to multiferroic materials.

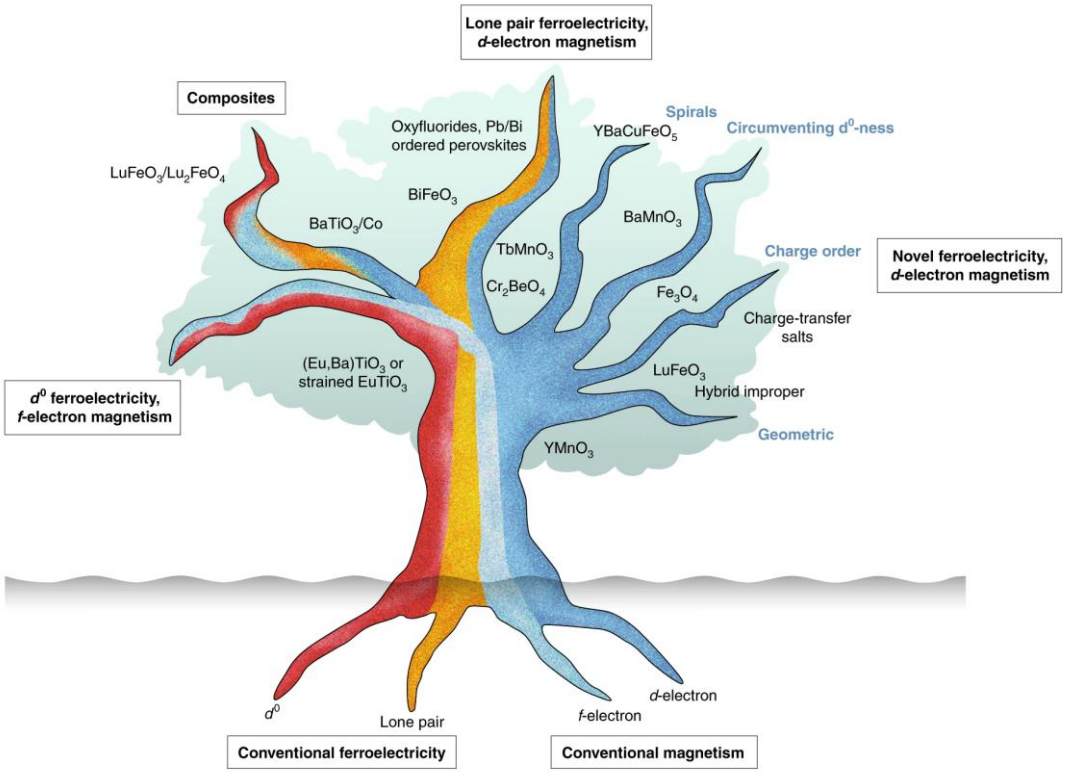

Figure 7: Four origins of conventual ferroelectricity and magnetism combining and leading to the many branches of multiferroic materials. Image taken from [27].

Research into the area of multiferroic materials began in the 1950s with the first multiferroic being a complex nickel iodine boracite ($Ni_3B_7O_{13}I$) structure [28]. Early research in Russia in the 1950s focused on the substitution of magnetic ions into

ferroelectric perovskites. These often had low Curie or Néel temperatures due to the dilute concentration of magnetic ions present [29]. The area of multiferroic research has experienced a rapid increase in attention over the last 20 years [30].

The materials under study in this work were developed with the aim of producing materials with both ferroelectric and ferromagnetic behaviours. When coupling between ferroelectric and ferromagnetic order parameters occurs, this is termed a magnetoelectric multiferroic material. Magnetoelectric multiferroic materials allow switching of the magnetisation through the application of an electric field or conversely, controlling the ferroelectric properties through an applied magnetic field. 'Electrically written and magnetically read' memory devices are an attractive practical application of this property due to the potentially high memory density and lower energy consumption (10-18 J per switch) [31] of such a device and a prototype magnetoelectric-random access memory (MERAM) device has recently been developed [32]. Another application is based on multiferroic tunnel junctions (MFTJs) that consist of two asymmetric oxide and/or metal electrodes separated by an ultra-thin multiferroic barrier layer [33]. Theoretically this could lead to four-state memory based on simultaneous electric and magnetic resistance states and steps towards developing CMOS compatible multiferroic materials which retain their ferroelectricity behaviour when scaled-down to 5 nm thicknesses are being explored [27].

The coexistence of ferroelectric and ferromagnetic behaviour in a single phase material is challenging, as the two processes require different electronic configurations present in the associated atomic orbitals. Ferroelectricity is usually induced by a distortion to the crystal symmetry creating a non-centrosymmetric structure. The electrical polarisation is commonly driven by electron density donation (i.e. from oxygen) into the empty valence shell of a first row transition metal (d^0). On the other hand, ferromagnetic behaviour requires unpaired electrons (d^n) in the valence shell. The alignment of the unpaired electrons is what produces the net magnetic moment of the ferromagnet. A method for overcoming this incompatibility between ferroelectricity and ferromagnetism is to have a chemical structure which

can accommodate two or more different types of cations. For example in $BiFeO_3$, the most well studied multiferroic material at present, the d^5 electrons of Fe^{3+} contribute to the magnetic behaviour while the lone pair electrons on the Bi^{3+} ions contribute to the off-centre symmetry and electric dipoles necessary for ferroelectricity. $BiFeO_3$ is ferroelectric, however the magnetic order in $BiFeO_3$ is primarily antiferromagnetic and it only displays a weak, canted ferromagnetism moment [34]. While $BiFeO_3$ can find uses in applications such as magnetoelectric random access memory (MERAM), where by means of interfacial exchange coupling in a composite heterostructure, an antiferromagnetic and ferroelectric magnetoelectric multiferroic can be used to switch the magnetisation of the ferromagnet using a voltage [35], $BiFeO_3$ would not be suitable for low-energy spintronics due to the cycloidal nature of its magnetic order which prohibits linear magnetoelectric coupling.

1.4. Perovskites and related materials

1.4.1. Overview and definitions

The multiferroic $BiFeO_3$ belongs to a family of materials known as perovskites. The name perovskite was given to the mineral $CaTiO_3$ which was discovered in the Ural mountains in 1839 by the German scientist Gustav Rose [36]. Perovskite has since come to refer more generally to compounds with the same ABX_3 structure as the original $CaTiO_3$. Perovskites have found many practical uses such as piezoelectrics, ferroelectrics, spintronics, photovoltaic devices and high temperature superconductors. Their wide range of practical uses is due to their enormous chemical and structural flexibility [36].

In the ideal form, the crystal structure of the cubic ABX_3 perovskite can be described as consisting of corner sharing $[BX_6]$ octahedra with the A cation occupying the 12-fold coordination site formed in the middle of the cube of eight such octahedra (figure 8) [37]. When oxygen is the anion, the charge of A and B must equal to 6. This can be achieved through a variety of combinations, such as A^{3+} and B^{3+} or A^{2+} and B^{4+}. It is also possible to have mixed compounds such as $AB_{0.5}B'_{0.5}X_3$. [1]. While X is often

O or F, some compounds containing nitride or hydride have been synthesised. *A*-site cations are generally larger (> 110 pm radius) such as Ba^{2+} or La^{3+} and *B*-site cations are smaller (< 110 pm radius) such as Ti^{4+}, Nb^{5+} and Fe^{3+} [1].

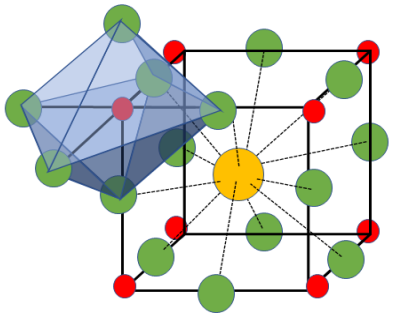

Figure 8: Idealised perovskite structure ABX_3, *A* (yellow) is the 12 fold coordinate cation, *B* (red) is the 6 fold coordinate cation and green is the *X* anion.

An idealised perovskite has a high-symmetry cubic structure. However, perovskites can adopt lower symmetry structures involving rotation of BX_6 octahedra, or where some bond lengths are elongated and others are shortened. This distortion may be due to Jahn Teller effect as the structure seeks a lower energy state by removing degeneracy. The distorted perovskite structure leads to the distinct polarisation states necessary for ferroelectric behaviour, as discussed in section 1.1.2. To estimate the degree of distortion, the ratio of the two expressions for the cell length can be used to calculate the Goldschmidt's tolerance factor t [38],

$$t = \frac{(r_A + r_O)}{\sqrt{2}(r_B + r_O)} \qquad (1.2)$$

Where r_A is the radius of the *A*-site cation, r_B is the radius of the *B*-site cation and r_O the radius of oxygen (*X*-site anion). An idealised cubic perovskite has a tolerance factor of 1. When the *B* cations are larger and/or the *A* cations are smaller than t < 1.

1.5. Aurivillius phase family of materials

1.5.1. Overview and definitions

The Aurivillius phase family of materials is a homologous series of bismuth based, naturally layered oxides. They have the general formula $Bi_2O_2(A_{m-1}B_mO_{3m+1})$ and consist of $mABO_3$ perovskite blocks separated by $[Bi_2O_2]^{2+}$ interlayers, with the primary growth axis along the *c*-axis direction and possess anisotropic properties. This family of materials was first described by Aurivillius in 1949 [39] and since then have practical use as high-temperature lead-free ferroelectrics due to their generally high Curie temperature (T_C > 500 °C [40]). More recently, they have been increasingly investigated as potential frameworks for magnetoelectric multiferroic materials. This is due to their inherent ferroelectric behaviour and their potential to accommodate magnetic ions within their structure.

The chemical composition of the perovskite blocks can vary widely within certain size and valence constraints, with the *A*-site occupied by a large 12-coordinate cation and the *B*-site occupied by a smaller 6-coordinate octahedral cation. Possible atoms for occupying the *A*-site include Na^{1+}, K^{1+}, Ca^{2+}, Sr^{2+}, Ba^{2+}, Pb^{2+} and Bi^{3+} and at the *B*-site; Fe^{3+}, Ti^{4+}, Nb^{5+}, W^{6+}, Ta^{5+} and Cr^{3+} [41]. This chemical variability can lead to Aurivillius compounds such as $Bi_4Ti_3O_{12}$, $SrBi_4Ti_4O_{15}$ or Bi_2WO_6. Due to the constrains imposed on the perovskite blocks by the $[Bi_2O_2]^{2+}$ interlayers Armstrong *et al.* [42] proposed that the range of ions that can be accommodated at the *B*-site must have atomic radii between 0.58 and 0.645 Å. This upper size limit of atomic radii is actually lower than that of an independent perovskite block because of the stain imposed by the $[Bi_2O_2]^{2+}$ interlayers.

The Aurivillius phase family of materials form a homologous series based on "*m*", the number of perovskite blocks between $[Bi_2O_2]^{2+}$ interlayers (figure 9). For example, $Bi_4Ti_3O_{12}$, $Bi_5Ti_3FeO_{15}$ and $Bi_6Ti_3Fe_2O_{18}$ have *m* = 3, 4 and 5 perovskite units respectively. Aurivillius phase structures with *m* = 1 to 9 have so far been fabricated [40]. The accommodation of larger numbers of perovskite blocks would be increasingly unfavourable due to the internal strain limitations [43].

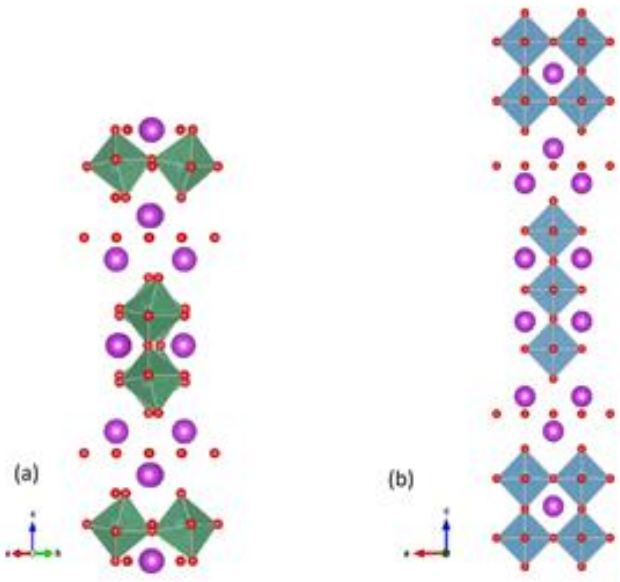

Figure 9: Aurivillius phase materials *m* = 2 and *m* = 3 Aurivillius phases, (a), Bi_3TiNbO_9 space group *A*21*am* and (b), $Bi_4Ti_3O_{15}$ space group *I*4/*mmm*. Image adapted form [41].

1.5.2. Polar and ferroelectric Aurivillius phase materials

The Aurivillius phase materials are well known ferroelectrics and have been utilized as high-temperature lead-free ferroelectrics due to their generally high Curie temperature (T_C > 500°C [40]). The origin of the ferroelectricity is in the perovskite units. The fluorite-like $[Bi_2O_2]^{2+}$ interlayer is paraelectric and does not retain electrical polarisation. Structural basis of ferroelectricity in the perovskite units is due to the displacement of the *A*-site and *B*-site cations accompanied by rotation tilt of the BO_6 octahedral [44, 45]. As discussed in section 1.1.2 the low symmetry phase adopted by the Aurivillius phases below their Curie temperature leads to the creation of distinct polarisation states. Elongation of the *c*-axis due to the Jahn Teller distortion to remove degeneracy reduces the energy of the system. As discussed in section 1.4.1, the Goldschmidt's tolerance factor *t* can used as a measure of distortion of the perovskite unit. Suárez *et al.* demonstrated the relationship between Tc and tolerance factor in Aurivillius materials [46]. The T_C was found to increase with

decreasing values of *t*. A tolerance factor below 0.985 is necessary for octahedral tilting in Aurivillius materials [47]. Increasing the tilt of the perovskite unit can affect the polarisation values. For example when the *A*-site cation Bi^{3+} was substituted by Sr^{2+} in the Aurivillius material $SrBi_2Ta_2O_9$ it resulted in a greater structural distortion and higher polarisation along the *a*-axis. The substituted compound also had a higher Curie temperature than the parent sample [48].

It has lately been demonstrated that ferroelectricity can persist in exfoliated Aurivillius phase nano-flakes. These flakes were only 2.4 nm thick, which is half of the normal crystal unit cell thickness [49].

Below their Curie temperature, Aurivillius phase structures with an odd number of perovskite blocks such as $Bi_4Ti_3O_{12}$ (*m* = 3) transition from the paraelectric space group *I*4/*mmm* phase to the orthorhombic *B*2*cb* phase [44, 50]. Aurivillius structures with an even number of perovskite blocks, such as $Bi_5Ti_3FeO_{15}$ (figure 10) and $SrBi_4Ti_4O_{15}$ (*m* = 4) or $SrBi_2Ta_2O_9$ and $Sr_{0.85}Bi_{2.1}Ta_2O_9$ (*m* = 2), transition from the *I*4/*mmm* paraelectric phase to the *A*21*am* space group [51, 52] (figure 10).

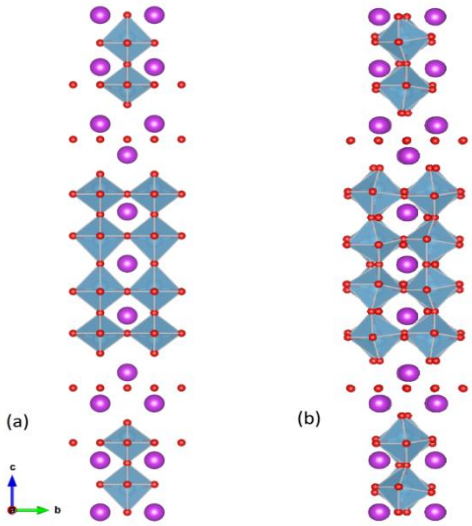

Figure 10: The Aurivillius material $Bi_5Ti_3FeO_{15}$ in its (a) paraelectric *I*4/*mmm* phase and (b) ferroelectric *A*21*am* phase. Image taken from [41].

The main polarisation direction in Aurivillius materials is along the a/b axis. Aurivillius materials with an even number of perovskite blocks between the $[Bi_2O_2]^{2+}$ interlayer retain a mirror symmetry perpendicular to the *c*-axis. This prohibits out-of-plane polarisation in *even*-layered Aurivillius phases and the polarisation is confined to the lateral plane. Retention of the mirror plane is not energetically favourable in Aurivillius phase structures with an odd number of perovskite blocks [44].

1.5.3. Magnetic Aurivillius phases

Development of true room temperature multiferroic materials is difficult due to the competing electronic requirements for ferroelectricity and ferromagnetism. The conventional route to ferroelectricity is to have cations with an empty *d* orbital, which enables hybridization between orbitals that stabilize the noncentrosymmetric polar structure; while ferromagnetism requires transition metals with partially filled *d* orbitals for exchange interactions to occur between unpaired electrons in nearby atoms [29]. This contraindication between the origins of ferromagnetism and ferroelectricity means that single-phase room temperature multiferroics are exceedingly rare and thus their material properties are currently limited. Attempts to overcome these contradictory requirements have included the creation of composite materials of a ferroelectric material and a ferromagnetic material [53, 54]. An alternative approach is the design of single-phase materials that accommodate two different types of cations, possessing both empty and partially filled orbitals to drive both ferroelectricity and ferromagnetism, respectively. In this regard the Aurivillius phase family of materials provides a versatile scaffold in which both of these types of atoms can be accommodated.

Previous work from our group has demonstrated rare room temperature multiferroic behaviour in the *m* = 5 Aurivillius system, $Bi_6Ti_xFe_yMn_zO_{18}$ (B6TFMO; x = 2.80 to 3.04; Y = 1.32 to 1.52; Z = 0.54 to 0.64) [55]. Thus far this is the only multiferroic material

demonstrating intrinsic ferroelectric / ferromagnetic properties to a defined confidence level (≥ 99.5 %) in thin film form [56].

A vital aspect to the development of a multiferroic material is the percolation of magnetic atoms within the Aurivillius structure. Long-range magnetic ordering requires that magnetic ions be located close together in the crystal lattice. Theoretically the percentage of magnetic atoms necessary for percolation in the crystal structure is 31 % for nearest neighbours and 14 % for next nearest neighbour interactions [50]. The promotion of NN (nearest neighbour) long-range order is beneficial for multiferroic materials as NN coupling is stronger than NNN (next nearest neighbour). The calculated magnetic Heisenberg coupling constants of the 4-layered (m = 4) $Bi_5Ti_3FeO_{15}$ NN interactions were J_{NN} = 40-50 meV as compared to NNN which was J_{NNN} = 1-2 meV [50].

The Aurivillius phase materials are highly anisotropic and this is reflected in their magnetic behaviour. For example, a $Bi_7Fe_{2.4}Co_6Ti_3O_{21}$ material had a M_R of 1.50 emu/g parallel to the *c*-axis and M_R of 1.17 emu/g perpendicular to the *c*-axis. The divergence in magnetic behaviour along different axis increased with an increasing number of perovskite blocks [57]. Increasing the number of perovskite blocks was found to increase the magnetic response in $Bi_{m+1}Fe_{m-3}Ti_3O_{3m+1}$ (m = 6, 7, 8, 9) materials. This was attributed to the increasing lattice disorder and increased probability of Fe^{3+} - O - Fe^{3+} coupling interactions in the larger Aurivillius structures [58].

One important issue in the area of multiferroic research is the phase purity of the materials produced. It is possible that magnetic behaviour observed in a sample may actually be due to small concentrations of magnetic secondary phases. For example, small concentrations of magnetic phase $CoFe_{2-x}Ti_xO_4$ in $Bi_5Ti_3Fe_{0.7}Co_{0.3}O_{15}$ were found to be responsible for an observed weak magnetic response of 6.37 emu/cm^3 at room temperature. The percentage volume of secondary phases in the bulk was determined to be just 3.95 % [59]. The concentration of these secondary phases can be very small and so avoid detection by analysis methods such a x-ray diffraction.

Statistical methods can be employed to define a confidence level that the observed magnetic response is intrinsic to the material and not due to secondary phases [56].

Secondary phases can form as a response to an unstable structure, due to changes of the electroneutrality and/or size of the ions. One method to increase the magnetic ion content while maintaining an electronically balanced stoichiometry is aliovalent substitution. This involves the co-substitution of two atoms, one with a higher oxidation state and one with a lower oxidation state than the atom that is being removed [41].

$$2X^{3+} \rightarrow Y^{4+} + Z^{2+} \qquad (1.3)$$

Aliovalent substitution has been used at the *B*-site of Aurivillius materials such as in $Bi_5Ti_3Fe_1O_{15}$ where Ti^{4+} was replaced by Fe^{3+} and Nb^{5+} [60] and at the *A* and *B*-sites of $Bi_5Ti_3Fe_1O_{15}$; where Bi^{3+} was substituted with Th^{4+} and Ti^{4+} was substituted by Fe^{3+} [61].

1.5.4. Aurivillius phase thin films

The development of thin films materials has been highlighted as a pressing concern for the practical use of multiferroic technologies [12]. A disadvantage of using thin films is that the ferroelectric and ferromagnetic behaviour can be diminished at a smaller scale. However, thin films have the advantage of experiencing epitaxial strain applied by the substrate. For example, the multiferroic material $BiFeO_3$ showed improved polarisation as a thin film (50 mC/cm^2) than the bulk material (6.1 mC/cm^2). This was caused by the change in lattice parameters of $BiFeO_3$ imposed by the substrate [62]. The use of $SrTiO_3$ epitaxial substrates allows the fabrication of the metastable $BiMnO_3$ without the need for a high pressure environment [63].

The Aurivillius phase materials have a large *c*-axis growth direction meaning that thin films may consist of only a few unit cells. Fortunately, ferroelectric behaviour has been shown to persist in exfoliated Aurivillius phase nano-flakes which were only 2.4 nm thick [49] and in other $Bi_5Ti_3FeO_{15}$ thin films grown on epitaxial $NdGaO_3$ substrates [64].

Previous work on room temperature multiferroic Aurivillius materials $Bi_6Ti_xFe_yMn_zO_{18}$ (B6TFMO; x = 2.80 to 3.04; Y = 1.32 to 1.52; Z = 0.54 to 0.64) [55] found a preferred occupation of inner perovskites by Fe and Mn driven by strain- and electrostatic-energy factors. This increases the probability of nearest neighbour magnetic interactions in the central layer by up to 90 % [65, 66]. Computational studies have proposed that the stain applied by substrates can further drive the partitioning of Fe to the inner perovskites away from the $[Bi_2O_2]^{2+}$ interlayer [67]. This strain engineering could be a valuable method of increasing Fe - Fe near-neighbour interactions without the need to increase the overall concentration of Fe in a material. This is important for the magnetic properties of the material, as long range magnetic ordering requires proximity between ions.

In figure 11, the pseudo lattice parameters of some common substrates and ferroelectric metal oxides are illustrated. Substrates with a smaller pseudo lattice parameter than the film will induce compressive strain on the film and substrates with a larger pseudo lattice parameter will apply tensile strain to the film.

A common concern in the deposition process of Aurivillius materials is the volatility of bismuth. Growth on epitaxial substrates can produce crystalline films at lower temperatures than on a non-epitaxial substrate. This can remove the need for a post anneal step in the fabrication process. For Aurivillius phase materials composed of bismuth this can avoid loss of volatile bismuth from the system.

As well as imposing strain on the lattice structure, epitaxial substrates can impose specific orientations on the crystal growth. As the Aurivillius phase materials are highly anisotropic in their properties, this can have large implications on their properties such as electrical polarisation [68-70].

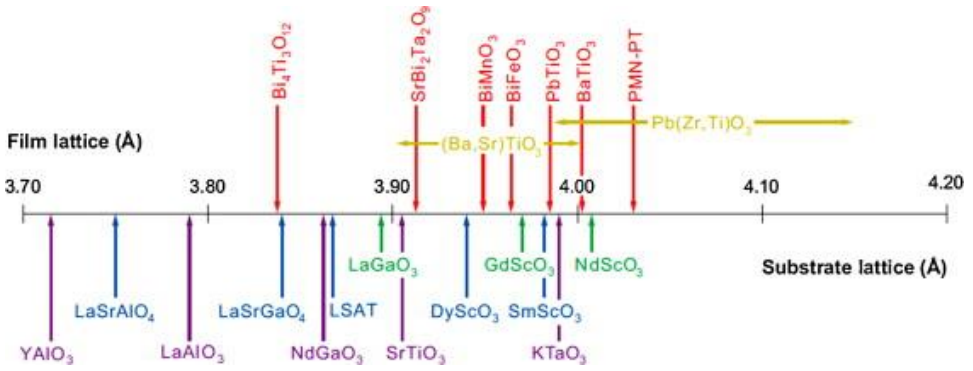

Figure 11: Pseudo lattice parameters of some common substrates compared to ferroelectric perovskite materials. Image taken from [12].

1.5.5. Optical properties of Aurivillius materials

Interest in the optical properties of Aurivillius phase materials has been increasing over the last few years. Particularly their potential use as photocatalytic materials which could find practical uses in the photodegradation of organic pollutants or in solar water splitting applications [71, 72]. The photocatalytic splitting of water was first demonstrated by Honda and Fujishima in 1972 with TiO_2 [73]. Absorption of photons induces charge separation and generates electron hole pairs. Band bending at the interface would drive the minority charge carriers to the interface. The electrical potential difference at the material/liquid interface drives the water splitting reaction. The band gap of a material is the energy needed to promote an electron from its valence band to its conduction band. For a material to be used to enable a water splitting process, the band gap must be sufficiently large to drive the water splitting reaction. The theoretical minimum energy required is 1.23 eV however, due to loss processes such as charge recombination, the actual energy required is higher. The valence band should be lower than the oxygen formation potential and the conduction band should be higher the hydrogen formation potential (figure 12). Similarly in photodegradation the formation of charge carriers can be used in chemical reactions to break down organic matter [74-76].

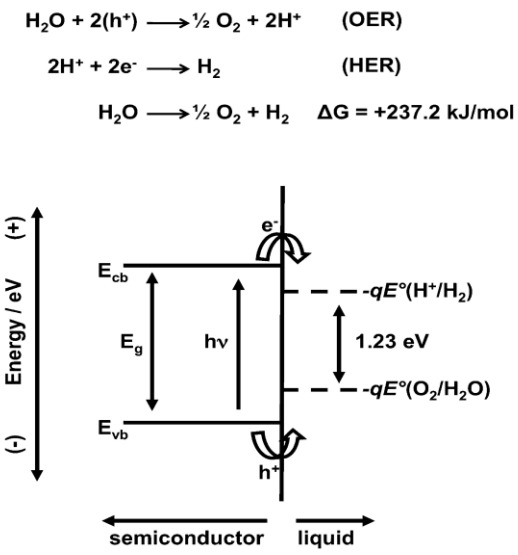

Figure 12: The oxygen evolution reaction (OER) and hydrogen evolution reaction (HER) during the water splitting process. Image taken from [77].

Bismuth based materials have attracted attention as photocatalytic materials due to the Bi^{3+} lone pair and oxygen hybridised orbitals [78]. The Aurivillius materials possess several characteristic which make them potentially efficient photocatalytic materials. They tend to have band gaps suitable for the absorption of light from the visible region of the solar spectrum ($Bi_5Ti_3CrO_{15}$ has a band gap energy of E_g ~ 2.46 eV [72]). Aurivillius materials are often used in conjunction with TiO_2. TiO_2 is a good water splitting catalyst but it has the disadvantage of only absorbing light in the UV region of the solar spectrum. By combining with Aurivillius materials it can utilised the visible region of the solar spectrum [79]. The absorption spectrum of the Aurivillius materials can also be modified through substitution [80] [81]. Furthermore, the spontaneous polarisation in the Aurivillius structures may help charge separation of the negative electron and positive hole charge carriers [82].

1.6. Aims for this body of work

Despite their novel properties and variety of potential uses, there is currently a lack of multiferroic materials. Common limitations to the development of multiferroic materials are the difficulties for ferroelectricity and ferromagnetism to co-existence

in a single phase, the persistence of ferromagnetic behaviour at room temperature and issues with the occurrence of secondary impurity phases contributing to the measured magnetic response.

Previous work by Keeney *et al*. [55] developed a the Aurivillius material $Bi_6Ti_{2.8}Fe_{1.52}Mn_{0.68}O_{18}$ that was found have genuine room temperature multiferroic behaviour (saturation magnetization (M_S) value of 215 emu/cm^3 and in-plane saturation polarization (P_s) values of > 26 μC/cm^2 [65]) and this was shown to be intrinsic to the Aurivillius material to a ≥ 99.5 % confidence level [56].

The overarching aim of this thesis is to explore methods of increasing the magnetic ion concentration or to locally concentrate magnetic ions within the Aurivillius phase materials.

Ferromagnetic behaviour could be improved by increasing the concentration of magnetic ions. However, there may a limit to the successful substitution of magnetic ions before the formation of secondary impurity phases occurs. Due to changes in valence or size there, is a limit to the amount of ions that can be tolerated within the structure. To fully investigate the effect of ion substitution a systematic study of the m = 5 Aurivillius phase $Bi_6Ti_xFe_yMn_zO_{18}$ within this thesis will examine the structural response to changes in the chemical composition (chapter 4).

A possible driving force behind the formation of secondary phases is the structural response to an unbalanced stoichiometry in the material due to the substitution of ions with a different valence than that of the parent material. To prevent a forbidden net charge, structural rearrangement may occur yielding associated secondary phases. To prevent the formation of an unbalanced stoichiometry, aliovalent substitution has been proposed [50] as a method of increasing the concentration of magnetic ions without producing an unbalanced stoichiometry in the material. Aliovalent substitution involves the co-substation of ions of a higher and lower charge, for example the co-substitution of Fe^{3+} and Nb^{5+} for Ti^{4+} in m = 4 $Bi_5Ti_3Fe_1O_{15}$ to maintain a net neutral charge. The aim of this investigation (chapter 3) is to determine if the aliovalent substitution successfully allows for the iron content to be

increased in the material without the formation of secondary phases. Materials will be tested for their structural, optical, piezoelectric and magnetic properties. Solubility limits on the successful co-substitution of iron and niobium will be determined.

An alternative to increasing the concentration of magnetic ions is to locally concentrate the magnetic ions in the structure. In order to achieve this, the work presented here (chapters 5 and 6) utilises the sequential DLI-CVD method which introduces the precursors into the reaction chamber in the order that mimics the Aurivillius structure. Previous work by Deepak *et al.* successfully used sequential DLI-CVD to fabricate *m* = 3 Aurivillius materials $Bi_4Ti_3O_{12}$ [83] and $Bi_4Ti_{2.5}Fe_{0.5}O_{12}$ [84].

In this work this method is further investigated to form the higher '*m*' phases and the inclusion of manganese into the material. Using the sequential DLI-CVD method attempts to locally concentrate the magnetic ions, iron and manganese, to the inner perovskite blocks will be investigated. Proximity between ions is necessary for long range magnetic coupling to occur.

To summarise, the main aims of this work area as follows:

- Exploration of aliovalent substitution for the development of phase pure multiferroic materials. The structural, piezoelectric and magnetic properties will be examined and solubility limits for the inclusion of iron and niobium will be established.
- A systematic study of the $Bi_6Ti_xFe_yMn_zO_{18}$ Aurivillius phase to establish solubility limits for the successful substitution of magnetic ions, iron and manganese.
- Development of sequential chemical vapour deposition methods to locally concentrate magnetic ions to the inner perovskite units. The structural, piezoelectric and magnetic properties of these materials will be examined.

1.7. References

[1] P. Atkins and T. Overton, *Shriver and Atkins' inorganic chemistry*. Oxford University Press, USA, 2010.

[2] J. Curie and P. Curie, "Développement par compression de l'électricité polaire dans les cristaux hémièdres à faces inclinées," *Bulletin de minéralogie,* vol. 3, no. 4, pp. 90-93, 1880.

[3] J. Valasek, "Piezo-Electric and Allied Phenomena in Rochelle Salt," *Physical Review,* vol. 17, no. 4, pp. 475-481, 04/01/ 1921, doi: 10.1103/PhysRev.17.475.

[4] J. Valasek, "Piezo-electric activity of Rochelle salt under various conditions," *Physical Review,* vol. 19, no. 5, p. 478, 1922.

[5] G. Busch and P. Scherrer, "Eine neue seignette-elektrische Substanz," *Naturwissenschaften,* vol. 23, no. 43, pp. 737-737, 1935.

[6] J. C. Slater, "Theory of the transition in KH2PO4," *The Journal of Chemical Physics,* vol. 9, no. 1, pp. 16-33, 1941.

[7] V. Ginzburg, "Polarizasyon and piezoelectric effect in BaTiO3 near the ferroelectric transition point," *Zh. Eksp. Teor. Fiz,* vol. 19, pp. 36-41, 1949.

[8] A. Devonshire, "Theory of ferroelectrics," *Advances in physics,* vol. 3, no. 10, pp. 85-130, 1954.

[9] C. Kittel, "Theory of Antiferroelectric Crystals," *Physical Review,* vol. 82, no. 5, pp. 729-732, 06/01/ 1951, doi: 10.1103/PhysRev.82.729.

[10] P. Anderson, "Fizika dielektrikov," *Akad. Nauk SSSR, Moscow,* 1960.

[11] W. Cochran, "Crystal stability and the theory of ferroelectricity," *Advances in Physics,* vol. 9, no. 36, pp. 387-423, 1960.

[12] L. W. Martin, Y. H. Chu, and R. Ramesh, "Advances in the growth and characterization of magnetic, ferroelectric, and multiferroic oxide thin films,"

Materials Science and Engineering: R: Reports, vol. 68, no. 4-6, pp. 89-133, 2010, doi: 10.1016/j.mser.2010.03.001.

[13] R. Seshadri and N. A. Hill, "Visualizing the role of Bi 6s “lone pairs” in the off-center distortion in ferromagnetic BiMnO3," *Chemistry of materials,* vol. 13, no. 9, pp. 2892-2899, 2001.

[14] E. K. Akdogğan and A. Safari, "Thermodynamics of ferroelectricity," in *Piezoelectric and Acoustic Materials for Transducer Applications*: Springer, 2008, pp. 3-16.

[15] D. Damjanovic, "Hysteresis in piezoelectric and ferroelectric materials," 2006.

[16] P. Weiss, "L'hypothèse du champ moléculaire et la propriété ferromagnétique," *J. Phys. Theor. Appl.,* vol. 6, no. 1, pp. 661-690, 1907.

[17] W. Heisenberg, "Zur theorie des ferromagnetismus," in *Original Scientific Papers Wissenschaftliche Originalarbeiten*: Springer, 1985, pp. 580-597.

[18] L. Néel, "Influence des fluctuations du champ moléculaire sur les propriétés magnétiques des corps," in *Annales de physique*, 1932, vol. 10, no. 18, pp. 5--105.

[19] E. C. Stoner, "LXXX. Atomic moments in ferromagnetic metals and alloys with non-ferromagnetic elements," *The London, Edinburgh, and Dublin Philosophical Magazine and Journal of Science,* vol. 15, no. 101, pp. 1018-1034, 1933.

[20] S. F. A. Kettle, "Magnetic properties of transition metal complexes," in *Physical Inorganic Chemistry: A Coordination Chemistry Approach*, S. F. A. Kettle Ed. Berlin, Heidelberg: Springer Berlin Heidelberg, 1996, pp. 185-210.

[21] B. O’Driscoll, E. C. Ferré, C. T. Stevenson, and C. Magee, "The significance of magnetic fabric in layered mafic-ultramafic intrusions," in *Layered Intrusions*: Springer, 2015, pp. 295-329.

[22] P. G. de Gennes, "Effects of Double Exchange in Magnetic Crystals," *Physical Review,* vol. 118, no. 1, pp. 141-154, 04/01/ 1960, doi: 10.1103/PhysRev.118.141.

[23] J. B. Goodenough, "Theory of the role of covalence in the perovskite-type manganites [La, M (II)] Mn O 3," *Physical Review,* vol. 100, no. 2, p. 564, 1955.

[24] J. B. Goodenough, "An interpretation of the magnetic properties of the perovskite-type mixed crystals La1−xSrxCoO3−λ," *Journal of Physics and Chemistry of Solids,* vol. 6, no. 2, pp. 287-297, 1958/08/01/ 1958, doi: https://doi.org/10.1016/0022-3697(58)90107-0.

[25] J. Kanamori, "Superexchange interaction and symmetry properties of electron orbitals," *Journal of Physics and Chemistry of Solids,* vol. 10, no. 2-3, pp. 87-98, 1959.

[26] H. Schmid, "Multi-ferroic magnetoelectrics," *Ferroelectrics,* vol. 162, no. 1, pp. 317-338, 1994.

[27] N. A. Spaldin and R. Ramesh, "Advances in magnetoelectric multiferroics," *Nature materials,* vol. 18, no. 3, pp. 203-212, 2019.

[28] E. Ascher, H. Rieder, H. Schmid, and H. Stössel, "Some properties of ferromagnetoelectric nickel-iodine boracite, Ni3B7O13I," *Journal of Applied Physics,* vol. 37, no. 3, pp. 1404-1405, 1966.

[29] N. A. Hill, "Why Are There so Few Magnetic Ferroelectrics?," *The Journal of Physical Chemistry B,* vol. 104, no. 29, pp. 6694-6709, 2000/07/01 2000, doi: 10.1021/jp000114x.

[30] N. A. Spaldin, "Multiferroics beyond electric-field control of magnetism," *Proceedings of the Royal Society A,* vol. 476, no. 2233, p. 20190542, 2020.

[31] S. Manipatruni, D. E. Nikonov, and I. A. Young, "Beyond CMOS computing with spin and polarization," *Nature Physics,* vol. 14, no. 4, pp. 338-343, 2018.

[32] S. Manipatruni *et al.*, "Scalable energy-efficient magnetoelectric spin-orbit logic," *Nature,* vol. 565, no. 7737, pp. 35-42, Jan 2019, doi: 10.1038/s41586-018-0770-2.

[33] M. Gajek *et al.*, "Tunnel junctions with multiferroic barriers," *Nature materials,* vol. 6, no. 4, pp. 296-302, 2007.

[34] D. Lebeugle *et al.*, "Room-temperature coexistence of large electric polarization and magnetic order in Bi Fe O 3 single crystals," *Physical Review B,* vol. 76, no. 2, p. 024116, 2007.

[35] M. Bibes and A. Barthélémy, "Towards a magnetoelectric memory," *Nature materials,* vol. 7, no. 6, pp. 425-426, 2008.

[36] J. P. Attfield, P. Lightfoot, and R. E. Morris, "Perovskites," *Dalton Transactions,* vol. 44, no. 23, pp. 10541-10542, 2015.

[37] M. Johnsson and P. Lemmens, "Crystallography and chemistry of perovskites," *arXiv preprint cond-mat/0506606,* 2005.

[38] J. B. Goodenough, "Electronic and ionic transport properties and other physical aspects of perovskites," *Reports on Progress in Physics,* vol. 67, no. 11, pp. 1915-1993, 2004, doi: 10.1088/0034-4885/67/11/r01.

[39] B. Aurivillius, "Mixed bismuth oxides with layer lattices. 2. Structure of Bi4Ti3O12," *Arkiv for Kemi,* vol. 1, no. 6, pp. 499-512, 1950.

[40] N. A. Lomanova, M. I. Morozov, V. L. Ugolkov, and V. V. Gusarov, "Properties of aurivillius phases in the Bi4Ti3O12-BiFeO3 system," *Inorganic Materials,* vol. 42, no. 2, pp. 189-195, 2006, doi: 10.1134/s0020168506020142.

[41] J. Halpin and L. Keeney, "Naturally Layered Aurivillius Phases: Flexible Scaffolds for the Design of Multiferroic Materials," *OAJ Materials and Devices,* vol. 5, no. 1, 2020.

[42] R. A. Armstrong and R. E. Newnham, "Bismuth titanate solid solutions," *Materials Research Bulletin,* vol. 7, no. 10, pp. 1025-1034, 1972/10/01/ 1972, doi: https://doi.org/10.1016/0025-5408(72)90154-7.

[43] T. Kikuchi, "Stability of layered bismuth compounds in relation to the structural mismatch," *Materials Research Bulletin,* vol. 14, no. 12, pp. 1561-1569, 1979.

[44] R. E. Newnham, R. W. Wolfe, and J. F. Dorrian, "Structural basis of ferroelectricity in the bismuth titanate family," *Materials Research Bulletin,* vol. 6, no. 10, pp. 1029-1039, 1971/10/01/ 1971, doi: https://doi.org/10.1016/0025-5408(71)90082-1.

[45] C. H. Hervoches and P. Lightfoot, "A Variable-Temperature Powder Neutron Diffraction Study of Ferroelectric Bi4Ti3O12," *Chemistry of Materials,* vol. 11, no. 11, pp. 3359-3364, 1999/11/01 1999, doi: 10.1021/cm991090d.

[46] D. Y. Suárez, I. M. Reaney, and W. E. Lee, "Relation between tolerance factor and Tc in Aurivillius compounds," *Journal of Materials Research,* vol. 16, no. 11, pp. 3139-3149, 2011, doi: 10.1557/jmr.2001.0433.

[47] H. Irie, M. Miyayama, and T. Kudo, "Structure dependence of ferroelectric properties of bismuth layer-structured ferroelectric single crystals," *Journal of Applied Physics,* vol. 90, no. 8, pp. 4089-4094, 2001.

[48] Y. Shimakawa, Y. Kubo, Y. Nakagawa, T. Kamiyama, H. Asano, and F. Izumi, "Crystal structures and ferroelectric properties of SrBi2Ta2O9 and Sr0.8Bi2.2Ta2O9," *Applied Physics Letters,* vol. 74, no. 13, pp. 1904-1906, 1999, doi: 10.1063/1.123708.

[49] L. Keeney *et al.*, "Ferroelectric Behavior in Exfoliated 2D Aurivillius Oxide Flakes of Sub-Unit Cell Thickness," *Advanced Electronic Materials,* vol. n/a, no. n/a, p. 1901264, 2020/01/30 2020, doi: 10.1002/aelm.201901264.

[50] A. Y. Birenbaum and C. Ederer, "Potentially multiferroic Aurivillius phaseBi5FeTi3O15: Cation site preference, electric polarization, and magnetic coupling from first principles," *Physical Review B,* vol. 90, no. 21, 2014, doi: 10.1103/PhysRevB.90.214109.

[51] C. H. Hervoches, J. T. S. Irvine, and P. Lightfoot, "Two high-temperature paraelectric phases inSr0.85Bi2.1Ta2O9," *Physical Review B,* vol. 64, no. 10, 2001, doi: 10.1103/PhysRevB.64.100102.

[52] C. H. Hervoches, A. Snedden, R. Riggs, S. H. Kilcoyne, P. Manuel, and P. Lightfoot, "Structural Behavior of the Four-Layer Aurivillius-Phase Ferroelectrics SrBi4Ti4O15 and Bi5Ti3FeO15," *Journal of Solid State Chemistry,* vol. 164, no. 2, pp. 280-291, 2002, doi: 10.1006/jssc.2001.9473.

[53] C.-W. Nan, M. I. Bichurin, S. Dong, D. Viehland, and G. Srinivasan, "Multiferroic magnetoelectric composites: Historical perspective, status, and future directions," *Journal of Applied Physics,* vol. 103, no. 3, p. 031101, 2008/02/01 2008, doi: 10.1063/1.2836410.

[54] H. Palneedi, V. Annapureddy, S. Priya, and J. Ryu, "Status and Perspectives of Multiferroic Magnetoelectric Composite Materials and Applications," *Actuators,* vol. 5, no. 1, 2016, doi: 10.3390/act5010009.

[55] L. Keeney *et al.*, "Magnetic Field-Induced Ferroelectric Switching in Multiferroic Aurivillius Phase Thin Films at Room Temperature," *Journal of the American Ceramic Society,* vol. 96, no. 8, pp. 2339-2357, 2013/08/01 2013, doi: 10.1111/jace.12467.

[56] M. Schmidt *et al.*, "Absence of Evidence ≠ Evidence of Absence: Statistical Analysis of Inclusions in Multiferroic Thin Films," *Scientific Reports,* vol. 4, no. 1, p. 5712, 2014/07/16 2014, doi: 10.1038/srep05712.

[57] W. Gu, X. N. Li, S. J. Sun, L. Y. Zhu, Z. P. Fu, and Y. L. Lu, "Magnetocrystalline anisotropy in the Co/Fe codoped Aurivillius oxide with different perovskite layer number," *Journal of the American Ceramic Society,* vol. 101, no. 6, pp. 2417-2427, Jun 2018, doi: 10.1111/jace.15424.

[58] G. Wang *et al.*, "Layer Effects on the Magnetic Behaviors of Aurivillius Compounds Bin+1Fen−3Ti3O3n+1(n= 6, 7, 8, 9)," *Journal of the American Ceramic Society,* vol. 99, no. 4, pp. 1318-1323, 2016, doi: 10.1111/jace.14108.

[59] L. Keeney *et al.*, "Room temperature ferroelectric and magnetic investigations and detailed phase analysis of Aurivillius phase Bi5Ti3Fe0.7Co0.3O15 thin films," *Journal of Applied Physics,* vol. 112, no. 5, p. 052010, 2012, doi: 10.1063/1.4745936.

[60] C. Chen *et al.*, "Effect of Nb and more Fe ions co-doping on the microstructures, magnetic, and piezoelectric properties of Aurivillius Bi5Ti3FeO15 phases," *Journal of Applied Physics,* vol. 120, no. 21, p. 214104, 2016, doi: 10.1063/1.4971256.

[61] V. G. Vlasenko, V. A. Shuvaeva, S. I. Levchenkov, Y. V. Zubavichus, and S. V. Zubkov, "Structural, electrical and magnetic characterisation of a new Aurivillius phase Bi5−xThxFe1+xTi3−xO15 (x=1/3)," *Journal of Alloys and Compounds,* vol. 610, pp. 184-188, 2014, doi: 10.1016/j.jallcom.2014.04.045.

[62] J. Wang *et al.*, "Epitaxial BiFeO3 multiferroic thin film heterostructures," *science,* vol. 299, no. 5613, pp. 1719-1722, 2003.

[63] E. Langenberg, M. Varela, M. García-Cuenca, C. Ferrater, F. Sánchez, and J. Fontcuberta, "Thin films in ternary Bi–Mn–O system obtained by pulsed laser deposition," *Materials Science and Engineering: B,* vol. 144, no. 1-3, pp. 138-142, 2007.

[64] E. Gradauskaite *et al.*, "Robust In-Plane Ferroelectricity in Ultrathin Epitaxial Aurivillius Films," *Advanced Materials Interfaces,* vol. 7, no. 14, p. 2000202, 2020.

[65] A. Faraz *et al.*, "Direct visualization of magnetic-field-induced magnetoelectric switching in multiferroic aurivillius phase thin films," *Journal of the American Ceramic Society,* vol. 100, no. 3, pp. 975-987, 2017, doi: 10.1111/jace.14597.

[66] L. Keeney, C. Downing, M. Schmidt, M. E. Pemble, V. Nicolosi, and R. W. Whatmore, "Direct atomic scale determination of magnetic ion partition in a room temperature multiferroic material," *Sci Rep,* vol. 7, no. 1, p. 1737, May 11 2017, doi: 10.1038/s41598-017-01902-1.

[67] A. Y. Birenbaum and C. Ederer, "Controlling the cation distribution and electric polarization with epitaxial strain in Aurivillius-phase Bi5FeTi3O15," *Applied Physics Letters,* vol. 108, no. 8, p. 082903, 2016, doi: 10.1063/1.4942668.

[68] T. Watanabe and H. Funakubo, "Controlled crystal growth of layered-perovskite thin films as an approach to study their basic properties," *Journal of Applied Physics,* vol. 100, no. 5, p. 051602, 2006/09/01 2006, doi: 10.1063/1.2337357.

[69] T. Watanabe, H. Funakubo, and K. Saito, "Ferroelectric property of epitaxial Bi4Ti3O12 films prepared by metalorganic chemical vapor deposition," *Journal of Materials Research,* vol. 16, no. 1, pp. 303-307, 2001.

[70] S. Nakashima *et al.*, "Structural and ferroelectric properties of epitaxial Bi5Ti3FeO15 and natural-superlattice-structured Bi4Ti3O12–Bi5Ti3FeO15 thin films," *Journal of Applied Physics,* vol. 108, no. 7, p. 074106, 2010/10/01 2010, doi: 10.1063/1.3491023.

[71] Z. Gu, J. Qian, R. Wang, M. Lv, X. Xu, and C. Luo, "Aurivillius compound Bi5Ti3CrO15 as a visible-light-active photocatalyst for hydrogen production from water," *Journal of Energy Chemistry,* vol. 62, pp. 572-580, 2021.

[72] Y. Wang, M. Zhang, J. Wu, Z. Hu, H. Zhang, and H. Yan, "Ferroelectric and photocatalytic properties of Aurivillius phase Ca2Bi4Ti5O18," *Journal of the American Ceramic Society,* vol. 104, no. 1, pp. 322-328, 2021.

[73] A. Fujishima and K. Honda, "Electrochemical Photolysis of Water at a Semiconductor Electrode," *Nature,* 10.1038/238037a0 vol. 238, no. 5358, pp. 37-38, 07/07/print 1972.

[74] Q. Yang, M. Luo, K. Liu, H. Cao, and H. Yan, "A composite of single-crystalline Bi 2 WO 6 and polycrystalline BiOCl with a high percentage of exposed (00 l) facets for highly efficient photocatalytic degradation of organic pollutants," *Chemical Communications,* vol. 55, no. 40, pp. 5728-5731, 2019.

[75] H. Li, Y. Chen, W. Zhou, H. Gao, and G. Tian, "Tuning in BiVO4/Bi4V2O10 porous heterophase nanospheres for synergistic photocatalytic degradation of organic pollutants," *Applied Surface Science,* vol. 470, pp. 631-638, 2019.

[76] O. Monfort *et al.*, "Comparative study between pristine and Nb-modified BiVO4 films employed for photoelectrocatalytic production of H2 by water splitting and for photocatalytic degradation of organic pollutants under simulated solar light," *Catalysis Today,* vol. 280, pp. 51-57, 2017.

[77] M. G. Walter *et al.*, "Solar water splitting cells," (in eng), *Chem Rev,* vol. 110, no. 11, pp. 6446-73, Nov 10 2010, doi: 10.1021/cr1002326.

[78] Y. Huang, L. Mi, J. Qin, S. Bi, and H. J. Seo, "Synthesis, optical, and magnetic properties of six-layered Aurivillius bismuth ferrititanate," *Journal of the American Ceramic Society,* vol. 102, no. 6, pp. 3555-3566, 2019.

[79] F. Orudzhev *et al.*, "Atomic layer deposition of mixed-layered Aurivillius phase on TiO2 nanotubes: synthesis, characterization and photoelectrocatalytic properties," *Nanomaterials,* vol. 10, no. 11, p. 2183, 2020.

[80] M. M. Seyfouri *et al.*, "New insights on the substantially reduced bandgap of bismuth layered perovskite oxide thin films," *Journal of Materials Chemistry C,* vol. 9, no. 9, pp. 3161-3170, 2021.

[81] T. Wang *et al.*, "Tunable polarization and magnetization at room-temperature in narrow bandgap Aurivillius Bi 6 Fe 2−x Co x/2 Ni x/2 Ti 3 O 18," *Ceramics International,* vol. 43, no. 12, pp. 8792-8799, 2017, doi: 10.1016/j.ceramint.2017.04.010.

[82] X. Yin *et al.*, "Morphology effect on photocatalytic activity in Bi3Fe0.5Nb1.5O9," *Nanotechnology,* vol. 29, no. 26, p. 265706, 2018/05/03 2018, doi: 10.1088/1361-6528/aabdba.

[83] N. Deepak, P. F. Zhang, L. Keeney, M. E. Pemble, and R. W. Whatmore, "Atomic vapor deposition of bismuth titanate thin films," *Journal of Applied Physics,* vol. 113, no. 18, p. 187207, 2013.

[84] N. Deepak, P. Carolan, L. Keeney, M. E. Pemble, and R. W. Whatmore, "Tunable nanoscale structural disorder in Aurivillius phase, n= 3 Bi 4 Ti 3 O 12 thin films and their role in the transformation to n= 4, Bi 5 Ti 3 FeO 15 phase," *Journal of Materials Chemistry C,* vol. 3, no. 22, pp. 5727-5732, 2015.

Chapter 2

2. Experimental methods

2.1. Synthesis methods

2.1.1. Chemical solution deposition

Chemical solution deposition (CSD) is a facile and economical method for sample synthesis. The relatively low cost of apparatus and chemical precursors needed for CSD allows for the easy synthesis of relatively large sample sets. For example, as shown in the work presented in chapters 3 and 4 of this thesis, an extensive series of Aurivillius phase samples having different stoichiometries can be made and then subjected to analysis. In this way a wide range of materials can be screened such that the most promising materials can then be selected for synthesis via more specialised vacuum-based growth techniques. In this work, CSD was used to produce an extensive set of samples which facilitated the investigation of how changes in chemical composition affects material structure (chapter 4) and permitted the exploration of new chemical components (such as Niobium in chapter 3) before investing in the more costly precursors required for vacuum-based growth techniques.

In CSD, the precursors are initially maintained in solution. Following this, the deposition and heat treatment steps are performed to form the product material. In this work the precursor solutions for CSD are prepared in organic solvents and when spin coated and heated form a film of the Aurivillius material. CSD is a growth method that relies on mixing the correct ratio of precursors so as to achieve the desired stoichiometry [1]. The stoichiometry can thus be easily controlled by varying the amount of precursor used. The general procedure used for chemical solution deposition of Aurivillius materials used throughout this work is shown in figure 1. This recipe is based on previously published work [2]. The precursor materials and solvents were chosen as they readily dissolve the precursors and produce stable solutions without precipitation. The precursor materials have chelating ligands that allow for the desired reactions to occur while also not engaging in side reactions while in solution. The ligands must also be effectively removed by evaporation of the

solvent during the heat treatment steps so as not to produce carbon contaminates in the thin film material.

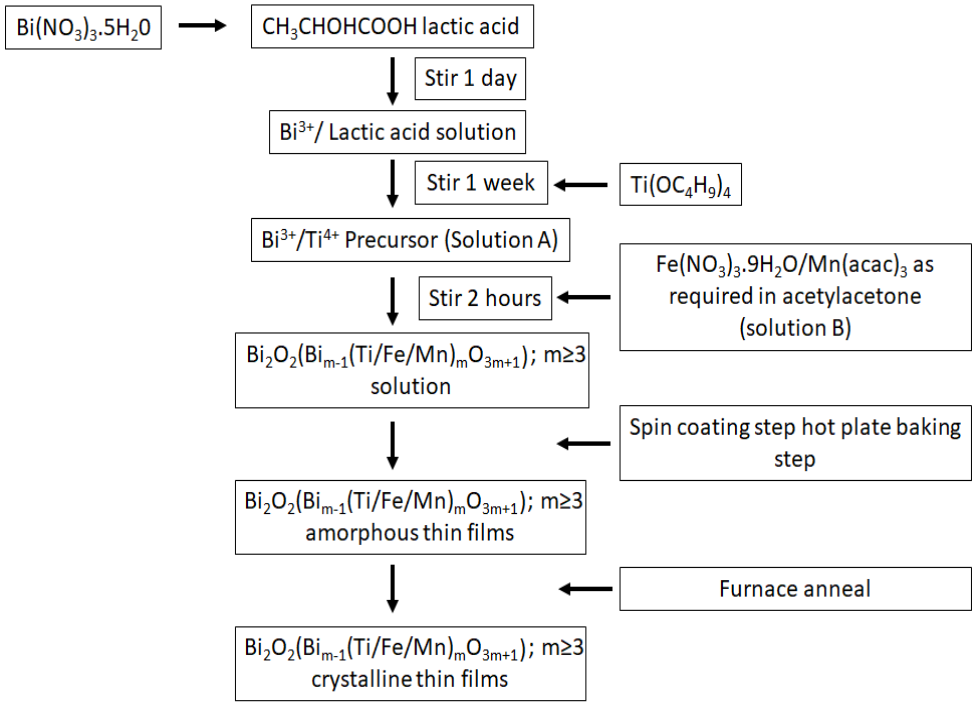

Figure 1: The stepwise recipe for the chemical solution deposition of BTFMO Aurivillius materials.

The precursors used are shown in figure 2 (a-g). The bismuth precursor is bismuth (III) nitrate pentahydrate $Bi(NO_3)_3.5H_2O$ (reagent grade, 98 %, Sigma-Aldrich) and was weighed out in the correct amount necessary to have an excess of 17.5 % Bi present in the solution. Having an excess of Bi is a common precaution taken to compensate for the volatility of Bi. The optimal excess Bi content was determined in a previous study involving the chemical solution deposition of Aurivillius compounds [2]. The Bi precursor was added to lactic acid $C_3H_6O_3$ (ACS reagent, ≥ 8 5%, Sigma-Aldrich) in a 50 ml beaker with a magnetic stirrer bar and covered with Parafilm. This solution was left to spin at room temperature for approximately 24 hrs. The Ti precursor titanium (IV) butoxide $Ti(OC_4H_9)_4$ (reagent grade, 97 %, Sigma-Aldrich) was then weighed and added to the solution. This was labelled as solution A and it was allowed to stir continuously for approximately one week. After that week, solution B was made. The Fe precursor, iron (III) nitrate nonahydrate $Fe(NO_3)_3.9H_2O$ (ACS reagent, ≥ 98 %,

Sigma-Aldrich), was weighed and dissolved in acetylacetone (≥ 99.5 % (GC), Sigma-Aldrich) and allowed to stir for one hour until fully dissolved. If either manganese (III) acetylacetone $Mn(acac)_3$ (99.9+ %, Strem Chemicals, Inc.) or niobium (V) ethoxide ($Nb(OC_2H_5)_5$) (99.9+ %, Strem Chemicals, Inc) was being added they would be added after the Fe precursor had been fully dissolved (figure 3 (a)). Additional precautions were taken when using the Nb precursor as it is air sensitive. The Nb precursor was stored in a nitrogen environment and was added to the solution while been maintained within a nitrogen filled glove bag (figure 3 (b and c)).

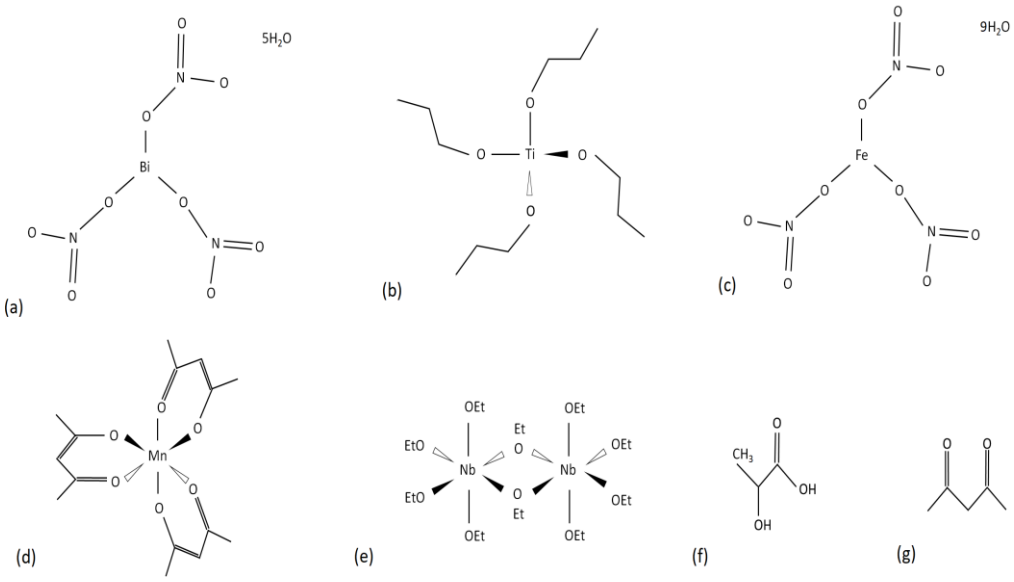

Figure 2: The precursors used in this work during chemical solution deposition. $Bi(NO_3)_3.5H_2O$ (a), $Ti(OC_4H_9)_4$ (b), $Fe(NO_3)_3.9H_2O$ (c), $Mn(acac)_3$ (d), ($Nb(OC_2H_5)_5$) (e), lactic acid $C_3H_6O_3$ (f) and acetylacetone $CH_3COCH_2COCH_3$ (g).

When all the precursors were added, solution B was allowed to mix for a further hour. Then solution B was added dropwise into solution A while it was still stirring gently on the magnetic stirring plate. The combined solutions were allowed to mix thoroughly for one hour. The solution was passed through a 5 µm nylon filter attached to a syringe and transferred to a glass bottle with a screw cap for storage. Filtering was performed to remove any large particulates such as dust particles.

The thin films were deposited on the same day that the final solution was made. The solution was deposited by spin coating (figure 3) the solution onto 2-inch diameter sapphire wafer substrates (University Wafer Inc.). The instrument used was the SCS 6800 spin coater series. The substrates were first preheated on a thermocouple-controlled aluminium (Al) block attached to a hot place maintained at 300°C (figure 4 (d)). This was to remove any surface moisture, e.g., ambient H_2O. The substrate was allowed to cool for a minute and then placed onto the chuck of the spin coater. If the substrate was still hot when the solution was applied, there could be issues with incomplete coverage of the film over the substrate resulting from the rapid, forced evaporation. The solution was drawn into a syringe and a 5 µm nylon filter attached. Several drops, (1-2 ml), which was enough to cover the substrate, were dropped from the syringe onto the sapphire substrate. The substrate was then spun with the typical setting being 2000 rpm or 30 seconds. The substrate with the freshly deposited film was then removed and placed on the Al block heated to 300 °C. This pre anneal step was maintained for ten minutes and was performed to remove the organic ligands and solvents. The boiling point of acetylacetone is 138 °C and 122 °C for lactic acid. The boiling point of the organic precursors bismuth (III) nitrate pentahydrate 80 °C, titanium(IV) ethoxide 150 °C, manganese (III) acetylacetone 160 °C and niobium (V) ethoxide 142 °C. During this anneal step, the sample colour changed from dark brown to a dull yellow (figure 4 (e)). The sample was removed and allowed to cool before being placed carefully in its sample box.

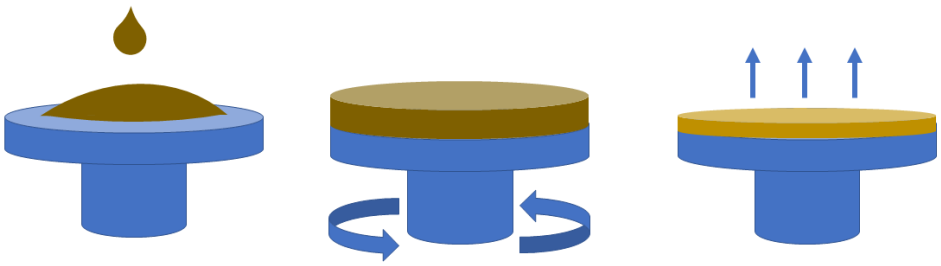

(a) (b) (c)

Figure 3: Diagram of the steps involved in the spin coat process, (a), several drops of the precursor solution are dropped into the substrate, (b), the chuck spins and (c), evaporation of the solvent occurs producing a thin film.

Since the as-deposited samples were found to be polycrystalline, further annealing was necessary in order to crystallise the material. To do this, the samples were annealed under atmospheric conditions in a laboratory furnace (Thermo Scientific Thermolyne industrial benchtop muffle furnace) at 850 °C for 1 hour. The furnace was left to cool down slowly to room temperature before the sample was carefully removed.

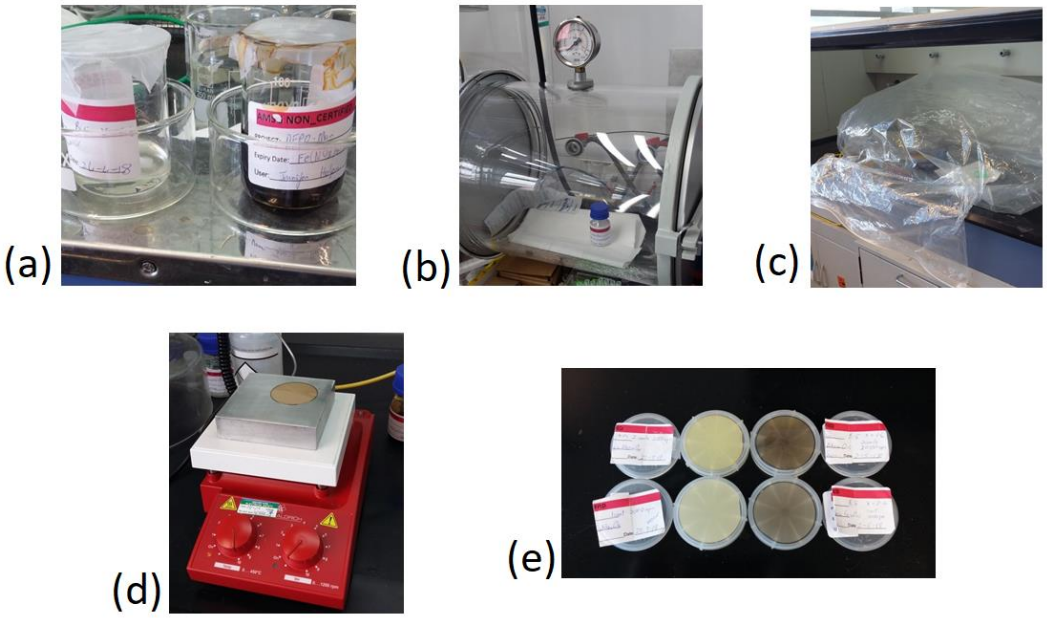

Figure 4: (a), Solution A (left) and Solution B (right) on a magnetic stirring plate, (b), storage of the Nb precursor under nitrogen in a glove box, (c), the glove bag filled with nitrogen containing the precursor solutions, (d), the Al block on hot plate and (e), the samples before annealing step (right) and the samples after annealing step (left).

CSD is a versatile deposition method but has its drawbacks such as difficulty in reliably making continuous ultra-thin films (< 30 nm) [3]. The crystalline Aurivillius

platelets produced using the method outlined above had a range of thicknesses from 28 to 84 nm. The thickness of the materials can be controlled through the viscosity of the solution, the rotation speed and duration the spin coating process to produce thicker films. However, a more suitable deposition method for producing continuous ultra-thin films on epitaxial substrates is chemic vapour deposition.

2.1.2. Chemical vapour deposition

Chemical vapour deposition (CVD) is a general term used for deposition techniques that use gaseous precursors to deposit a film of solid material on a substrate. The gaseous precursors react on or near the substrate through a chemical reaction to produce the solid material. There are a range of techniques that belong to the CVD family such as direct liquid injection CVD, metal-organic vapour CVD, atmospheric pressure CVD, low pressure CVD, ultra-high vacuum CVD, aerosol-assisted CVD, microwave plasma assisted CVD and atomic layer deposition (ALD) [4].

The principal of action of CVD is that a flow of gaseous precursors is passed over a substrate and a chemical reaction occurs either near or on the substrate to form a solid material film over the substrate,

$$Precursor\ reactants_{(g)} \rightarrow Solid\ material_{(s)} + Gaseous\ products_{(g)} \qquad (2.1)$$

The types of reactions than may occur during the CVD processes include, thermal decomposition, reduction, exchange and coupled reactions [4].

In CVD it is very common to engineer the reactor such that a laminar flow of gases is created over the substrate surface. The gas phase precursor reactants flow over the substrate and due to the laminar flow gas dynamics, the gas directly over the substrate will form a stagnant boundary layer. A boundary layer is an area of the fluid (gas or liquid) where the flow velocity, temperature and concentration of the precursor molecules is different to that in the bulk flow. The areas above the substrate can be divided into different reaction zones shown in figure 5. Zone 1 is the stagnant boundary layer where homogeneous reactions occur. Heterogeneous reactions occur in zone 2 at the interface between the gas and the film surface. As

CVD usually uses high temperatures there is sufficient energy available for solid state reactions to occur in the material (zone 3). The substrate may also be involved in reactions in zone 4 and 5.

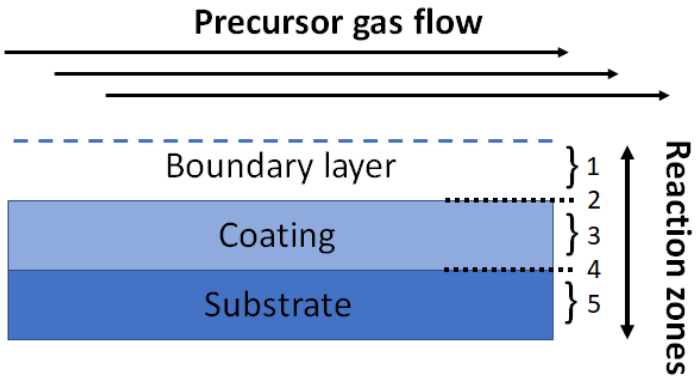

Figure 5: Diagram showing the different reaction zones present over the substrate in a typical laminar flow CVD process; (1) stagnant boundary layer, (2) substrate surface interface heterogeneous reactions, (3) bulk material, (4) substrate film interface and (5) substrate.

The physiochemical reaction steps of CVD are depicted in figure 6. Initially the precursors are evaporated and transported over the substrate using a carrier gas which may be either inert or reactive. The gas phase homogeneous reactions occur in the boundary layer above the substrate and precursor reactants or the products of homogeneous reactions are transported to the substrate surface (mass diffusion) where adsorption occurs. Heterogeneous reactions occur between the gas phase reactants and the surface. Then solid-state reactions occur, with diffusion and nucleation of the material on the substrate to form a film. This is followed by the desorption and removal of excess materials and any by-products.

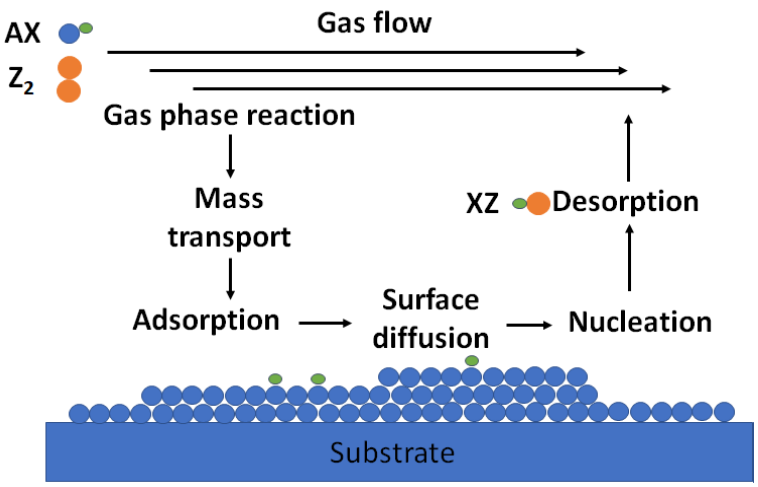

Figure 6: Diagram showing the physiochemical reaction steps of a theoretical CVD reaction. Molecules AX and Z_2 are introduced in the gas flow. Adsorption occurs of AX at the surface. The ligands X are removed through a reaction with Z_2.

CVD instruments can be divided into hot and cold wall reactors. In hot wall reactors, the walls of the reactor are heated as well as the substrate. This means that reactions can also occur on the walls of the reactor. A build-up of material on the reactor chamber walls may lead to contamination and introduction of impurities to the material being deposited on the substrate. Homogeneous reactions in the gas flow may also occur. In cold wall reactors, only the substrate is heated. This reduces the risk of contamination from previous growth runs, however the large temperature gradient can affect the fluid dynamics within the chamber and may lead to uneven coverage on the substrate.

CVD has several advantages over CSD, such as deposition at higher temperatures (100 °C to 1300 °C [5]), which can eliminate the need for a post anneal step. CVD enables deposition of thin films of uniform thickness, low porosity and is suitable for scaling up to cover large surface areas (15 x 4 inch or 8 x 6 inch wafers [6]). Epitaxial films can be readily grown using CVD due to the high temperatures and low supersaturation of precursor chemicals. The energy supplied by a high deposition temperature results in a high surface mobility of the absorbed material at the substrate and allows the material to adopt an epitaxial relationship to the substrate.

In selective area CVD, an area of the substrate is selectively deposited either through the uses of masks or by locally energising an area through microwaves or lasers. A disadvantage of CVD over CSD is the higher cost of equipment and precursors and the limited number of precursor injection lines, which limits the number of precursors that can be attached to a CVD kit. For example, our instrument, the AIXTRON AIX 200/4FE DLI-CVD, has four precursor lines.

CVD is particularly suited for the deposition of our Aurivillius thin films as it has a higher oxygen pressure than other techniques such as pulsed laser deposition (PLD), molecular beam epitaxy (MBE) or splutter deposition. The higher oxygen pressure helps to prevent migration or desorption of volatile elements such as Bi which can cause the formation of impurity phases in the material [3].

Important parameters in CVD that affect the quality of the film produced include the nature of the precursors, the growth temperature and the reactor pressure. In terms of precursor, ideal precursors will be volatile at moderate temperatures, be nontoxic with a long shelf life and will be easy to handle. In addition they will possess a high chemical purity, give a high yield, will be compatible with other precursors and will display a sufficiently large difference between its decomposition and evaporation temperatures [7]. The precursors used during this work are shown in figure 6. The precursor materials were dissolved in toluene with the $Bi(THD)_3$, $Ti(O\text{-}iPr)_2(THD)_2$, and $Fe(THD)_3$ (supplier Epivalence Ltd) having a concentration of 0.1 M (where THD represents tetramethylheptanedionate and O-iPr represents isopropoxide). The $Mn(THD)_3$ chemical (supplier STREM chemicals) was dissolved in toluene with a concentration of 0.025 M. An advantage of liquid injection CVD is that the precursor containers do not need to be heated and this extends their shelf life.

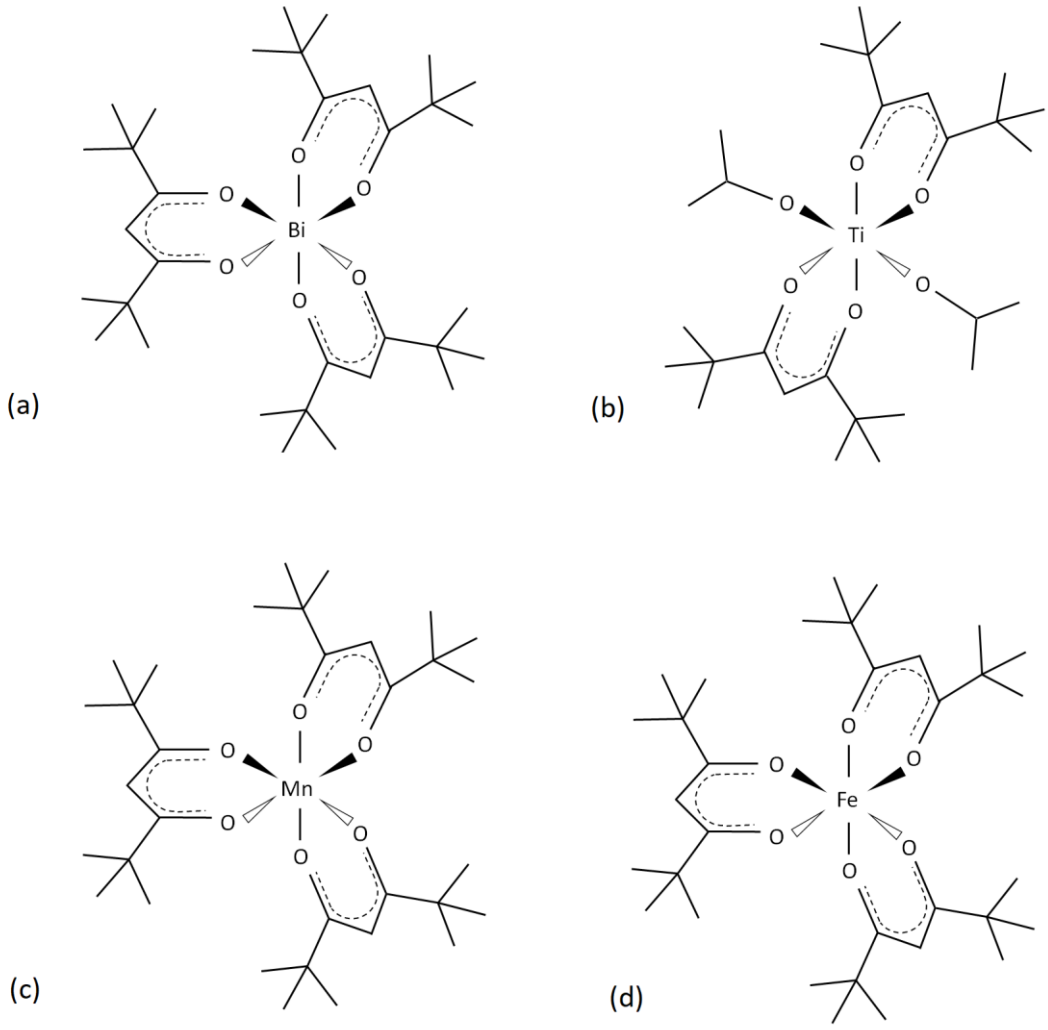

Figure 7: Precursors used during chemical vapour deposition,(a), $Bi(THD)_3$, (b), $Ti(O\text{-}iPr)_2(THD)_2$, (c) $Mn(THD)_3$ and (d) $Fe(THD)_3$.

The temperature of the reaction must be sufficient to provide the necessary energy required for reactions to take place and for the evaporation of the precursors into the gas phase. If the rate limiting step of a reaction is thermodynamic, the growth rate is controlled by the temperature. If the temperature is too high the material may begin to desorb form the substrate or unwanted side reaction may occur (figure 8).

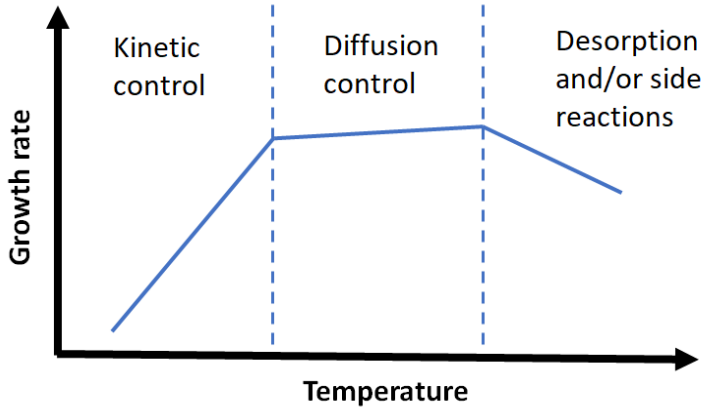

Figure 8: The effect of temperature on the growth rate of a material. Kinetic control, diffusion control and desorption from the substrate of pre-reactions in a typical CVD process.

Pressure affects the gas flow patterns which can lead to non-uniform coverage. At low pressures, gas molecules have a longer mean free path than at higher, e.g. atmospheric pressures. A shorter mean free path of precursors at higher pressures can lead to gas phase reactions. Low pressure allows the gaseous precursors to reach the thinner stagnant boundary layer to prior to reaction at the surface of the substrate.

The CVD system used throughout this work was a direct liquid injection CVD system (DLI-CVD). In DLI-CVD the precursors are liquid, or, as in our case, solids dissolved in a solvent [7]. The liquid (the solution) is injected directly into a vaporiser to produce an aerosol. The instrument used throughout these experiments was the AIXTRON AIX 200/4FE DLI-CVD system. Figure 9 and 10 shows some photographs of parts of the reactor.

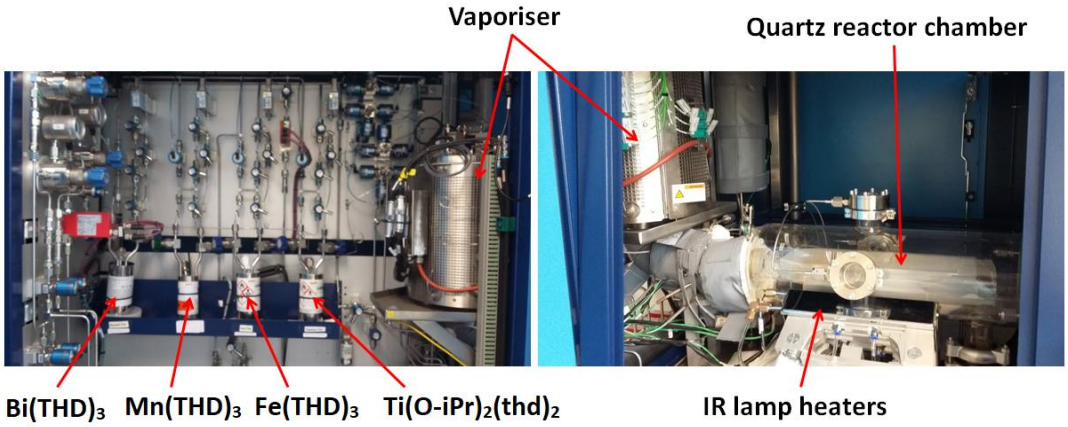

(where THD = 2,2,6,6-tetramethyl 3,5-heptanedionate; O-iPr = isopropoxide)

Figure 9: Photographs of the Aixtron CVD kit used in this work. The precursor bottles and lines connected to the vaporiser (left picture) and the reaction chamber and heating lamps (right picture).

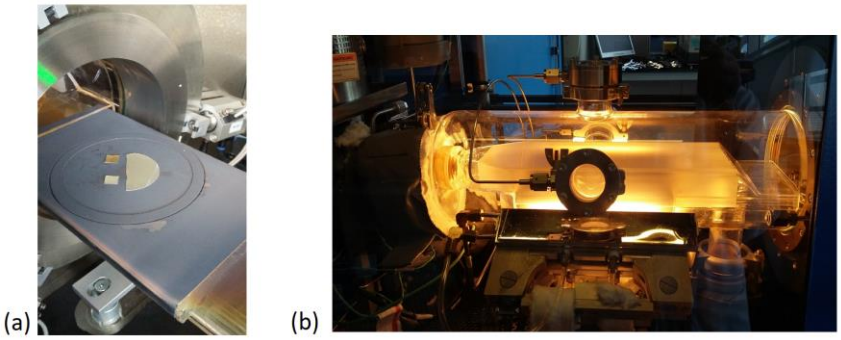

Figure 10: Pictures of the susceptor plate with samples on it before being closed (a) and IR lamps heating the reaction chamber during a growth run (b).

The layout of the Aixtron system is shown in figure 11. The precursor solutions are contained in stainless steel containers. The precursor solution is injected into the vaporiser with flow meters controlling the volume of precursor being injected. A TriJet™ evaporation unit is used on this Aixtron kit. This is a non-contact evaporation system which means a flow of nitrogen gas along the walls of the unit prevents contact between the precursors and the surface of the vaporiser. This helps to prevent undesirable reactions occurring on the surface of the vaporiser walls. The precursors are vapourised within the TriJet™ evaporation unit and the gaseous flow

is introduced to the reaction chamber. The lines are kept at an elevated temperature to prevent condensation and blockage. The reaction chamber consists of a quartz liner and rotating susceptor plate where the substrate is placed. This system is a hot walled reactor meaning the deposition of material occurs on the walls of the quartz liner. The instrument is designed to minimise this by directing most of the reactants over the substrates. The quartz liner is removed periodically and cleaned in 1 M HCl to remove any build-up of material. With these precautions in place, reactions at the hot-wall have not become an issue affecting the quality of our thin film samples. The chemical precursors, in oxygen and nitrogen gas, flow over the substrate and are removed through the exhaust system. The vacuum pump creates the low-pressure environment in the reaction chamber. Unreacted precursors and by-products are removed by a scrubber system to prevent the release of potentially toxic or harmful chemicals to the environment.

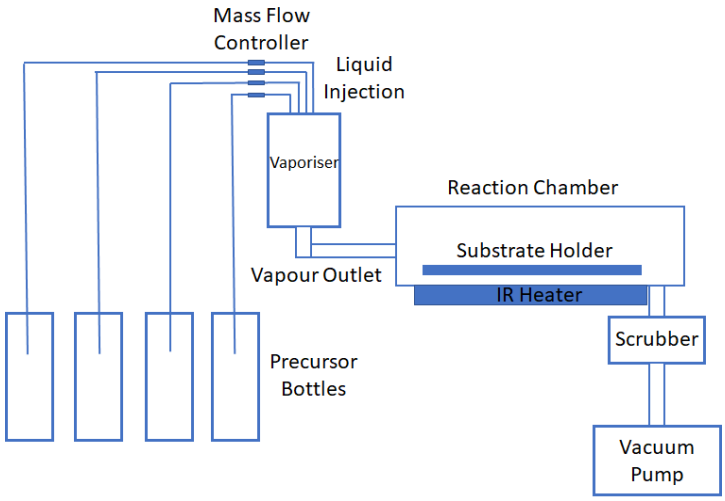

Figure 11: Schematic of the setup of the liquid injection-chemical vapour deposition system.

Various parameters can be changed and the CVD recipe tailored for a particular growth run to influence the material being deposited.

- Pulse frequency - the number of pulsed injections per second. This parameter influences the growth rate.
- Number of pulses - determines the thickness of the films deposited.
- Valve opening times – the stoichiometry of the Aurivillius materials is controlled through control of the ratio of precursor solution volumes. The volume of precursor is controlled through the valve opening times.
- Temperature – sufficient energy must be present for the desired reaction to proceed. Temperature can also affect grain growth size.
- Offset – the pulsed injections can be offset in time to control the order that precursors are introduced into the reaction chamber

The use of different offset parameters was used in the work in this thesis (chapters 5 and 6). This technique was developed in 2004 by Weber *et al* [8] and was named atomic vapour deposition (AVD®). However, as the deposition is not restricted to the deposition of a single atomic layer as in atomic layer deposition (ALD) this name will not be used further. In this work it is called sequential DLI-CVD to distinguish it from conventional simultaneous DLI-CVD. Sequential CVD has been used for the deposition of metal oxide materials such as HfO_2 [9] metal–insulator–metal (MIM) capacitors [10] [11] and in a comparison study between AVD and ALD [12]. Sequential CVD was used to deposit three-layered and four-layered Aurivillius materials $Bi_5Ti_3Fe_1O_{15}$ [13], $Bi_4Ti_3O_{12}$ [14] in previous work.

The difference between conventional simultaneous DLI-CVD and sequential DLI-CVD is depicted in figure 12. This sequential DLI-CVD method was used to mimic the structure of the Aurivillius material and to purposefully drive the occupation the inner perovskite sites of the Aurivillius structure by the Mn and Fe ions. The benefit of this would be to locally increase the concentration of the magnetic ions in the material with the aim of developing materials with long range magnetic ordering, which requires close proximity between the magnetic ions. In this thesis, another growth recipe was developed (figure 12 (c)) that consisted of a constant Bi pulse to prevent a local deficiency of Bi during the growth process (chapter 5).

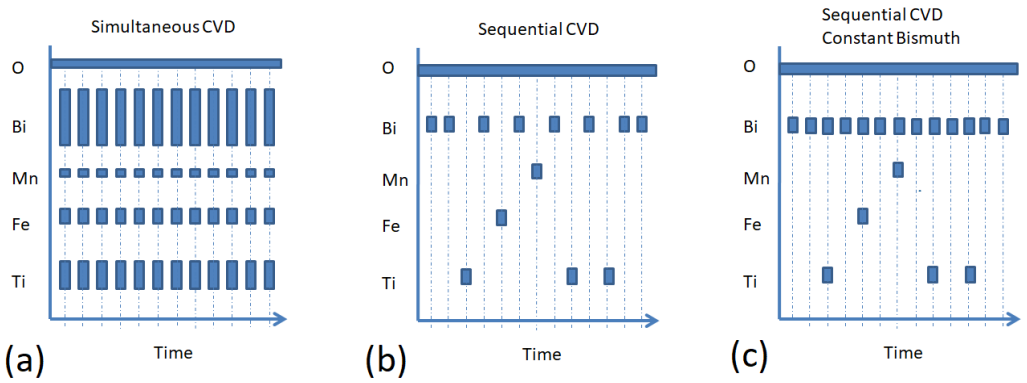

Figure 12: Schematic showing the recipes for the growth of an Aurivillius phase material via the use (a) simultaneous DLI-CVD, (b) sequential DLI-CVD and (c) sequential DLI-CVD with constant bismuth.

As well as variations to the order of the pulse injections in the growth recipe, other parameters that were varied include the growth temperature (chapter 6) and the pulse gap between precursor injections (chapter 5). The typical growth recipe parameters are listed in table 1 and specific details about the growth recipes are provided in chapters 5 and 6. The number of injections corresponds to the thickness of the film produced. For the standard recipe used, consisting of 20 repetitions of the recipe outlines in figure 12, the films produced on LSAT substrates deposited at 710 °C had a thickness of approximately 30 nm.

Table 1

Reaction chamber pressure	9 mbar
Reaction chamber temperature	610 – 710 °C
Vaporiser temperature	220 °C
Precursor line temperature	220 °C
Injector opening times	1 to 10 ms
Injector pulse gap	1, 5 and 10 s
Number of injections per pulse	10

Frequency of injections	1 Hz
Nitrogen flow	2000 sccm
Oxygen flow	1000 sccm

2.2. Structural analysis

2.2.1. X-ray diffraction

X-ray diffraction (XRD) is extremely important for the characterisation of the Aurivillius crystalline materials. XRD can help to identify different crystalline phases and mixed layered phases. In particular for Aurivillius phase materials the number of perovskite blocks between the $(Bi_2O_2)^{2+}$ interlayers can be determined from an X-ray diffraction pattern. The effect of the substitution of atoms with different ionic radii can also be observed in changes to the XRD peak pattern.

The principal underpinning XRD is the interaction of monochromatic X-rays with the ordered array of atoms in a crystalline structure. The monochromatic beam of X-rays is generated by bombarding a metal target (commonly Cu) with an accelerated stream of electrons. The stream of electrons ejects core electron close to the nucleus of the metal atoms. Outer electrons then fall down to fill these vacancies emitting energy corresponding to the energy difference between levels in the process. This emitted energy is in the form of monochromatic X-rays. X-rays (λ = 10^{-11} m to 10^{-8} m) are diffracted from planes of atoms within a crystalline solid (*d*-spacings = 10^{-10} m to 10^{-8} m) and can constructively interfere to produce a diffracted beam. By the analysis of these diffracted X-rays as a function of scattering angle, a crystal structure can be determined. The diffraction of an X-ray beam from a sample under examination enables angle resolved patterns, characteristic to a particular material. The angle at which diffraction peaks appear can act as a fingerprint to identify the material [15].

The angle at which the diffracted X-rays interfere constructively to yield a detected peak at that scattering angle is given by the Bragg condition,

$$n\lambda = 2d \sin\theta \qquad (2.2)$$

Where n is an integer, λ is the wavelength of the X-ray, θ is the angle between the incoming X-ray the sample surface and d is the interplanar spacing (figure 13).

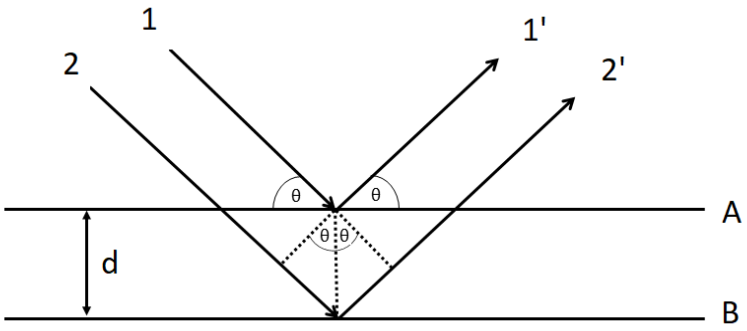

Figure 13: Schematic representation of the Bragg condition. Incoming X-rays 1 and 2 are reflected off the crystal planes A and B in the material, the x-rays are deflected an angle θ and the deflected X-rays 1' and 2' are detected.

A library of patterns, such as that produced by the Joint Committee on Powder Diffraction Standards (JCPDS), can be utilised as a reference source to determine crystal structure. These reference patterns are mostly of powdered samples which tend to be polycrystalline in nature. These have a random orientation of crystallites and so several reflections over a wide range of diffracted angles will be observed. For a thin film sample, there may be a preferred crystallographic orientation and so only certain reflections will be observed. Aurivillius thin films, for example, have a preferred growth axis along the *c*-axis direction and hence the majority of peaks in the XRD patterns of Aurivillius phase thin films are related to the (00*l*) reflections. Information about the material can be obtained from the peak position relative to a reference pattern and the orientation of the crystalline material.

The full width-half maxima (FWHM) of the peaks can be used to indicate periodic structural disorder in layered materials, such as the Aurivillius phases. As the reflection patterns of different *m* Aurivillius phases can occur at similar 2θ values the

presence of intergrowths of two different *m* phases could be observed in the XRD pattern as one broad peak instead of two separate reflections. Therefore, a trend in increased FWHM throughout a series may indicate an increased presence of intergrowths of different *m* Aurivillius phases. A mixture of phases having different inter-atomic spacing may result in X-ray scattering over wider angles, thus resulting in broader and less intense peaks. Detection of the presence of secondary phases is also possible by XRD, provided that the detection limit of the XRD instrumentation is lower than the concentration of secondary phases in the material. At low percent volumes of secondary phases relative to the main sample, peaks or signals corresponding to secondary phases may be lower in intensity than the instrument noise and therefore not visible by the XRD technique. A detection limit of 1-3 volume % was assumed for the XRD instruments used throughout these studies.

Data obtained from XRD can be used to characterise the physical properties of materials. The Lotgering factor (*f*) provides a measure of the orientation distribution of crystallites in a material and can indicate a preference for a particular orientation, e.g. (00*l*) [16]. The Lotgering factor is given by,

$$f = \frac{P - P_0}{1 - P_0} \qquad (2.3)$$

where,

$$P = \frac{\sum I(00l)}{\sum I(hkl)} \text{ and } P_0 = \frac{\sum I(00l)_0}{\sum I(hkl)_0} \qquad (2.4)$$

In these equations, ΣI(*hkl*) is the sum of the intensities from all the peak reflections of the sample under analysis, ΣI(00*l*) is the sum of the intensities of all (00*l*) reflections of the sample and $\Sigma I(00l)_0$ and $\Sigma I(hkl)_0$ are the corresponding values from a randomly oriented sample.

The pseudo lattice parameters of the Aurivillius phase materials can be obtained using the relationship between the orthorhombic system and the interplanar distances from the Bragg condition.

$$\frac{1}{d^2} = \frac{h^2}{a^2} + \frac{k^2}{b^2} + \frac{l^2}{c^2} \qquad (2.5)$$

The relative crystalline factor (Q) was derived from a modified form of the Scherrer equation [17]. The equation is modified because Aurivillius phase materials are orthorhombic and not cubic and so it is not possible to obtain a value for the particle size, but rather the value of Q allows for a comparison of samples to each other:

$$Q = \frac{1}{\beta Cos\theta} \qquad (2.6)$$

Where β is the FWHM (in radians) and θ is the angle of diffraction.

Most of the XRD analysis presented in this thesis are 2θ scans of the Aurivillius materials. 2θ is the angle between the incident X-ray beam and the deflected beam. Other angles that can used for complete analysis of a material are depicted in figure 14. The angle between the plane of the surface and the incident X-ray beam is denoted as ω. The angle φ represents the rotation of the sample around the axis normal to the sample surface and ψ is the angle between the axis normal to the (*hkl*) planes of the material and the diffraction plane.

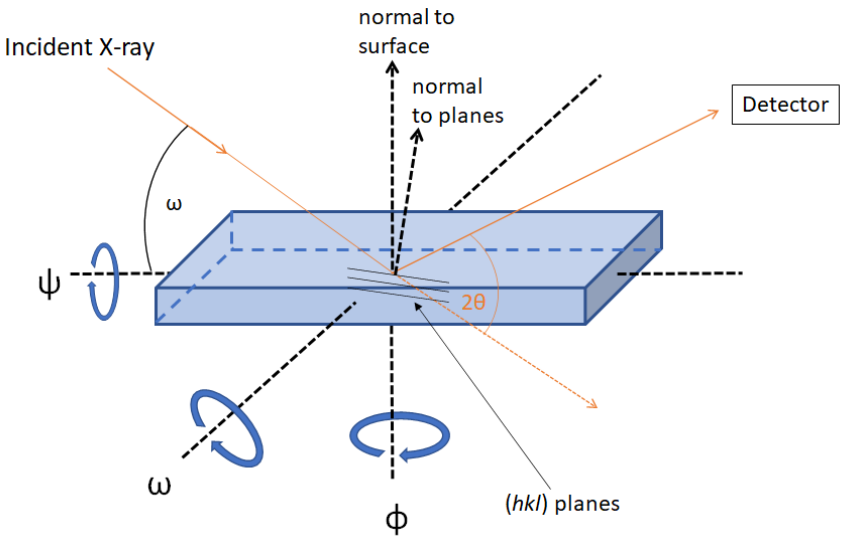

Figure 14: Schematic depicting the four different angles used in XRD analysis.

In this work two different instruments were used to perform XRD structural analysis. A Phillips X'Pert PW3719 MPD diffractometer (Cu Kα radiation λ = 0.1541876 nm)

and a Panalytical X'Pert MRD diffractometer (Cu Kα radiation λ = 0.1541876 nm). The exact experimental conditions employed are provided in the following chapters. The typical scan range was from 6 ° to 40 ° 2θ and a step size of 0.005 °.

Additional XRD analysis was performed in collaboration with the University of Liverpool using a Rigaku Smartlab with a 16 kW Cu rotating anode, a 2-bounce Ge monochromator and a Hypix detector. Out-of-plane scans (standard symmetric $\theta/2\theta$ configuration) and rocking curves (varying ω at a fixed 2θ angle) were performed. The schematic in figure 14 shows the four angles that can be used for XRD analysis. In rocking curve measurements (also called omega scans) the sample is analysed by varying ω at a fixed 2θ angle. Information about the phase purity and crystal quality can be obtained from this type of analysis.

2.2.2. Atomic force microscopy

Atomic force microscopy (AFM) is a type of scanning probe microscopy (SPM) that was first developed in 1986 by Binning, Gerber and Quate [18]. Since then, it has become a valuable tool for the analysis of sample topography at the micron to nanometre scale. Materials such as semiconductors, polymers or biological materials can be imaged using this technique [19]. AFM has advantages over SPM as it does not need to be performed under vacuum conditions and does not require conductive samples. AFM utilises the interactive forces between the cantilever tip and the samples surface to produce images of the surface topography. The AFM probe is raster scanned across the sample surface and the interactions of the probe tip with the surface forces changes the position of the cantilever. This change is detected by the reflection of a laser light off the flat top of the cantilever into a four-directional photodiode. For example, as the tip interacts with a higher region of the sample, then the amplitude of the cantilever adjusts. This adjustment changes the angle of reflection of the laser. Such changes are detected and used to generate an image of the topological features of the sample surface. The setup of an AFM instrument is shown in figure 15.

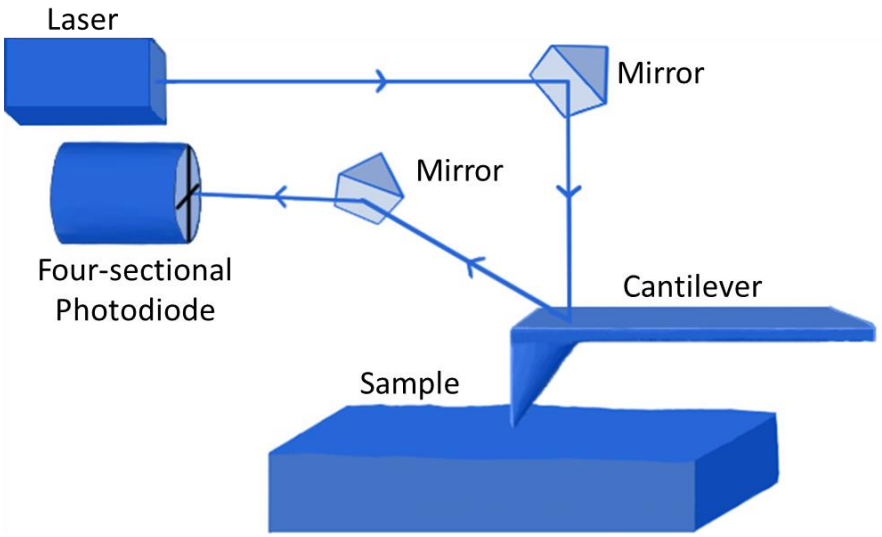

Figure 15: Schematic representation of the set up required for atomic force microscopy

AFM analysis can broadly be divided into two different modes: static and dynamic. The static mode (also called the continuous or contact mode) consists of constant contact between the sample and the probe tip. The dynamic modes include tapping mode (also known as amplitude modulation intermittent contact, AC or vibrational mode), non-contact mode (also known as frequency modulation mode) [20] and Peak-force Tapping mode.

In the continuous mode, the height above and the force between the tip and the surface are kept constant. A computer-controlled feedback system maintains a constant cantilever deflection. The applied voltage is adjusted to maintain constant force and deflection. The adjustments to the phase and amplitude signals are utilised to produce an image of the surface. This method is generally used for very flat and hard samples where contact between the tip and surface will cause minimal damage to either. The closer the AFM probe tip is to the sample surface the more it will deflect as shown in figure 16. As the tip is initially lowered to the surface the voltage is constant, indicating the free air deflection voltage. At the contact point, the tip interacts with the forces exerted from the surface of the sample. The set point

voltage is determined from the contact point and is set by the user. The deflection of the cantilever away from its relaxed position at zero voltage will be associated with a voltage. Deflection towards the surface will be a negative voltage and the deflection away from the surface will be a positive voltage.

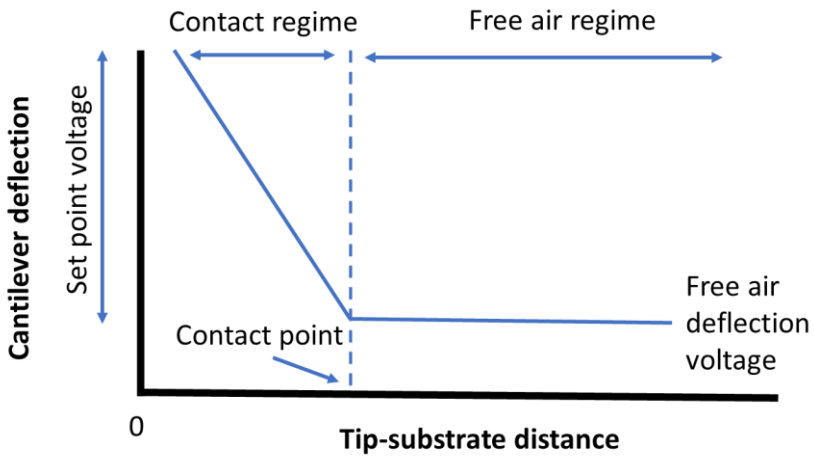

Figure 16: The potential force of intermolecular interactions on approaching the sample surface.

The tapping mode of AFM utilises intermittent contact between the tip and the sample surface. This is a more commonly used measurement technique for AFM topography imaging compared with the constant mode. The tapping mode is particularly useful to overcome potential issues caused by moisture. A film of moisture is common on materials stored and measured in ambient conditions. Capillary forces due to the moisture could drag the tip laterally if it were measured in constant mode. Intermittent tapping also has advantages over constant mode as it generally results in less damage to the probe tip. In this mode the amplitude of the cantilever oscillations is kept constant at or near its resonance frequency. The tip is brought down to the sample surface until it is in the repulsive regime. In the repulsive regime the resonance amplitude of the cantilever decreases the closer the tip approaches the sample surface (figure 17). During raster scanning, the amplitude of the oscillations is monitored and a feedback system is used to keep the oscillation

constant. The change in phase is also monitored. The changes to these two properties are used to produce amplitude and phase images of the material. Height and force images can also be generated during tapping mode.

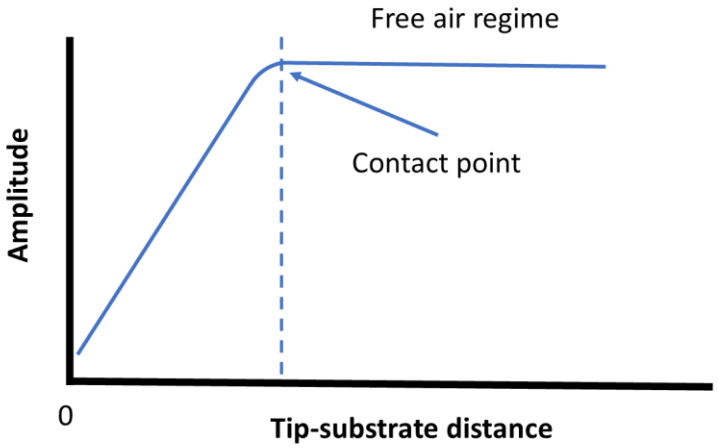

Figure 17: A typical amplitude modulated AFM force plot. The amplitude of the tip oscillation decreases as it approaches the sample surface due to the interactions between the tip and electrostatic, dipole-dipole, piezoelectric and Van der Waal forces.

In non-contact mode, as the name suggests, the tip does not come into contact with the sample surface. The cantilever is kept oscillating at a constant amplitude above the sample at resonance frequency. In the amplitude modulation mode, the resonance frequency of the cantilever is affected by forces from the sample. An attractive force on the cantilever causes a decrease in resonant frequency, therefore the resonant frequency is decreased from the original drive frequency and the amplitude decreases. A repulsive force on the probe causes an increase in resonant frequency, therefore the resonant frequency is increased from the original drive frequency and the amplitude increases. The feedback information required to adjust the drive frequency and maintain constant amplitude is used to produce an image of the surface topography. Soft samples, such as biological samples that could be damaged from contact modes, can be analysed in this way.

Additional AFM analysis in the PeakForce Tapping® mode was used in conduction with the Bruker AFM instrument during this work. Similar to tapping mode, the probe periodically taps the sample surface and by measuring directly the deflection of the cantilever a feedback loop is used to keep forces below 10 pN. This helps maintain the sample and tip integrity and produce high-resolution imaging [21].

An AFM probe consists of a sharp tip on the free end of a cantilever attached to a holder. The tip is usually a few nanometres in scale and the cantilever a few hundred nanometres in scale. The cantilever holder or chip is large enough to be held by the user using tweezers. AFM probes are commonly made from silicon. Coatings can be applied to the probe such as gold, platinum, cobalt or chromium depending on the required imaging mode.

The resolution of AFM is dependent on the shape of the probe tip. A sharper tip will map the surface more closely than a wider tip will (figure 18). However, tips are eroded after repeated use due to contact with the surface. The tip may also "pick up" contaminates from the surface which could produce images that do not accurately reflect the surface topography. Contact between the probe tip and the surface could also damage the sample.

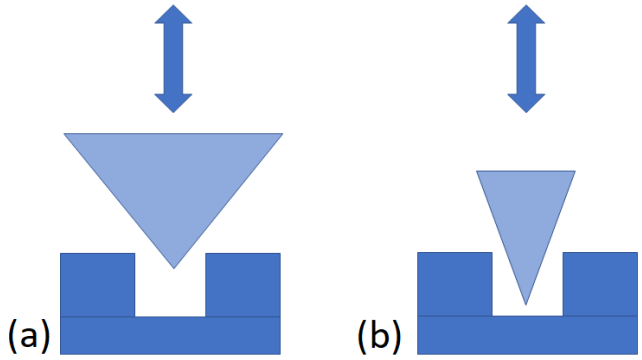

Figure 18: The narrower an AFM probe the closer the tip can map the surface of the material.

The AFM analysis conducted throughout this project, unless otherwise stated, was performed in the AC tapping mode using an Asylum Research MFP-3D AFM

instrument. The first order harmonic resonance frequency is determined before measuring the sample and the drive frequency is set at or near the resonance frequency. The AFM cantilevers used were Olympus AC240TS probes (Al reflex coated, 15 nm tip radius, 70 kHz resonant frequency). Additional AFM images were obtained using a Bruker Dimension Icon AFM instrument in PeakForce Tapping mode. Scan size = 5 x 5 µm or 1 x 1 µm; scan rate = 1 Hz (sometimes 0.5 Hz was used); Scan angle = 0 ° or 90 °. The AFM probe used in these measurements was a Bruker SCANASYST-AIR probe, Al reflex coated, 2 nm tip radius, 70 kHz resonant frequency. The narrow tip of these probes allowed a greater level of detail belonging to the surface to be imaged (figure 18).

2.2.3. Piezoresponse force microscopy

The Aurivillius materials are well known ferroelectrics [22] and this behaviour was examined throughout this work using piezoresponse force microscopy (PFM). The converse piezoelectric effect is a change in the structure of a material when subjected to an applied electric field. Piezoresponse force microscopy (PFM) is an analysis technique first developed in 1992 by Güthner and Darnsfeld [23]. PFM exploits the converse piezoelectric effect to visualise ferroelectric domain patterns in piezoelectric materials. All ferroelectric materials are also piezoelectric and pyroelectric. In the PFM technique, an electric field is applied which is lower than the coercive field of the material. This probing signal, V_{ac} causes local mechanical strain and distortions in the piezoelectric sample due to the converse piezoelectric effect (figure 19). The material can locally expand or contract under the applied electric field. To perform PFM analysis, an Asylum Research MFP-3D AFM instrument was used in this work and the probes used were Olympus AC240TM electrilevers (Ti/Pt coated silicon probes, Al reflex coated, 15 nm tip radius, 70 kHz resonant frequency)).

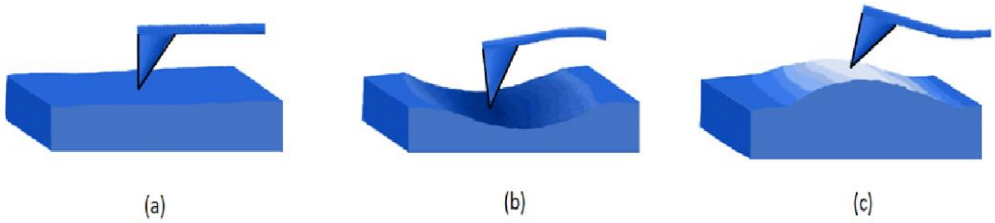

Figure 19: In piezoresponse force microscopy a locally applied electric field causes deformation of the material. This is shown for vertical PFM (a), no applied electric field, (b), contraction and (c), expansion under the applied field.

Ferroelectric materials are defined as materials possessing a spontaneous and reversible electrical polarisation. When an electric field is applied to a piezoelectric material the electric dipoles align along the direction of the applied field. In ferroelectric materials (a subset of piezoresponse materials) the dipoles remain in this aligned position when the electric field is removed and if an electric field is applied in the opposite direction the dipoles will switch to align along that direction [24].

PFM, similar to AFM, uses feedback from the laser light reflected from the cantilever to produce data about the material under study and to examine the relationship between an applied electric field and mechanical strain in the material. This electro-mechanical relationship is described by the converse piezoelectric effect. In the converse piezoresponse effect the vertical displacement of the sample surface under an applied voltage is given by,

$$\Delta z = \kappa(d_{33}V + (Q_{33}/t)V^2) \qquad (2.7)$$

Where z is displacement along the z axis, κ is constant of proportionately, d_{33} is the piezoelectric coefficient, V is the applied voltage, Q_{33} is the electrorestrictive coefficient and t is the sample thickness. The voltage applied to the tip, V_{tip}, is given by,

$$V_{tip} = V_{dc} + V_{ac}\cos(\omega t) \qquad (2.8)$$

Where V_{dc} is the direct current and V_{ac} is the alternating current applied to the conductive tip. Assuming the drive voltage is well below the contact resonance frequency of the cantilever the displacement is given by,

$$\Delta z = d_{33}V_{dc} + d_{33}V_{ac}\cos(\omega t + \varphi) \qquad (2.9)$$

Where ω is the angular frequency and φ is phase.

Application of AC bias to conductive tip during contact mode imaging:

$$V_{tip} = V_{ac}\cos(\omega t) \qquad (2.10)$$

results in surface displacement (*d*) and deflection of cantilever due to converse piezoelectric effect. The general case for the out-of-plane direction is:

$$\Delta Z = \pm d_{zz}V_{ac}\cos(\omega t + \varphi) \qquad (2.11)$$

and for the in-plane direction are:

$$\Delta L = \pm d_{zx}V_{ac}\cos(\omega t + \varphi) \qquad (2.12)$$

$$\Delta L = \pm d_{zy}V_{ac}\cos(\omega t + \varphi) \qquad (2.13)$$

The phase refers to the orientation of the polarisation in domains. Domains are areas where the polarisation aligns in the same direction. The phase can be 0 or 180 ° if the domains are oriented normal to the surface. The phase will determine if the sample locally expands or contracts under the applied field (figure 20). Domains with a polarisation direction normal to the sample pointing up are denoted as c and pointing down as c-. When a positive voltage is applied to a c- domain then it locally expands [25]. The surface oscillations of the sample are in phase with the tip voltage therefore, φ = 0 °. Applying a positive voltage to a c domain will result in the sample contracting. The phase in this case would be φ = 180 ° (figure 20).

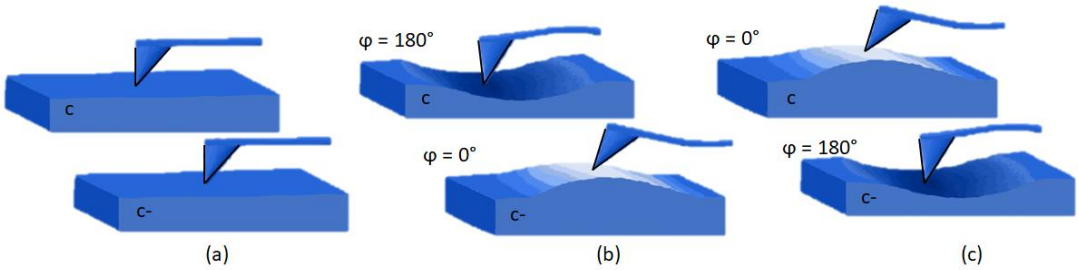

Figure 20: The piezoresponse of a sample during PFM analysis, (a) a material under no applied electric field, (b) the response of a material under an applied positive voltage, the sample expands or contracts depending on the orientation of the polarization within domains and (c) the application of a negative voltage to the same area which results in expansion or contraction.

Single frequency measurements were used to analyse the vertical (out of plane) and lateral (in plane) piezoelectric response simultaneously. The vertical displacement of the cantilever was detected for vertical PFM (figure 21 (a)) and the lateral displacement of the materials was detected by the torsional bending of the cantilever (figure 21 (b)). The direction of the tip displacement provides information on the orientation of the polarisation domains [26]. In this work, both the vertical and lateral measurements are performed at a single frequency of 15 kHz.

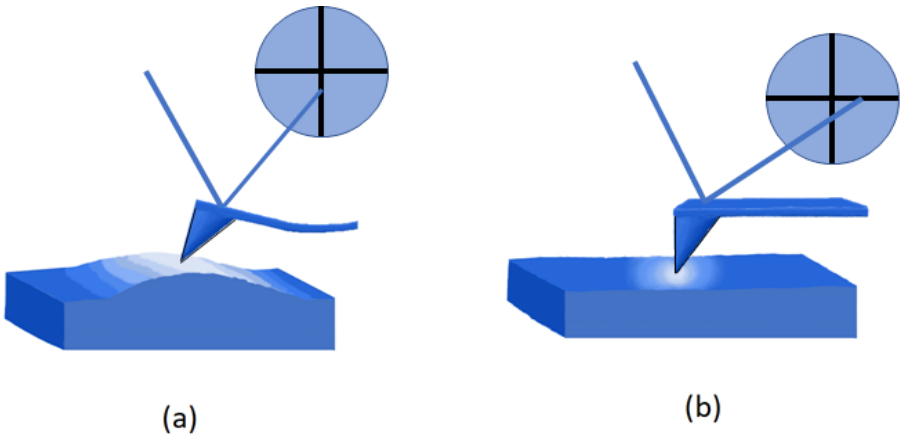

Figure 21: PFM measurements in the vertical (a) and lateral (b) mode. In the vertical mode the tip is deflected along the vertical axis and is detected in the four dimensional photodiode. In the lateral mode the lateral distortion of the sample under the applied electric field results in torsional twisting of the cantilever which is detected along the horizontal axis of the four sectional photodiode.

The typical piezoresponse displacement of a sample surface is in the range of a few picometres and PFM measurements can be hampered by a low signal-to-noise ratio. To improve the signal-to-noise ratio the drive amplitude (V_{ac}) can be increased, but this may damage a sample or the tip. To improve measurements of samples having a low piezoresponse, a method known as Dual AC-Resonance Tracking - PFM (DART-PFM) [27] has been developed by commercial AFM developers. DART-PFM uses a feedback system to detect cantilever deflections and reduce the influence of instrumental cross talk. Using this method, it is possible to measure samples with a small piezoresponse without the need for a large voltage which may cause damage to the sample. The small piezoresponse signal is boosted by measuring at the cantilever resonance frequency. Due to resonance enhancement, this provides a larger signal. However the drawback to imaging at contact resonance is that measurements are affected by cross talk with topography as the tip moves over the sample surface. Changes in the sample surface can shift the frequency, causing the measured amplitude to either decrease or increase and therefore can introduce errors to the analysis. In DART-PFM, this is counteracted by using the feedback mechanism, using an amplitude feedback loop which tracks the contact resonance frequency as shown in figure 22. Changes to the amplitude ($A_2 - A_1 \neq 0$) are detected and used as input feedback to adjust the resonance drive frequencies, thereby maintaining constant amplitude as the probe scans over the sample surface. The DART-PFM mode was used to measure the vertical and lateral piezoresponse of the Aurivillius materials to examine the out-of-plane and in-plane polarisations of the materials. When measuring in the vertical mode, the cantilever is tuned with drive frequencies operating near contact resonance for the vertical (280-350 kHz) mode.

When measuring in the lateral mode, the cantilever is tuned to the drive frequency operating near contact resonance for the lateral mode (650 to 700 kHz).

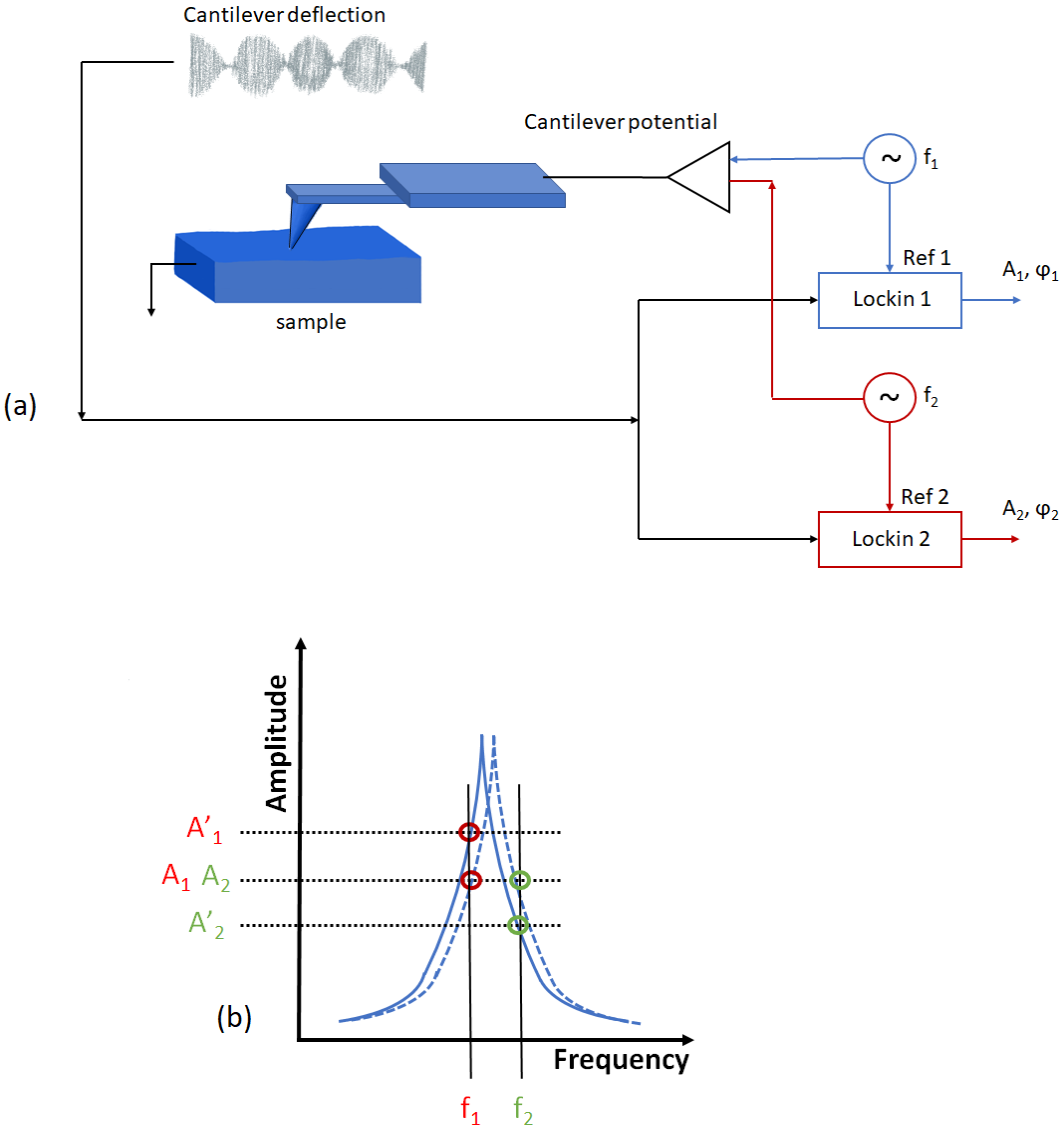

Figure 22: A schematic of DART- PFM showing, (a), the feedback loop used to correct changes to the resonance frequency to reduce the effects of instrumental cross talk and boost the piezoresponse signal and (b) changes to the measured amplitude are detected and used as input feedback to adjust the resonance drive frequencies as the probe scans across the changing sample surface.

Variable magnetic field PFM (VMF-PFM) was performed using the Variable Field Module2 (VFM2) compatible for use with the MFP-3D (AFM). The VFM2 uses a rare earth magnet to produce a magnetic field (figure 23), with the strength of the magnetic field applied to the sample depending on the rotation angle of the magnet. For analysis of the Aurivillius materials, PFM of the materials was performed while varying the strength and direction of the magnetic field. Measurements were taken at 2500 G to -2500 G in 500 G intervals. The rotation of the magnet was stopped during PFM measurements and maintained at a constant magnetic field to avoid interference due to mechanical movement of the magnet during imaging. Polarisation domains were monitored by PFM at a particular magnetic field strength in order to determine if a change in the polarisation direction was occurring. This would indicate whether ferroelectric polarisation could be switched by an applied magnetic field and thus enables nano-scale investigations of whether a material displays magnetoelectric properties.

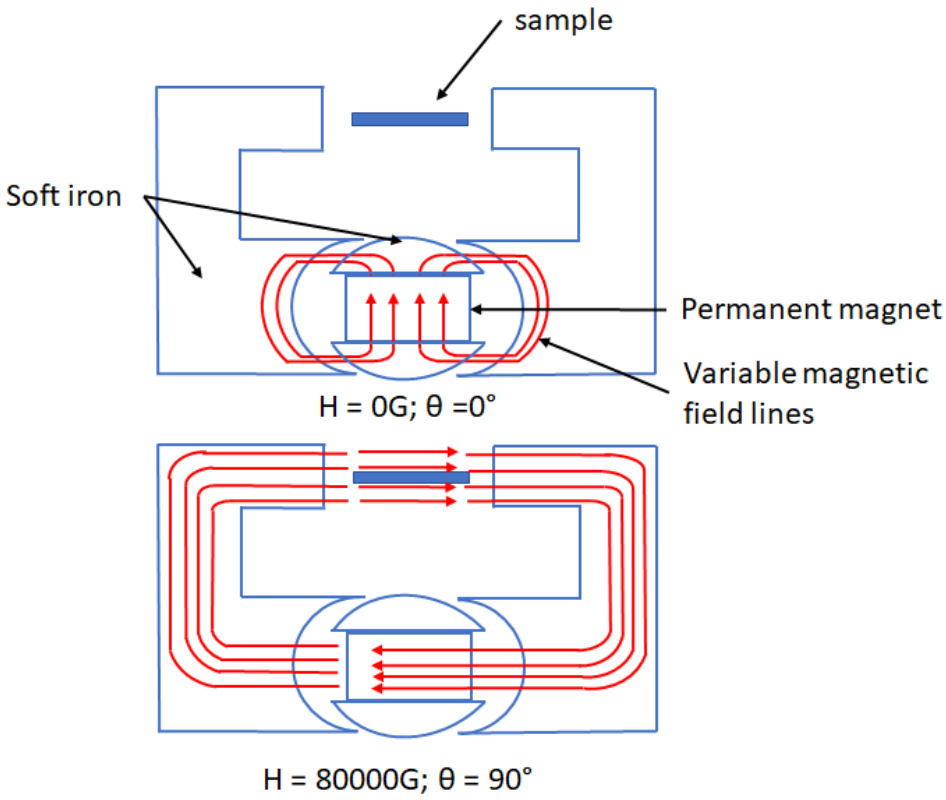

Figure 23: A schematic diagram depicting the setup of the VFM2. When the rare earth magnet is at 0 ° or 180 °, the magnetic flux is directed away from the sample.

As the magnet rotates, increased magnetic flux is directed at the sample with maximum magnetic field magnitude at 90 ° or 270 °. Adapted from [28].

2.2.4. Scanning electron microscopy

Scanning electron microscopy is a non-destructive analysis technique that is used to determine the topography and morphology of a material [15, 29]. Electrons are negatively charged, low mass particles that can be deflected by Coulombic or electrostatic interactions with the positively charged nuclei or other electrons of atoms. An incident electron, from a beam of highly charged energetic electrons, excites an electron in the sample (losing some of its energy in the process). The excited electron travels towards the surface of the sample and if it has enough energy, it excites the surface and is called a secondary electron. The detection of these secondary electrons is the basis of electron microscopy.

The limitation of what scale can be measured by any form of microscopy is determined by the 'wavelength' of the probe used. For optical microscopy the resolution limit is given by the Rayleigh criterion,

$$\delta = \frac{0.61\lambda}{\mu \sin \beta} \qquad (2.14)$$

Where λ is wavelength of the light, μ is the refractive index of the viewing medium , β is the semi-angle of collection of the magnifying lens and δ is the resolution for the light microscope [30]. Visible might microscopy cannot image at the atomic scale as the wavelength is too large (380 - 750 nm). However, when electrons are accelerated under a high potential, they have a smaller wavelength and can image in the nanometre range. An electron gun, consisting of a filament of tungsten, is used to generate the beam of electrons. Electromagnetic lenses are then used to focus the electron beam onto the sample.

A beam of accelerated electrons (primary electrons (PE)) will interact with a sample in a number of possible ways.

- Elastic scattering or backscattering electrons (BSE): PE are reflected with a change in direction but with the same energy.
- Inelastic scattering of secondary electrons (SE): PE interact with the material and SE are emitted from the outer shell of the atoms in a different direction and with less energy than the PE.
- The emission of X-rays will occur after the interaction of primary electrons with the sample matter.
- The emission of characteristic Auger electrons will occur after the interaction of PE with the sample matter

SEM principally uses the detection of secondary electrons to produce an image of the sample surface. Secondary electrons are more sensitive to the topography of the sample than back scattered electrons. The contrast of the image is determined by the number of electrons that leave the material and reach the detector.

The SEM instrument used throughout this work was the Zeiss Supra 40 SEM which requires the use of a conductive material to prevent the build-up of charge on the materials. For insulating materials such as the Aurivillius materials, a conductive gold layer was applied to the surface by sputter coating.

2.2.5. Transmission electron microscopy

Transmission electron microscopy (TEM) is another form of electron microscopy performed under high vacuum. As in SEM, a beam of electrons is generated using an electron gun. In TEM this high-powered beam of electrons is fired through a thin lamella of the sample and the interactions of the electrons which pass through the sample are detected and used to construct an image of a cross section of the material [15]. The resolution of TEM can allow imaging on the atomic scale and provides valuable information on the crystal structure, such as the presence of stacking faults or out-of-phase boundaries which can occur in Aurivillius materials.

For TEM analysis a thin lamella (approx. 100 nm thick) cross section of the sample was prepared. First, electron beam induced deposition (EBID) and ion beam induced

deposition (IBID) were used to deposit protective layers of carbon and platinum on the material. The lamella was further thinned using a focused ion beam (FIB). The instrument used was FEI DualBeam Helios Nanolab 600i. This thin lamella was then imaged using a Jeol TEM JEM – 2100 instrument.

Further TEM analysis was performed at University of Limerick. Scanning transmission electron microscopy (STEM) analysis was carried out using a Thermo-Fisher Scientific double tilt STEM holder in the Thermo-Fisher Scientific FEI double aberration-corrected monochromated Titan Themis Z at the University of Limerick. The microscope was operated at 300 kV. The imaging mode used was STEM at 146 mm camera length with a 50 - µm C2 aperture.

2.2.6. Energy dispersive X-ray spectroscopy

Energy dispersive X-ray spectroscopy (EDS or EDX) uses the X-rays emitted from a material induced by the interactions of primary electrons from an accelerated electron beam. The electron beam ionises the material by ejecting an electron from a core electron shell of the atom. This vacancy is filled by an electron from an outer shell dropping down to the core shell accompanied by the emission of energy [15]. This energy is in the form of X-rays. The X-rays that are emitted from a material are characteristic to that element, since the energy differences between electron shells is different for different elements. The chemical composition of a material can thus be determined by analysis of the X-rays. EDS can be used to detect localised areas of secondary phases that may not be in sufficient concentration to be detected using XRD. When combined with TEM, the individual location of atoms within the crystal structure can be determined. This was particularly useful for the work described in this thesis, as the objective is to determine if there is a preferred occupancy of elements for specific sites within the Aurivillius crystal structure.

EDS was performed using a FEI Helios Nanolab High Resolution Scanning Electron Microscope with attached Oxford X-Max 80 detector and Aztec analysis software.

2.2.7. Optical spectroscopy

Ultraviolet and visible light spectroscopic analysis was performed on selected Aurivillius materials. Adsorption, transmission, and reflection of light (wavelength 280 – 800 nm) by the materials were examined. The interaction of the material with light can inform our understanding of the physical and chemical properties of a material and can enable measurement of a material's band gap. Ultra-violet and visible light spectroscopy are both non-destructive analysis techniques.

The optical measurement in this work were performed on thin film samples grown on sapphire substrates. This can result in the sample coverage, grain size and morphology of the Aurivillius material influencing the results due to scattering effects. To minimise the effects of morphology and particle size, powdered samples can be mixed with reference materials such as KBr and NaCl and pressed into pellets for analysis.

Transmission measurements were performed in chapter 3 with a Perkin Elmer λ950 spectrometer with and integrated sphere attachment. The integrated sphere has a coating of a highly reflective material such as barium titanium/sulfate which gathers light that has been scattered by the material at different angles. Direct reflectance was measured on the Perkin Elmer λ950 spectrometer using a universal reflectance accessory. Diffuse reflectance was determined using an UV-2401 PC recording spectrometer.

The percentage absorbance of the material was calculated using the following equation,

$$\%A = 100 - \%T - (\%R_{direct} + \%R_{diffuse}) \qquad (2.15)$$

The absorption coefficient (α) was calculated from the relationship between the absorbance (A) and the thickness of the film (t),

$$\alpha = 2.303\ \frac{A}{t} \qquad (2.16)$$

and these values were then used to construct a Tauc plot from which the band gap of these materials could be extrapolated. The Tauc expression [31] is given by,

$$(\alpha h\nu) = B(h\nu - E_G)^n \qquad (2.17)$$

Where E_G is the optical band gap energy (eV), B is a scaling constant, n = 1 or 1/2 for direct or indirect transitions, respectively. A value for the band gap can be estimated by extrapolating from the linear part of a plot of $\alpha h\nu^r$ against eV to the x-axis.

2.2.8. Photoelectrochemical analysis

An investigation into the photocatalytic properties of the Aurivillius materials was performed and is discussed in the appendix to chapter 3 of this work. The set-up of this experiment is shown in figure 24. The principle behind this experiment was to monitor the % absorption of light by a solution containing a dye and a piece of the sample. Normal to the beam of white light going through the cuvette was a 365 nm light source that illuminated the samples in the dye solution. If the material was a photocatalytic, then the light would induce charge separation in the material. These charges could then interact will the dye in the water causing it to degrade. As the dye degrades that the % absorption would decrease. The dye used was methylene blue in a 0.1 M solution in MilliQ water (18.2 MΩ cm at 25°C). Methylene blue undergoes a colour change from blue to colourless when it is reduced. The solution (1 ml) was placed in the cuvette and measurements started without illumination. A small stirrer bar was placed at the bottom of the cuvette and set to spin at a slow speed to keep the solution moving but not fast enough to displace the sample when it was in the cuvette. The movement of the solution was required in order to avoid the solution becoming inhomogeneous as dye degradation occurred at the sample surface. After 30 minutes the sample was added to the cuvette carefully so as not to block the beam of white light going into the spectrometer. The cuvette with the sample was left for a further 30 minutes in the dark before the light source was turned on. After 1 hour of measurement the light source was turned off and a further 30 minutes of measurement was performed in the dark. The light was turned on for a further 30 minutes and a final 30 minutes of measurements in the dark. During these measurements, a cover was placed over the set-up to prevent ambient light

interference. This cover had to be removed when the sample was inserted and quickly replaced. The experimental method is similar to that used by Kegel *et al.* [32].

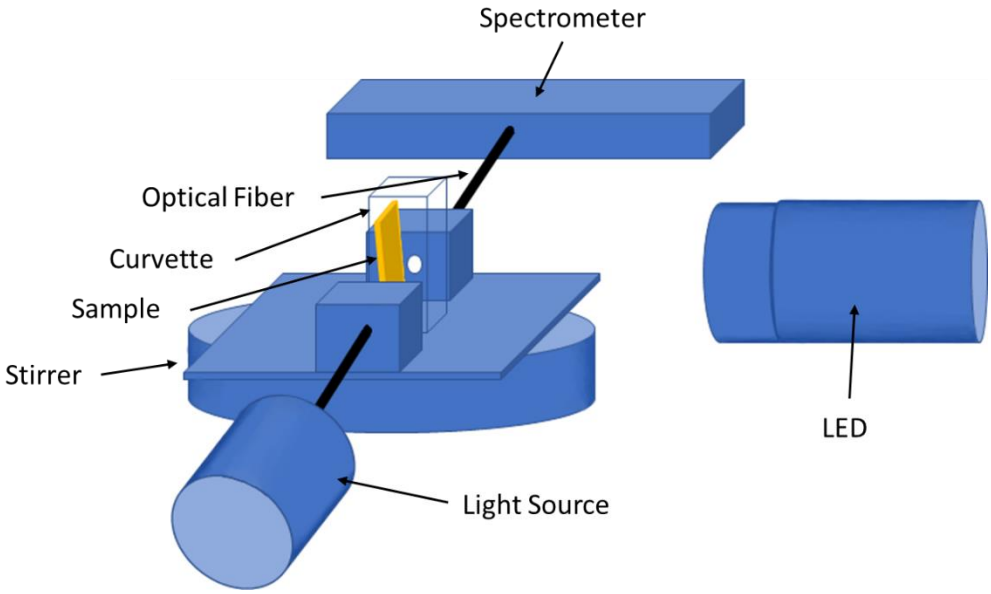

Figure 24: Diagram showing the experimental set up for optical measurements of photocatalytic measurements.

2.2.9. Magnetic measurements

The aim of this body of work was the development of Aurivillius phase materials that exhibit room temperature magnetic properties in addition to ferroelectric properties. To that end, it was important to analyse the magnetic response (M) as a function of temperature (T) and to measure the magnetic response (M) to an applied magnetic field (H). A magnetic field hysteresis loop is depicted in figure 25 (b). Ferromagnetic materials will exhibit a non-linear MH response and a net magnetisation at zero applied field (after the field is removed) and switchable magnetic polarisation behaviour. While paramagnetic and diamagnetic materials will produce a linear response going through the origin.

The magnetic behaviour of selected samples were also examined over a range of temperatures. The samples were cooled from room temperature to 4 K without an applied magnetic field. A magnetic field was then applied and the magnetic moment

measured producing the Zero Field Cooled (ZFC) measurement curve. The magnetic field was maintained and the sample was cooled down to 4 K and then warmed back to room temperature producing what is referred to as the Field Cooled (FC) line, shown figure 25 (a). The remanent magnetisation is the magnetisation remaining when the applied field has been removed [33]. A ferromagnetic/antiferromagnetic material will display a remanent magnetisation between the field cooled and zero field cooled measurements. The temperature at which the FC and ZFC diverge signifies the transition temperature, below which the material exhibits ferroelectric/antiferroelectric behaviour.

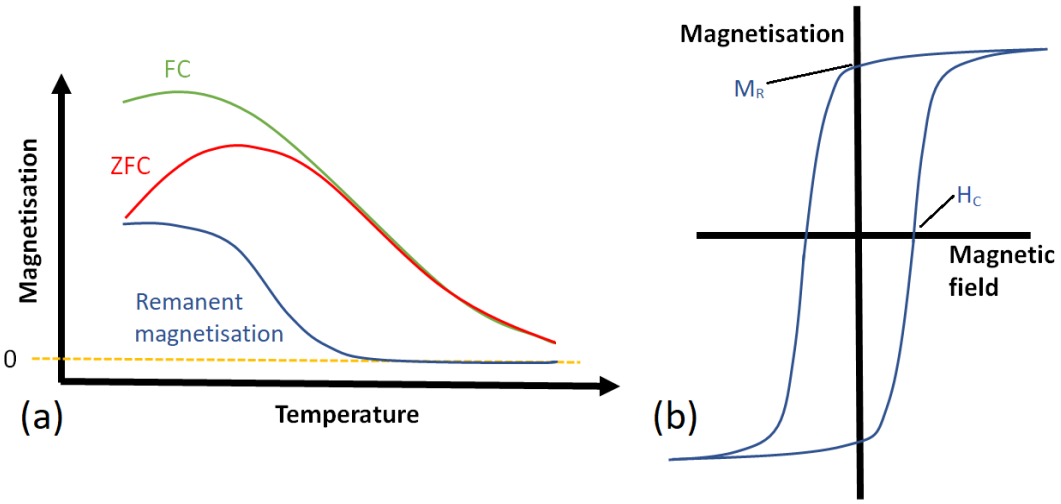

Figure 25: Idealised behaviour of a ferromagnetic material, (a) the magnetic response of a ferromagnetic material with respect to temperature when cooled in the presence of magnetic field (FC) and when cooled without an applied magnetic field (ZFC) and (b) a hystersis loop of a ferromagnetic material displaying a remanent magnetic response with respect to applied magentic field. M_R is the remanent magnetisation and H_C is the coercive field.

The instrument used for this analysis was a Quantum Designs MPMS 3 Magnetometer with a field range of ±70 kOe and a temperature range 1.8 to 400 K. The schematic in figure 26 shows the setup of this instrument. A current is induced in the detection coils when a disturbance to the magnetic signal is observed. No current is induced in response to uniform magnetic fields with a linear change in

magnetic gradient. The shape of the current signal is determined by the size and shape of the sample. The current in the detection coil is inductively coupled to the SQUID (Superconducting QUantum Interference Device). The SQUID converts the current to voltage [34]. A more detailed diagram of a SQUID circuit is shown in figure 27. The magnetic disturbance measured at the pick-up coil generates a current in the superconducting loop consisting of the input and pick-up coil. There are two Josephson tunnel junctions shunted with resistors in the primary coil. These help to eliminate hysteresis in the tunnel junction current - voltage characteristics. The output voltage from the Josephson tunnel junctions corresponds to the magnetic signal from the input coil. This voltage is modulated by the modulating coil and converted to a magnetic moment. The use of a SQUID allows for the measurement of magnetic susceptibilities with a high sensitivity [33].

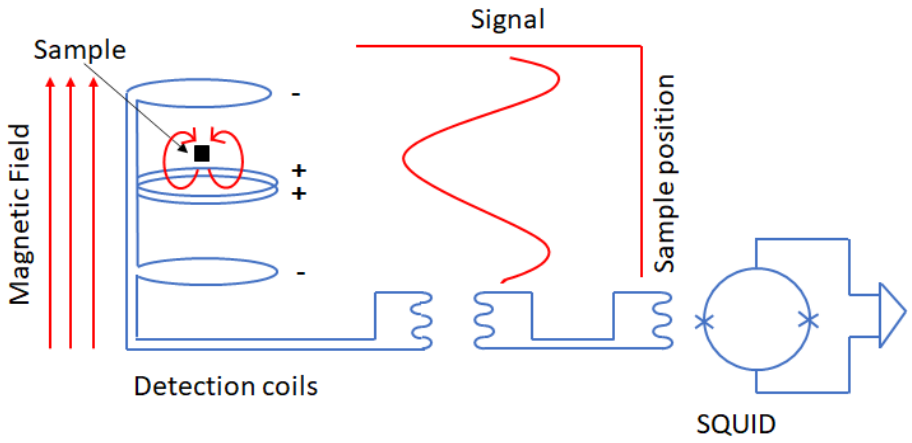

Figure 26: A simplified diagram showing the setup of the detection hardware for the MPMS 3 Magnetometer. Redrawn from [34].

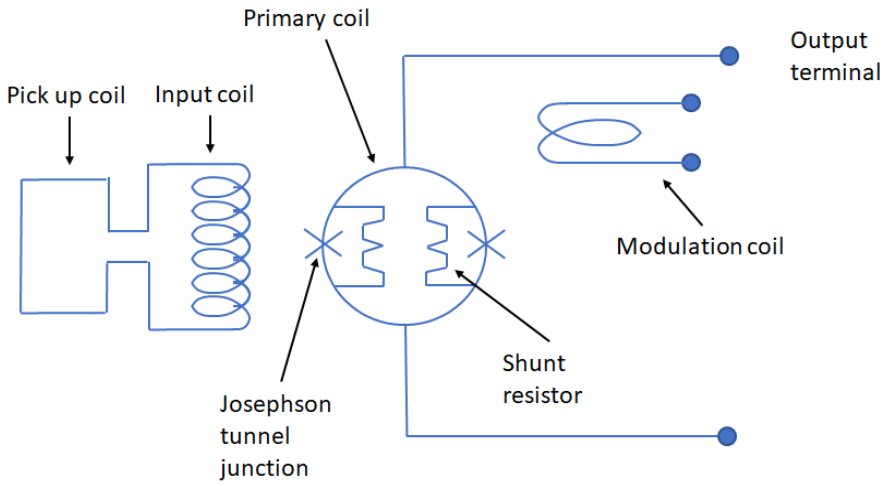

Figure 27: Equivalent circuit of a SQUID (Superconducting QUantum Interference Device) magnetometer. Redrawn form [33].

A thorough demagnetisation process was conducted before analysis of the sample, using a procedure similar to that outlined in detail in the paper by Maity *et al*. [35]. The sample was demagnetised by applying an oscillating magnetic field with a step wise decrease in amplitude to zero. Hysteresis loops (MH curves) were collected over a ± 70 kOe field range. The magnetic response to temperature was measured with a cooling rate of 10 K / minute. The insulated vacuum chamber is cooled with liquid helium. The orientation of the sample is in-plane with the magnetic field during measurement.

2.3. References

[1] C. Glynn and C. O'Dwyer, "Solution Processable Metal Oxide Thin Film Deposition and Material Growth for Electronic and Photonic Devices," *Advanced Materials Interfaces,* vol. 4, no. 2, p. 1600610, 2017, doi: https://doi.org/10.1002/admi.201600610.

[2] L. Keeney, C. Groh, S. Kulkarni, S. Roy, M. E. Pemble, and R. W. Whatmore, "Room temperature electromechanical and magnetic investigations of ferroelectric Aurivillius phase Bi5Ti3(FexMn1−x)O15 (x = 1 and 0.7) chemical

solution deposited thin films," *Journal of Applied Physics,* vol. 112, no. 2, p. 024101, 2012/07/15 2012, doi: 10.1063/1.4734983.

[3] J. Schwarzkopf and R. Fornari, "Epitaxial growth of ferroelectric oxide films," *Progress in Crystal Growth and Characterization of Materials,* vol. 52, no. 3, pp. 159-212, 2006.

[4] J.-O. Carlsson and P. M. Martin, "Chapter 7 - Chemical Vapor Deposition," in *Handbook of Deposition Technologies for Films and Coatings (Third Edition)*, P. M. Martin Ed. Boston: William Andrew Publishing, 2010, pp. 314-363.

[5] https://www.cvdequipment.com/systems/production-equipment/lpcvd-systems/ (accessed 17/02/2021.

[6] https://www.aixtron.com/en/products/AIX%202800G4-TM_p89 (accessed 17-02-2021.

[7] V. Astié, C. Millon, J.-M. Decams, and A. Bartasyte, *Direct liquid injection chemical vapor deposition*. IntechOpen, 2019.

[8] U. Weber *et al.*, "AVD® technology for deposition of next generation devices," *Microelectronics Reliability,* vol. 45, no. 5-6, pp. 945-948, 2005, doi: 10.1016/j.microrel.2004.11.019.

[9] P. K. Baumann *et al.*, "Innovative Deposition Technology for Advanced Materials," *ECS Transactions,* vol. 28, no. 1, p. 137, 2010.

[10] M. Lukosius *et al.*, "Electrical and Morphological Properties of ALD and AVD Grown Perovskite-Type Dielectrics and Their Stacks for Metal-Insulator-Metal Applications," *ECS Journal of Solid State Science and Technology,* vol. 1, no. 1, pp. N1-N5, 2012, doi: 10.1149/2.023201jss.

[11] M. Lukosius, C. B. Kaynak, S. Kubotsch, T. Blomberg, G. Ruhl, and C. Wenger, "Properties of atomic-vapor and atomic-layer deposited Sr, Ti, and Nb doped Ta2O5 Metal–Insulator–Metal capacitors," *Thin Solid Films,* vol. 520, no. 14, pp. 4576-4579, 2012, doi: 10.1016/j.tsf.2011.10.199.

[12] M. Schumacher, P. K. Baumann, and T. Seidel, "AVD and ALD as Two Complementary Technology Solutions for Next Generation Dielectric and Conductive Thin-Film Processing," *Chemical Vapor Deposition,* vol. 12, no. 2-3, pp. 99-108, 2006, doi: https://doi.org/10.1002/cvde.200500027.

[13] P. F. Zhang, N. Deepak, L. Keeney, M. E. Pemble, and R. W. Whatmore, "The structural and piezoresponse properties of c-axis-oriented Aurivillius phase Bi5Ti3FeO15 thin films deposited by atomic vapor deposition," *Applied Physics Letters,* vol. 101, no. 11, p. 112903, 2012, doi: 10.1063/1.4752007.

[14] N. Deepak, P. Carolan, L. Keeney, M. E. Pemble, and R. W. Whatmore, "Tunable nanoscale structural disorder in Aurivillius phase, n= 3 Bi 4 Ti 3 O 12 thin films and their role in the transformation to n= 4, Bi 5 Ti 3 FeO 15 phase," *Journal of Materials Chemistry C,* vol. 3, no. 22, pp. 5727-5732, 2015.

[15] S. E. Dann, "Characterization of solids," in *Reactions and Characterization of Solids*, 2000, pp. 48-80.

[16] F. K. Lotgering, "Topotactical reactions with ferrimagnetic oxides having hexagonal crystal structures—I," *Journal of Inorganic and Nuclear Chemistry,* vol. 9, no. 2, pp. 113-123, 1959/02/01/ 1959, doi: https://doi.org/10.1016/0022-1902(59)80070-1.

[17] P. Scherrer, "Nachr Ges wiss goettingen," *Math. Phys.,* vol. 2, pp. 98-100, 1918.

[18] G. Binnig, C. F. Quate, and C. Gerber, "Atomic force microscope," *Physical review letters,* vol. 56, no. 9, p. 930, 1986.

[19] F. J. Giessibl, "Advances in atomic force microscopy," *Reviews of Modern Physics,* vol. 75, no. 3, pp. 949-983, 07/29/ 2003, doi: 10.1103/RevModPhys.75.949.

[20] R. García and R. Pérez, "Dynamic atomic force microscopy methods," *Surface Science Reports,* vol. 47, no. 6, pp. 197-301, 2002/09/01/ 2002, doi: https://doi.org/10.1016/S0167-5729(02)00077-8.

[21] https://www.bruker.com/en/products-and-solutions/microscopes/materials-afm/afm-modes/peakforce-tapping.html (accessed 10/04/2021.

[22] R. E. Newnham, R. W. Wolfe, and J. F. Dorrian, "Structural basis of ferroelectricity in the bismuth titanate family," *Materials Research Bulletin,* vol. 6, no. 10, pp. 1029-1039, 1971/10/01/ 1971, doi: https://doi.org/10.1016/0025-5408(71)90082-1.

[23] P. Güthner and K. Dransfeld, "Local poling of ferroelectric polymers by scanning force microscopy," *Applied Physics Letters,* vol. 61, no. 9, pp. 1137-1139, 1992.

[24] E. Soergel, "Piezoresponse force microscopy (PFM)," *Journal of Physics D: Applied Physics,* vol. 44, no. 46, p. 464003, 2011, doi: 10.1088/0022-3727/44/46/464003.

[25] F. Felten, G. Schneider, J. M. Saldaña, and S. Kalinin, "Modeling and measurement of surface displacements in BaTiO 3 bulk material in piezoresponse force microscopy," *Journal of Applied Physics,* vol. 96, no. 1, pp. 563-568, 2004.

[26] S. V. Kalinin, B. J. Rodriguez, and S. Jesse, "Vector piezoresponse force microscopy," *Microscopy and Microanalysis,* vol. 12, no. 3, pp. 206-220, 2006.

[27] B. J. Rodriguez, C. Callahan, S. V. Kalinin, and R. Proksch, "Dual-frequency resonance-tracking atomic force microscopy," *Nanotechnology,* vol. 18, no. 47, p. 475504, 2007, doi: 10.1088/0957-4484/18/47/475504.

[28] https://afm.oxinst.com/assets/uploads/products/asylum/documents/VFM4-26MAR2018-web.pdf (accessed 01/01/2021.

[29] B. Fahlman, "Materials chemistry. 2007," ed: Dordrecht, Netherlands: Springer.

[30] Y. Liao, "Practical electron microscopy and database," ed: Global Sino, 2006.

[31] D. L. Wood and J. Tauc, "Weak Absorption Tails in Amorphous Semiconductors," *Physical Review B,* vol. 5, no. 8, pp. 3144-3151, 04/15/ 1972, doi: 10.1103/PhysRevB.5.3144.

[32] J. Kegel, V. Z. Zubialevich, M. Schmidt, I. M. Povey, and M. E. Pemble, "Effect of surface and defect chemistry on the photocatalytic properties of intentionally defect-rich ZnO nanorod arrays," *ACS applied materials & interfaces,* vol. 10, no. 21, pp. 17994-18004, 2018.

[33] L. Keeney *et al.*, "Magnetic Field-Induced Ferroelectric Switching in Multiferroic Aurivillius Phase Thin Films at Room Temperature," *Journal of the American Ceramic Society,* vol. 96, no. 8, pp. 2339-2357, 2013/08/01 2013, doi: 10.1111/jace.12467.

[34] Q. Design, "Magnetic Property Measurement System MPMS 3 User's Manual," *Quantum Design,* 2016.

[35] T. Maity, S. Goswami, D. Bhattacharya, and S. Roy, "Superspin glass mediated giant spontaneous exchange bias in a nanocomposite of BiFeO 3− Bi 2 Fe 4 O 9," *Physical review letters,* vol. 110, no. 10, p. 107201, 2013.

Chapter 3

This chapter represents an adapted version of the publication:

J. C. Halpin, M. Schmidt, T. Maity, M. E. Pemble, and L. Keeney, "Compositional tuning of the Aurivillius phase material $Bi_5Ti_{3-2x}Fe_{1+x}Nb_xO_{15}$ ($0 \leq x \leq 0.4$) grown by chemical solution deposition and its influence on the structural, magnetic and optical properties of the material," *IEEE Transactions on Ultrasonics, Ferroelectrics, and Frequency Control,* vol. 68, no. 2, pp. 303-313, Feb. 2021, doi: 10.1109/TUFFC.2020.2997406.

Changes to the publication were only made in regards to formatting requirements and to provide further clarification at the request of examiners.

3. Compositional tuning of the Aurivillius phase material $Bi_5Ti_{3-2x}Fe_{1+x}Nb_xO_{15}$ ($0 \leq x \leq 0.4$) grown by chemical solution deposition and its influence on the structural, magnetic and optical properties of the material

3.1. Abstract

A series of Aurivillius phase materials, $Bi_5Ti_{3-2x}Fe_{1+x}Nb_xO_{15}$ (x = 0, 0.1, 0.2, 0.3 and 0.4), was fabricated by chemical solution deposition. The effects of aliovalent substitution for the successful inclusion of Fe^{3+} and Nb^{5+} by replacing Ti^{4+} was explored as a potential mechanism for increasing magnetic ion content within the material. The structural, optical, piezoelectric and magnetic properties of the materials were investigated. It was found that a limit of x = 0.1 was achieved before the appearance of secondary phases as determined by X-ray diffraction. Absorption in the visible region increased with increasing values of x, up to x = 0.3, corresponding to the transition from the valence band to the conduction band of the Fe-e_g energy level. Piezoresponse force microscopy measurements demonstrated that the lateral piezoelectric response increased with increasing values of x. Magnetic measurements of $Bi_5Ti_{2.8}Fe_{1.1}Nb_{0.1}O_{15}$ exhibited a weak ferromagnetic response at 2 K, 150 K and 300 K of 2.2, 1.6, 1.5 emu/cm^3 with H_c ~ 40, 36, 34 Oe respectively. The remanent magnetisation, M_R, of this sample was found to be higher than the range of reported values for the $Bi_5Ti_3Fe_1O_{15}$ parent phase. Elemental analysis of this sample by energy dispersive X-ray analysis did not provide any evidence for the presence of iron rich secondary phases. However, it is noted that a series of measurements at varying sample volumes and instrument resolutions is still required in order to put a defined confidence level on the $Bi_5Ti_{2.8}Fe_{1.1}Nb_{0.1}O_{15}$ material being a single-phase multiferroic.

3.2. Introduction

The Aurivillius phase family of materials provides a versatile scaffold in which different types of cations driving ferroelectricity and ferromagnetism can be accommodated. This family of materials is a homologous series of bismuth based, naturally layered oxides. They have the general formula $Bi_2O_2(A_{m-1}B_mO_{3m+1})$ and consist of $mABO_3$ perovskite blocks separated by $[Bi_2O_2]^{2+}$ interlayers, with the primary growth axis along the *c*-axis direction. $Bi_4Ti_3O_{12}$ is a well-studied member of the Aurivillius family. It has three perovskite units (m = 3) between the $[Bi_2O_2]^{2+}$ interlayers. The insertion of a $BiFeO_3$ unit (a well-known antiferromagnetic multiferroic), to produce the $Bi_5Ti_3Fe_1O_{15}$ composition (m = 4), has been proposed as a route towards the creation of a multiferroic Aurivillius phase [1]. $Bi_5Ti_3Fe_1O_{15}$ prepared by chemical solution deposition was found to have a remanent polarisation of 14.1 mC/cm^2 and leakage current of 2.3^10^{-6} A/cm^2 [2]. The superexchange mechanism of magnetic coupling, common in insulating magnetic oxides, is a short-range mechanism involving coupling between electrons on cations via a intervening anion [3]. Long range magnetic order, yielding a bulk magnetic signal throughout a sample, requires a sufficient concentration of magnetic ions to be located close to each other in the material. Increasing the concentration of magnetic ions in a material increases the probability of magnetic ions being near neighbours (NN) or next near neighbours (NNN) to each other. For these reasons it is desirable to increase the concentration of iron in $Bi_5Ti_3Fe_1O_{15}$. However, due to differences in valence and atomic radii of Ti^{4+} and Fe^{3+}, the ability to simply replace one with the other is limited and can lead to the formation of defects such as oxygen vacancies or stacking faults caused by intergrowths of alternating m values as the material reorders to accommodate the change in valence. This may also lead to the formation of associated secondary phase impurities. Chemical solution deposition was used by Liu *et al*. to prepare a series of nanoparticulate materials of $Bi_5Ti_{3-x}Fe_{1+x}O_{15}$ [4] with Fe^{3+} substitution. No impurity peaks were detected by XRD in the compositions up to x = 0.6. The increased iron content was found to improve the visible light photodegradation of Rhodamine B dye solutions but the potential magnetic

properties were not studied. Liu *et al*. propose that the formation of Ti^{3+} was occurring to maintain a stable material without anion vacancies or defects [4]. The possibility of using aliovalent substitution was proposed by Brienbaum *et al.* [5] as a method to increase the Fe content of the Aurivillius materials.Co-substitution or aliovalent substitution of Fe^{3+} and Nb^{5+} at the Ti^{4+} site has been used in previous work on $Bi_5Ti_3FeO_{15}$ (*m* = 4) [6] and $Bi_4Ti_3O_{12}$ (*m* = 3) [7] materials fabricated using a solid-state reaction method. Lavado *et al*. [7] reached a limit of x = 0.5 ($Bi_4Ti_{3-2x}Nb_xFe_xO_{12}$) before secondary impurity phases were detected using XRD, having sub-threshold magnetic percolation (17 %) to allow for long-range magnetic order with strong magnetic coupling. Chen *et al*. [6] did not see the expected increase in magnetic response even at 35 % Fe occupation of the *B*-sites in the *m* = 4 Aurivillius structure, which is above the theoretical percolation threshold for NN interactions. These ceramic materials were fabricated using solid state reaction methods. With these previous studies in mind, the objective of this present study is to attempt to systematically increase the concentration of Fe^{3+} ions in thin films of Aurivillius compound $Bi_5Ti_3FeO_{15}$ using aliovalent substitution of Fe^{3+} and Nb^{5+} ions at the Ti^{4+} ion sites, to create a series of thin film materials that have a generic formula of $Bi_5Ti_{3-x}Fe_{1+x}Nb_xO_{15}$. This has enabled a study of the structural properties of the resulting thin film materials to examine the influence of the materials composition and structure on the observed magnetic percolation. To the best of our knowledge this study represents the first of its kind by clearly demonstrating weak ferromagnetic behaviour in an aliovalent substituted $Bi_5Ti_{2.8}Fe_{1.1}Nb_{0.1}O_{15}$ sample prepared via chemical solution deposition.

3.3. Experimental

Details of the Chemical Solution Deposition method are presented in chapter 2 of this thesis (section 2.1). The specific procedure used for these materials is presented here. Chemical solution deposition was the method used to fabricate the sample series; $Bi_5Ti_{3-2x}Fe_{1+x}Nb_xO_{15}$ (x = 0, 0.1, 0.2, 0.3 and 0.4). Details of this method are outlined in a previous publication [8] with the additional step of including niobium (figure 1). The

precursors were weighed out in the proportions desired for the stoichiometry targeted. The bismuth precursor was present at 17.5 % excess. This is a common precaution when using bismuth due to its volatility at the relatively high annealing temperatures used. Previous work on *m* = 4 Aurivillius phases demonstrates that use of such an excess of bismuth mitigates the effects of bismuth migration and prevents the formation of secondary phase impurities such as pyrochlore $Bi_2Ti_2O_7$ [9]. The precursors $Bi(NO_3)_3.5H_2O$ (reagent grade, 98 %, Sigma-Aldrich) and $Ti(OC_4H_9)_4$ (reagent grade, 97 %, Sigma-Aldrich) were dissolved in lactic acid (ACS reagent, ≥ 85 %, Sigma-Aldrich) at room temperature with constant stirring for a week to form Solution A. $Fe(NO_3)_3.9H_2O$ (ACS reagent, ≥ 98 %, Sigma- Aldrich) and ($Nb(OC_2H_5)_5$) (99.9+ %, Strem Chemicals, Inc.) were dissolved in acetylacetone (≥ 99.5 % (Gas Chromatography grade), Sigma-Aldrich) to form Solution B. As the niobium precursor was moisture sensitive, these steps were performed in a nitrogen filled glove-bag. Solution B was slowly added to Solution A and was mixed thoroughly under nitrogen. The solution was then spin coated at 2000 rpm for 30 seconds onto *c*-plane sapphire substrates. Sapphire substrates were chosen for their cost-effectiveness and because they are chemically stable at the processing temperatures used to crystallize the Aurivillius phases. Although Si(100) and α-quartz are also cost-effective, previous studies [25] demonstrate that a reaction between the bismuth-containing Aurivillius phases and silicon tends to occur at the interface between film and substrate to form an amorphous Bi_2O_3-SiO_2 phase (e.g. $Bi_4Si_3O_{12}$) on cooling. The samples were baked at 300°C for 10 minutes on a hot plate in air to remove the residual organic solvents. The as-deposited materials were amorphous, and crystallization was induced by annealing at 850°C in a conventional furnace for 1 hour. The average film thickness was calculated to be 47 nm after measurements of 21 points across a section of the sample imaged by TEM, with the thickest region being 84 nm and the thinnest being 28 nm. A flow chart of the experimental procedure is shown in figure 1.

Details of analysis methods and instruments used during this study are as follows: XRD was performed with a Phillips Xpert PW3719 MPD diffractometer, Cu Kα

radiation, 40 kV 35 mA, scan range 6° to 37.5°. Scanning electron microscopy (SEM) was performed using a Zeiss Supra 40 instrument.

Atomic Force Microscopy (AFM) and Piezoresponse Force Microscopy (PFM) were performed using an MFP-3DTM Asylum Research instrument. AFM was conducted in AC mode using Olympus AC240TS probes (Al reflex coated, 15 nm tip radius, 70 kHz resonant frequency). PFM was conducted in both single frequency and lateral Dual AC Resonance Tracking (DART-PFM) mode [10]. The DART-PFM mode was used to boost the vertical piezo signal. In this mode, the PFM signal is measured at the tip-sample contact resonance frequency, where the drive frequencies are adjusted as the probe scans over the changing sample topography in order to reduce topographical cross-talk. The probes used were Olympus AC240TM electrilevers (Ti/Pt coated silicon probes, Al reflex coated, 15 nm tip radius, 70 kHz resonant frequency)).

Transmission measurements in the ultra violet – visible (UV-vis) range were performed on a Perkin Elmer λ950 spectroscope with an integrated sphere attachment and direct reflectance was measured on the same instrument using a Universal Reflectance Accessory. Diffuse reflectance was measured using a Shimadzu UV-2401 PV UV-vis recording spectroscope. The percentage absorption was calculated using the relationship $A\% = 100 - T\% - (R\%_{direct} + R\%_{diffuse})$.

For high resolution TEM (HR-TEM) cross-sections of the films were prepared for micro-structural analysis using a FEI DualBeam Helios NanoLab 600i Focussed Ion Beam (final thinning at 93 pA 30 kV, final polish 5 kV 47 pA). Microstructural analysis was performed using HR-TEM (Jeol 2100 transmission electron microscope; 200 kV; double tilt holder).

EDX spectra were obtained using a FEI Helios Nanolab High-Resolution Scanning Electron Microscope with attached Oxford X-Max 80 detector and Aztec analysis software.

The magnetic measurements were carried out in Quantum Design's MPMS 3 magnetometer (±70 kOe field range, 1.8 – 400 K temperature range). Before each measurement the samples were demagnetized using an appropriate

demagnetization protocol [11]. The hysteresis loops (MH curves) were measured at ±70 kOe field range at different temperatures. The temperature dependent magnetization (MT) was measured at a 10 K/min cooling rate. The orientation of the sample is in-pane with the magnetic field during measurement.

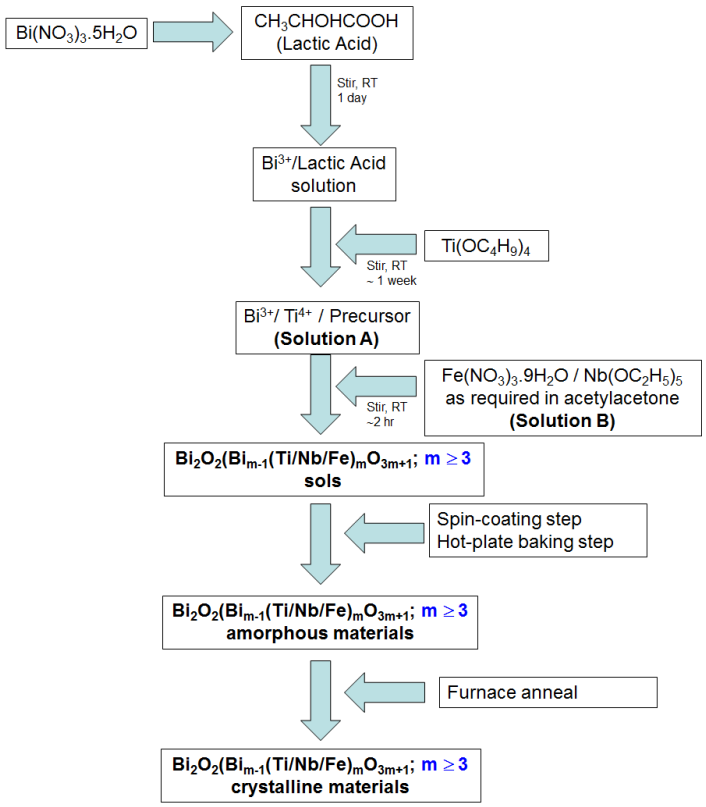

Figure 1: Flow chart depicting the experimental steps involved in preparing the $Bi_5Ti_{3-x}Fe_{1+x}Nb_xO_{15}$ (*m* = 4) Aurivillius sample series by chemical solution deposition.

3.4. Results and Discussion

3.4.1. XRD analysis

A sample series $Bi_5Ti_{3-2x}Fe_{1+x}Nb_xO_{15}$ with x = 0, 0.1, 0.2, 0.3 and 0.4 (hereafter referred to as Bi5Nb0, Bi5Nb0.1, etc.) was fabricated using chemical solution deposition on *c*-plane sapphire substrates. The as-deposited samples were amorphous and light brown in colour. After annealing at 850°C for 1 hour the samples underwent a structural change to form the crystal structure accompanied by a colour change to

pale yellow. XRD of the sample series confirmed the formation of the *m* = 4 Aurivillius material. There was a preferred orientation for the growth axis perpendicular to the substrate, in the *c*-axis direction, with a majority of the peaks corresponding to (00*l*) reflections (figure 2). As will be shown in AFM, SEM and TEM images, a number of the Aurivillius plates lie at an angle to the substrate which accounts for the small (020) reflection observed (figure 3 (a)). This peak is most intense for the x = 0.2 sample. We note that there is a general decrease in the intensity of the peaks corresponding to the *m* = 4 Aurivillius phase as x increases. The Lotgering factor [12] provides a measure of the texture of the samples. Background to the Lotgering factor (*f*) calculations is covered in section 2.2.1 of this thesis,

$$f = \frac{P - P_0}{1 - P_0} \qquad (3.1)$$

where,

$$P = \frac{\sum I(00l)}{\sum I(hkl)} \text{ and } P_0 = \frac{\sum I(00l)_0}{\sum I(hkl)_0} \qquad (3.2)$$

Here, ΣI(00l) is the sum of the intensities of all (00*l*) reflections, ΣI(*hkl*) is the sum of the intensities from all the peak reflections of the material and $\Sigma I(00l)_0$ and $\Sigma I(hkl)_0$ are the corresponding values from a randomly oriented sample. The intensities of a randomly oriented sample were obtained from the XRD values generated by using VESTA software [13] from the data provided by Lui *et al*. in their paper on $Bi_5Ti_3FeO_{15}$ [4]. There was insignificant decrease in the Lotgering factor between samples Bi5Nb0 (f = 0.996 ± 0.02) and Bi5Nb0.1 (f = 0.991 ± 0.02). No significant changes to the preferred *c*-axis orientation were observed on increasing "x"

The reflections of the Bi5Nbx series were indexed from a simulated XRD plot generated by using VESTA software [13] from the same data provided by Lui *et al*. [4]. This corresponded to the orthorhombic space group $A2_1am$. As the concentration of Fe^{3+} and Nb^{5+} increases, the intensity of the peaks tends to decrease (indicating a decreased crystallinity), and peaks broaden and shift position. The peak occurring at ≈ 21.6° is common to several Aurivillius phases, for example the (008) reflection of *m*

= 3, the (00<u>1</u>0) reflection of m = 4 and the (00<u>1</u>2) reflection of the *m* = 5 Aurivillius phase occur at a similar 2θ value. As a consequence, little change is observed at this peak position, regardless of the type of *m* Aurivillius structure. While the (004), (006), (008), (00<u>1</u>2), (0014) and (00<u>1</u>6) peaks shift position on increasing x, the peaks also become broad and asymmetric, making it difficult to assign their true peak positions. The peak shift for these reflections is accompanied by the appearance of the (222) and possibly the (444) reflection of the pyrochlore bismuth titanium oxide ($Bi_2Ti_2O_7$) phase (JCPDF 32-0118) at 14.6° and 29.6° in the Bi5Nb0.2, Bi5Nb0.3 and Bi5Nb0.4 samples. The formation of this secondary phase indicates that stoichiometric $Bi_5Ti_{2.6}Fe_{1.2}Nb_{0.2}O_{15}$, $Bi_5Ti_{2.4}Fe_{1.3}Nb_{0.3}O_{15}$, and $Bi_5Ti_{2.2}Fe_{1.4}Nb_{0.4}O_{15}$ compositions have not been formed. Small peaks (at 2theta positions of 10.6° and 16.0°) indicate the formation of the *m* = 3 Aurivillius phase $Bi_4Ti_3O_{12}$ (JCPDF 35-0795) which can be seen in samples with x > 0.1. Another strong reflection (008) expected for this (*m* = 3) phase at 21.6°, however note that this would overlap with the (00<u>1</u>0) reflection of the *m* = 4 phase.

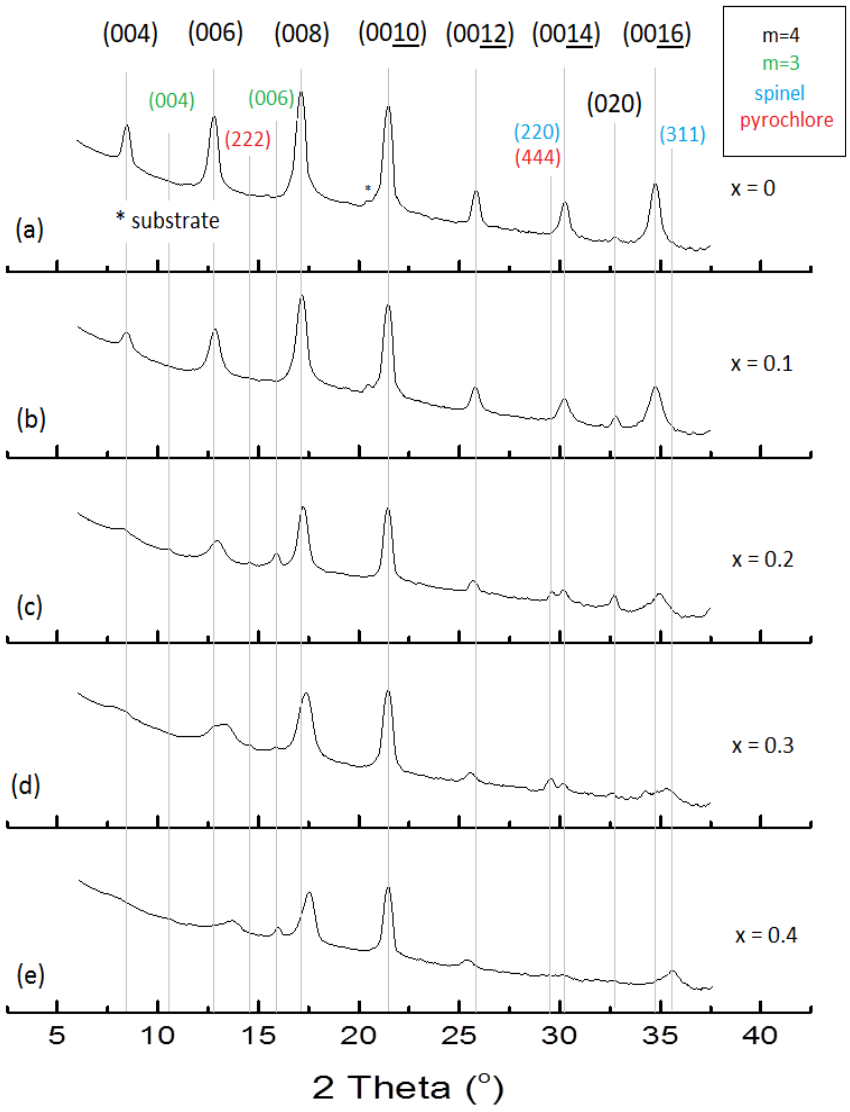

Figure 2: XRD graphs of the Bi5Nb series (a) Bi5Nb0, (b) Bi5Nb0.1, (c) Bi5Nb0.2, (d) Bi5Nb0.3, (e) Bi5Nb0.4. Indexed to $Bi_5Ti_3Fe_1O_{15}$ *m* = 4 space group *A*2$_1$*am* (black), $Bi_4Ti_3O_{12}$ *m* = 3 space group *B*2*cb* (green), pyrochlore $Bi_2Ti_2O_7$ space group *Fd*3*m* (red) and spinel Fe_3O_4 space group *Fd*3*m* (blue).

Note that no peaks corresponding to the haematite phase, Fe_2O_3 (JCPDF 89-0599), were observed ((220) reflection occurs at ~ 33.2°) within the detection limit of the instrument (typically 1-3 vol %). The magnetite spinel phase, Fe_3O_4 (JCPDF 89-0951), has a (311) reflection at ~ 35.4° which overlaps with the *m* = 4 (00<u>16</u>) reflection. A

peak at 29.6°, seen in samples Bi5Nb0.2 and Bi5Nb0.3, aligns with the (220) reflection of magnetite. This occurs in the same range as the (444) reflection of pyrochlore $Bi_2Ti_2O_7$, therefore it is not possible to definitively assign this peak. Considering the observed presence of secondary phases in samples of x greater than 0.1, we determine that the Aurivillius structure cannot support the increased concentration of Fe/Nb above x = 0.1. Subsequent characterisation of ferroelectric and ferromagnetic properties focused on the x = 0.1, Bi5Nb0.1 sample.

The *b* and *c*-axis pseudo lattice parameters were calculated from the XRD measurements using the following relationship (3) between the pseudo lattice parameters of the orthorhombic system and the interplanar distances from the Bragg condition.

$$\frac{1}{d^2} = \frac{h^2}{a^2} + \frac{k^2}{b^2} + \frac{l^2}{c^2} \quad (3)$$

As there was no (*h*00) reflection over this scan range it was not possible to calculate the *a*-axis pseudo lattice parameter. The *b*-axis pseudo lattice parameter, which increases with Fe^{3+} and Nb^{5+} addition, was calculated from a single (020) reflection. It was found that the error associated with the calculated *c*-axis pseudo lattice parameter becomes significant above values of x = 0.1 (figure 3 (a)). This can be attributed to the decrease in sample purity and the occurrence of secondary phases having *d* spacings similar to the *m* = 4 Aurivillius phase. There is a general decrease in the intensity and sharpness of the peaks corresponding to the *m* = 4 Aurivillius phase as x increases. If we take a value for the *a*-axis parameter of 5.4698 Å from the detailed work of Hervoches *et al*. [14] we calculate a unit cell volume of 1237.83 (± 0.02) and 1236.36 (± 0.80) $Å^3$ for Bi5Nb0 and Bi5Nb0.1, respectively. This is comparable to the values obtained by Chen *et al*. [6] for the ceramic materials of similar composition. The Goldschmidt tolerance factor (*t*) (section 1.4.1) [15] was calculated for the series and decreased from 0.8539 to 0.8526 for x = 0 to x = 0.4. *t* is a measure of the tilt of the perovskite unit [16]. Insertion of larger atoms at the *B*-site of the perovskite blocks changes bond lengths in the structure causing increased rotation of the perovskite octahedra [15]. The small decrease in tolerance factor indicates that the tilt of the octahedral unit is increasing as the series progresses due

to the insertion of the larger Fe^{3+} (0.645 Å) and Nb^{5+} (0.640 Å) for Ti^{4+} (0.605 Å) at the *B*-site [17].

As the Aurivillius materials are orthorhombic and not cubic, the Scherrer equation could not be used to estimate particle size but instead was used in a modified form to provide a measure of the crystalline quality of the materials. The relative crystalline factor (Q) was derived from a modified form of the Scherrer equation (3.4) [18].

$$Q = \frac{1}{\beta Cos\theta} \qquad (3.4)$$

Where β is the FWHM (full width at half maximum) (in radians) and θ is the angle of diffraction. The averaged FWHM of the (008), (00$\underline{1}$0) and (00$\underline{1}$2) peaks were used in the calculation (figure 3 (b)). The value of Q decreased with increasing Fe and Nb concentration. This was as expected due to the formation of secondary phases at higher Fe and Nb concentrations. An abrupt decrease in the value of Q for the Bi5Nb0.3 and Bi5Nb0.4 samples corresponds to the appearance of significant proportion of secondary phases in the XRD patterns of these materials. The balance of evidence collected from XRD data supports that a solution limit of x = 0.1 is reached for this series before the appearance of secondary phases. Peak broadening due to particle size effects is a possible alternative explanation for the broadening of the XRD peaks, however AFM data (section 3.4.4) suggests that there is no noticeable change in the coverage or roughness of the samples throughout the series. Furthermore, the deposition method was the same for all the samples and variation in film thickness is minimal. This supports a conclusion that peak broadening and shifting changes observed in the XRD data for the series is due to chemical composition and structural changes.

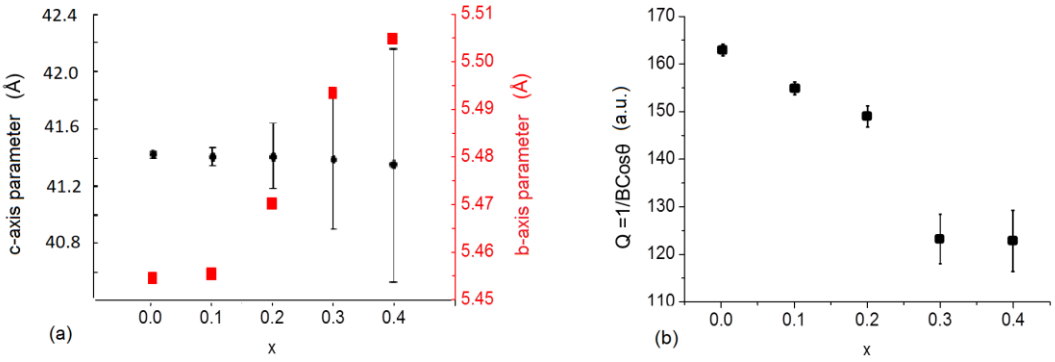

Figure 3: The b and c–axis parameters (a) and the relative crystalline quality factor (b) calculated form XRD measurements.

3.4.2. TEM analysis

A typical TEM image of the Bi5Nb0.1 sample is shown in figure 4. From the TEM measurements, unit cell thickness was measured to be 41.4 ± 0.3 Å compared to a *c*-axis parameter value of 41.40 Å calculated from XRD measurements. An error of (at least) 10% should be applied to measurements taken from the TEM images. Both the Aurivillius phase and the sapphire substrate are crystalline, but they are not lattice matched. The pseudo-cubic lattice parameter for Bi5Nb0.1 (calculated by the method of [19]) is 3.88 Å, which is considerably different to the lattice constant *a* = 4.78 Å for sapphire (+23.20 % lattice mis-match). The sapphire substrate therefore acts simply as a mechanical support for the Aurivillius materials and there is no epitaxial relationship affecting crystal growth. The thickness of the plates measured ranged from 28 to 84 nm. This corresponds to a range of 8 to 20 unit cells within the plate like grains. SEM (figure 5) and AFM (figure 6) images demonstrate that film coverage was not continuous over the sample surface and several grains lie partially on top of each other. This overlapping tendency of the grains means that several plates are tilted at the region where they meet and lie at an angle with respect to the substrate surface. For example, the image presented in figure 4 demonstrates that for the

region of the sample imaged, the *c*-axis was inclined at an angle of approximately 2 ° with respect to the substrate.

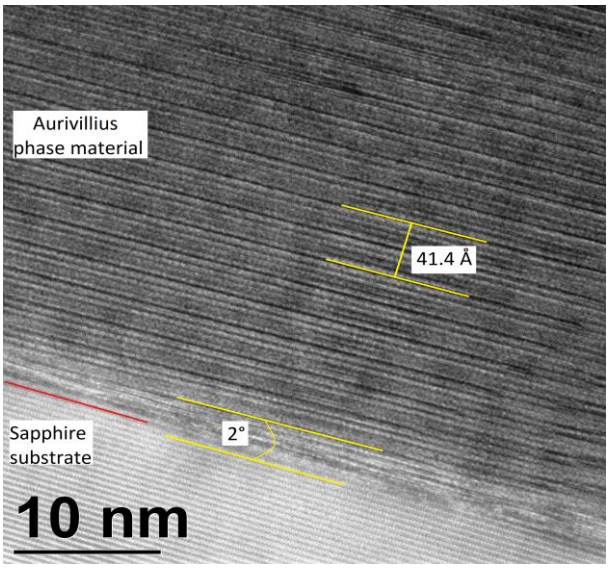

Figure 4: TEM image of the Bi5Nb0.1 sample.

3.4.3. Scanning electron microscopy analysis

The topography of the material was examined using SEM and AFM. Analysis of the amorphous materials before annealing showed there was complete coverage over the substrate. During crystallization, the materials contracted exposing some of the substrate underneath. SEM images show the characteristic plate like grains common for Aurivillius materials (figure 5). A majority of plates lie parallel to the sapphire substrate, but some are positioned at an angle where plates overlap.

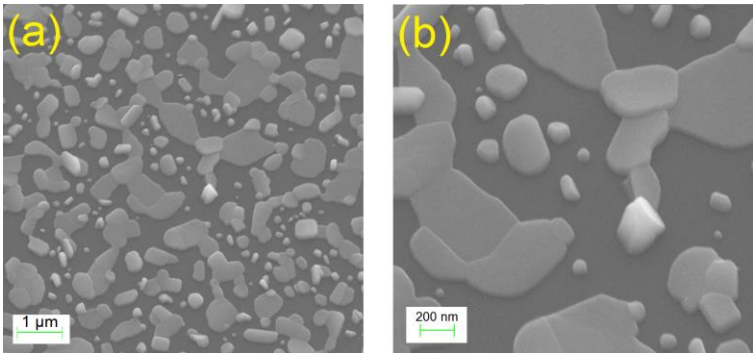

Figure 5: SEM images at a 45° tilt of Bi5Nb0.1 Aurivillius materials showing the plate like grains that predominantly lie parallel to the substrate.

3.4.4. Atomic force microscopy analysis

From AFM measurements of the sample series (figure 6) the average percentage coverage was found to be between 54-72 % for the Bi5Nbx series and the RMS roughness between 26-30 nm. There was no significant trend observed through the sample series as the average values obtained for each sample fell within the standard deviation error of the other samples in that series.

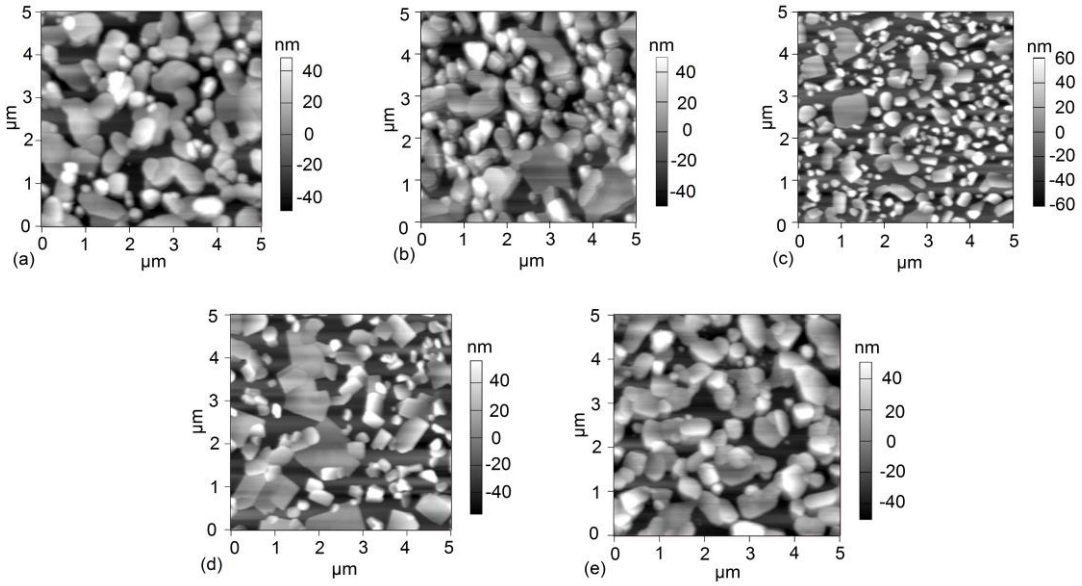

Figure 6: AFM topography images (a) Bi5Nb0, (b) Bi5Nb0.1, (c) Bi5Nb0.2, (d) Bi5Nb0.3 and (e) Bi5Nb0.4.

3.4.5. Optical analysis

Since there has been a growing interest in the use of $Bi_5Ti_3Fe_1O_{15}$ materials as photocatalytic materials, the optical properties of the niobium-substituted materials synthesized here were also investigated using the method described by Figures S3 and S4 in Appendix 3. Two major challenges to the development of photocatalytic materials are: that the materials absorb in the visible light region of the solar spectrum and that charge separation occurs within the materials. The Aurivillius materials such as $Bi_5Ti_3Fe_1O_{15}$ are attractive candidates for use as photocatalysts as they generally absorb in the visible region and are naturally layered materials [20, 21]. Layered materials have been noted as having good charge separation capabilities which prevents the separated charges recombining before the catalytic reaction such as water splitting can occur [22, 23]. In figure 7 the absorption spectra for the sample series is shown. Similar to previous work [4, 24] two clear absorption bands can be seen. Band 1 (400-460 nm) corresponds to the transition from the valence band (VB) to the Ti3*d* conduction band (CB). The VB of these $Bi_5Ti_3Fe_1O_{15}$ samples was determined to be made up of O2p + Fe-t_{2g} + Bi6s energy levels [25]. Band 2 corresponds to the transition from the VB to CB of Fe-e_g. This is a smaller energy difference and so occurs at higher wavelengths 470-530 nm. Values of the band gap energy were obtained from extrapolation of the inflection point of an associated Tauc plot (3.5) [26],

$$(\alpha hv) = B(hv - E_G)^n \quad (3.5)$$

where E_G is the band gap energy (eV), hv is photon energy (eV) and B is a scaling constant and n = 1 or 1/2 for direct and indirect transition respectively. Band gap values of 2.17 ± 0.07 eV, 2.30 ± 0.01 eV, 2.38 ± 0.01 eV, 2.19 ± 0.02 eV, and 2.23 ± 0.02 eV were obtained for Bi5Nb0 to Bi5Nb0.4, respectively. These band gaps were found from the extrapolation of the inflection point relating to band 1. Theoretically, the

inclusion of greater concentrations of iron into the Aurivillius structure would affect the optical properties, however no significant change in band gap was observed upon Fe and Nb substitution in this work. We note that E_G values in previous reports of $Bi_5Ti_3Fe_1O_{15}$ materials tend to vary, with values of 2.03 eV [27], 2.38 eV [21], 2.59 eV [4] and 3.31 eV [28] reported for $Bi_5Ti_3Fe_1O_{15}$ materials. It is important to note that the morphology of the material can impact on the absorption of light and variations in sample coverage and roughness through the series may contribute to variations observed in the calculated band gap values. With increased substitution, the absorption was found to increase in the region of band 2. Absorption of wavelengths at 500 nm increased by ~ 5% for the Bi5Nb0.3 sample before decreasing again for the Bi5Nb0.4 sample. Some common impurity phases that occur in the later samples of the series include Fe_3O_4 and $Bi_2Ti_2O_7$. A range of band gaps for Fe_3O_4 nanoparticles have been reported ~1.88 and 2.08 eV dependent on particle size [29]. The band gap of $Bi_2Ti_2O_7$ fabricated by chemical solution deposition was found to be 2.95 eV [30]. It is possible that the presence of secondary phases would affect the absorption spectrum obtained.

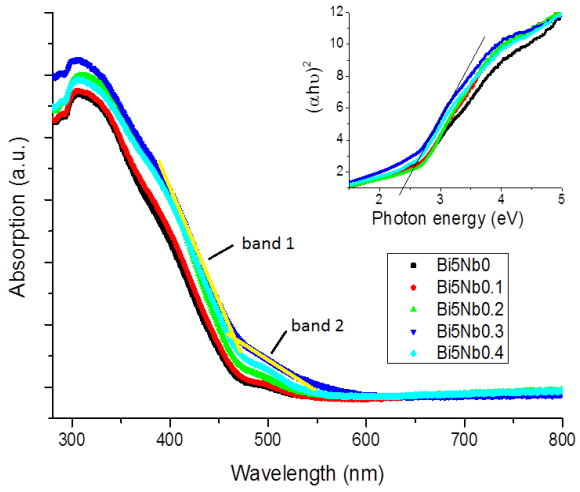

Figure 7: Absorption spectra for the Bi5Nb series. The insert displays the Tauc plot of band 1.

The photocatalytic behaviour was analysed using the experimental set-up depicted in figure S1. A portion of the samples $Bi_5Ti_{2.8}Fe_{1.1}Nb_{0.1}O_{15}$ and $Bi_5Ti_{2.2}Fe_{1.4}Mn_{0.4}O_{15}$ were analysed for their response to light and if there any degradation of the dye solution (methylene blue in a 0.1 M solution in MilliQ water (18.2 MΩ cm at 25 °C)) that would indicate that a photochemical reaction was occurring at the sample surface. A colour change occurs when methylene blue is reduced, changing from blue to colourless solution. The results of the absorbance of light over time through the dye solution are presented in figure S2. There was no change to the absorption of light during the analysis indicating that methylene blue was not being reduced.

3.4.6. Piezoresponse force microscopy

The $Bi_5Ti_3Fe_1O_{15}$ Aurivillius materials are well known ferroelectrics. The primary polarization axis is along the *a*/*b* direction parallel to the $[Bi_2O_2]^{2+}$ interlayer [31]. Single frequency measurements (measurement frequency 15 kHz) of simultaneous lateral and vertical response (figure 8 (a-f) and figures S3 to S6 in Appendix 3) clearly demonstrate the expected anisotropy of the polarization. Additional single frequency PFM measurements of the other samples in this series are presented in appendix to this chapter (figures S3 - S6). Simultaneous single frequency measurements (measurement frequency 15 kHz) show a much larger response in the lateral direction relative to the vertical direction (figure 9 (a)). The linearity of lateral piezoresponse (pm) with drive amplitude (V_{ac}) was verified to support piezoelectric behaviour (figure 9 (b)). The presence of a small vertical response can be attributed to the fact that not all the grains are lying parallel to the substrate in the *c*-axis direction (see figure 2). Furthermore, grain overlaps can be observed (figures 5 and 6) leading to an out-of-plane tilt of the Aurivillius plate-like grain whereby the vertical PFM tip has access to the in-plane polarization component [32]. As seen in the TEM analysis (figure 4), some of the plates do not lie parallel to the substrate.

An increasing piezoresponse in both the lateral and vertical directions was observed with increased substitution. The change in piezo response is greater than the esds

and is determined to be real. This increase may be due to the increased distortion of the perovskite units shown by the increase in *b*-axis pseudo lattice parameter which arises as the larger atoms (Fe or Nb) are substituted for Ti [15]. Lattice distortion was also reflected in slight changes in the a and b pseudo lattice parameters of a W/Cr co-substituted $Bi_4Ti_3O_{12}$ Aurivillius system [33]. A similar series of materials deposited by Chen *et al.* [6] using solid state reaction method found results that are comparable to ours. They determined that the unit cell volume was increasing with Fe/Nb content and that there was an increase in the piezoresponse in both the out-of-plane and in-plane directions although it should be noted that there is a random orientation of the Aurivillius platelets. Lui *et al.* [4] found increased distortion of the lattice along the *a*/*b*-axis with increased substitution of the Fe at the Ti sites. The distortion of the perovskite lattice due to octahedral rotation is well known to affect the polarization behaviour of the Aurivillius materials [15]. An inverse relationship exists, where the Curie temperature (T_C) and the Goldschmidt tolerance factor were found to increase and as *t* decreases [16]. In previous work, insertion of ions leading to an increased distortion of the perovskite unit resulted in an increase in the polarization coefficients [34, 35]. A decrease in lattice distortion was found to decrease the polarization coefficients [36].

Given the relatively low piezoresponse, topography cross-talk is likely also to have some contribution to the single frequency vertical PFM images obtained. Imaging of Bi5Nb0.1 with lateral DART-PFM (figure 8 (g-i)) mode reduces topography cross talk and amplifies the piezoresponse. The average response of the negatively polarized domains differs to that of the positive ones, indicating that these films are naturally self-polarized. Clear grain boundaries can be seen. All samples in the Bi5Nb series demonstrated piezoelectric behaviour and there were no observable differences in the DART-PFM images of the different samples in the series.

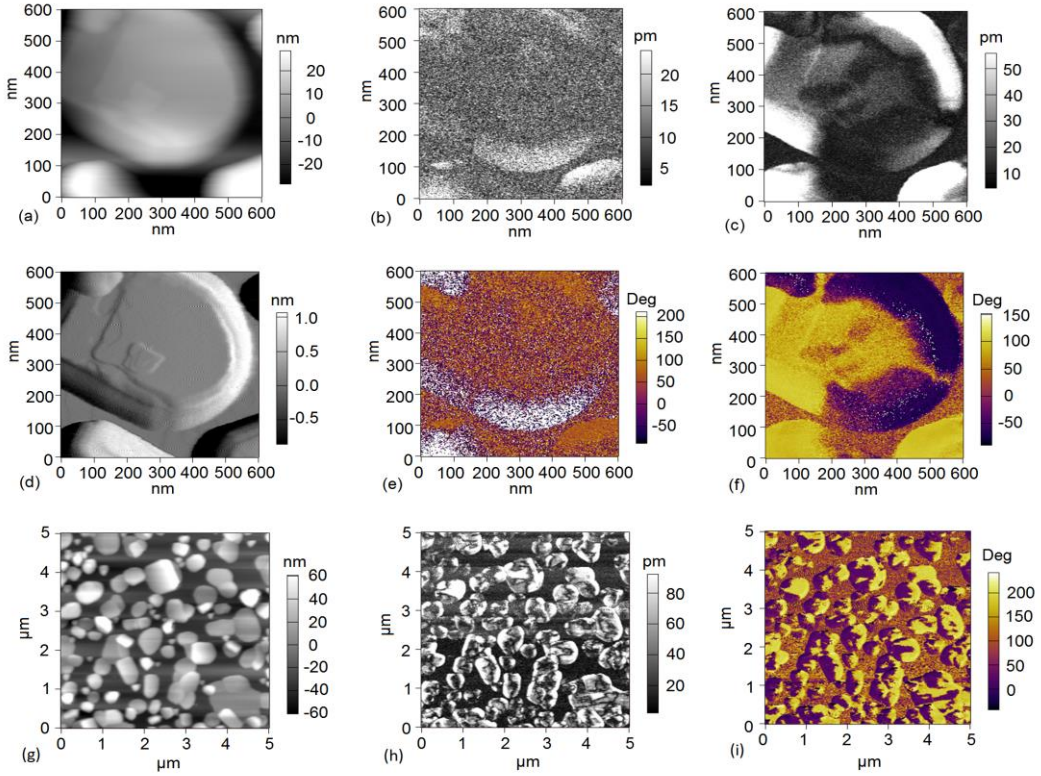

Figure 8: Single frequency PFM measurements of $Bi_5Ti_{2.8}Fe_{1.1}Nb_{0.1}O_{15}$, (a) height, (b) vertical amplitude, (c) lateral amplitude, (d) vertical deflection, (e) vertical phase and (f) lateral phase. Representative lateral DART PFM images (g) height, (h) amplitude and (i) phase of Bi5Nb0.1 sample.

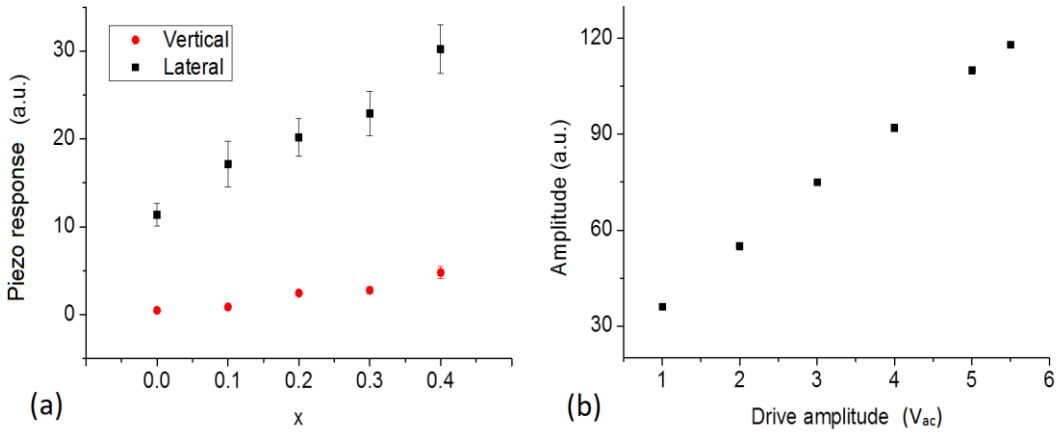

Figure 9: Relative piezoresponse in the lateral and vertical direction for the Bi5Nbx sample series (a). The error bars represent the standard deviation between measurements at five different areas on the sample. The lateral piezoresponse as a function of increasing drive amplitude of sample Bi5Nb0.1 (b). Note that the piezoresponse has not been normalized to pm/V, it has been displayed in picometers (pm) to allow for the change in the piezoresponse as a function of voltage to be demonstrated.

3.4.7. Magnetic analysis

The theoretical concentration of iron atoms over the four available *B*-sites in the structure is 25 %, 27.5 %, 30 %, 32.5 % and 35 % for x = 0, 0.1, 0.2, 0.3, 0.4, respectively. For a random distribution of atoms throughout the four *B*-sites available, the probability of strong nearest neighbour (NN) coupling requires 31% occupation and 14% occupation is required when considering both weak next-nearest neighbour (NNN) coupling and NN coupling [37]. NNN results in a weak magnetic response compared to NN interactions. Therefore, a stronger magnetic signal would be expected for Bi5Nb0.3 and Bi5Nb0.4. However, it is clear from XRD measurements that secondary phases occur at concentrations of $x \geq 0.2$ making them unsuitable for magnetic analysis. Therefore, the Bi5Nb0.1 sample was chosen for magnetic measurements as secondary phases were not observed for this sample during bulk XRD measurements. Unsaturated magnetic hysteresis loops (MH curves) were obtained for this sample when measured at temperatures of 2, 150 and 300 K. The orientation of the sample is in-pane with the magnetic field during measurement and the diamagnetic contribution of the substrate has been subtracted from the MH curve results. The sample shows weak ferromagnetic behaviour at all three temperatures (figure 10 (a)). The remanent magnetization (M_R) was measured as 2.2 emu/cm^3 or 0.28 emu/g at 2 K, 1.6 emu/cm^3 or 0.2 emu/g at 150 K and 1.5 emu/ cm^3 or 0.19 emu/g at 300 K. M_R can be influenced by extrinsic factors such as grain size and orientation; therefore, it can be difficult to compare results with different

fabrication methods. This can help to explain the variation in reported values of M_R in the literature. Thin films of $Bi_6Ti_{2.8}Fe_{1.52}Mn_{0.68}O_{18}$ fabricated using a very similar experimental procedure exhibited a comparable magnetic response of M_R = 0.18 emu/cm^3 and saturation magnetization (M_S) = 6.05 emu/cm^3 at 300 K [9]. Mao *et al*. observed a significant difference in samples of $Bi_5Ti_3Fe_1O_{15}$ prepared by a multi-calcination procedure compared to the traditional solid-state reaction method [38]. While Song *et al*. also observed differences between their six perovskite layered materials, fabricated by chemical solution deposition, and previous literature reports [39]. $Bi_5Ti_3Fe_1O_{15}$ prepared by conventional solid state reaction was found to have a weak ferromagnetic response of M_R = 0.122 memu/g [40] and 1.36 × 10^{-3} memu/g [41]. For previously reported $Bi_5Ti_3Fe_1O_{15}$ thin films fabricated by chemical solution deposition, M_S = 1.7 emu/cm^3 [42], 0.21 emu/cm^3 [27], 5.1 emu/cm^3 [2] and 0.21 emu/cm^3 [28] were reported. It must be noted that a purity assessment of the samples used for magnetic measurements seldom accompanies the reported magnetization values. Trace (~0.01 vol.%) [43, 44] amounts of undetected impurities present in the sample may be responsible for the variance in magnetization values reported. The coercivity (H_C) was measured as being ~40 Oe at 2K, which slightly decreases with increase of temperature (figure 10 (a)). The magnetization was examined as a function of decreasing temperature (figure 10 (b)) with an applied field of 20 Oe. The difference between the field-cooled (FC) and zero field cooled (ZFC) curve below 100 K clearly indicates a ferromagnetic response from a single magnetic phase. This is also confirmed by the remanence (REM) magnetization curve, which is positive and decreases with increase of temperature. This work confirms ferromagnetic behaviour at room temperature and above (up to 350 K as experimented), indicating the potential use of the Bi5Nb0.1 material for room temperature multiferroic device applications. Based on a *B*-site iron occupation of 27.5% for this sample, the magnetic response observed can be attributed to weak NNN interactions, if the iron is randomly distributed over the available *B*-sites. However, experimental [45, 46] and computational [5] studies have indicated that the partitioning of Fe ions throughout the Aurivillius structure is not evenly distributed over all available perovskite layers and that preferential magnetic ion partitioning

may increase magnetic percolation within particular perovskite layers. There are two non-equivalent *B*-sites present in the *m* = 4 structure. The outer perovskite layers are adjacent to the $(Bi_2O_2)^{2+}$ interlayer and experience a different environment compared to the two inner perovskite layers. There is an electrostatic preference for the more-highly-charged Ti^{4+} to occupy the outer sites close to the outer layer of oxygen ions in the $[Bi_2O_2]^{2+}$ [47]. There is also a strain energy which serves to drive cations larger than Ti^{4+} away from the layers closest to the $[Bi_2O_2]^{2+}$ layers [19, 48]. This would concentrate the iron atom to the inner perovskite blocks. Similar partitioning of Cr was observed in $Bi_5Ti_3Cr_1O_{15}$ systems as demonstrated by neutron diffraction experiments [49]. Theoretical calculations [5] indicate that the strength of the NN couplings for magnetic cations located within inner sites (J_{NN} ~43 to 46 meV) is more than twice that for adjacent inner to outer site (J_{NN} ~12 to 20 meV) NN coupling interactions, therefore distribution of magnetic cations within these inner layers is crucial to the percolation and strength of magnetic interactions within the Aurivillius phases.

The super exchange interaction between Fe^{3+} - O - Fe^{3+} atoms would be predicted to give rise to antiferromagnetic behaviour. However, the MH relationship for an antiferromagnetic behaviour is linear [7]. It is possible that the ferromagnetic response observed here is due to a Fe^{3+}- O - Fe^{2+} super exchange mechanism. Another possible cause for the weak ferromagnetism might be that it arises from spin canting, as described for $BiFeO_3$ [41, 47]. The H_C (figure 10(a)) and the magnetization (figure 10(b)) decrease with an increase in temperature (T) for Bi5Nb0.1 which is similar to the model system $BiFeO_3$ and other multiferroic ferromagnets [11, 50, 51]. Given the relatively weak ferromagnetic signal observed for Bi5Nb0.1, changes in H_C and M_R as a function of temperature are relatively small.

To investigate possible magnetoelectric switching, the samples $Bi_5Ti_{2.8}Fe_{1.1}Nb_{0.1}O_{15}$ and $Bi_5Ti_{2.2}Fe_{1.4}Mn_{0.4}O_{15}$ were imaged using PFM under a varying magnetic field. PFM analysis was performed at various magnetic field strengths. The field was increased at 500 G intervals to ±2500 G. The results of this analysis is depicted in figure S7 and S8 in Appendix 1. There was no observable change to the polarisation direction or

magnitude when the magnetic field was reversed, meaning that magnetoelectric switching was not observed in these experiments. Crystallite orientation with respect to magnetic field direction may be a factor affecting the lack of magnetoelectric coupling observed for these samples [52].

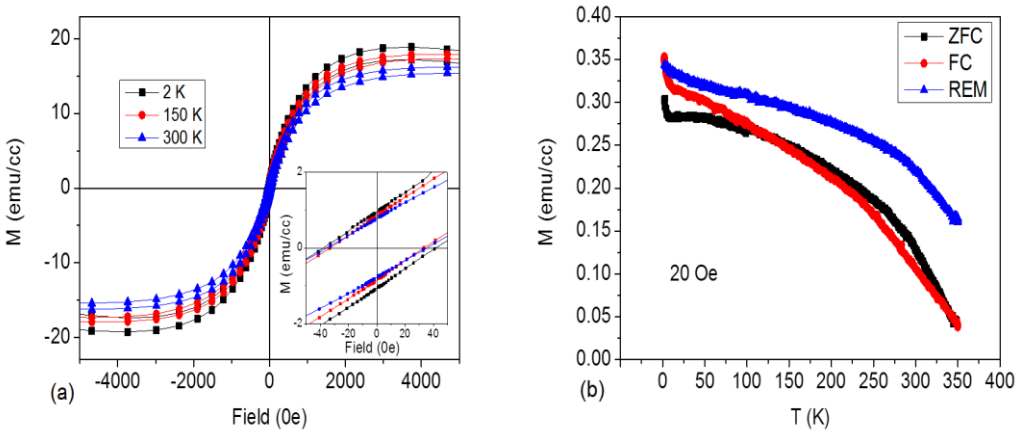

Figure 10: MH curves after subtraction of the diamagnetic contribution of the substrate magnetic measurements for Bi5Nb0.1 (a). A small magnetic signal of approximately 2.2, 1.6 and 1.5 emu/cm^3 and a H_c ~ 40, 36, 34 Oe at 2, 150 and 300K was detected under zero applied magnetic field (inset (a)). MT graph showing the zero field cooled (ZFC), field cooled (FC) and remnant (REM) curves (b).

3.4.8. Energy dispersive X-ray spectroscopy analysis

The exact same Bi5Nb0.1 sample piece that was used for magnetic measurements was then analysed by surface SEM/EDX (figure 11). Scans of the sample did not show any micron-sized observable Fe clusters which could indicate secondary impurity phases such as Fe_2O_3 or the magnetic spinel phase Fe_3O_4. Considering the observed magnetic signal at 300 K was 0.19 emu/g, the presence of just 0.0095 vol. % of Fe_3O_4 in the sample could be responsible for this weak magnetic signal. Based on the EDX data we have, we can rule out inclusions greater than 3 µm contributing significantly to the magnetic signal measured. It would be necessary to perform the full procedure

developed by Schmidt *et al*. to put a defined confidence level on a material being a single-phase material. This would require a series of measurements at varying sample volumes and instrument resolutions and full statistical analysis [43].

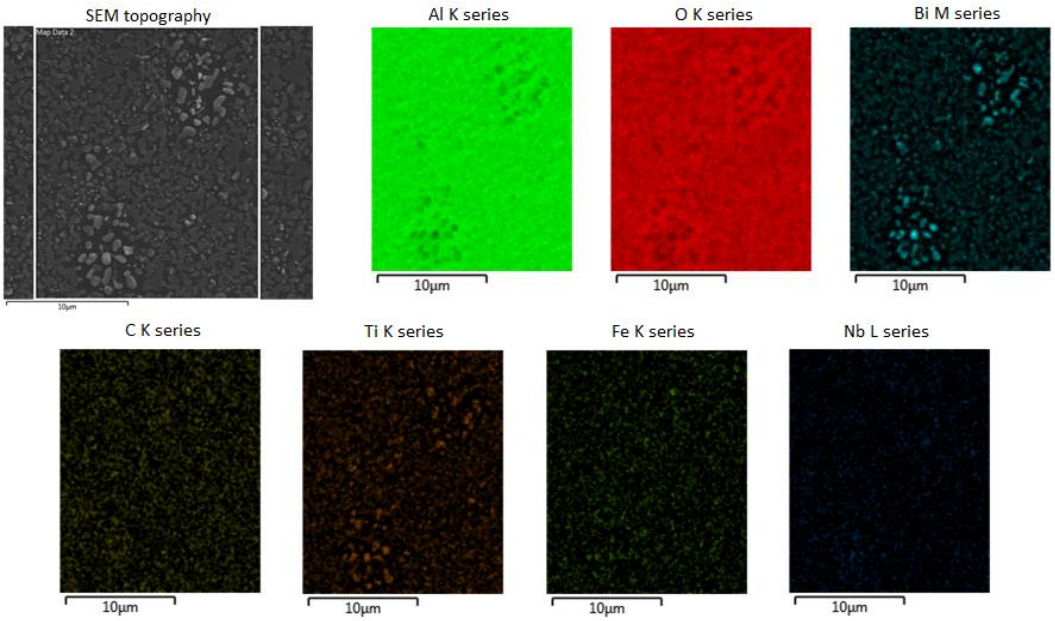

Figure 11: Surface SEM topography and EDX surface analysis of the Bi5Nb0.1 sample.

3.5. Conclusion

In this work a series of Aurivillius phase materials were synthesized using chemical solution deposition, which was found to be a facile, relatively simple way to control the material stoichiometry. The following samples were prepared; $Bi_5Ti_{3-x}Fe_{1+x}Nb_xO_{15}$ with x = 0, 0.1, 0.2, 0.3, 0.4. Using aliovalent substitution the concentration of Fe and Nb was increased in the material while the Ti concentration decreased. The effects of the variation in stoichiometry on the physical, optical, and electrical properties were examined. The change in pseudo lattice parameters was attributed to the insertion of larger atoms at the *B*-site of the perovskite and the resulting increase in distortion of the perovskite unit. The majority of peaks corresponded to 00*l* reflections. However, the formation of additional secondary phases indicates that substitution after x = 0.1 is not stoichiometric. This suggests a solution limit of x = 0.1 for this

series. Lui *et al.* [4] used their XRD data to determine the computational bond lengths. They found increasing distortion of the lattice structure with increased substitution of Fe for Ti. This increased distortion may determine the limit of Fe that can be supported within the structure. Using PFM, it was established that as expected, the major polarization was along the *a*/*b* axis. The piezoresponse was found to increase with increased Fe and Nb substitution in both the lateral and vertical direction, indicating that the ferroelectric behaviour of the material was enhanced, and not adversely affected by the magnetic ion substitution. A small ferromagnetic response was observed at room temperature for the Bi5Nb0.1 sample, which is desirable for multiferroic device applications. The magnitude of the M_R response was found to be higher than many of a range of reported values for the $Bi_5Ti_3Fe_1O_{15}$ parent phase; however extrinsic factors such as sample fabrication methods make comparison difficult. While EDX analysis did not show any iron-rich impurity inclusions in this sample, the possibility of an inhomogeneous distribution of secondary impurity phases cannot be dismissed due to the limit of detection of the analysis methods used thus far. There is a range of results in the literature concerning similar compositions where it is claimed that the concentration of Fe has been successfully increased. However many of these rely on XRD analysis alone to determine the phase purity of the material [4, 6]. Lavado *et al.* [7] determine a solution limit for the $Bi_4Ti_3O_{12}$ m = 3 Aurivillius phase and the phase purity of the materials below this limit is supported by XRD and EDX analysis. A similar series of materials deposited by Chen *et al.* [6] using solid state reaction method found results that are comparable to ours. They determined that the unit cell volume was increasing with Fe/Nb content and that there was an increase in the piezoresponse in both the out-of-plane and in-plane directions although it should be noted that there is a random orientation of the Aurivillius platelets. The magnetic measurements do not show robust magnetic ordering predicted by Birenbaum *et al.* [5] even at the higher concentrations of Fe. They do not observe secondary phases from XRD data even at the higher concentration of Fe/Nb. Lui *et al*. [4] directly substituted Fe for Ti and observed no secondary phases from XRD data even at the higher concentration of Fe. This range of results illustrates the complicated nature of the Aurivillius

materials. It is possible that the different fabrication methods may influence the properties obtained.

3.6. References

[1] F. Kubel and H. Schmid, "X-ray room temperature structure from single crystal data, powder diffraction measurements and optical studies of the aurivillius phase Bi5(Ti3Fe)O15," *Ferroelectrics,* vol. 129, no. 1, pp. 101-112, 1992/05/01 1992, doi: 10.1080/00150199208016980.

[2] Y. Bai, J. Chen, and S. Zhao, "Magnetoelectric fatigue of Ho-doped Bi 5 Ti 3 FeO 15 films under the action of bipolar electrical cycling," *RSC Advances,* vol. 6, no. 47, pp. 41385-41391, 2016.

[3] L. W. Martin, Y. H. Chu, and R. Ramesh, "Advances in the growth and characterization of magnetic, ferroelectric, and multiferroic oxide thin films," *Materials Science and Engineering: R: Reports,* vol. 68, no. 4-6, pp. 89-133, 2010, doi: 10.1016/j.mser.2010.03.001.

[4] X. Liu, L. Xu, Y. Huang, C. Qin, L. Qin, and H. J. Seo, "Improved photochemical properties of Aurivillius Bi 5 Ti 3 FeO 15 with partial substitution of Ti 4+ with Fe 3+," *Ceramics International,* vol. 43, no. 15, pp. 12372-12380, 2017, doi: 10.1016/j.ceramint.2017.06.103.

[5] A. Y. Birenbaum and C. Ederer, "Potentially multiferroic Aurivillius phaseBi5FeTi3O15: Cation site preference, electric polarization, and magnetic coupling from first principles," *Physical Review B,* vol. 90, no. 21, 2014, doi: 10.1103/PhysRevB.90.214109.

[6] C. Chen *et al.*, "Effect of Nb and more Fe ions co-doping on the microstructures, magnetic, and piezoelectric properties of Aurivillius Bi5Ti3FeO15 phases," *Journal of Applied Physics,* vol. 120, no. 21, p. 214104, 2016, doi: 10.1063/1.4971256.

[7] C. Lavado and M. G. Stachiotti, "Fe3+/Nb5+ co-doping effects on the properties of Aurivillius Bi4Ti3O12 ceramics," *Journal of Alloys and Compounds,* vol. 731, pp. 914-919, 2018, doi: 10.1016/j.jallcom.2017.10.112.

[8] L. Keeney *et al.*, "Room temperature ferroelectric and magnetic investigations and detailed phase analysis of Aurivillius phase Bi5Ti3Fe0.7Co0.3O15 thin films," *Journal of Applied Physics,* vol. 112, no. 5, p. 052010, 2012, doi: 10.1063/1.4745936.

[9] L. Keeney, C. Groh, S. Kulkarni, S. Roy, M. E. Pemble, and R. W. Whatmore, "Room temperature electromechanical and magnetic investigations of ferroelectric Aurivillius phase Bi5Ti3(FexMn1−x)O15 (x = 1 and 0.7) chemical solution deposited thin films," *Journal of Applied Physics,* vol. 112, no. 2, p. 024101, 2012/07/15 2012, doi: 10.1063/1.4734983.

[10] B. J. Rodriguez, C. Callahan, S. V. Kalinin, and R. Proksch, "Dual-frequency resonance-tracking atomic force microscopy," *Nanotechnology,* vol. 18, no. 47, p. 475504, 2007, doi: 10.1088/0957-4484/18/47/475504.

[11] T. Maity, S. Goswami, D. Bhattacharya, and S. Roy, "Superspin glass mediated giant spontaneous exchange bias in a nanocomposite of BiFeO 3− Bi 2 Fe 4 O 9," *Physical review letters,* vol. 110, no. 10, p. 107201, 2013.

[12] F. K. Lotgering, "Topotactical reactions with ferrimagnetic oxides having hexagonal crystal structures—I," *Journal of Inorganic and Nuclear Chemistry,* vol. 9, no. 2, pp. 113-123, 1959/02/01/ 1959, doi: https://doi.org/10.1016/0022-1902(59)80070-1.

[13] K. Momma and F. Izumi, "VESTA 3 for three-dimensional visualization of crystal, volumetric and morphology data," *Journal of applied crystallography,* vol. 44, no. 6, pp. 1272-1276, 2011.

[14] C. H. Hervoches, A. Snedden, R. Riggs, S. H. Kilcoyne, P. Manuel, and P. Lightfoot, "Structural Behavior of the Four-Layer Aurivillius-Phase Ferroelectrics SrBi4Ti4O15 and Bi5Ti3FeO15," *Journal of Solid State Chemistry,* vol. 164, no. 2, pp. 280-291, 2002, doi: 10.1006/jssc.2001.9473.

[15] J. B. Goodenough, "Electronic and ionic transport properties and other physical aspects of perovskites," *Reports on Progress in Physics,* vol. 67, no. 11, pp. 1915-1993, 2004, doi: 10.1088/0034-4885/67/11/r01.

[16] D. Y. Suárez, I. M. Reaney, and W. E. Lee, "Relation between tolerance factor and Tc in Aurivillius compounds," *Journal of Materials Research,* vol. 16, no. 11, pp. 3139-3149, 2011, doi: 10.1557/jmr.2001.0433.

[17] R. Shannon, "Revised effective ionic radii and systematic studies of interatomic distances in halides and chalcogenides," *Acta Crystallographica Section A,* vol. 32, no. 5, pp. 751-767, 1976, doi: doi:10.1107/S0567739476001551.

[18] P. Scherrer, "Nachr Ges wiss goettingen," *Math. Phys.,* vol. 2, pp. 98-100, 1918.

[19] R. A. Armstrong and R. E. Newnham, "Bismuth titanate solid solutions," *Materials Research Bulletin,* vol. 7, no. 10, pp. 1025-1034, 1972/10/01/ 1972, doi: https://doi.org/10.1016/0025-5408(72)90154-7.

[20] G. Naresh and T. K. Mandal, "Excellent Sun-Light-Driven Photocatalytic Activity by Aurivillius Layered Perovskites, Bi5–xLaxTi3FeO15 (x = 1, 2)," *ACS Applied Materials & Interfaces,* vol. 6, no. 23, pp. 21000-21010, 2014/12/10 2014, doi: 10.1021/am505767c.

[21] J. S. Jang *et al.*, "Synthesis and characterization of aurivillius phase Bi5Ti3FeO15 layered perovskite for visible light photocatalysis," *Journal of the Ceramic Society of Japan,* vol. 117, no. 1371, pp. 1268-1272, 2009, doi: 10.2109/jcersj2.117.1268.

[22] Y. Hu *et al.*, "Layered perovskite oxides and their derivative nanosheets adopting different modification strategies towards better photocatalytic performance of water splitting," *Renewable and Sustainable Energy Reviews,* vol. 119, p. 109527, 2020/03/01/ 2020, doi: https://doi.org/10.1016/j.rser.2019.109527.

[23] L. Jiang, S. Ni, G. Liu, and X. Xu, "Photocatalytic hydrogen production over Aurivillius compound Bi3TiNbO9 and its modifications by Cr/Nb co-doping,"

Applied Catalysis B: Environmental, vol. 217, pp. 342-352, 2017, doi: 10.1016/j.apcatb.2017.06.012.

[24] L. Cao *et al.*, "Photovoltaic properties of Aurivillius Bi4NdTi3FeO15 ceramics with different orientations," *Journal of Alloys and Compounds,* vol. 800, pp. 134-139, 2019, doi: 10.1016/j.jallcom.2019.05.307.

[25] S. Sun, W. Wang, H. Xu, L. Zhou, M. Shang, and L. Zhang, "Bi5FeTi3O15 Hierarchical Microflowers: Hydrothermal Synthesis, Growth Mechanism, and Associated Visible-Light-Driven Photocatalysis," *The Journal of Physical Chemistry C,* vol. 112, no. 46, pp. 17835-17843, 2008/11/20 2008, doi: 10.1021/jp807379c.

[26] D. L. Wood and J. Tauc, "Weak Absorption Tails in Amorphous Semiconductors," *Physical Review B,* vol. 5, no. 8, pp. 3144-3151, 04/15/ 1972, doi: 10.1103/PhysRevB.5.3144.

[27] M. Wu, Z. Tian, S. Yuan, and Z. Huang, "Magnetic and optical properties of the Aurivillius phase Bi5Ti3FeO15," *Materials Letters,* vol. 68, pp. 190-192, 2012/02/01/ 2012, doi: https://doi.org/10.1016/j.matlet.2011.09.113.

[28] W. Bai *et al.*, "Electrical, magnetic, and optical properties in multiferroic Bi5Ti3FeO15 thin films prepared by a chemical solution deposition route," *Journal of Applied Physics,* vol. 109, no. 6, p. 064901, 2011, doi: 10.1063/1.3553879.

[29] S. A. Kulkarni, P. S. Sawadh, P. K. Palei, and K. K. Kokate, "Effect of synthesis route on the structural, optical and magnetic properties of Fe3O4 nanoparticles," *Ceramics International,* vol. 40, no. 1, Part B, pp. 1945-1949, 2014/01/01/ 2014, doi: https://doi.org/10.1016/j.ceramint.2013.07.103.

[30] W. F. Yao *et al.*, "Photocatalytic property of bismuth titanate Bi2Ti2O7," *Applied Catalysis A: General,* vol. 259, no. 1, pp. 29-33, 2004.

[31] R. E. Newnham, R. W. Wolfe, and J. F. Dorrian, "Structural basis of ferroelectricity in the bismuth titanate family," *Materials Research Bulletin,*

vol. 6, no. 10, pp. 1029-1039, 1971/10/01/ 1971, doi: https://doi.org/10.1016/0025-5408(71)90082-1.

[32] L. Keeney *et al.*, "Ferroelectric Behavior in Exfoliated 2D Aurivillius Oxide Flakes of Sub-Unit Cell Thickness," *Advanced Electronic Materials,* vol. n/a, no. n/a, p. 1901264, 2020/01/30 2020, doi: 10.1002/aelm.201901264.

[33] Y. Chen *et al.*, "Ion Doping Effects on the Lattice Distortion and Interlayer Mismatch of Aurivillius-Type Bismuth Titanate Compounds," (in eng), *Materials (Basel, Switzerland),* vol. 11, no. 5, p. 821, 2018, doi: 10.3390/ma11050821.

[34] J. Yuan, R. Nie, Q. Chen, J. Xing, and J. Zhu, "Evolution of structural distortion and electric properties of BTN-based high-temperature piezoelectric ceramics with tungsten substitution," *Journal of Alloys and Compounds,* vol. 785, pp. 475-483, 2019, doi: 10.1016/j.jallcom.2019.01.210.

[35] Y. Bai, J. Chen, R. Tian, and S. Zhao, "Enhanced multiferroic and magnetoelectric properties of Ho, Mn co-doped Bi5Ti3FeO15 films," *Materials Letters,* vol. 164, pp. 618-622, 2016/02/01/ 2016, doi: https://doi.org/10.1016/j.matlet.2015.11.083.

[36] Z. Peng *et al.*, "Crystal structure, dielectric and piezoelectric properties of Ta/W codoped Bi3TiNbO9 Aurivillius phase ceramics," *Current Applied Physics,* vol. 14, no. 12, pp. 1861-1866, 2014/12/01/ 2014, doi: https://doi.org/10.1016/j.cap.2014.10.011.

[37] Ł. Kurzawski and K. Malarz, "Simple Cubic Random-Site Percolation Thresholds for Complex Neighbourhoods," *Reports on Mathematical Physics,* vol. 70, no. 2, pp. 163-169, 2012/10/01/ 2012, doi: https://doi.org/10.1016/S0034-4877(12)60036-6.

[38] X. Mao, W. Wang, H. Sun, Y. Lu, and X. Chen, "Influence of different synthesizing steps on the multiferroic properties of Bi5Fe1Ti3O15 and Bi5Fe0.5Co0.5Ti3O15 ceramics," *Journal of Materials Science,* vol. 47, no. 6, pp. 2960-2965, 2012/03/01 2012, doi: 10.1007/s10853-011-6129-9.

[39] D. P. Song, J. Yang, Y. X. Wang, J. Yang, and X. B. Zhu, "Magnetic and ferroelectric properties of Aurivillius phase Bi7Fe3Ti3O21 and their doped films," *Ceramics International,* vol. 43, no. 18, pp. 17148-17152, 2017, doi: 10.1016/j.ceramint.2017.09.136.

[40] X. Chen, X. B. Zeng, F. Yang, X. Kong, C. Wei, and P. Su, "Room temperature magnetoelectric coupling in Bi5Ti3FeO15 ceramics," in *Advanced Materials Research*, 2013, vol. 668: Trans Tech Publ, pp. 762-766.

[41] X. Y. Mao, W. Wang, and X. B. Chen, "Electrical and magnetic properties of Bi5FeTi3O15 compound prepared by inserting BiFeO3 into Bi4Ti3O12," *Solid State Communications,* vol. 147, no. 5, pp. 186-189, 2008/08/01/ 2008, doi: https://doi.org/10.1016/j.ssc.2008.05.025.

[42] H. Sun *et al.*, "Multiferroic behaviour and the magneto-dielectric effect in Bi5FeTi3O15thin films," *Journal of Physics D: Applied Physics,* vol. 45, no. 38, p. 385001, 2012/09/03 2012, doi: 10.1088/0022-3727/45/38/385001.

[43] M. Schmidt *et al.*, "Absence of Evidence ≠ Evidence of Absence: Statistical Analysis of Inclusions in Multiferroic Thin Films," *Scientific Reports,* vol. 4, no. 1, p. 5712, 2014/07/16 2014, doi: 10.1038/srep05712.

[44] A. Faraz *et al.*, "Exploring ferroelectric and magnetic properties of Tb-substituted m = 5 layered Aurivillius phase thin films," *Journal of Applied Physics,* vol. 123, no. 12, p. 124101, 2018/03/28 2018, doi: 10.1063/1.5009986.

[45] L. Keeney, C. Downing, M. Schmidt, M. E. Pemble, V. Nicolosi, and R. W. Whatmore, "Direct atomic scale determination of magnetic ion partition in a room temperature multiferroic material," *Sci Rep,* vol. 7, no. 1, p. 1737, May 11 2017, doi: 10.1038/s41598-017-01902-1.

[46] N. A. Lomanova, V. G. Semenov, V. V. Panchuk, and V. V. Gusarov, "Structural changes in the homologous series of the Aurivillius phases Bin+1Fen−3Ti3O3n+3," *Journal of Alloys and Compounds,* vol. 528, pp. 103-108, 2012, doi: 10.1016/j.jallcom.2012.03.040.

[47] G. Catalan and J. F. Scott, "Physics and Applications of Bismuth Ferrite," *Advanced Materials,* vol. 21, no. 24, pp. 2463-2485, 2009/06/26 2009, doi: 10.1002/adma.200802849.

[48] T. Kikuchi, "Stability of layered bismuth compounds in relation to the structural mismatch," *Materials Research Bulletin,* vol. 14, no. 12, pp. 1561-1569, 1979.

[49] A. T. Giddings, M. C. Stennett, D. P. Reid, E. E. McCabe, C. Greaves, and N. C. Hyatt, "Synthesis, structure and characterisation of the n= 4 Aurivillius phase Bi5Ti3CrO15," *Journal of Solid State Chemistry,* vol. 184, no. 2, pp. 252-263, 2011.

[50] I. Vrejoiu *et al.*, "Interfacial strain effects in epitaxial multiferroic heterostructures of Pb Zr x Ti 1− x O 3⁄ La 0.7 Sr 0.3 Mn O 3 grown by pulsed-laser deposition," *Applied Physics Letters,* vol. 92, no. 15, p. 152506, 2008.

[51] J. Xiong *et al.*, "Ferromagnetic–Antiferromagnetic Coupling by Distortion of Fe/Mn Oxygen Octahedrons in (BiFeO3) m (La0. 7Sr0. 3MnO3) n Superlattices," *Small,* vol. 13, no. 18, p. 1700107, 2017.

[52] A. Faraz *et al.*, "Direct visualization of magnetic-field-induced magnetoelectric switching in multiferroic aurivillius phase thin films," *Journal of the American Ceramic Society,* vol. 100, no. 3, pp. 975-987, 2017, doi: 10.1111/jace.14597.

Chapter 4

4. Necessity for structural reorganisation to accommodate increased magnetic cation content across the Aurivillius-phase $Bi_6Ti_xFe_yMn_zO_{18}$ (x = 3.2 – 1.6, y = 1.2 - 1.95, z = 0.3 - 0.9) series

4.1. Abstract

The $Bi_6Ti_xFe_yMn_zO_{18}$ (B6TFMO) Aurivillius phase, is a rare example of a single-phase room temperature multiferroic, displaying saturation magnetization (M_S) values of 215 emu/cm^3 and in-plane saturation polarization (P_s) values of $>$ 26 μC/cm^2. With the aim of increasing the proportion of magnetic ions within the B6TFMO structure, this study examined the effect of *B*-site substitution in this Aurivillius material. Four series of Aurivillius materials with a target composition of $Bi_6Ti_xFe_yMn_zO_{18}$ (x = 3.2 – 1.6, y = 1.2 - 1.95, z = 0.3 - 0.9) (*m* = 5) were fabricated by chemical solution deposition. XRD and TEM analysis demonstrates that the formation of the higher *m* = 6 Aurivillius phases occurred when the occupancy of Ti^{4+} at the *B*-sites fell below 52 %. It is reasoned that the rearrangement is driven by the need to accommodate the differences in cation radii and oxidation state when Ti^{4+} is substituted by Fe^{3+} and Mn^{3+}. We propose that oxidation of Mn^{3+} to Mn^{4+} is occurring in the material, however above a threshold of 8 % nominal Mn^{4+}, the *m* = 5 structure can no longer tolerate the smaller Mn^{4+} ion and the structure forms the *m* = 6 phase in order to accommodate the additional manganese at a lower average manganese oxidation state. This work provides valuable insight into the design and development of new multiferroic phases by defining a solubility limit of 48 % magnetic ion content that can be accommodated at the *B*-site of the multiferroic Aurivillius phase structure.

4.2. Introduction

The Aurivillius phase materials, $Bi_2O_2(A_{m-1}B_mO_{3m+1})$, provide a versatile framework for the design of multiferroic materials [1]. The Aurivillius phase materials are well known ferroelectrics and they can accommodate cations such as Fe, Mn, and Cr at their *B*-sites which can contribute to magnetic super-exchange interactions. Indeed,

the manganese and iron-containing $Bi_6Ti_xFe_yMn_zO_{18}$ (*m* = 5) (B6TFMO) Aurivillius phase system is an example of a rarely found single-phase room temperature multiferroic [2].

For the B6TFMO materials mentioned above, the magnetic ion content was 44 % of *B*-site cations. The percentage of magnetic ions in a 3D lattice necessary for percolation is 31 % for nearest neighbour interactions (NN) and 14 % for NN and next nearest interactions (NNN) for a random distribution of the magnetic ions [3]. To demonstrate the difference between NN and NNN interactions, in the 4-layered (*m* = 4) $Bi_5Ti_3FeO_{15}$ Aurivillius material the calculated magnetic Heisenberg coupling constants of the NN interactions result in stronger magnetic coupling (J_{NN} = 40-50 meV) compared to NNN which has weaker magnetic coupling (J_{NNN} = 1-2 meV) [4].

Therefore, the insertion of an increased volume of magnetic ions would be beneficial in terms of the promotion of long-range magnetic ordering within the material. However, a limit to the concentration of Fe and Mn that can be tolerated within the Aurivillius phase structure is expected, not only based on cation radii differences (0.605, 0.645 and 0.645 Å for Ti^{4+}, Fe^{3+} and Mn^{3+}, respectively [5]), but also considering that these cations have a nominal valence of 3+ and are substituted in place of Ti, having a nominal valence of 4+.

In this study we systematically examine the effect of varying the concentrations of the three *B*-site atoms: Ti, Fe and Mn in the *m* = 5 system $Bi_6Ti_xFe_yMn_zO_{18}$ (x = 3.2 to 1.6, y = 1.2 to 1.9, z = 0.3 to 0.9). The aim of this study is to determining the limit of magnetic ion inclusion in the *m* = 5 Aurivillius structure. The substitution of Ti^{4+} by Mn^{3+}/Fe^{3+} would necessitate oxidation state change from the Mn or Fe to maintain a balance stoichiometry assuming that there are no vacancies.

Assuming that oxide ion vacancies do not play a role [6-8], Snedden *et al.* have suggest that in Aurivillius phases with *m* > 1 the formation of oxide ion vacancies may not be favourable [6], we speculate that oxidation of Mn^{3+} to Mn^{4+} occurs in order to maintain a balanced stoichiometry when Ti^{4+} is substituted for manganese/iron. The formation of the *m* = 6 phase is observed to occur when the average oxidation state on Mn is above +3.44. This is close to the value (+3.2) observed by Zurbuchen *et al.* for a *m* = 6 manganese-containing composition [8]. However, there is a limit to the

solubility of the smaller Mn^{4+} cation and we observe a threshold of 8 % of nominal Mn^{4+} (ionic radius of 0.53 Å [5]) that can be tolerated within the *m* = 5 structure. This corresponds to a solubility limit of 48 % magnetic cations at the *B*-site. We present XRD and TEM results demonstrating that above this threshold, rearrangement of the Aurivillius structure into the *m* = 6 phase occurs in order to accommodate increased levels of magnetic cations at a lower average manganese oxidation state.

4.3. Experimental

A chemical solution deposition method was used to fabricate the $Bi_6Ti_xFe_yMn_zO_{18}$ compositions using a procedure similar to that previously reported [2]. The precursors $Bi(NO_3)_3.5H_2O$ (reagent grade, 98 %, Sigma-Aldrich) and $Ti(OC_4H_9)_4$ (reagent grade, 97 %, Sigma-Aldrich) were dissolved in lactic acid (ACS reagent, ≥ 85 %, Sigma-Aldrich) at room temperature with constant stirring for approximately one week to form Solution A. $Fe(NO_3)_3.9H_2O$ (ACS reagent, ≥ 98 %, Sigma-Aldrich) and ($Mn(acac)_3$) (99.9+ %, Strem Chemicals, Inc.) were dissolved in acetylacetone (≥ 99.5 % (GC), Sigma-Aldrich) to form Solution B. Solution B was added to solution A and mixed for one hour. This precursor solution was placed dropwise onto a *c-m* sapphire wafer and then spin coated at 2000 rpm for 30 seconds. The wafer with deposited film was then pre-annealed at 300 °C for ten minutes to remove the organic solvents and then annealed at 850 °C for one hour in ambient atmosphere and pressure in order to crystallize the films.

The general formulas of the different series were as follows; series 1: $Bi_6Ti_3Fe_{1.6-x}Mn_{0.4+x}O_{18}$ (x = 0, 0.1, 0.2, 0.3 and 0.4), series 2: $Bi_6Ti_{3.2-x}Fe_{1.5}Mn_{0.3+x}O_{18}$ (x = 0, 0.1, 0.2, 0.3, 0.4, 0.5 and 0.6), series 3: $Bi_6Ti_{3.2-x}Fe_{1.3+x}Mn_{0.5}O_{18}$ (x = 0, 0.1, 0.2, 0.3, 0.4, 0.5 and 0.6) and series 4 $Bi_6Ti_xFe_yMn_zO_{18}$ (x = 3.2 to 1.6, y = 1.2 to 1.9, z = 0.3 to 0.9).

X-ray diffraction measurements (XRD) were performed using a Philips X'pert PW3719 MPD diffractometer, Cu Kα radiation, 40 kV, 35 mA and 2θ range of 6 ˚ - 40 ˚. The *m* = 5 Aurivillius phase was indexed from calculated XRD patterns generated using VESTA software [9] using data from García-Guaderrama *et al*. [10]. The *m* = 6 phase was indexed from calculated XRD patterns using data from Krzhizhanovskaya *et al.* [11].

Atomic Force Microscopy (AFM) and Piezo Force Microscopy (PFM) were performed using an MFP-3D^{TM} Asylum Research instrument. AFM was conducted in AC mode using Olympus AC240TS probes (Al reflex coated, ~7 nm tip radius, 70 kHz resonant frequency). PFM was conducted in both single frequency and lateral Dual AC Resonance Tracking (DART-PFM) mode [12] using Olympus AC240TM electrilevers (Ti/Pt coated silicon probes, Al reflex coated, ~15 nm tip radius, 70 kHz resonant frequency).

Scanning electron microscopy (SEM) was performed on Zeiss Supra 40 instrument and samples were coated with a twenty second gold coat (3-6 nm thickness) before measurement to prevent charging during imaging.

Lamella cross sections of the films were prepared using a FEI DualBeam Helios NanoLab 600i Focused Ion Beam instrument. High resolution transmission electron microscopy (HR-TEM) was performed using Jeol 2100 transmission electron microscope; 200kV; double tilt holder.

4.4. Results and Discussion

4.4.1. XRD analysis

Series 1, 2 and 3 systematically vary the concentrations of two of the three types of *B*-site cations while keeping the concentration of the third type constant. The XRD analysis of series 1, 2 and 3, overall consistent with an *m* = 5 Aurivillius structure, are given in figure 1. In series 1, the concentrations of Fe and Mn are varied while Ti remains constant. This was considered isovalent substitution since both Fe and Mn are nominally in the 3+ oxidation state in a neutral B6TFMO Aurivillius stoichiometry. They also have similar ionic radii [5], although the Jahn-Teller effect can tend to elongate $Mn^{3+}O_6$ octahedra [13].

In figure 1(a) the XRD of this sample series 1 is shown. There is only a slight shift (~0.4 °) in 2θ peak positions accompanied by peak broadening as the concentration of Mn increases and Fe decreases. For example, the (00<u>10</u>) peak FWHM is 0.45 ° for x = 0 and is 0.50 ° for x = 4 ($Bi_6Ti_3Fe_{1.6-x}Mn_{0.4+x}O_{18}$). This may indicate some structural disorder within the samples, such as the formation of regions where there are

intergrowths of Aurivillius phases having differing *m* structures. Such intergrowths are commonly observed in Aurivillius samples [14] and we do observe some areas of *m* = 4 in TEM analysis of the series 4 materials which will be discussed later. This XRD data shows that isovalent substitution of Mn for Fe does not lead to the significant structural rearrangement to another Aurivillius phase as we see in the heterovalent substitution in series 2 and 3.

In series 2 (figure 1(b)) as the Ti content decreases and Mn content increases, there is a clear gradual shift in peaks away from the *m* = 5 structure and towards the *m* = 6 Aurivillius phase. This is an example of heterovalent substitution as Ti is nominally 4+ while the Mn precursor used is nominally 3+ within a charge-balanced B6TFMO Aurivillius stoichiometry. A similar trend in asymmetric peak shift is observed in series 3 (figure 1(c)) where Ti decreases and Fe increases in concentration. The Mn^{3+} (0.645 Å) and Fe^{3+} (0.645 Å) cations have a larger radius than Ti^{4+} (0.605 Å). This difference in size may also contribute to the distortion of the crystal structure.

The presence of secondary phases can occur when fabricating Aurivillius materials and since some of these phases could be magnetic in nature, it is obviously important to search for their presence when investigating these materials as potential multiferroics. Small levels of secondary phases have been identified in previous work on Aurivillius materials having different compositions as the source of the observed magnetic behaviour [12, 15]. No peaks corresponding to common secondary impurity phases were observed in the XRD analysis of the materials under study in this work. However, it should be noted that the positions of some of these potential impurity peaks would overlap with peaks of the Aurivillius material. For example, for the magnetite spinel phase Fe_3O_4, the reflections of the (220) peak at 29.6 ° and (311) peak at 35.4 ° overlap with the (00<u>16</u>) and (00<u>20</u>) reflection of the Aurivillius *m* = 5 phase, respectively. The XRD instrument also has a detection limit of 1-3 % volume, therefore if secondary phases were present below this volume, they would not be detected.

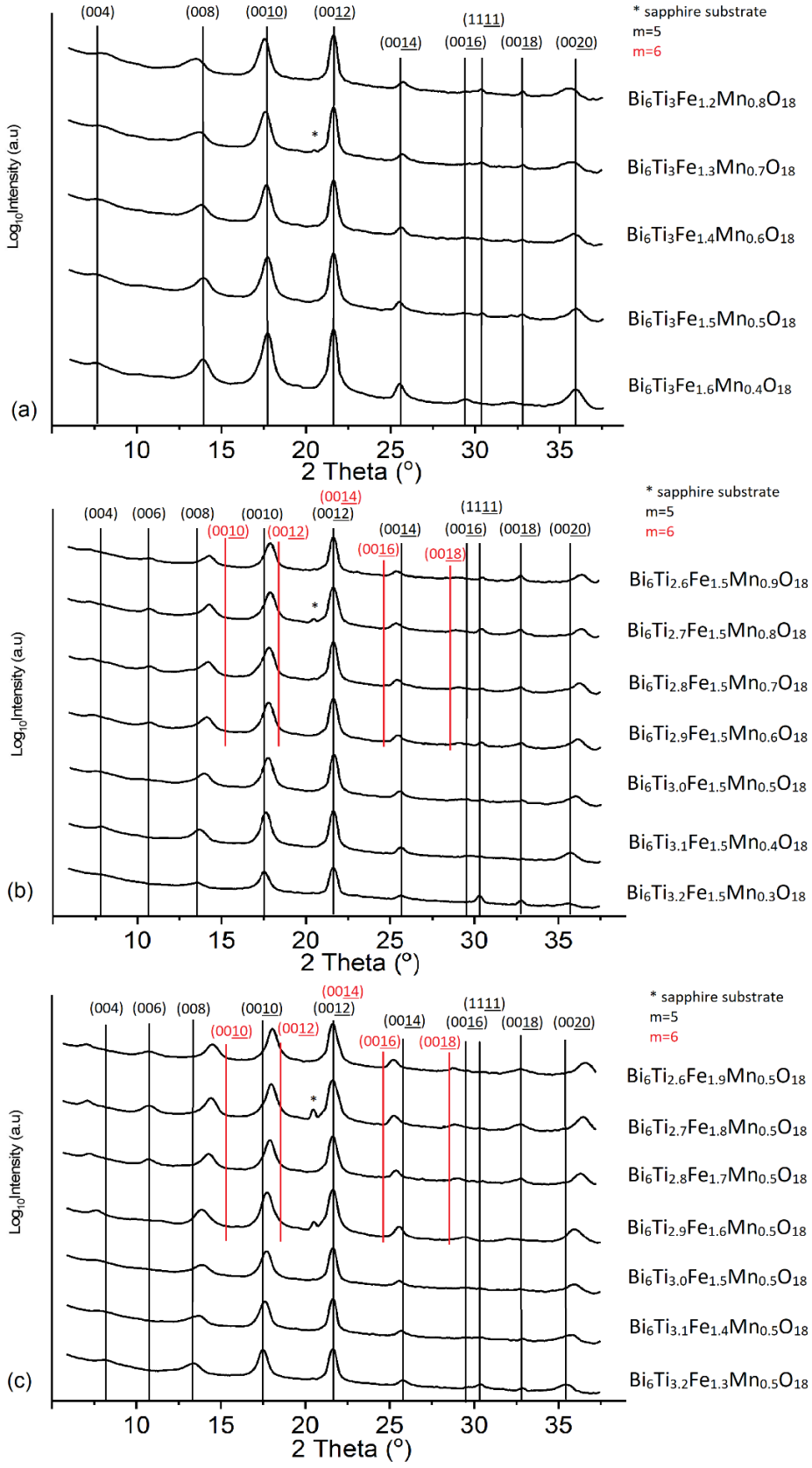

Figure 1: XRD plots of series 1 (a), series 2 (b) and series 3 (c).

It was not possible to use the Scherrer equation to calculate the size of the particles as the Aurivillius materials have an orthorhombic crystal structure not cubic. Therefore, a modified version of the Scherrer equation (section 2.2.1) [16], known as the crystalline quality factor, was used to quantify the crystalline quality of these materials using data from the XRD measurement in figure 1. The details of this method are presented in the experimental chapter of this thesis (section 2.2.1). The results of these calculations for series 1 are presented in figure 2 and show that the change in Q is much smaller than the error. The error bars represent the standard deviation between the results of the individual peaks. For series 2 and 3, the error was also significantly large so that there was no clear trend in the change in Q (figure S1 and S2). Series 2 change in Q 33 ± 44 and series 3 change in Q 14 ± 38. The large error is due to the significant peak broadening caused by the presence of different *m* Aurivillius phases.

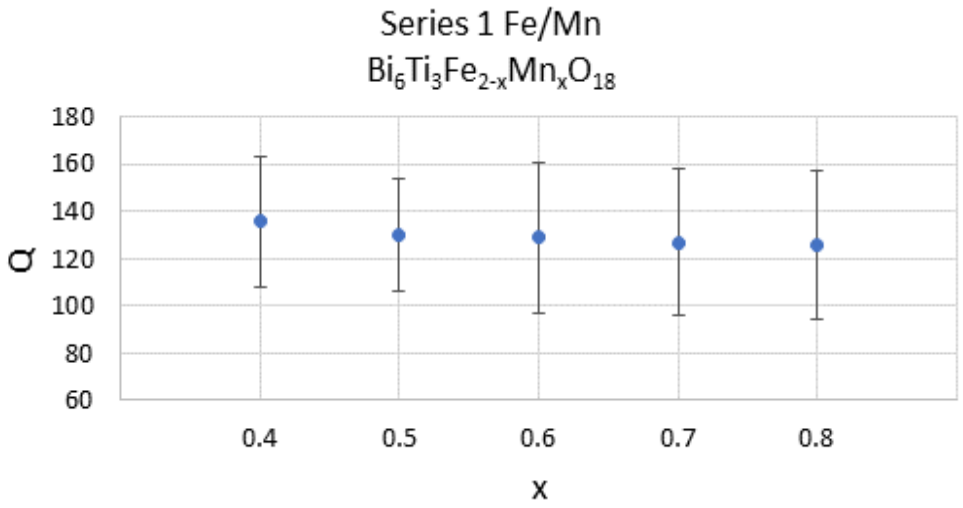

Figure 2: Crystalline quality factor (Q) for series one.

The concentration of Ti was further lowered in the samples of series 4. The XRD patterns of series 4 (figure 3) clearly show the overall transition of *m* = 5 to *m* = 6 corresponding to the decrease in Ti^{4+} and the increase in Fe^{3+} and Mn^{3+}. The broadening of the asymmetric peaks may be due to secondary phases occurring such as iron or manganese rich perovskites, however, the presence of *m* = 6 is confirmed

in TEM analysis of these materials which is discussed later in this chapter. Other potential causes of peak broadening could be due to size effects [17] but these sample were deposited using the same deposition method throughout the four series and this consistency should eliminate any significant variation in film thickness and instead the observed trend in peak broadening/shift can be attributed to the systematic variation of the stoichiometry.

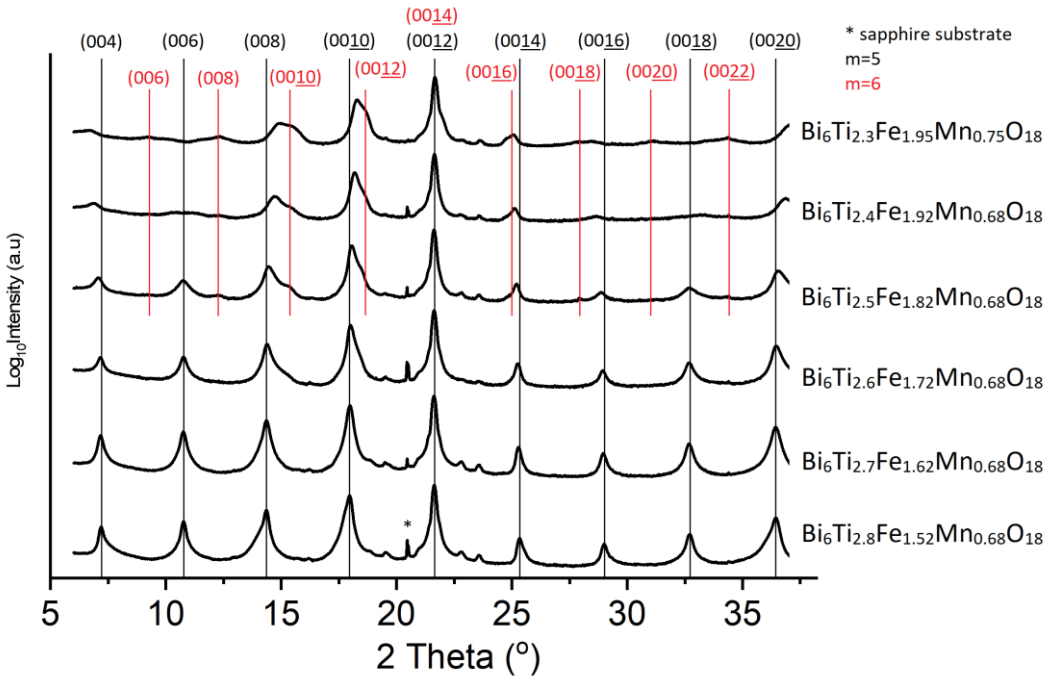

Figure 3: XRD analysis of series 4.

The increased structural stacking disorder of series 4 is reflected in the full width half maxima (FWHM) values given in table 1. This data is presented as a graph in figure S3. The FWHM increases as the Ti concentration decreases through the series. The appearance of peaks corresponding to reflections of the *m* = 6 phase indicates a more disordered periodic structure and causes broadening of the XRD peaks. While there is a clear shift to the *m* = 6 phase, we know from TEM analysis that regions of *m* = 4 also occur in the materials (figure 13).

Table 1. FWHM values for XRD reflections of series 4

	Sample	(008)	(00<u>1</u>0)	(00<u>1</u>4)
1	$Bi_6Ti_{2.8}Fe_{1.52}Mn_{0.68}O_{18}$	0.587 ± 0.029	0.557 ± 0.018	0.387 ± 0.003
2	$Bi_6Ti_{2.7}Fe_{1.62}Mn_{0.68}O_{18}$	0.635 ± 0.037	0.537 ± 0.031	0.361 ± 0.014
3	$Bi_6Ti_{2.6}Fe_{1.72}Mn_{0.68}O_{18}$	0.734 ± 0.032	0.686 ± 0.011	0.379 ± 0.011
4	$Bi_6Ti_{2.5}Fe_{1.82}Mn_{0.68}O_{18}$	1.075 ± 0.088	0.738 ± 0.013	0.390 ± 0.012
5	$Bi_6Ti_{2.4}Fe_{1.92}Mn_{0.68}O_{18}$	1.156 ± 0.051	0.743 ± 0.018	0.446 ± 0.024
6	$Bi_6Ti_{2.3}Fe_{1.95}Mn_{0.75}O_{18}$	1.429 ± 0.142	0.780 ± 0.268	0.546 ± 0.013

The *c*-axis pseudo lattice parameter was calculated from the XRD analysis of the series 4 samples and the results are presented in figure 4. The shift in the peak positions ((008), (00<u>1</u>0) and (00<u>1</u>4)) results in a greater uncertainty as the series progresses to lower titanium content. The error represents the standard deviation between the values obtained from the different peak reflections. The $Bi_6Ti_{2.8}Fe_{1.52}Mn_{0.68}O_{18}$ material had a *c*-axis value of 49.29 ± 0.199 Å while the $Bi_6Ti_{2.3}Fe_{1.95}Mn_{0.75}O_{18}$ material had a value of 50.19 ± 3.52 Å. The increasing error can be attributed to the broader peaks due to the presence of different '*m*' Aurivillius phases. The *c*-axis parameters for series 1, 2 and 3 are presented in figure S4. Due to the Jahn-Teller effect leading to the elongation of $Mn^{3+}O_6$ octahedra, which might give longer *c* parameter than otherwise anticipated.

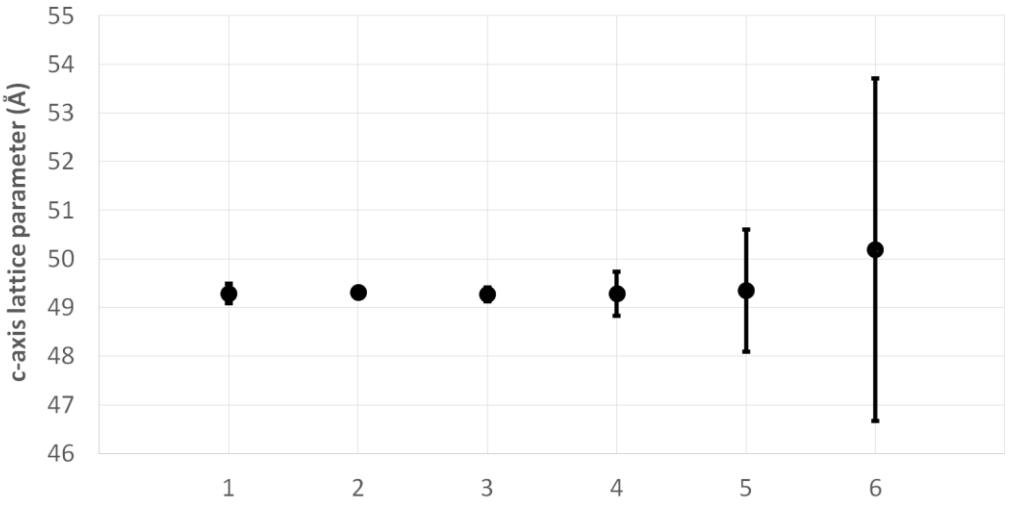

Figure 4: Series 4 *c*-axis pseudo lattice parameters, sample numbers correspond to samples presented in Table 1.

4.4.2. AFM analysis

The effect of substitution on the morphology of these materials was also examined. Li *et al*. reported a slight increase in grain size in Mn-substituted $Bi_5Ti_3Fe_1O_{15}$, possibly due to different thermal dynamic behaviours of Mn and Fe ions [18]. In this work, no clear trend was observed with the substitution of Fe for Mn from the AFM height images (figure 5) of the series 1 ($Bi_6Ti_3Fe_{1.6-x}Mn_{0.4+x}O_{18}$ (x = 0, 0.1, 0.2, 0.3 and 0.4)) materials (figure 2). The RMS roughness of the materials through this series ranged from 16 - 27 nm, however the error obtained from the standard deviation between the four measurement sites was significantly large over the growth series (figure 6). A range of different sized grains are visible from 10 - 20 nm in diameter to larger grains ≈ 2 μm in diameter. It is difficult to identify if these larger grains are individual grains or several grain adjacent to each other. For example, the SEM image in figure 8 seems to show several grains merged together.

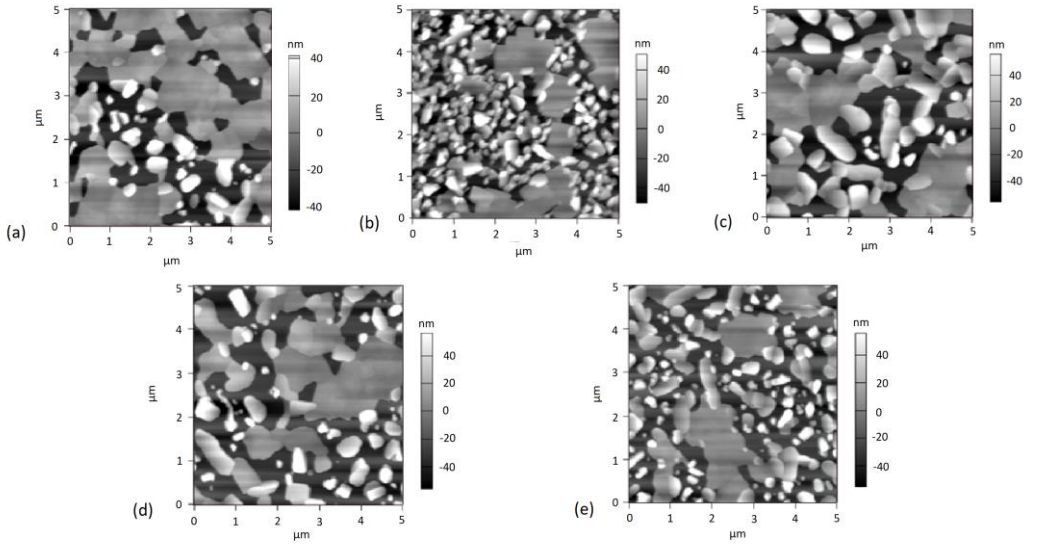

Figure 5: AFM height images of $Bi_6Ti_3Fe_{1.6-x}Mn_{0.4+x}O_{18}$ (a) x = 0, (b) x = 0.1, (c) x = 0.2, (d) x = 0.3 and (e) x = 0.4 for series 1 with an area of 5 μm^2.

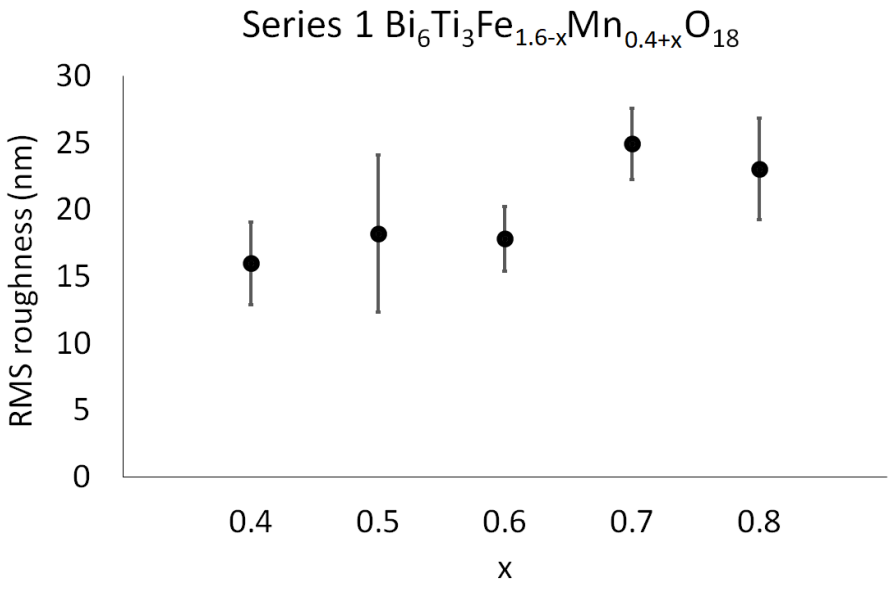

Figure 6: Root mean square roughness from AFM images of series 1 with error bars representing the standard deviation between different measurements sites on the material.

4.4.3. SEM analysis

Further analysis of the morphology is presented as SEM images in figure 7. The typical topography of these samples shows a majority of the grains lying parallel to the substrate and incomplete coverage of the film over the substrate. The incomplete coverage can be clearly seen in the SEM image in figure 8. Only one spin coat was applied during the fabrication of these materials and contraction of the material during the post anneal step may have contributed to the incomplete coverage of the substrate. It is noteworthy that the sapphire substrate does not possess a simple epitaxial relationship with the Aurivillius material, although other possible effects such as surface tension, wetting and/or deposition technique could contribute to the observed morphology. This incomplete coverage was also observed in the samples discussed in chapter 3. In chapters 5 and 6, a different deposition technique and the use of epitaxial substrates produces thin films with complete coverage of the substrate.

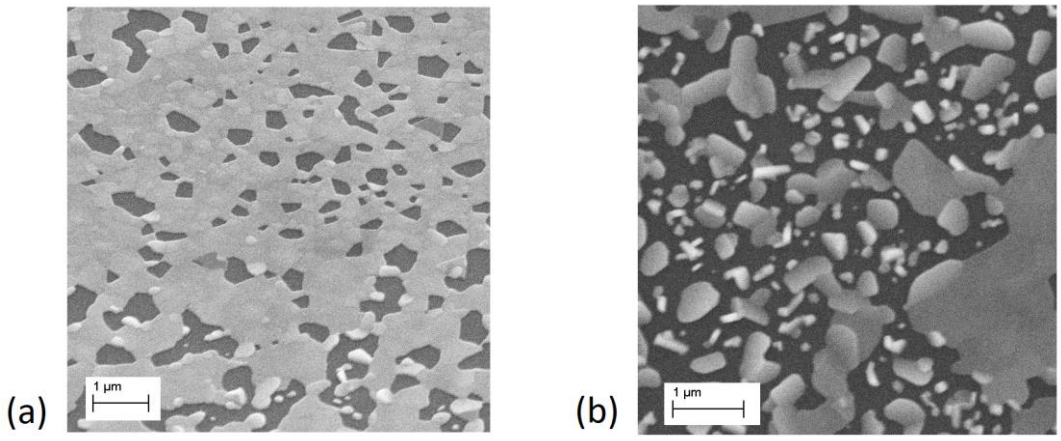

Figure 7: Representative SEM images of (a), $Bi_6Ti_3Fe_{1.6}Mn_{0.4}O_{18}$ and (b), $Bi_6Ti_3Fe_{1.2}Mn_{0.8}O_{18}$ of series 1 at 45° tilt.

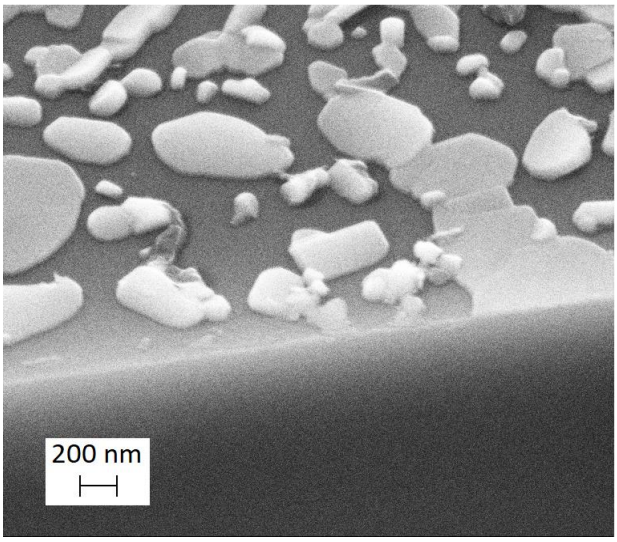

Figure 8: SEM of $Bi_6Ti_3Fe_{1.2}Mn_{0.8}O_{18}$ of series 1 at 45 ° tilt showing the edge of the substrate and the incomplete coverage of the substrate by the Aurivillius material.

To determine the mismatch between the Aurivillius phase and the substrate, the pseudo lattice parameter was calculated using the method given by Newnham and Armstrong [19],

$$a_p = 1.33r_B + 0.6r_A + 2.36\ \text{Å} \qquad (4.1)$$

Where r_A is the eight fold coordinate radius value of the A-site ion (Bi^{3+}) and r_B is the six fold coordinate radii values of the B-site ions (Ti^{4+}, Mn^{3+} and Fe^{3+}). The pseudo lattice parameter of $Bi_6Ti_3Fe_{1.5}Mn_{0.5}O_{18}$ was calculated to be a_p = 3.85 Å, using radii values found in the paper by Shannon [5]. The lattice parameters of the sapphire substrate is a = 4.78 Å. This is a 24.2 % lattice mismatch between the substrate and the Aurivillius material. This difference is too large for there to be an epitaxial relationship between the substrate and the Aurivillius grains.

4.4.4. PFM analysis

The Aurivillius materials are well known ferroelectric materials and polarisation in these materials is predominantly along the a/b in-plane direction [1]. To examine the

local ferroelectric response, PFM analysis was performed on the samples. A set of representative PFM images are shown in figure 7. For Aurivillius phase materials with an odd number of perovskite blocks, a small polarisation is expected along the *c*-axis out-of-plane direction [20]. This is clearly seen in figure 9 where the lateral and vertical piezoresponse have been measured simultaneously. Also as can be seen from the AFM and SEM (figures 5, 7 and 8) images some of the grains lie at an angle to the sapphire substrate which may make some of the in-plane polarisation response accessible to the vertical PFM measurement.

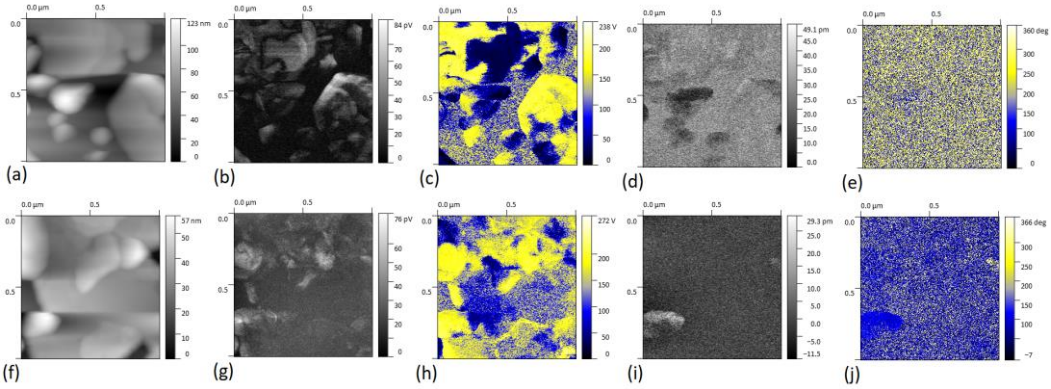

Figure 9: Single frequency PFM response in the lateral and vertical direction; series 3 x = 0 (a) height, (b) lateral amplitude, (c) lateral phase, (d) vertical amplitude (e) vertical amplitude and series 3 x = 0.6 (f) height, (g) lateral amplitude, (h) lateral phase, (i) vertical amplitude and (j) vertical amplitude.

A small polarisation along the *c*-axis is expected in the *m* = 5 Aurivillius phases due to the structure having an odd number of perovskite blocks [20], where retention of the mirror plane is not energetically favourable. This enables a minor out-of-plane polarisation to exist in the *c*-direction for odd-layered phases, in conjunction with a major in-plane polarisation. On the other hand, polar Aurivillius phases having even numbers of *m* perovskite layers, such as the *m* = 6 Aurivillius phase, retain a mirror plane perpendicular to the *c*-axis. This prohibits out-of-plane polarisation in even-layered Aurivillius phases and the polarisation is confined to the lateral plane. Therefore a fully *c*-axis orientated *m* = 6 sample would not be expected to show

polarisation response along the out-of-plane *c*-axis. To examine if a decrease in the vertical amplitude response could be observed in the PFM analysis, the lateral and vertical amplitude response was measured for series 3 (figure 10) where there is an increased shift in the XRD patterns (figure 1 (c)) towards the *m* = 6 phase with increased 'x'. There was no clear trend in the vertical piezoresponse through the series. It is apparent that any variation to the out-of-plane response is offset by the tilted nature of the Aurivillius phase grains (figures 5, 7, 9) and a portion of the in-plane piezoresponse being detected during the vertical measurement, precluding measurement of a true *c*-axis out-of-plane response.

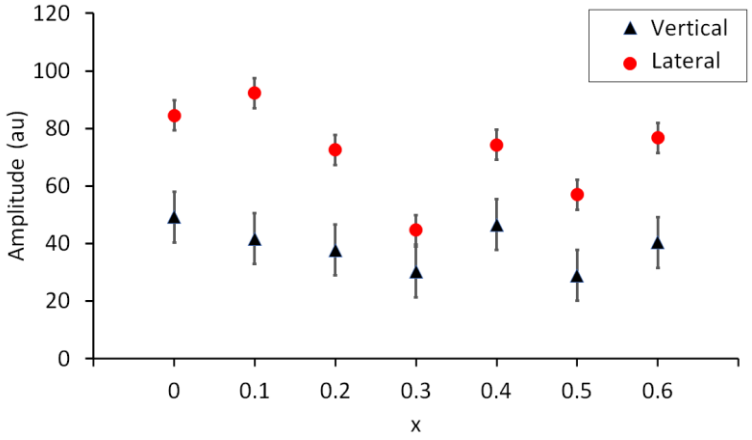

Figure 10: PFM amplitude response in the vertical and lateral direction of series 3.

The substitution of iron and manganese into the structure and decrease in titanium does not seem to diminish the piezoresponse of these materials. Work by Zurbuchen *et al.* on *m* = 6 $Bi_7(Ti,Mn)_6O_{21}$ Aurivillius materials found the piezoresponse diminished with substitution [8].

To reduce the effects of instrumental cross talk and boost the signal of a weaker piezoresponse, DART-PFM was performed on the samples. A representative image is shown in figure 11. These materials are naturally self-polarised and clear 180° domains can be seen. Additional DART PFM images for materials in series 1 are presented in figure S5.

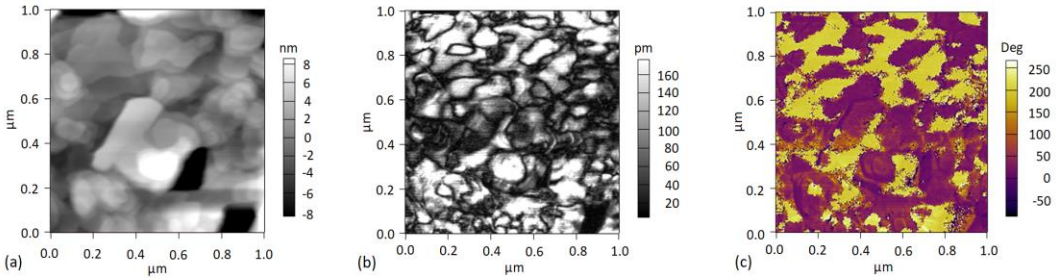

Figure 11: Representative DART lateral PFM measured the out of plane (a) height (b) amplitude and (c) phase response of $Bi_6Ti_{2.9}Fe_{1.6}Mn_{0.5}O_{18}$ in series 3.

4.4.5. TEM analysis

TEM analysis confirms the presence of intergrowths of different *m* Aurivillius phases. The thickness of a unit cell along the growth axis (*c*) of Aurivillius materials can be estimated using the formula;

$$c/2 = f + h \qquad (4.2)$$

Where h = m*p. The thickness of the $[Bi_2O_2]^{2+}$ interlayer (f) is 4.08 Å, the average thickness of the perovskite blocks (p) tends to be ≈ 4 Å and *m* is the number of perovskite blocks [3]. For *m* = 5, c = 49.3 Å and *m* = 6, c = 57.5 Å. For a mix of *m* = 5 and *m* = 6 i.e. *m* = 5.5, c = 53.4 Å. Indeed, we observe this within the TEM images in figure 13 (a) and (b).

In figure 13 (a), although XRD data (figure 3) demonstrates an overall *m* = 5 structure for the $Bi_6Ti_{2.8}Fe_{1.52}Mn_{0.68}O_{18}$ composition, TEM imaging shows that there are local areas within the film displaying unit cell lengths corresponding to intergrowths of *m* = 6 Aurivillius structures (5.7 ± 0.03 nm) and unit cells with a mix of *m* = 5 and *m* = 6 Aurivillius structures (5.3 ± 0.04 nm).

Similarly in figure 13 (b) for the $Bi_6Ti_{2.6}Fe_{1.72}Mn_{0.68}O_{18}$ composition, the TEM imaging shows that there are local areas within the film displaying unit cell lengths of 5.3 ± 0.03 nm which infers a mixture of *m* = 5 (~ 4.9 nm) and *m* = 6 (~ 5.7 nm). The

$Bi_6Ti_{2.83}Fe_{1.52}Mn_{0.65}O_{18}$ composition in figure 13 (c) demonstrates the complexity of the materials and that the majority of the sample is *m* = 5, but there are regions of the *m* = 4 Aurivillius phase present also. A mix of *m* = 5 and *m* = 4 *c*-axis length of 4.2 ± 0.03 nm and for *m* = 5 is 4.6 ± 0.03 nm.

The length of the *c*-axis of these materials is similar to other Aurivillius phases with similar compositions such as for $Bi_5Ti_3FeO_{15}$ (*m* = 4) where the *c*-axis parameter was 4.104 ± 0.004 nm determined from XRD and TEM analysis [21]. From XRD analysis, $Bi_6Ti_{2.5}Fe_{1.75}Mn_{0.75}O_{18}$ (*m* = 5) had a *c*-axis parameter of 4.928 nm and $Bi_7Ti_3Fe_3O_{21}$ (*m* = 6) was 5.7554 nm [2].

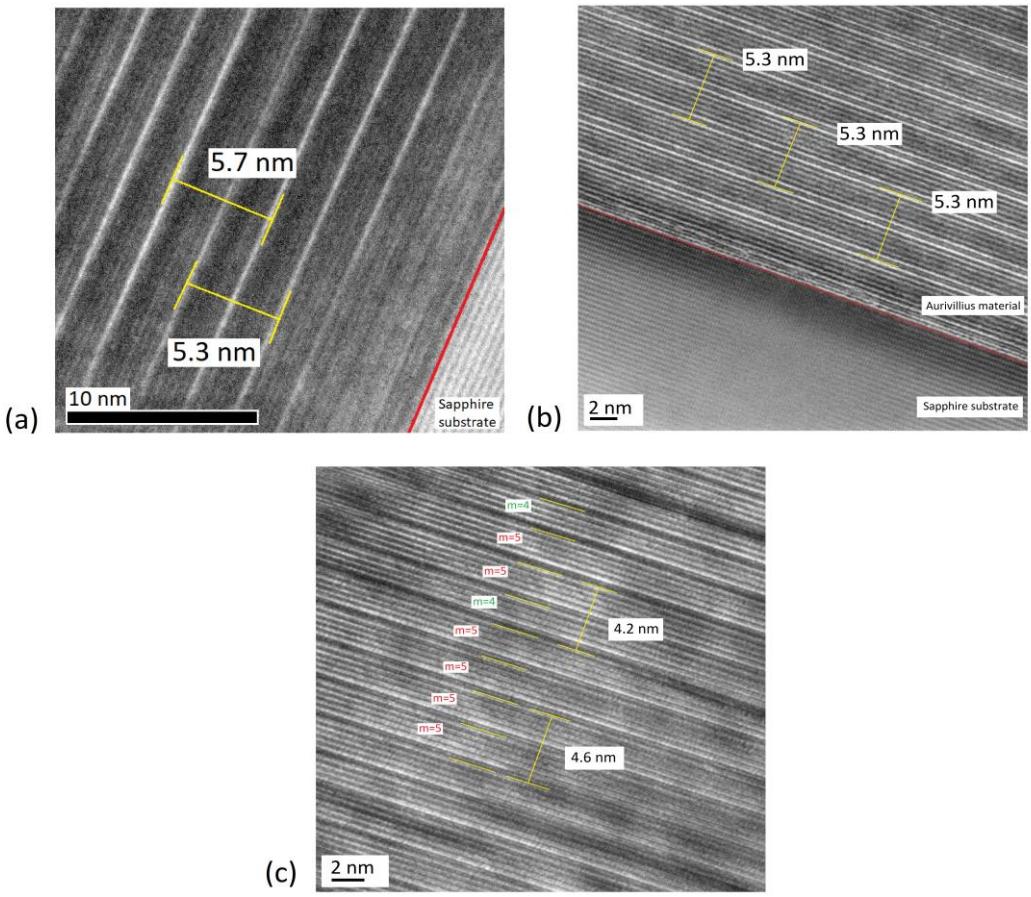

Figure 13: TEM images of (a), $Bi_6Ti_{2.8}Fe_{1.52}Mn_{0.68}O_{18}$, (b) $Bi_6Ti_{2.6}Fe_{1.72}Mn_{0.68}O_{18}$ and (c), $Bi_6Ti_{2.83}Fe_{1.52}Mn_{0.65}O_{18}$ from series 4.

4.4.6. Discussion

The appearance of the *m* = 6 Aurivillius phase reflections in the XRD patterns corresponds with a decreased concentration of Ti in the structure. The increased concentration of Mn and Fe is desirable for increasing the magnetic ion content. However, the substitution of the lower valence Mn^{3+} and Fe^{3+} for Ti^{4+} results in an unbalanced stoichiometry. A charge balanced stoichiometry could be achieved through a change in the oxidation state of the substituting cations to the 4+ oxidation state.

The presence of Fe^{4+} has been reported in the domain walls of $BiFeO_3$ materials through detailed HAADF and EELS analysis. The Fe^{4+} accumulates at the domain wall alongside bismuth vacancies due to the different electrostatic environment, away from the domain walls Fe^{3+} predominates [22, 23]. In another study, the substitution of Ni^{2+} for Fe^{3+} in $BiFeO_3$ created a charge imbalance but this did not result in the formation of Fe^{4+} to compensate, instead the material favoured the formation of oxygen vacancies evident from the higher density of free carriers and resulting higher conduction of the Ni substituted materials [24]. As can be seen with the previous examples, the oxidation of Fe^{3+} to Fe^{4+} is not favoured outside of specific conditions such as near domain walls. However, there is experimental evidence for the variable valence of Mn^{3+} to Mn^{4+} in perovskite materials. In work by Selbach *et al.* [25, 26], the presence of Mn^{4+} was utilised to charge compensate the excess oxygen content in $BiFe_{0.7}Mn_{0.3}O_{3+\delta}$ materials. Thermogravimetry was used to determine the nonstoichiometric oxygen content of $\delta = 0.059$ in the manganese containing sample. There was no corresponding excess oxygen ($\delta < 0.01$) in the $BiFeO_{3+\delta}$ material indicating that Fe^{4+} was not formed during the fabrication process [25, 26].

The substitution of Ti^{4+} by Fe^{3+} and Mn^{3+} could be accompanied by the formation of compensating oxygen vacancies, however previous work by Snedden *et al.* has demonstrated that the occurrence of oxygen vacancies in the Aurivillius materials is not favourable [6].

From these previous arguments, we reason that the decrease in Ti^{4+} is compensated for by the oxidation of Mn^{3+} to Mn^{4+}. Previous work with Aurivillius materials has

failed to form phase pure structures with Mn^{4+} [7]. It was proposed that the ionic radii of Mn^{4+} (0.53 Å) is too small to be tolerated in the Aurivillius structure [19]. It is expected therefore that there will be a limit to how much Mn^{4+} can be tolerated before the rearrangement of the structure becomes more favourable than the oxidation of Mn.

In order to determine what that limit may be, the proportion of titanium, iron and manganese at the *B*-site of the materials was determined from the stoichiometries expected from the ratio of precursors used during synthesis. It is assumed that the proportion of Mn^{4+} present is proportional to the concentration necessary to maintain a charge balanced Aurivillius material. The method presented in appendix 2 was followed to calculate the proportion of Mn^{3+} and Mn^{4+} that may occur. The resulting concentrations of the various *B*-site atoms for series four are shown in Table 2. The table is arranged in order of decreasing Ti concentration and samples with an * correspond to the samples shown in figure 3. The appearance of *m* = 6 phase (as observed in the XRD and TEM analysis) follows a systematic trend with decreasing Ti concentration. The phase rearrangement observed in this work occurs when the concentration of Fe and Mn at the *B*-site of the perovskite units is above 48 % or when the nominal concentration of Mn^{4+} is < 8 % see table 2. The average Mn oxidation state for the *m* = 5 and *m* = 6 structure has been calculated also. It can be seen that when the average oxidation state of Mn in the m = 5 structure is larger than ≈ 3.4 the appearance of *m* = 6 begins to occur. This is a similar threshold observed by Zurbuchen *et al.* [8] ($Mn^{3.2+}$) and McCabe and Greaves [7] ($Mn^{3.4+}$).

Table 2: Proportion of *B*-site ions and calculated Mn(IV) concentrations

Composition	Ti *B*-site (%)	Fe *B*-site (%)	Mn *B*-site (%)	Mn(IV) % of Mn	% Mn(IV) overall	Average Mn oxidation state *m* = 5	Average Mn oxidation state *m* = 6	*m* phase
$Bi_6Ti_3Fe_{1.4}Mn_{0.6}O_{18}$	60	28	12	0	0	+3.00	+2.17	5
$Bi_6Ti_{2.83}Fe_{1.52}Mn_{0.65}O_{18}$	56.6	30.4	13.0	26	3.38	+3.26	+2.49	5
$Bi_6Ti_{2.83}Fe_2Mn_{0.17}O_{18}$	56.6	40.0	3.4	100	3.40	+4.00	+1.06	5
$Bi_6Ti_{2.81}Fe_{1.52}Mn_{0.67}O_{18}$	56.2	30.4	13.4	29	3.89	+3.28	+2.54	5

*$Bi_6Ti_{2.8}Fe_{1.52}Mn_{0.68}O_{18}$	56	30.4	13.6	30	4.08	+3.29	+2.56	5
$Bi_6Ti_{2.78}Fe_{1.52}Mn_{0.70}O_{18}$	55.6	30.4	14.0	32	4.48	+3.31	+2.60	5
$Bi_6Ti_{2.75}Fe_{1.52}Mn_{0.73}O_{18}$	55	30.4	14.6	34	4.96	+3.34	+2.66	5
*$Bi_6Ti_{2.7}Fe_{1.62}Mn_{0.68}O_{18}$	54	32.4	13.6	45	6.12	+3.44	+2.71	5
*$Bi_6Ti_{2.6}Fe_{1.72}Mn_{0.68}O_{18}$	52	34.4	13.6	59	8.02	+3.59	+2.85	~5
$Bi_6Ti_{2.58}Fe_{1.77}Mn_{0.65}O_{18}$	51.6	35.4	13.0	64	8.32	+3.65	+2.88	~5
$Bi_6Ti_{2.6}Fe_{1.77}Mn_{0.63}O_{18}$	52	35.4	12.6	64	8.06	+3.63	+2.84	~5
$Bi_6Ti_{2.56}Fe_{1.77}Mn_{0.67}O_{18}$	51.2	35.4	13.4	66	8.84	+3.66	+2.91	~5
$Bi_6Ti_{2.53}Fe_{1.77}Mn_{0.70}O_{18}$	50.6	35.4	14	68	9.52	+3.67	+2.96	~5
$Bi_6Ti_{2.50}Fe_{1.77}Mn_{0.73}O_{18}$	50	35.4	14.6	69	10.07	+3.68	+3.00	5+6
*$Bi_6Ti_{2.5}Fe_{1.82}Mn_{0.68}O_{18}$	50	36.4	13.6	75	10.2	+3.74	+3.00	5+6
*$Bi_6Ti_{2.4}Fe_{1.92}Mn_{0.68}O_{18}$	48	38.4	13.6	89	12.10	+3.88	+3.15	5+6
$Bi_6Ti_{2.3}Fe_2Mn_{0.70}O_{18}$	46	40.0	14.0	100	14.0	+4.00	+3.29	5+6
*$Bi_6Ti_{2.3}Fe_{1.95}Mn_{0.75}O_{18}$	46	39.0	15	93	13.95	+3.93	+3.27	5+6

In table 3 the chemical composition of the *m* = 5 $Bi_6Ti_{2.3}Fe_{1.95}Mn_{0.75}O_{18}$ composition has been rearranged to the *m*=6 phase, to demonstrate how the formation of the higher *m* = 6 Aurivillius phase would accommodate the higher concentration of magnetic cations while maintain a balanced stoichiometry. The *m* = 5 $Bi_6Ti_{2.3}Fe_{1.95}Mn_{0.75}O_{18}$ composition has been rearranged to the *m* = 6 phase, where it would then assume the $Bi_7Ti_{2.76}Fe_{2.34}Mn_{0.9}O_{21}$ composition. Note that there is a sufficient excess of bismuth included in the chemical solution deposition process to allow for a change in composition to an *m* = 6 phase. The relative proportion of the *B*-site atoms, including Mn, is the same for both arrangements (Mn 15 %) but the proportion of Mn^{4+} needed to achieve a charge balanced stoichiometry is lower for the *m* = 6 phase (3.9 % Mn^{4+} for *m* = 6) compared with the *m* = 5 (13.95 % Mn^{4+}) structure. We note that for the m = 5 structure in Table 3, an average manganese oxidation state of +3.93 is calculated (assuming oxidation states of +4 and +3 for titanium and iron, respectively). However, when the same ratio of titanium, iron and manganese cations are presented in an *m* = 6 structure, the average manganese oxidation state is calculated to be +3.27. The latter is within the range shown for the stable Aurivillius phase compositions shown by Zurbuchen *et al.* [8] ($Mn^{3.2+}$) and McCabe and Greaves [7] ($Mn^{3.4+}$). The *m* = 6 $Bi_7Mn_{3.75}Ti_{2.25}O_{21}$ Aurivillius phase reported by Zurbuchen *et al.* enabled 62.5 % manganese to be accommodated at the *B*-site, however a ferroelectric response could not be measured for this material.

The inability to tolerate *B*-site concentrations of Mn^{4+} above 8 % may be the driving force behind structural rearrangement and the formation of a higher Aurivillius phase. We have direct evidence from TEM analysis that the formation of the *m* = 6 phase is occurring as the concentration of Ti decreases and Fe and Mn increases. Evolution of the *m* = 6 phase on increased Fe and Mn content is also evident from XRD studies. There is also the possibility that in response to increased concentration of iron and manganese, secondary phases such as Fe or Mn-rich perovskites or spinel phases may occur. The presence of such phases may be hidden in XRD analysis due to an overlap of peak positions. For example, for the magnetite spinel phase Fe_3O_4, the reflections of the (220) peak at 29.6 ° and (311) peak at 35.4 ° overlap with the (00$\underline{16}$) and (00$\underline{20}$) reflection of the Aurivillius *m* = 5 phase, respectively. Further work would involve a through statistical analysis to determine the phase purity of these materials [27].

Calculation of the tolerance factors for series 4 are given in appendix 2 supplementary section of this work (figure S6). When the calculation was performed assuming that all Mn is in the 3+ oxidation state then the tolerance factor of the perovskite unit increases as the concentration of Ti decreases. However, when the proportion of Mn^{3+} and Mn^{4+} calculated in Table 3 are used for the calculation, the tolerance factor of the perovskite unit decreases with decreasing Ti^{4+}. This is due to the smaller radius of Mn^{4+} (0.53 Å). It is noted that rearrangement to the higher phase would also decrease the tolerance factor of the perovskite unit.

Table 3: Calculation of stoichiometry for *m* = 5 and *m* = 6 Aurivillius phases

	Ti(IV) *B*-Site %	**Fe(III) *B*-Site %**	**Mn *B*-Site %**	**Mn(IV) % of Mn**	**Mn(IV)% overall**	**Tolerance factor**
$Bi_6Ti_{2.3}Fe_{1.95}Mn_{0.75}O_{18}$ *m*=5	46	39	15	93	13.95	0.850
$Bi_7Ti_{2.76}Fe_{2.34}Mn_{0.9}O_{21}$ *m*=6	46	39	15	26	3.9	0.865

4.5. Conclusion

Previous work has shown genuine room temperature multiferroic behaviour in the $Bi_6Ti_xFe_yMn_zO_{18}$ B6TFMO (*m* = 5) material [2]. In order to increase long-range magnetic ordering it would be desirable to increase the concentration of magnetic cations in these materials. The aim of this work was to assess the solubility limit to the concentration of magnetic Fe and Mn cations that can be accommodated within the m = 5 Aurivillius phase structure. This work presents the results of four systematic growth studies that test the structural changes undergone by the Aurivillius *m* = 5 material $Bi_6Ti_xFe_yMn_zO_{18}$ (x = 3.2 – 1.6, y = 1.2 - 1.9, z = 0.3 - 0.9) during substitution at the *B*-site.

Analysis of the materials using XRD and TEM shows that when the proportional concentration of Ti^{4+} is lowered below 52 %, there was a notable reorganisation to a mixed phase sample containing the *m* = 6 Aurivillius phase alongside the *m* = 5 main phase. The proportion of the *m* = 6 phase within the *m* = 5 phase matrix increased with decreased Ti^{4+} content. We argue that the lowering of Ti^{4+} in the material is compensated by the oxidation of Mn^{3+} to Mn^{4+} in order to maintain a charge balance stoichiometry. However the difference in cation radius limits the concentration of Mn^{4+} which can be accommodated by the structure. These results indicate that above 8 % of Mn^{4+} (or 48 % magnetic ion content at the *B*-site), the *m* = 5 sample must reorganise, and increased regions of the material adopt the higher *m* = 6 phase.

Further calculations show that by adopting the higher *m* = 6 phase, the relative proportion of Mn^{4+} necessary for charge neutrality in the material decreases (table 3) and the structure is more tolerant to the increased magnetic cation content. Accordingly, the average calculated oxidation state for the manganese cation also decreases. The piezoresponse of these materials does not seem to be affected by substitution.

This work offers a valuable insight into the limiting factors affecting the substitution of magnetic ions at the *B*-site of the Aurivillius materials which should be considered during the development of multiferroic materials. The presence of Mn^{4+} also has important implications for the type of magnetic behaviour as the Mn^{3+} - O - Mn^{4+} and

Fe^{3+} - O - Mn^{4+} double exchange mechanism produces ferromagnetic behaviour compared to the superexchange mechanism between Mn^{3+} - O - Mn^{3+} which produces antiferromagnetic behaviour [28, 29].

4.6. Acknowledgements

The authors gratefully acknowledge the support of Science Foundation Ireland Principle Investigator Award Number 15/IA/3015 DEPO-Man, 'Design, Deposition and Exploitation of Novel Micro and Nano-scale Materials and Devices for Advanced Manufacturing' and the support of the Royal Society and Science Foundation Ireland (SFI) University Fellowship UF 140263.

4.7. References

[1] R. E. Newnham, R. W. Wolfe, and J. F. Dorrian, "Structural basis of ferroelectricity in the bismuth titanate family," *Materials Research Bulletin,* vol. 6, no. 10, pp. 1029-1039, 1971/10/01/ 1971, doi: https://doi.org/10.1016/0025-5408(71)90082-1.

[2] L. Keeney *et al.*, "Magnetic Field-Induced Ferroelectric Switching in Multiferroic Aurivillius Phase Thin Films at Room Temperature," *Journal of the American Ceramic Society,* vol. 96, no. 8, pp. 2339-2357, 2013/08/01 2013, doi: 10.1111/jace.12467.

[3] Ł. Kurzawski and K. Malarz, "Simple Cubic Random-Site Percolation Thresholds for Complex Neighbourhoods," *Reports on Mathematical Physics,* vol. 70, no. 2, pp. 163-169, 2012/10/01/ 2012, doi: https://doi.org/10.1016/S0034-4877(12)60036-6.

[4] A. Y. Birenbaum and C. Ederer, "Potentially multiferroic Aurivillius phaseBi5FeTi3O15: Cation site preference, electric polarization, and magnetic coupling from first principles," *Physical Review B,* vol. 90, no. 21, 2014, doi: 10.1103/PhysRevB.90.214109.

[5] R. Shannon, "Revised effective ionic radii and systematic studies of interatomic distances in halides and chalcogenides," *Acta Crystallographica Section A,* vol. 32, no. 5, pp. 751-767, 1976, doi: doi:10.1107/S0567739476001551.

[6] A. Snedden, S. M. Blake, and P. Lightfoot, "Oxide ion conductivity in Ga-doped Aurivillius phases—a reappraisal," *Solid State Ionics,* vol. 156, no. 3, pp. 439-445, 2003/01/01/ 2003, doi: https://doi.org/10.1016/S0167-2738(02)00690-2.

[7] E. McCabe and C. Greaves, "Structural and magnetic characterisation of Bi 2 Sr 1.4 La 0.6 Nb 2 MnO 12 and its relationship to “Bi 2 Sr 2 Nb 2 MnO 12”," *Journal of Materials Chemistry,* vol. 15, no. 1, pp. 177-182, 2005.

[8] M. Zurbuchen *et al.*, "Synthesis and characterization of an n= 6 Aurivillius phase incorporating magnetically active manganese, Bi 7 (Mn, Ti) 6 O 21," *Applied Physics Letters,* vol. 91, no. 3, p. 033113, 2007.

[9] K. Momma and F. Izumi, "VESTA 3 for three-dimensional visualization of crystal, volumetric and morphology data," *Journal of applied crystallography,* vol. 44, no. 6, pp. 1272-1276, 2011.

[10] M. García-Guaderrama, L. Fuentes-Montero, A. Rodriguez, and L. Fuentes, "Structural characterization of Bi6Ti3Fe2O18 obtained by molten salt synthesis," *Integrated ferroelectrics,* vol. 83, no. 1, pp. 41-47, 2006.

[11] M. Krzhizhanovskaya *et al.*, "Aurivillius Phases in the Bi4Ti3O12/BiFeO3 System: Thermal Behaviour and Crystal Structure," *Zeitschrift für anorganische und allgemeine Chemie,* vol. 631, no. 9, pp. 1603-1608, 2005, doi: 10.1002/zaac.200500130.

[12] L. Keeney *et al.*, "Room temperature ferroelectric and magnetic investigations and detailed phase analysis of Aurivillius phase Bi5Ti3Fe0.7Co0.3O15 thin films," *Journal of Applied Physics,* vol. 112, no. 5, p. 052010, 2012, doi: 10.1063/1.4745936.

[13] J. B. Goodenough, "Jahn-Teller phenomena in solids," *Annual review of materials science,* vol. 28, no. 1, pp. 1-27, 1998.

[14] M. Zurbuchen *et al.*, *Morphology, structure, and nucleation of out-of-phase boundaries (OPBs) in epitaxial films of layered oxides*. 2007, pp. 1439-1471.

[15] A. Faraz *et al.*, "Exploring ferroelectric and magnetic properties of Tb-substituted m = 5 layered Aurivillius phase thin films," *Journal of Applied Physics,* vol. 123, no. 12, p. 124101, 2018/03/28 2018, doi: 10.1063/1.5009986.

[16] P. Scherrer, "Nachr Ges wiss goettingen," *Math. Phys.,* vol. 2, pp. 98-100, 1918.

[17] C. F. Holder and R. E. Schaak, "Tutorial on Powder X-ray Diffraction for Characterizing Nanoscale Materials," *ACS Nano,* vol. 13, no. 7, pp. 7359-7365, 2019/07/23 2019, doi: 10.1021/acsnano.9b05157.

[18] Y. Li *et al.*, "Mn-doping composition dependence of the structures, electrical and magnetic properties, and domain structure/switching of Aurivillius Bi5Ti3FeO15 films," *Ceramics International,* vol. 45, no. 7, pp. 8634-8639, May 2019, doi: 10.1016/j.ceramint.2019.01.183.

[19] R. A. Armstrong and R. E. Newnham, "Bismuth titanate solid solutions," *Materials Research Bulletin,* vol. 7, no. 10, pp. 1025-1034, 1972/10/01/ 1972, doi: https://doi.org/10.1016/0025-5408(72)90154-7.

[20] S. Trolier-McKinstry, "Crystal chemistry of piezoelectric materials," in *Piezoelectric and Acoustic Materials for Transducer Applications*: Springer, 2008, pp. 39-56.

[21] P. F. Zhang, N. Deepak, L. Keeney, M. E. Pemble, and R. W. Whatmore, "The structural and piezoresponse properties of c-axis-oriented Aurivillius phase Bi5Ti3FeO15 thin films deposited by atomic vapor deposition," *Applied Physics Letters,* vol. 101, no. 11, p. 112903, 2012, doi: 10.1063/1.4752007.

[22] A. Bencan, G. Drazic, H. Ursic, M. Makarovic, M. Komelj, and T. Rojac, "Domain-wall pinning and defect ordering in BiFeO3 probed on the atomic

and nanoscale," *Nature Communications,* vol. 11, no. 1, p. 1762, 2020/04/09 2020, doi: 10.1038/s41467-020-15595-0.

[23] T. Rojac *et al.*, "Domain-wall conduction in ferroelectric BiFeO3 controlled by accumulation of charged defects," (in English), *Nature Materials,* vol. 16, no. 3, pp. 322-327, 2017, doi: http://dx.doi.org/10.1038/nmat4799.

[24] X. Qi, J. Dho, R. Tomov, M. G. Blamire, and J. L. MacManus-Driscoll, "Greatly reduced leakage current and conduction mechanism in aliovalent-ion-doped BiFeO3," *Applied Physics Letters,* vol. 86, no. 6, p. 062903, 2005, doi: 10.1063/1.1862336.

[25] S. M. Selbach, T. Tybell, M.-A. Einarsrud, and T. Grande, "High-temperature semiconducting cubic phase of BiFe 0.7 Mn 0.3 O 3+ δ," *Physical Review B,* vol. 79, no. 21, p. 214113, 2009.

[26] S. M. Selbach, T. Tybell, M.-A. Einarsrud, and T. Grande, "Structure and Properties of Multiferroic Oxygen Hyperstoichiometric BiFe1− x Mn x O3+ δ," *Chemistry of Materials,* vol. 21, no. 21, pp. 5176-5186, 2009.

[27] M. Schmidt *et al.*, "Absence of Evidence ≠ Evidence of Absence: Statistical Analysis of Inclusions in Multiferroic Thin Films," *Scientific Reports,* vol. 4, no. 1, p. 5712, 2014/07/16 2014, doi: 10.1038/srep05712.

[28] J. B. Goodenough, "Theory of the role of covalence in the perovskite-type manganites [La, M (II)] Mn O 3," *Physical Review,* vol. 100, no. 2, p. 564, 1955.

[29] L. W. Martin, Y. H. Chu, and R. Ramesh, "Advances in the growth and characterization of magnetic, ferroelectric, and multiferroic oxide thin films," *Materials Science and Engineering: R: Reports,* vol. 68, no. 4-6, pp. 89-133, 2010, doi: 10.1016/j.mser.2010.03.001.

Chapter 5

5. Sequential direct liquid injection chemical vapour deposition of Aurivillius phase materials $Bi_5Ti_{2.9}Fe_{1.1}O_{15}$ and $Bi_5Ti_{2.8}Fe_{1.1}Mn_{0.1}O_{15}$ on epitaxial substrates

5.1. Abstract

With the aim of locally concentrating magnetic ions, such as iron and manganese, to the inner perovskite blocks a sequential direct liquid injection chemical vapour deposition (DLI-CVD) recipe was used to deposit layered Aurivillius phase thin films. Thin films were deposited at 710 °C and no post anneal step was necessary to crystallise the films. A recipe which mimicked the layered nature of the *m* = 5 phase was attempted during the deposition process, but the migration of volatile bismuth favoured the formation of the *m* = 4 phase. Thin films of $Bi_5Ti_{2.9}Fe_{1.1}O_{15}$ (BTFO) and $Bi_5Ti_{2.8}Fe_{1.1}Mn_{0.1}O_{15}$ (BTFMO) were deposited on epitaxial substrates, LSAT and STO. LSAT and STO applies tensile strain applies strain on the Aurivillius structure. The impact of inserting Mn on the structure and grain size was examined. The inclusion of Mn produced smaller grains and a slight broadening of peaks observed in the XRD analysis for the Mn containing samples. The piezoresponse of these materials in the lateral direction was significantly larger than the vertical response. The existence of out of plane polarisation indicated the presence of *m* = 3 or *m* = 5 Aurivillius phase in the films. Magnetic analysis demonstrated magnetic behaviour in the BTFMO LSAT, BTFO STO and BTFMO STO materials. The observation of ferroelectric magnetic behaviour may be attributed to Dzyaloshinskii-Moriya interactions that can cause weak ferromagnetism in antiferromagnetic systems due to spin canting.

5.2. Introduction

Previous work has successfully reported the development of an *m* = 5 Aurivillius phase $Bi_6Ti_xFe_yMn_zO_{18}$ (B6TFMO) (x = 2.80 − 3.04; y = 1.32 − 1.52; z = 0.54 − 0.64) room-temperature multiferroic which was fabricated using chemical vapour deposition (CVD) [1, 2]. Further analysis of this material showed a significant

preference for Mn to occupy the central perovskite layer [3]. This partitioning of the Mn cations occurs as a natural part of the growth process due to internal electrostatic and elastic energy gradients within the B6TFMO structure. Given the relatively dilute level of magnetic cations within the structure, it has been proposed that this partitioning of magnetic cations and subsequent increased magnetic cation interaction is responsible for the better than expected magnetic response, compared with that expected for a random distribution of magnetic ions throughout the material.

Therefore, with the aim of deliberately increasing the concentration of the Mn cations in the central perovskite units of the Aurivillius material, a sequential direct liquid injection CVD recipe was developed within this contribution. This type of deposition method was first proposed by Weber *et al.* and called Atomic Vapour Deposition [4], however given that the deposition is not strictly limited to one atomic layer at a time, it is herein referred to as sequential direct liquid injection (DLI) CVD. Sequential DLI-CVD (figure 1 (a)) is a modification of a typical DLI-CVD recipe (figure 1 (b), here referred to a simultaneous DLI-CVD). In sequential DLI-CVD, the injection of the precursor pulses is separated in time and the precursors enter the reaction chamber sequentially rather than simultaneously as in typical DLI-CVD. Deepak *et al.* successfully used sequential DLI-CVD with greater control over processing conditions at 650 °C to fabricate *m* = 3 Aurivillius materials $Bi_4Ti_3O_{12}$ [5] and at 700 °C to fabricate $Bi_4Ti_{2.5}Fe_{0.5}O_{12}$ [6] without the need for a post-anneal step on (001) STO substrates. Changes to the stoichiometry had a significant effect on these Aurivillius films deposited with the sequential DLI-CVD technique [6]. With the inclusion of Fe into the material, it was observed that the growth mode shifted from Stranski–Krastanov growth mode to layer-by-layer (Frank–Van der Merwe) growth mode.

In this work, a sequential DLI-CVD recipe was developed to target the manganese-containing *m* = 5 Aurivillius phase with the aim of replicating the layered nature of the room temperature multiferroic material, $Bi_6Ti_xFe_YMn_zO_{18}$ and to deliberately encourage an increased concentration of manganese cations at the central perovskite layer [1].

5.3. Experimental

The Aurivillius materials were fabricated using a direct liquid injection-chemical vapour deposition system (AIXTRON AIX 200/4FE DLI-CVD). A sequential DLI-CVD recipe (figure S1) was used which separated the injection sets of the metal precursors during the growth to mimic the Aurivillius structure (figure 1). For the standard growth recipe, each set of precursor injections was 10 s in duration with a pulse frequency of 1 Hz and there was a pulse gap of 5 s between each injection set. The deposition temperature was 710 °C. Precursor lines were heated to 220 °C to volatilise the liquid precursors. The precursor chemicals were $Bi(THD)_3$, $Mn(THD)_3$, $Fe(THD)_3$ and $Ti(O\text{-}iPr)_2(thd)_2$ (where THD = 2,2,6,6-tetramethyl 3,5-heptanedionate; O-iPr = isopropoxide). The chemical composition targeted was $Bi_6Ti_3Fe_2O_{18}$ and $Bi_6Ti_3Fe_{1.5}Mn_{0.5}O_{18}$. For each growth the single crystalline substrates, LSAT ($La_{0.26}Sr_{0.76}Al_{0.61}Ta_{0.37}O_3$ (100)), STO ($SrTiO_3$, (100)) and c-plane sapphire were placed on the rotating susceptor plate. The vapourised precursors were accompanied through the reaction chamber with a flow of 2000 sccm of nitrogen and 1000 sccm of oxygen gas. The recipe for one half unit cell shown in figure 1 was repeated 20 times to target a thin film of 10-unit cells. No post-anneal was performed.

X-ray diffraction (XRD) measurements were performed using an X'pert Diffractometer (Cu Kα radiation λ = 0.1541876 nm) (45 kV, 40 mA). The typical 2θ scan range was from 6 ° to 40 ° and a step size of 0.005 °. The XRD patterns throughout this work were indexed using reference XRD patterns that were generated using VESTA software [7] using data from Lui *et al.* [8] for *m* = 4, García-Guaderramaet *et al.* [9] for the *m* = 5 and Hervoches and Lightfoot for *m* = 3 Aurivillius phases [10].

Atomic force microscopy (AFM) measurements were performed in AC tapping mode using an Asylum research MFP-3D AFM instrument. The AFM probes used were Olympus AC240TS probes (Al reflex coated, 15 nm tip radius, 70 kHz resonant frequency). Scan rate = 1Hz and scan angle = 90 °. Additional AFM analysis was performed using a Bruker Dimension Icon instrument in PeakForce tapping mode.

Scan rate = 1 Hz and scan angle = 0 °. The AFM probes used were Bruker SCANASYST-AIR probe, Al reflex coated, 2 nm tip radius, 70 kHz resonant frequency.

An Asylum research MFP-3D AFM instrument was used for piezoresponse force microscopy (PFM) measurements. PFM was conducted in both single frequency and lateral Dual AC Resonance Tracking (DART-PFM) [11] modes. Polarisation direction was measured by single frequency PFM at 15 kHz. The vertical, lateral and 90 ° lateral piezoresponse was measured by manually rotating the sample 90 ° and measuring again. The probes used for PFM were Olympus AC240TM electrilevers (Ti/Pt coated silicon probes, Al reflex coated, 15 nm tip radius, 70 kHz resonant frequency)). Scan rate = 1 Hz and scan angle = 90 °.

Magnetic measurements were performed on a Quantum Designs MPMS 3 Magnetometer with a field range of ±50 kOe and a temperature range of 2 to 300 K.

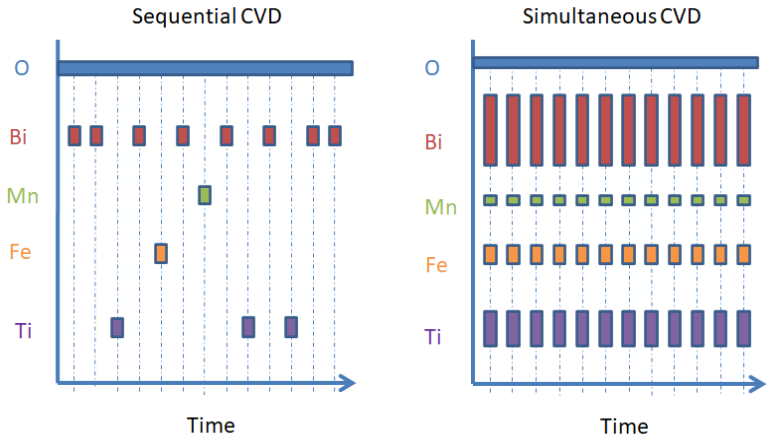

Figure 1: Image depicting the different growth methods, (a) sequential DLI-CVD, the method employed during this body of work and (b) conventional simultaneous DLI-CVD .

5.4. Results and discussion

5.4.1. Structural analysis of the Aurivillius phase

A series of growth runs was performed using the sequential DLI-CVD recipe on LSAT, STO and sapphire substrates at a deposition temperature of 710 °C. Growths were performed with an initial target stoichiometry for the *m* = 5 Aurivillius material, $Bi_6Ti_3Fe_2O_{18}$ (B6TFO) and $Bi_6Ti_3Fe_{1.5}Mn_{0.5}O_{18}$ (B6TFMO). A sequential DLI-CVD recipe that mimicked the $Bi_6Ti_3Fe_2O_{18}$ and $Bi_6Ti_3Fe_{1.5}Mn_{0.5}O_{18}$ phase is shown in figure 2. The *m* = 5 phase was targeted as it possesses a single central perovskite block (as opposed to the *m* = 4 structure which contains two inner layers). Given that a preference for Mn to occupy this central layer has been observed in previous work [3], it was proposed this layer-by-layer growth recipe could promote NN magnetic interactions required to achieve long range magnetic ordering.

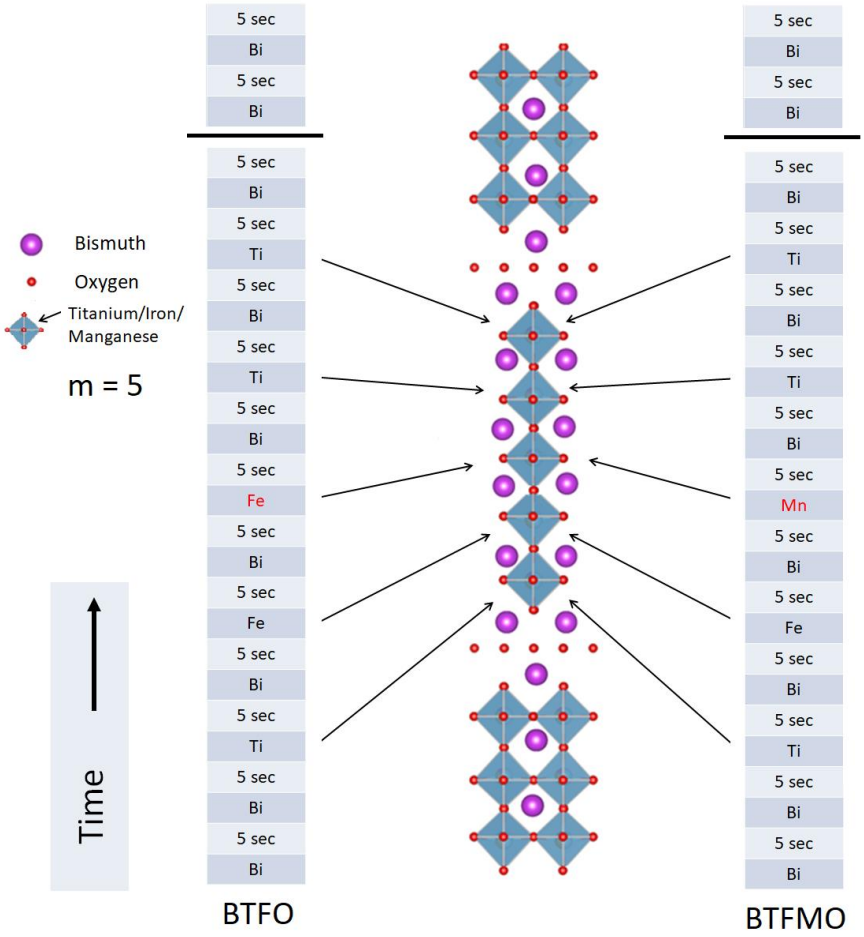

Figure 2: Diagram depicting the Sequential DLI-CVD recipe mimicking the structure of the Aurivillius material. Imaged generated using VESTA software [7] using data obtained from [9].

5.4.2. XRD analysis

While the *m* = 5 Aurivillius material was the intended target, the XRD analysis (see figure 3) showed that both the BTFO and BTFMO materials deposited on LSAT and STO indexed most closely with the *m* = 4 Aurivillius material and that an overall *m* = 5 phase was not achieved.

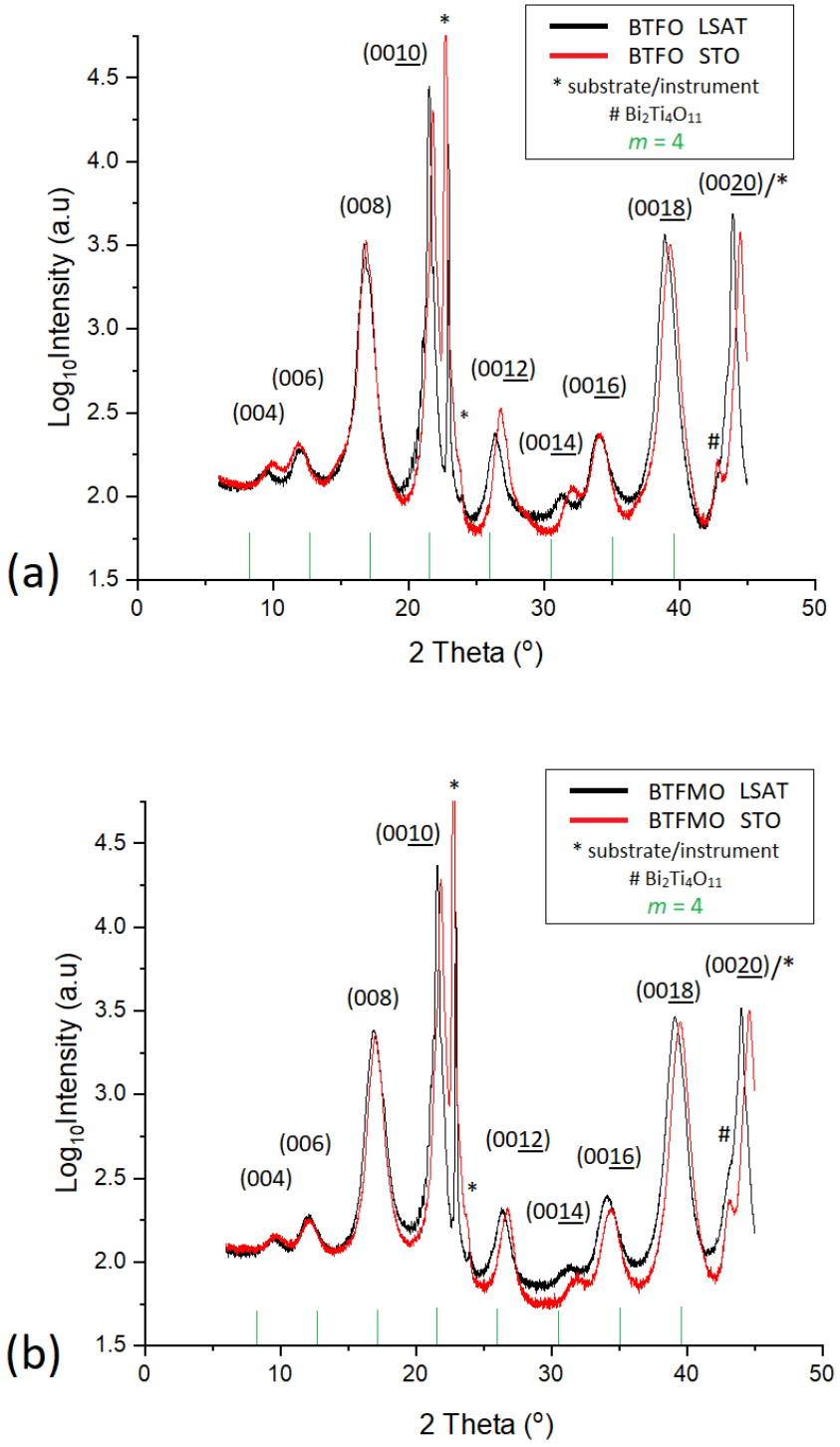

Figure 3: XRD analysis of sequential DLI-CVD growth of (a) BTFO on LSAT and STO and (b) BTFMO on LSAT and STO. Growth of the *m* = 4 Aurivillius phase was preferred for both materials.

Faraz *et al*. [2] and Keeney *et al*. [12] demonstrated that between 5 to 25 % excess bismuth was required to compensate for bismuth volatilisation in order to achieve the *m* = 5 B6TFMO phases during conventional DLI-CVD growths employing simultaneous pulses of precursors. Whereas Deepak *et al*. [6], showed that a much larger bismuth excess of between 68 to 110 % was required to enable a bismuth self-limiting growth process and formation of the desired Aurivillius phase when using a sequential DLI-CVD recipe. In this work, the relative concentration of precursors injected was determined from the precursor flow volumes used during the growth run. Precursor injection ratios of Bi:Ti:Fe of 6.9:3.6:1.4 were determined for the B6TFO targeted material and Bi:Ti:Fe:Mn of 6.7:3.5:1.4:0.1 were determined for the B6TFMO targeted material. Based on this, it was determined that the bismuth excess for a targeted *m* = 5 phase was only between 11 to 14 %. This work emphasises the need for a large excess of bismuth in order to achieve Aurivillius phases with higher '*m*' numbers by a sequential DLI-CVD growth mode.

Based on precursor injection ratios of Bi:Ti:Fe of 6.9:3.6:1.4 for the B6TFO targeted material and Bi:Ti:Fe:Mn of 6.7:3.5:1.4:0.1 for the B6TFMO targeted material, the stoichiometry of the materials was subsequently recalculated to reflect the formation of the *m* = 4 Aurivillius phases, BTFO and BTFMO. The *m* = 4 stoichiometries of the materials discussed in this work are given in table 1. The excess of Bi and the ratio of Bi to Ti during the growth process are also given.

Table 1: Details of sample stoichiometry and bismuth excess.

Sample name	Stoichiometry	Bi/Ti	% Bi excess
BTFO	$Bi_5Ti_{2.9}Fe_{1.1}O_{15}$	1.89	10 %
BTFMO	$Bi_5Ti_{2.8}Fe_{1.1}Mn_{0.1}O_{15}$	1.94	8 %
100 loops BTFMO	$Bi_5Ti_{2.6}Fe_{1.3}Mn_{0.1}O_{15}$	2.04	6 %

Despite not achieving the targeted *m* = 5 Aurivillius phase, the *m* = 4 materials produced were chosen for further examination of their properties. The sequential DLI-CVD recipe in figure 1 may still drive the partitioning of manganese towards the two inner layers of the structure to promote magnetic cation interactions.

While the materials deposited in this work (figure 3) indexed most closely to the *m* = 4 Aurivillius phase, deviations from the reference pattern were noted. Table 2 presents the full width half maxima (FWHM) and the deviation from the reference pattern for selected peaks from the BTFMO materials on LSAT and STO. The shifts correspond to differences between the position of the peak maxima in the grown samples and peak maxima positions of the *m* = 4 reference pattern. The deviation from the reference pattern indicates that intergrowths of lower or higher '*m*' Aurivillius phase structures may be present. For example, there may be intergrowth regions where *m* = 3 / *m* = 4 / *m* = 5 phases co-exist.

Table 2: FWHM of selected peaks and the shift in peak position from the reference pattern

Peak	FWHM BTFMO LSAT	FWHM BTFMO STO	Shift from reference BTFMO LSAT	Shift from reference BTFMO STO
(006)	1.383 ± 0.468	1.348 ± 0.110	-0.8° ± 0.0004°	-0.8°± 0.006°
(008)	1.593 ± 0.052	1.443 ± 0.010	-0.2°± 0.002°	-0.2°± 0.0002°
(0012)	1.184 ± 0.080	1.295 ± 0.074	+0.4°± 0.004°	+0.7°± 0.002°

These films are relatively thin, we see from TEM images that they have an average thickness of ≈ 52 ± 0.4 nm (figure 16). Size broadening effects may contribute to the broad peaks observed in the XRD data [13]. Additionally, we see from TEM images that there are significant stacking faults and out of phase boundaries in these materials (figure 16). When there is a sufficient concentration of defects present to

cause diffuse scattering of the X-rays, it can lead to the type of peak broadening/ shifts seen in the XRD (figure 3) [5]. Out of phase boundary (OPB) defects are common in layered structured materials with high levels of structural anisotropy such as the Aurivillius phases [14]. OPB defects disrupt areas where two Aurivillius layers would normally meet. Layers are displaced by a fraction of a unit cell along the *c*-axis relative to the other, meaning that a $(Bi_2O_2)^{2+}$ interlayer of one layer becomes adjacent to the perovskite blocks of the other layer.

One likely origin of these defects could be due to the escaping of volatile bismuth when subjected to the DLI-CVD process temperature of 710 °C [14]. Especially during epitaxial growth, the combination of high crystalline anisotropy and unidirectional growth fronts mean that structural rearrangement is limited to the surface layers of the growing film. The diffusion of Bi out of the film could be accommodated in the surface layers through structural rearrangement, but within the film Bi loss leads to crystallographic shear forming microstructural defects, such as OPB defects and stacking faults.

Another mechanism for OPB and stacking fault defect formation was discussed previously by Deepak *et al.*, where m = 3 $Bi_4Ti_{3-x}Fe_xO_{12}$ samples deposited using a sequential DLI-CVD recipe showed an increase in OPB defects with increasing proportion of Fe^{3+} in the material as it substituted for Ti^{4+} [6]. The difference in charge between Ti^{4+} and Fe^{3+} was compensated for by structural rearrangement of small regions of the material to an m = 4 phase, with associated OPB and stacking fault defects [15].

The differing '*m*' intergrowths, OPB defects and stacking faults would contribute to the complicated XRD patterns obtained. Attempts to calculate the crystalline quality using a modified version of the Scherrer equation (figure S2) and calculations of the *c*-axis parameters (figure S3) were deemed not accurate due to the large error introduced by the peak shift in the XRD pattern for these materials. From the TEM analysis it is known that anatase-like defects and OPBs are present in these materials, this is discussed further in section 5.4.8.

The presence of OPBs is not necessarily a detriment and may help to further concentrate the Mn towards the inner perovskite layers, further enhancing ferromagnetic behaviour. This has been observed in previous work, where atomic-resolution HAADF-STEM dark field and corresponding EDX images of *m* = 5 $Bi_6Ti_xFe_yMn_zO_{18}$ materials show that there is an increased concentration of Ti (≈ 12 %) and a decrease in Mn (≈ 13 %) around OPB regions. The preference for Ti to occupy sites adjacent to OPBs is possibly driven by a need to compensate for the localised Bi deficiencies. Where OPB regions exist, there is a corresponding increase in Fe (5 %) and Mn (8 %) in the central perovskite blocks, compared to regions free from OPBs [3].

The presence of common secondary impurity phases in these materials such as the pyrochlore $Bi_2Ti_2O_7$ which has the reflections 14.6 ° (222) and 29.6 ° (444) (JCPDF 32-0118) and the magnetic spinel phase Fe_3O_4 with the reflections 33.2 ° (220) and 35.4 ° (311) (JCPDF 89-0951) was not evident from the XRD analysis. A possible secondary phase at ≈ 43 ° may be due the (-406) reflection of $Bi_2Ti_4O_{11}$ monoclinic *B*2/*b* titanium-rich phase. The occurrence of $Bi_2Ti_4O_{11}$ was noted in previous materials deposited using a similar sequential growth process [6]. However it should be noted that many of these reflections overlap with peak position of the Aurivillius material and that the detection limit of the XRD instrument is limited, on the order of 1 - 3 vol %.

5.4.3. Influence of substrate on Aurivillius phase structure

Attempts to synthesise a crystalline Aurivillius phase on sapphire substrates were unsuccessful, with only pyrochlore $Bi_2Ti_2O_7$ (JCPDF 32-0118) being formed. This is likely due to the large lattice mismatch between the Aurivillius material and the sapphire substrates (see Table 3). The theoretical pseudo-tetragonal lattice parameter of the perovskite-type layer (a_p') in BTFO and BTFMO was calculated using the equation from Newnham and Armstrong [16],

$$a_p = 1.33r_B + 0.6r_A + 2.36\text{Å} \qquad (5.1)$$

Where r_A is the eight fold coordinate radius value of the *A*-site ion (Bi^{3+}) and r_B is the six fold coordinate radii values of the B-site ions (Ti^{4+} (0.605 Å), Mn^{3+} (0.645 Å) and Fe^{3+} (0.645 Å)). The pseudo lattice parameter of $Bi_5Ti_3Fe_1O_{15}$ and $Bi_5Ti_{2.5}Fe_{1.5}Mn_{0.5}O_{15}$ was calculated to be a_p' = 3.85 Å and a_p' = 3.85 Å respectively, using values of the effective ionic radius (IR) found in the paper by Shannon [17]. The pseudo lattice parameters for the LSAT, STO and sapphire substrates and the respective mis-match between these substrates and the a_p' of the BTFMO material are shown in table 3.

Table 3: Pseudo lattice parameters and mis-match between the substrates and the Aurivillius material

Substrate	Lattice parameters	Mis-match
LSAT	3.87 Å	+ 0.52 %
STO	3.905 Å	+ 1.41 %
Sapphire	4.78 Å	+ 19.46 %

As seen in Table 3, the LSAT and STO substrates have similar pseudo lattice parameters to the Aurivillius materials under study here. The +1.41 % and +0.52 % lattice mis-match between the LSAT and STO substrates and the BTFMO Aurivillius material causes tensile epitaxial strain on the material. This tensile strain causes the Aurivillius material to expand laterally. To maintain the total volume of the material the lattice shrinks along the *c*-axis to compensate. The STO applies a greater tensile strain than the LSAT substrate. This change in the pseudo lattice parameters can be observed in the XRD analysis in figure 4 (a); the material on STO has the (00<u>12</u>), (00<u>16</u>), (00<u>18</u>) and (00<u>20</u>) peaks shifted an average of 0.3 ° higher than the corresponding reflections of the material on LSAT.

Generally, the strain within the film applied by the substrate becomes relaxed further away from the substrate film interface as the film becomes thicker. To examine potential strain relaxation of Aurivillius films on LSAT and STO substrates, as a function

of film thickness, BTFMO was deposited with two types of film thickness. The standard recipe used for BTFO and BTFMO growths (figure 3 and figure 4 (a)) consisted of 20 loops. We know from TEM data that this forms films about 52 ± 0.4 nm thick. This is thicker than expected for a strictly layer by layer deposition process (≈ 40 nm), this is discussed further in section 5.4.8.

Growth of a thicker BTFMO film consisted of 100 loops of the sequential DLI-CVD recipe. This corresponded to a nominal 50 unit cells of the Aurivillius material although it is like to be more than this based on the results of the 20 loop recipe (section 5.4.8). XRD analysis of this 100 loop material, which has the nominal stoichiometry $Bi_5Ti_{2.6}Fe_{1.3}Mn_{0.1}O_{15}$, is shown in figure 4 (b).

Comparison between the thicker film (figure 4 (b)) and the thinner film (figure 4 (a)) indicates strain relaxation in the film as the material gets thicker. In figure 5, a closer look at the (00<u>18</u>) reflection clearly shows the shift in peak position for the thicker films. The positions of the (00<u>18</u>) peak maxima for both the materials (BTFMO LSAT 100 loops (39.23 ° ± 0.002 °) and BTFMO STO 100 loops (39.28 ° ± 0.001 °)) in the thicker film (figure 4 (b)) is at very similar peak position and occur between the values (39.19 ° ± 0.0003 ° to 39.48 ° ± 0.0002 °) obtained for the thinner films i.e. the BTFMO LSAT (00<u>18</u>) peak have slightly shifted higher (+ 0.04 °) and the BTFMO STO peak have shifted lower (0.20 v). In table 4, the values of the peaks positions and FWHM of the (00<u>18</u>) are presented.

Note that the shoulder on the peaks corresponding to the (008) and (00<u>20</u>) *m* = 4 Aurivillius reflection can be assigned as the (00<u>10</u>) and (00<u>24</u>) peak reflections respectively of *m* = 5 Aurivillius phase. It is most clearly seen in the thinner STO material due to peak shift caused by the substrate (figure 4 (a)). However, the reflections around 43 ° are difficult to definitively identify as the monoclinic $Bi_2Ti_4O_{11}$ phase due to the overlapping presence of Aurivillius phase and substrate peaks in that area. The peak reflections around 30 – 35 ° on the analysis of the 100 loop sample (figure 4 (b)) has been obscured due to instrumental interference when the sample size is < 0.5 cm x 0.5 cm. This is discussed in more detail in appendix 5, figure S4. The

BTFO and BTFMO samples in figure 3 are larger (1 cm^2) and not affected in the same way.

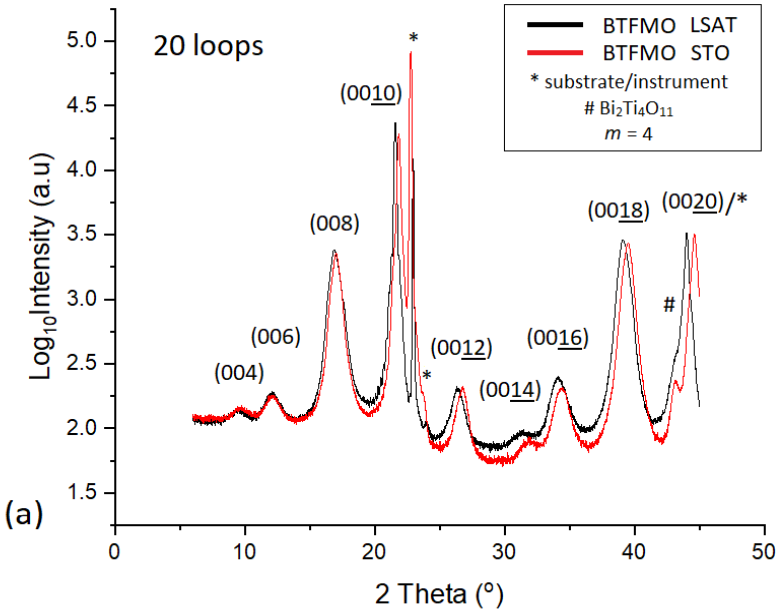

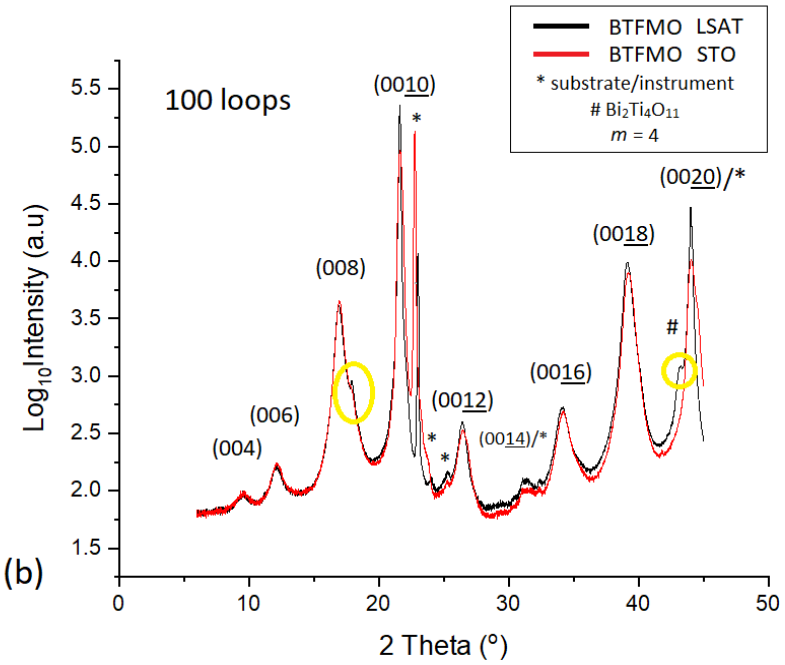

Figure 4: XRD analysis of the Aurivillius materials deposited by (a), 20 loops of the sequential DLI-CVD recipe on LSAT and STO and (b), 100 loops of the sequential DLI-CVD recipe on LSAT and STO. The shoulder on the (008) and (0020) peaks are marked with a yellow circle.

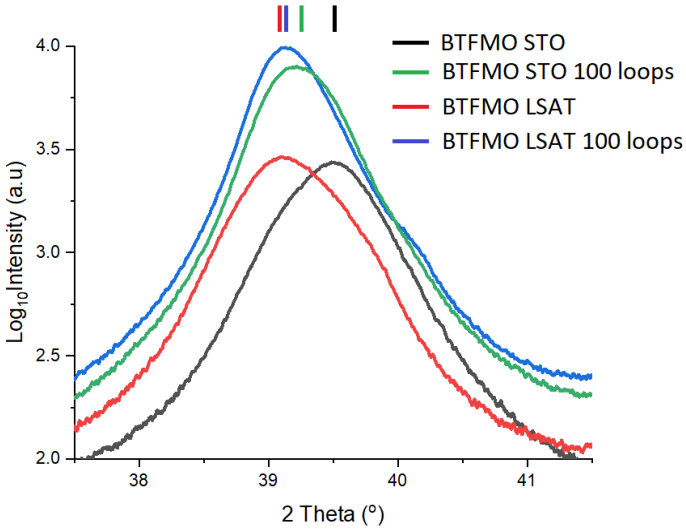

Figure 5: Comparison of the (0018) reflection for the 20 loop and 100 loop materials.

Table 4: The peak positions and FWHM of the (0018) reflection.

(0018)	BTFMO LSAT 20 loops	BTFMO LSAT 100 loops	BTFMO STO 20 loops	BTFMO STO 100 loops
Peak position	39.19 ° ± 0.0003 °	39.23 ° ± 0.002 °	39.48 ° ± 0.0002 °	39.28 ° ± 0.001 °
FWHM	1.700 ± 0.03	1.641 ± 0.07	1.698 ± 0.02	1.695 ± 0.03

5.4.4. Influence of Mn substitution on Aurivillius phase structure

The proportion of Mn in the BTFMO samples was relatively low at just 2.5 % of the *B*-site cations. Comparing the XRD analysis of the BTFO and BTFMO samples on the different substrates (figure 6) the addition of Mn had a small effect on FWHM (table 5) and the XRD peak positions (table 6). The FWHM increases for most peaks with the substitution of Mn. The (006) and (008) shift slightly higher while the (00$\underline{1}$0) peak position shifts slightly lower. The direction of these peak shifts may indicate the occurrence of a different *m* Aurivillius phase as was observed in chapter 4 following a reduced concentration for Ti in the material.

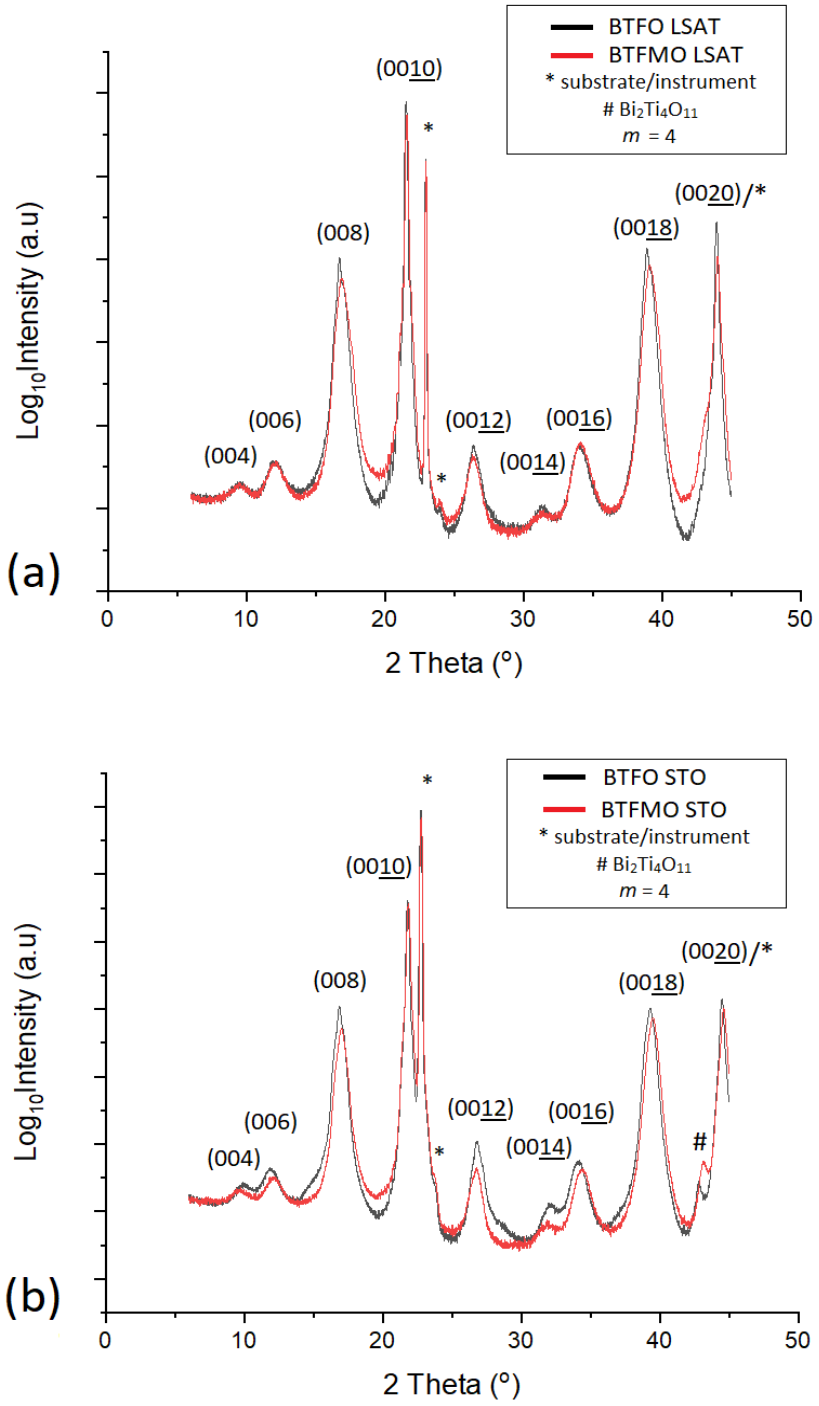

Figure 6: XRD analysis of sequential DLI-CVD growth of $Bi_5Ti_{2.9}Fe_{1.1}O_{15}$ BTFO and $Bi_5Ti_{2.8}Fe_{1.1}Mn_{0.1}O_{15}$ BTFMO on (a), LSAT and (b), STO substrates.

Table 5: FWHM of selected peaks

Peak	FWHM BTFO LSAT	FWHM BTFMO LSAT	FWHM BTFO STO	FWHM BTFMO STO
(006)	1.218 ± 0.033	1.383 ± 0.468	1.264 ± 0.131	1.348 ± 0.110
(008)	1.508 ± 0.019	1.593 ± 0.052	1.447 ± 0.055	1.443 ± 0.010
(0012)	1.280 ± 0.024	1.184 ± 0.080	1.169 ± 0.032	1.295 ± 0.074

Table 6: Peak position

Peak	BTFO LSAT	BTFMO LSAT	BTFO STO	BTFMO STO
(006)	12.103 ° ± 0.001 °	12.106 ° ± 0.001 °	11.882 ° ± 0.011 °	12.114 ° ± 0.007 °
(008)	16.848 ° ± 0.001 °	17.005 ° ± 0.002 °	16.896 ° ± 0.002 °	17.055 ° ± 0.001 °
(0012)	26.461 ° ± 0.001 °	26.382 ° ± 0.004 °	26.872 ° ± 0. 002 °	26.689 ° ± 0.002 °

5.4.5. AFM analysis

AFM images of BTFMO material deposited during the same growth run on different substrates are shown in figure 7. Deposition on LSAT and STO produces a smoother crystalline material (RMS roughness ≈ 900 pm) while the material deposited on sapphire is rougher (RMS roughness ≈ 14 nm) (figure 7).

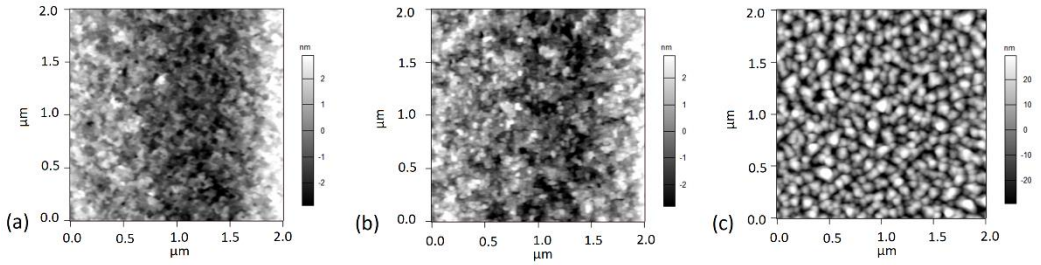

Figure 7: AFM BTFMO (a), LSAT, (b), STO and (c), sapphire substrates.

AFM images of the 100 loop samples are shown in figure 8. There is no notable increase in roughness in the thicker film compared to the 20 loop materials. The RMS roughness for BTFMO 100 loops LSAT and STO remains ≈ 1 nm.

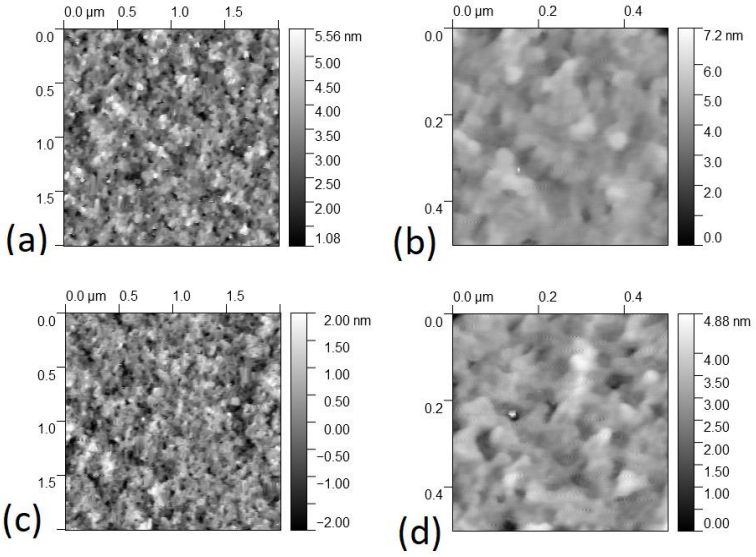

Figure 8: AFM height images of BTFMO LSAT 100 loops (a), 2 µm^2 and (b), 500 nm^2 and AFM height images of BTFMO STO 100 loops (c), 2 µm^2 and (d), 500 nm^2.

There is a notable difference in the surface morphology of the BTFO and BTFMO materials in the AFM height images in figure 9. The surface area of grains was determined (figures S5 and S6) and there is a higher distribution of smaller grains in

the Mn containing materials although there is no significant difference in the RMS roughness (≈900 pm) of the materials.

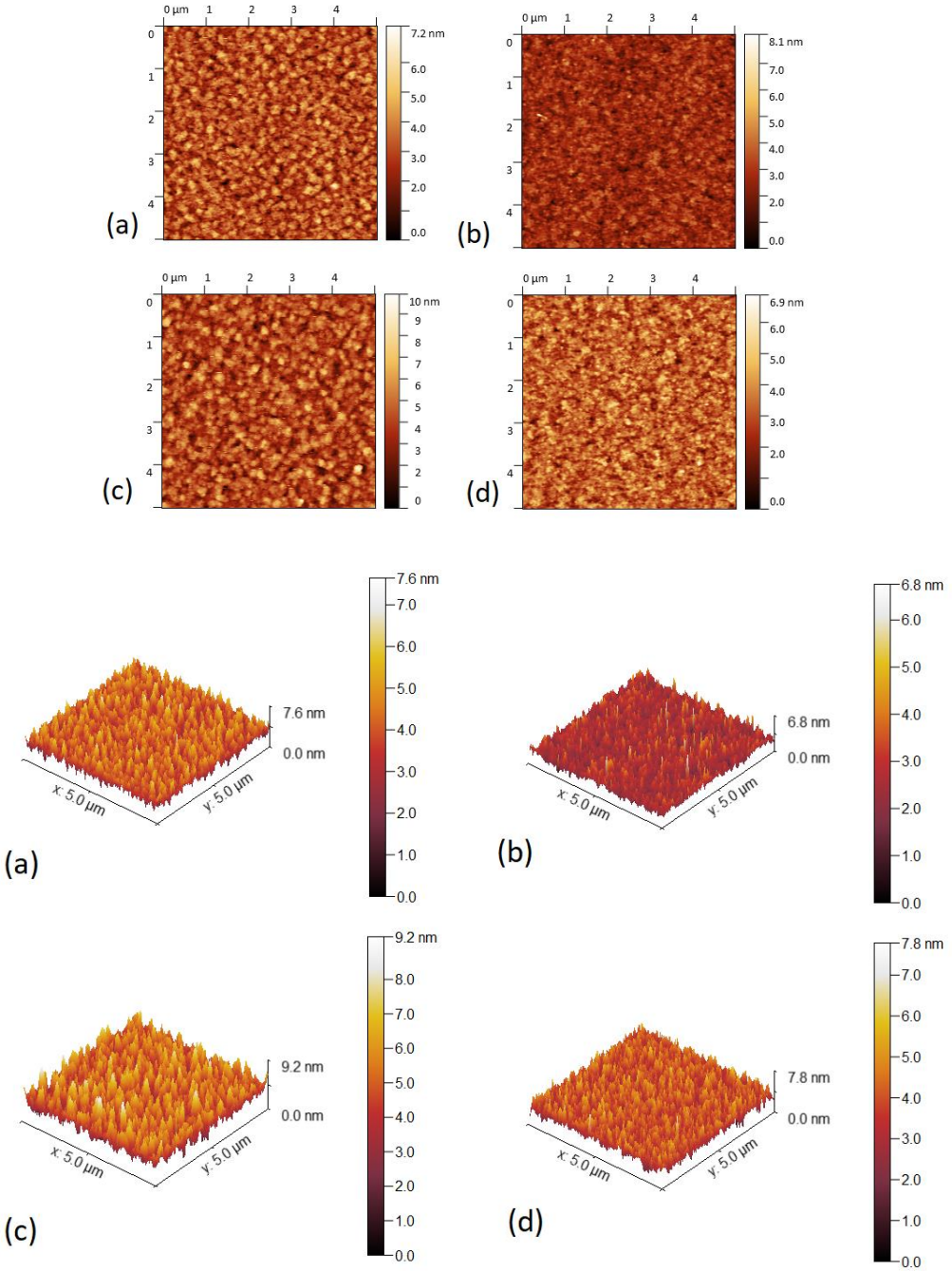

Figure 9: AFM height images of (a), BTFO LSAT, (b),BTFMO LSAT and (c), BTFO STO and (d), BTFMO STO.

5.4.6. Analysis of piezoresponse

Single frequency measurements (measurement frequency 15 kHz) simultaneously recorded the lateral and vertical response of the material to the applied field. The BTFO (figure 11) and BTFMO (figure 12) on LSAT materials were found to be piezoelectric and naturally self-polarised with 180 ° domains. Higher piezoresponses were observed in the lateral direction (relative piezoresponse values of 42 pm/V and 45 pm/V for BTFO and BTFMO on LSAT, respectively) compared with those measured in the vertical direction (relative piezoresponse values of 5 pm/V and 9 pm/V for BTFO and BTFMO on LSAT, respectively). A vertical piezoresponse would not be expected in a *m* = 4 Aurivillius system as the mirror symmetry along the *c*-axis prevents an out-of-plane polar component. The vertical response here may be due to *m* = 3 and *m* = 4 intergrowths. The m = 3 Aurivillius does have a small out of plane polarisation.

These are uncalibrated measurements and hence they are relative comparisons (not absolute values) using the same imaging conditions. To examine whether polarisation is anisotropic within the lateral plane, the sample was measured with the cantilever aligned parallel to the [100] substrate direction. Following this, the sample was then rotated by 90 ° so that the cantilever was aligned parallel to the [010] substrate direction and similar PFM measurements were performed again (figure 10). For the BTFO (figure 11) and BTFMO (figure 12) materials the lateral response was comparable along each direction. Gradauskaite *et al.* observed isotropic domain orientation at a thickness greater than a half unit cell of the $Bi_5Ti_3Fe_1O_{15}$ on epitaxial [001] $NdGaO_3$ (NGO) substrates and only in the ultra-thin film of a half unit cell thickness were anisotropic domains observed [18].

Due to lack of microscopic topographic markers on the sample surface, the exact same sample area could not be selected for study after physical sample rotation, however as the material has an epitaxial relationship to the substrate the directionality of the material with respect to the cantilever is known.

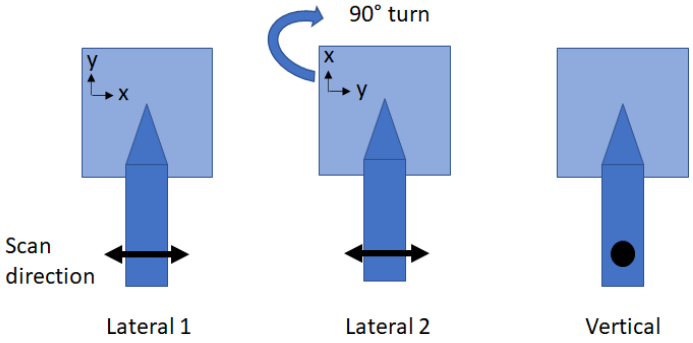

Figure 10: Schematic of sample and cantilever orientations to investigate polarisation anisotropy using PFM.

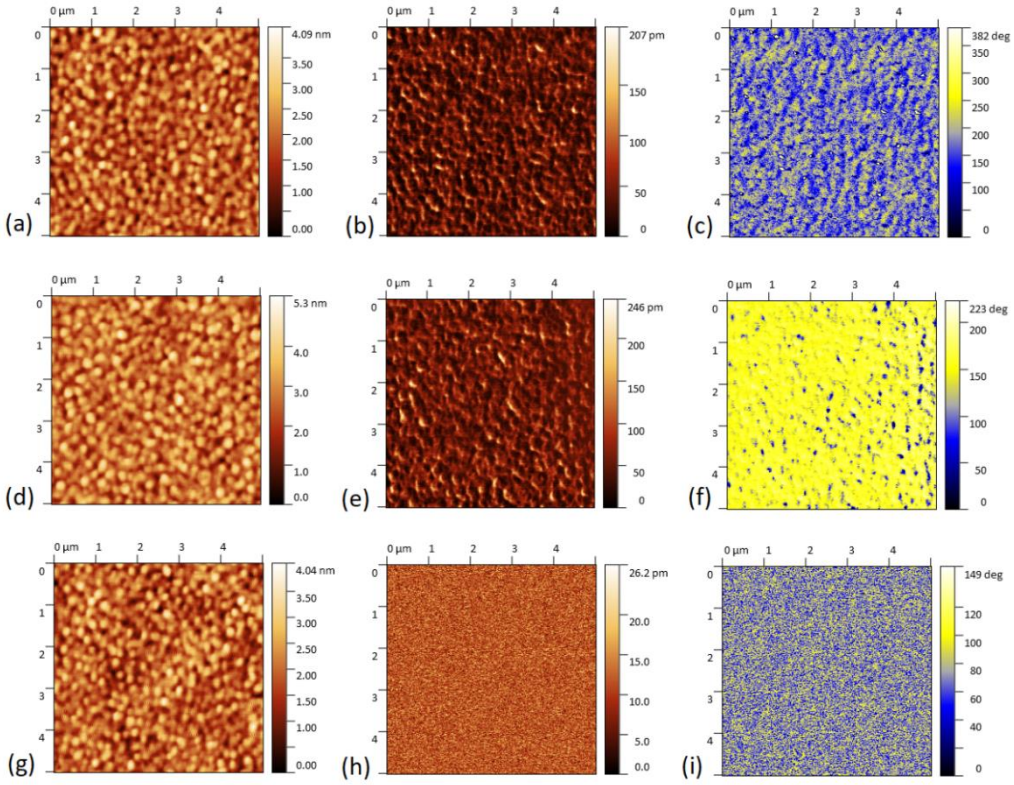

Figure 11: Single frequency PFM of BTFO on LSAT. The lateral 1 (a) height, (b) amplitude and (c) phase. Lateral 2, 90 ° rotation of the sample (d) height, (e)

amplitude and (f) phase. Vertical PFM response, (g) height, (h) amplitude and (i) phase.

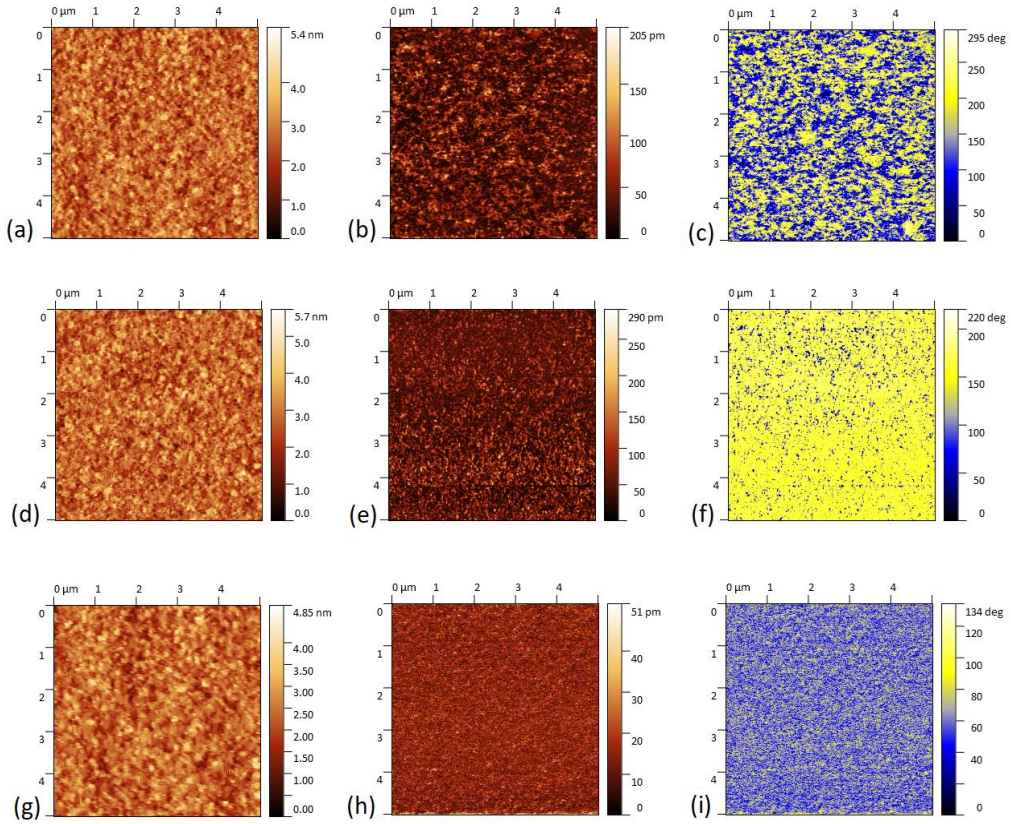

Figure 12: Single frequency PFM of BTFMO on LSAT. The lateral 1 (a) height, (b) amplitude and (c) phase. Lateral 2 90 ° rotation of the sample (d) height, (e) amplitude and (f) phase. Vertical PFM response, (g) height, (h) amplitude and (i) phase.

Due to the relatively small piezoresponse, a PFM method know as DART-PFM [11] was used to boost the signal during imaging of these samples. The feedback loop reduces instrumental crosstalk. The result of lateral DART-PFM measurements are shown in figure 13. The materials are found to be naturally self-polarized. The domains are smaller than those observed in samples deposited using chemical solution deposition

(CSD) (chapters 3 and 4). For example, an average domain size of 7.4 nm^2 was determined for a sample made by sequential DLI-CVD compared to an average 369.6 nm^2 for a sample made by CSD.

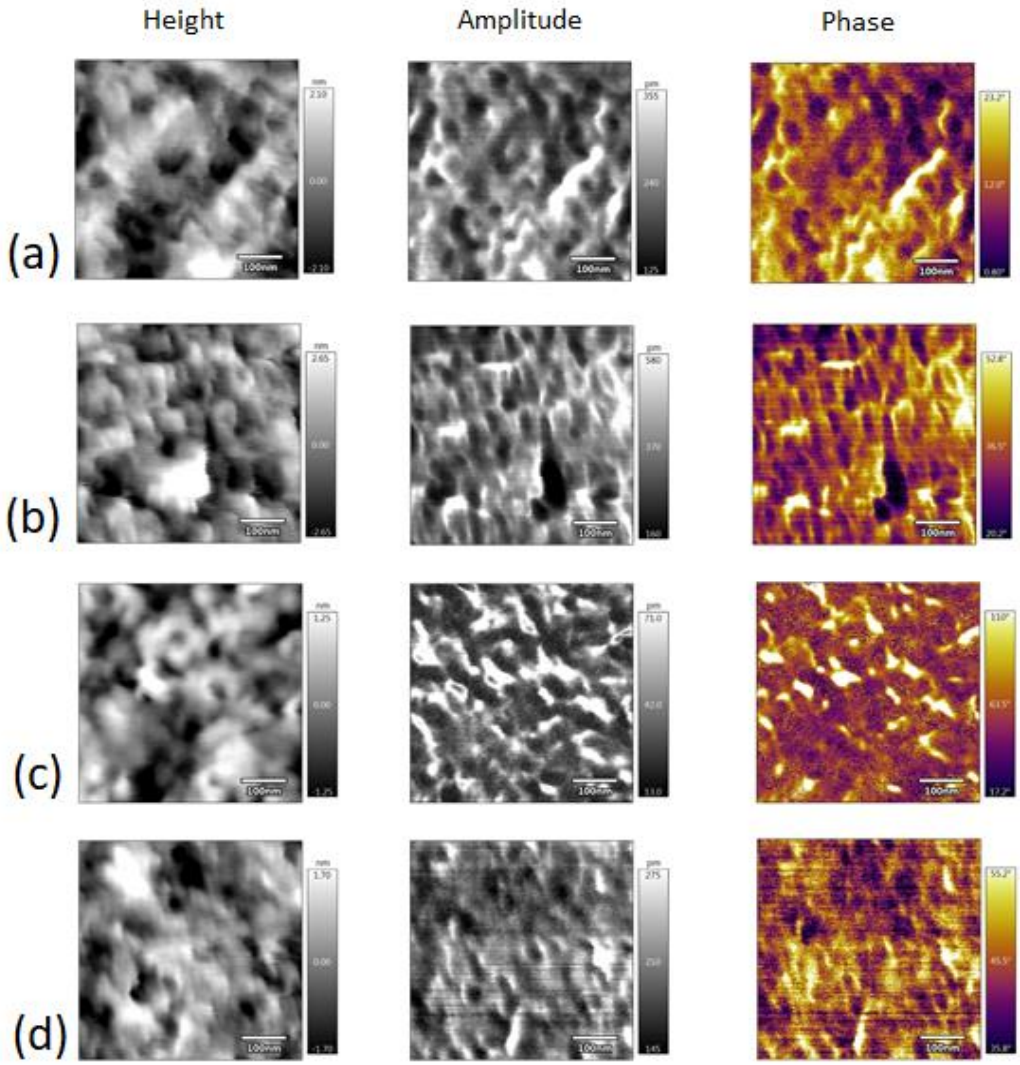

Figure 13: DART PFM (a) BTFO on LSAT, (b) BTFO on STO, (c) BTFMO on LSAT and (d) BTFMO on STO.

5.4.7. Analysis of magnetic properties

To investigate the magnetic behaviour of these materials, SQUID (Superconducting Quantum Interference Device) analysis of the BTFO and BTFMO samples on LSAT and

STO was performed. Hysteresis loops (MH curves) of the materials magnetic response to an applied magnetic field at a set temperature were recorded as well as the magnetic response over a temperature range (MT). MT measurements were performed under field cooled (FC) and zero field cooled (ZFC) conditions and the remanence (REM) was calculated from the ZFC-FC measurements. The magnetic field applied was 50 Oe. The orientation of the sample is in-plane with respect to the magnetic field during measurement and the diamagnetic contribution from the substrates has been subtracted from the results.

The BTFMO film on LSAT displayed a non-linear ('S'-shaped curve) MH response to the applied magnetic field throughout the range of temperatures the analysis was carried out under (figure 14 (a)). On increasing the temperature from 2 K to 200 K the magnetic response decreases, shown by the lower remanent magnetization (M_r) and coercivity (H_c) (Table S1). At higher temperatures, 250 K and 300 K, the magnetic response again increases. This suggests that a phase transition (from ferromagnetic to paramagnetic) occurs above 200 K. The FC and ZFC plots diverge around 130 K and the remanence decreases with increasing temperature (figure 14 (b)). The decrease in H_c and remanence with increasing temperature and the 'S'-shaped curves of the MH plot over the temperature range 2 K to 200 K are consistent with ferromagnetic behaviour. The increasing H_c at 250 K and 300 K but with a continued decrease in remanence over that range indicates paramagnetic behaviour.

The BTFO film on LSAT did not display ferromagnetic behaviour as the coercivity decreased with decreasing temperatures from 10 K to 2 K (figure 14(c)) (Table S2). This indicated diamagnetic behaviour. The FC-ZFC plots increase sharply at very low temperatures and above 20 K, both plots coincide together (figure 14(d)). This could possibly be explained by superparamagnetism originating from very small ferromagnetic nanodots (≈ 2 nm) in the film [19, 20]. These small particles would only be ferromagnetic at very low temperatures (< 20 K) and above that are superparamagnetic. This is supported by the MH curves where only the 2 K and 10 K (without diamagnetic subtraction) show hysteresis. The possible presence of such particles would need to be confirmed by detailed TEM analysis.

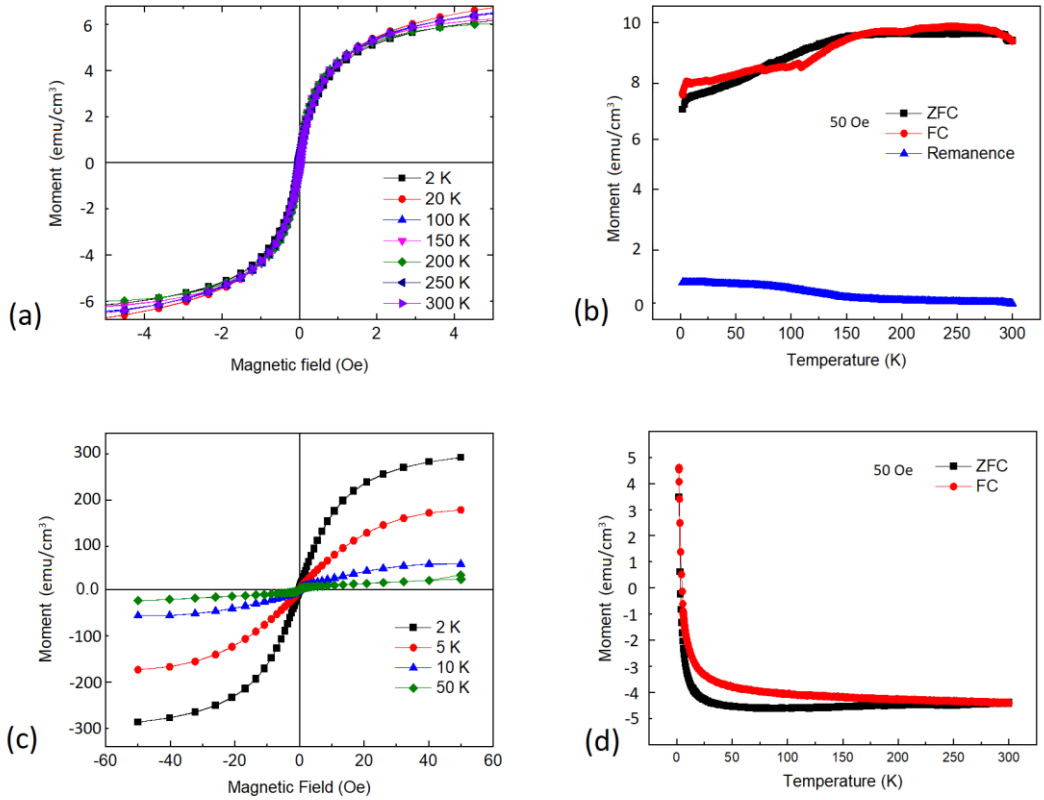

Figure 14: Magnetic measurements of (a) MH, and (b) MT for of BTFMO on LSAT and (c) MH and (d) MT for BTFO on an LSAT substrate.

The BTFMO on STO sample (figure 15 (a)) displayed a non-linear response to the applied magnetic field. There is divergence of the FC-ZFC plots below ≈ 280 K (figure 15 (b). The H_c and remanence for this material increase with decreasing temperature consistent with ferromagnetic behavior (table S3). There is a decrease in H_c at 2 K. As the material displays ferromagnetism at higher temperatures, the sharp increase in FC and ZFC moment can be attributed to antiferromagnetic spins from Fe^{3+}-Fe^{3+} interactions, rather than superparamagnetism as with the BTFO LSAT sample (figure 14(d)). The point at -50 kOe in figure 15 (a) is determined to be due to instrumental error during the analysis, perhaps due to fluctuations at high negative field.

The BTFO on STO sample (figure 15(c) and (d)) shows an increase in coercivity and remanence with decreasing temperature which would suggest ferromagnetic

behavior (table S4). There is a decrease in H_c between 10 K and 2 K. The FC and ZFC plot diverge below 265 K and there is a sharp increase in both the FC and ZFC at very low temperatures which may be due to possible antiferromagnetic interactions.

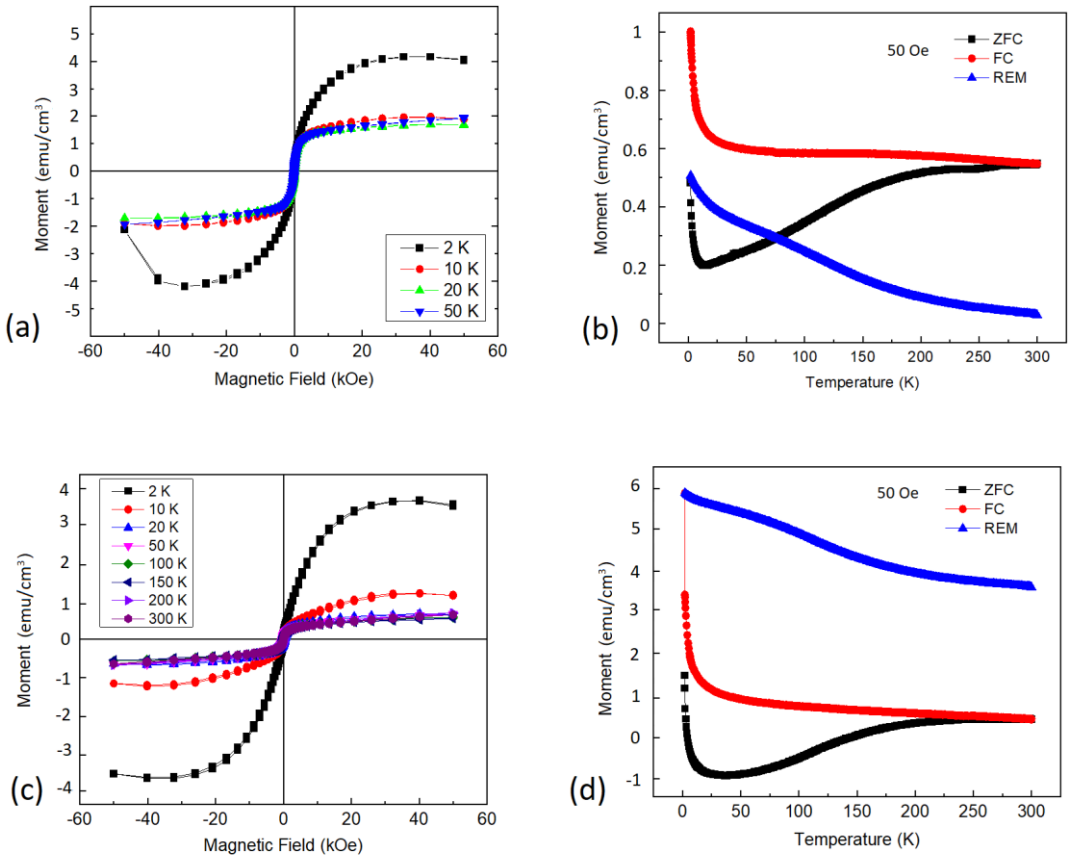

Figure 15: Magnetic measurements of (a) MH and (b) MT for BTFMO on a STO substrate and (c) MH and (d) MT for BTFO on a STO substrate.

Although ferromagnetic behaviour is observed below 200 K, ferromagnetic behaviour does not persist at room temperature, which is different to that observed for the *m* = 5 $Bi_6Ti_xFe_yMn_xO_{18}$ films [1, 2]. This may be due to the decreased concentration of magnetic ions present in the materials in this work. The percentage of magnetic ions, iron and manganese, at the *B* - sites of the BTFMO material is 30% and only 2.5% of this is manganese. Room temperature magnetic behaviour was observed in $Bi_6Ti_{2.8}Fe_{1.52}Mn_{0.68}O_{18}$ material, which had a concentration of 13 % manganese and a

total of 44 % iron and manganese at the *B*-sites [1, 2]. Computational work by Birenbaum *et al.* has shown the Curie temperature increases when the concentration of magnetic ions increases [21]. This may explain why the magnetic behaviour does not persist at room temperature for the samples presented in this work. For a random distribution of ions in a 3D lattice, a concentration of 31 % is necessary for near neighbour coupling and 14 % for next near neighbour [22]. According to the Goodenough-Kanamori rules [23] a super-exchange mechanism can occur between Mn^{4+} - O - Mn^{3+} or Mn^{4+} - O - Fe^{3+} which would result in ferromagnetic behaviour. Manganese is nominally in the 3+ oxidation state in these materials but it could readily oxidise to the Mn^{4+} state particularly in response to a decreased Ti^{4+} concentration as discussed in chapter 4. The observation of antiferromagnetic behaviour in BTFO on STO can be attributed to coupling between Fe^{3+} - O - Fe^{3+} or Mn^{4+} - O - Mn^{4+}. Ferromagnetic behaviour would not be expected for Fe^{3+} - O - Fe^{3+} or Mn^{4+} - O - Mn^{4+} interactions. If we assume that Ti has a 4+ oxidation state and Fe has a 3+ oxidation state, then the chemical formula $Bi_5Ti_{2.8}Fe_{1.1}O_{15}$ does not have a balanced charge. Theoretically, this could drive the formation of Fe^{4+} to maintain a balanced stoichiometry. Fe^{4+} - O - Fe^{3+} interaction would produce ferromagnetic behaviour. In other works, the presence of has been Fe^{4+} experimentally determined at the boundary walls of the $BiFeO_3$ material, however, away from the electrostatic environment of the domain wall the formation of Fe^{4+} was not observed and Fe^{3+} was dominant [24, 25]. Therefore, we do not expect Fe^{4+} to be present in these materials. Interactions between Fe^{3+} - O - Fe^{2+} could produce ferromagnetism but the formation of a lower oxidation state would not be favourable in this system [26, 27]. Perhaps it is more likely that the Dzyaloshinskii-Moriya interaction is responsible for the weak ferromagnetism observed. The Dzyaloshinskii-Moriya interaction can cause weak ferromagnetism in antiferromagnetic systems due to spin canting leading to a net magnetisation [28]. Spin canting was responsible for ferromagnetism in $BiFeO_3$ systems [29]. The observed M vs H plots could also be consistent with ferrimagnetism. It is difficult to conclude the sample behaviour to be ferrimagnetic and not ferromagnetic as that can be understood from the amount of moment. That

can be only be calculated if the exact structure of the sample and the details like ions per unit cell are known.

Computational studies by Birenbaum *et al.* investigated the site preference of iron in the $Bi_5Ti_3Fe_1O_{15}$ *m* = 4 Aurivillius phase [30]. They noted that the occupation of the inner perovskite blocks by Fe^{3+} was favoured over the occupation of the outer perovskites adjacent to the Bi_2O_2 interlayer. However, when the *c*/*a* lattice parameters became larger, such as the material being under compressive strain, there was an increase in occupation of the outer layers of the perovskite blocks. A more random distribution of Fe throughout all the available perovskite sites may explain the lack of magnetic response of the BTFO on LSAT material. This may explain why a larger magnetic response is observed in BTFMO on STO than BTFMO on LSAT. For example at 20 K, BTFMO on STO M_R = 3.51 emu/cm^3 (table S4) and BTFMO on LSAT M_R = 1.50 emu/cm^3 (table S1).

Further analysis, such as the detailed microstructural and statistical analysis as developed by Schmidt *et al.* [31], is necessary to confirm that the observed magnetic responses are intrinsic to the Aurivillius phase material and not due to small volumes of secondary impurity phases. Trace amounts (≈ 0.01 vol.%) of secondary impurities, if present, may be responsible for an observed magnetic response [32], therefore detailed purity analysis is required to exclude this possibility.

5.4.8. TEM analysis

TEM analysis for BTFO and BTFMO shown in figure 16. The thickness of these films is ≈ 52 ± 0.4 nm. This is thicker than expected for a strictly layer by layer deposition. To estimate the expected thickness of the film, the following equation can be used. The *c*-axis length of the *m* = 4 BTFMO Aurivillius material can be estimated by equation 5.2 [33];

$$c/2 = f + h \qquad (5.2)$$

where h = *m**p; p is the thickness of the perovskite block (p ≈ 4 Å), *m* is the number of perovskite blocks and f is the thickness of the fluorite $(Bi_2O_2)^{2+}$ interlayer which has

an average value of 4.08 Å [34]. Using this equation, 20 loops of the sequential DLI-CVD recipe would produce a film ≈ 40 nm thick. The presence of intergrowths of different *m* phases limits the usefulness of this calculation. It is clear from the TEM images that there is greater than 20 half-unit cells of the Aurivillius phases occurring. This is also complicated by the presence of out of phase boundaries, but 24 to 27 half-unit cells can be distinguished from the TEM images (figure 16).

We see also the presence of anatase-like defects which indicates migration of bismuth during the deposition process [35, 36]. The distinctive "S-shaped tunnels" are formed by the anatase-like chains together with the octahedra of the perovskite blocks. The S-shaped tunnels are occupied by and stabilised by double columns of lone pair, stereochemically active Bi^{3+} cations. The double Bi columns at the interfaces create a "zig-zag" pattern of Bi atoms between the perovskite blocks [35, 36].

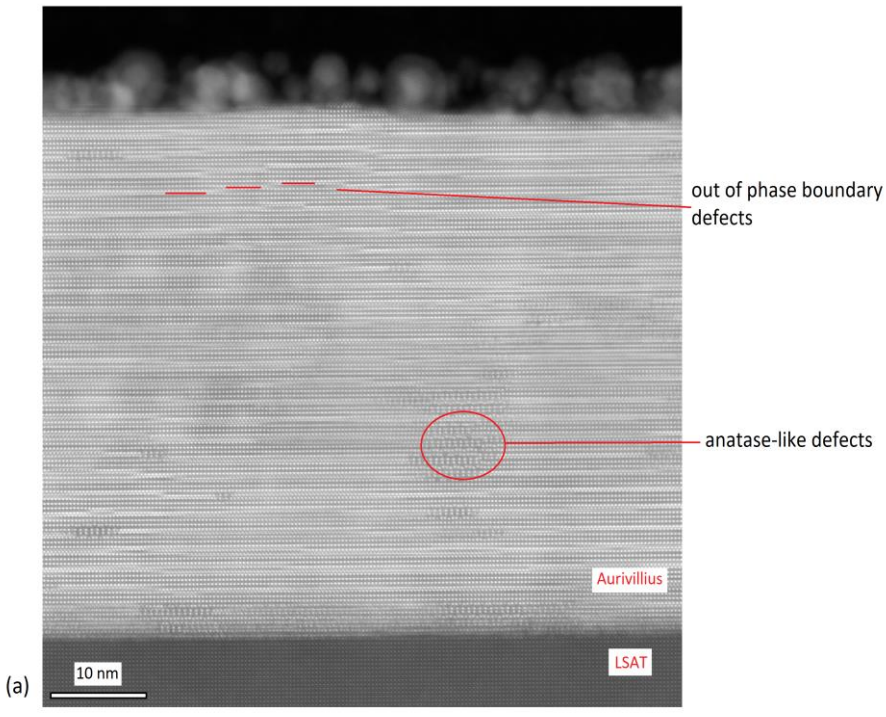

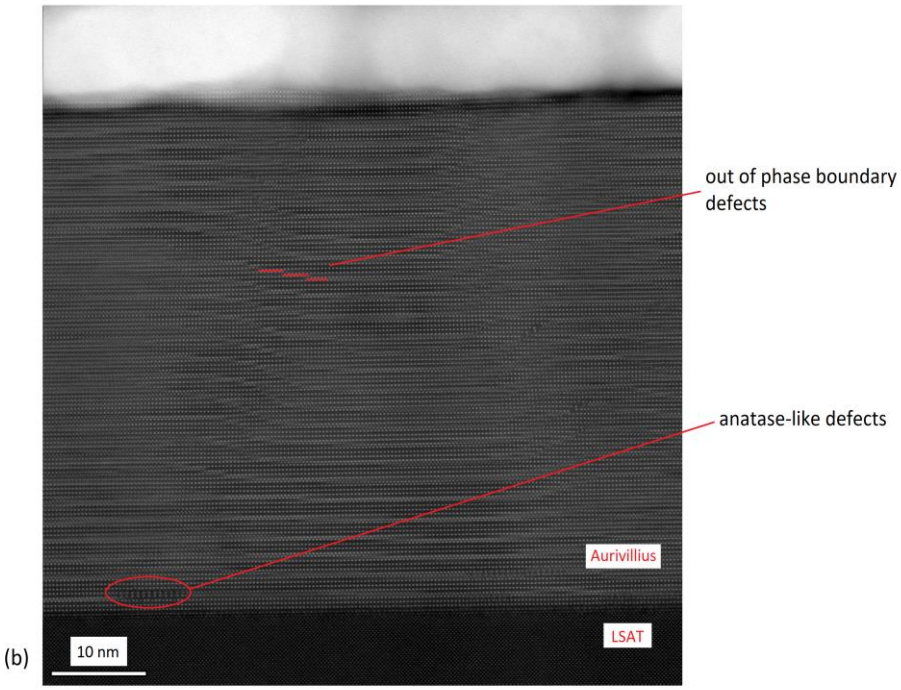

Figure 16: TEM images of (a) BTFO and (b) BTFMO material on LSAT substrates.

5.4.9. Discussion on the difficulties of synthesising Aurivillius phases with higher '*m*' numbers

The initial aim was this study was the fabrication of the *m* = 5 Aurivillius phase and the sequential DLI-CVD recipe used mimicked this structure. However, the lack of a large bismuth excess during the deposition process and also the proportion of Ti^{4+} to Fe^{3+}/ Mn^{3+} favoured the formation of the lower *m* phase. In addition to this, elastic strain mismatches between the $(Bi_2O_2)^{2+}$ interlayers and perovskite units has been proposed as the driving force behind the difficulty of fabricating Aurivillius materials with *m* > 4 [37]. Kikuchi notes that the actual lattice parameter, *a*, of $Bi_4Ti_3O_{12}$ (3.83 Å) is between that of the unconstrained (or "natural") lattice parameter for the $(Bi_2O_2)^{2+}$ layer ($a_{B'}$ = 3.80 Å) and that of the unconstrained perovskite block ($a_{p'}$ = 3.89 Å) [16]. This puts the perovskite blocks under compression, and the $(Bi_2O_2)^{2+}$ fluorite layers under tension. For a real lattice with lattice parameter, *a*, forces must be

balanced, therefore the stresses of the $(Bi_2O_2)^{2+}$ layer (expanding) must equal the sum of the stresses of the perovskite layers (contracting). Given that the modulus of $(Bi_2O_2)^{2+}$ layer is independent of composition of perovskite layers; the total bulk modulus must be proportional to the modulus of the perovskite layers. Kikuchi then performs calculations based on bulk compressibility's to predict the energy stability of the Aurivillius structures with different values of *m*. An increase in number of perovskite groups, *m*, gives an increase in pseudo-tetragonal lattice parameter, *a*, therefore increase in cell volume (*V*). It follows that the total strain energy, *E*, caused by the dilation of $(Bi_2O_2)^{2+}$ unit and the compression of perovskite-like units, increases with number of perovskite layers. Hence there is an increase in enthalpy of formation for higher *m* structures and it is therefore thermodynamically less favourable to synthesise higher *m* structures. The material may prefer the arrangement that balances this elastic strain, such as the formation of lower *m* = 4 and *m* = 3 Aurivillius phases in this contribution.

5.5. Conclusion

A sequential DLI-CVD growth recipe was developed with the objective of mimicking the *m* = 5 Aurivillius phase materials, $Bi_6Ti_3Fe_2O_{18}$ and $Bi_6Ti_3Fe_{1.5}Mn_{0.5}O_{18}$ on LSAT and STO substrates. However, using a 11 – 14 % bismuth excess and with precursor injection ratios for Bi:Ti:Fe of 6.9:3.6:1.4 and Bi:Ti:Fe:Mn of 6.7:3.5:1.4:0.1 for B6TFO and B6TFMO, respectively, an *m* = 4 phase was favoured instead. XRD analysis confirmed that the materials deposited indexed most closely with the lower *m* = 4 Aurivillius phase, with indications that intergrowths of *m* = 3 / *m* = 4 / *m* = 5 regions co-exist within the film. TEM analysis confirms the presence of out of phase boundary defects contributing the broad peaks observed in the XRD analysis.

The sequential DLI-CVD recipe failed to produce the desired *m* phase in this work however, future adjustment to the DLI-CVD recipe may yet produce the desired phase. In particular, increasing the total flow volumes used during the experiments to improve the run to run consistency and increasing the excess of Bi (> 68 %) available throughout the deposition process may help to overcome any local Bi

deficiency and possibly push the structure to form the higher *m* phase. Further experiments in this area would include investigating the effect of the growth temperature on the availability of Bi during the growth and targeting a B6TFO and B6TFMO *m* = 5 structure.

Despite not achieving the targeted *m* = 5 Aurivillius phase, the *m* = 4 materials produced were chosen for further examination of their properties. It was found that the LSAT and STO substrates induced tensile epitaxial strain on the BTFO and BTFMO Aurivillius films. This was seen as peak shifts in the XRD analysis, as the in-plane lattice expanded causing the *c*-axis to shorten. The influence of substrate strain on the film diminished in thicker films.

The BTFMO materials on LSAT and STO substrates exhibited a remanent magnetic response with respect to the applied magnetic field across the temperatures measured, with ferromagnetic behaviour up to 250 K and 280 K, respectively. In both cases, the magnetisation was higher than the corresponding BTFO films. This study, along with previous studies of the B6TFMO films [1, 2] demonstrates that the presence of manganese is a key factor promoting ferromagnetic behaviour in the Aurivillius phases. This is an encouraging result for the development of room temperature multiferroics, however a full suite of purity analysis needs to be performed to confirm the source of the magnetic signal, given that small volumes (≈ 0.01 vol.%) of secondary magnetic phases could produce such a response.

5.6. Acknowledgements

The authors gratefully acknowledge the support of Science Foundation Ireland Principle Investigator Award Number 15/IA/3015 DEPO-Man, ‘Design, Deposition and Exploitation of Novel Micro and Nano-scale Materials and Devices for Advanced Manufacturing’ and the support of the Royal Society and Science Foundation Ireland (SFI) University Fellowship UF 140263.

5.7. References

[1] L. Keeney *et al.*, "Magnetic Field-Induced Ferroelectric Switching in Multiferroic Aurivillius Phase Thin Films at Room Temperature," *Journal of the American Ceramic Society,* vol. 96, no. 8, pp. 2339-2357, 2013/08/01 2013, doi: 10.1111/jace.12467.

[2] A. Faraz *et al.*, "Direct visualization of magnetic-field-induced magnetoelectric switching in multiferroic aurivillius phase thin films," *Journal of the American Ceramic Society,* vol. 100, no. 3, pp. 975-987, 2017, doi: 10.1111/jace.14597.

[3] L. Keeney, C. Downing, M. Schmidt, M. E. Pemble, V. Nicolosi, and R. W. Whatmore, "Direct atomic scale determination of magnetic ion partition in a room temperature multiferroic material," *Sci Rep,* vol. 7, no. 1, p. 1737, May 11 2017, doi: 10.1038/s41598-017-01902-1.

[4] U. Weber *et al.*, "AVD® technology for deposition of next generation devices," *Microelectronics Reliability,* vol. 45, no. 5-6, pp. 945-948, 2005, doi: 10.1016/j.microrel.2004.11.019.

[5] N. Deepak, P. F. Zhang, L. Keeney, M. E. Pemble, and R. W. Whatmore, "Atomic vapor deposition of bismuth titanate thin films," *Journal of Applied Physics,* vol. 113, no. 18, p. 187207, 2013.

[6] N. Deepak, P. Carolan, L. Keeney, M. E. Pemble, and R. W. Whatmore, "Tunable nanoscale structural disorder in Aurivillius phase, n= 3 Bi 4 Ti 3 O 12 thin films and their role in the transformation to n= 4, Bi 5 Ti 3 FeO 15 phase," *Journal of Materials Chemistry C,* vol. 3, no. 22, pp. 5727-5732, 2015.

[7] K. Momma and F. Izumi, "VESTA 3 for three-dimensional visualization of crystal, volumetric and morphology data," *Journal of applied crystallography,* vol. 44, no. 6, pp. 1272-1276, 2011.

[8] X. Liu, L. Xu, Y. Huang, C. Qin, L. Qin, and H. J. Seo, "Improved photochemical properties of Aurivillius Bi 5 Ti 3 FeO 15 with partial substitution of Ti 4+ with Fe 3+," *Ceramics International,* vol. 43, no. 15, pp. 12372-12380, 2017, doi: 10.1016/j.ceramint.2017.06.103.

[9] M. García-Guaderrama, L. Fuentes-Montero, A. Rodriguez, and L. Fuentes, "Structural characterization of Bi6Ti3Fe2O18 obtained by molten salt synthesis," *Integrated ferroelectrics,* vol. 83, no. 1, pp. 41-47, 2006.

[10] C. H. Hervoches and P. Lightfoot, "A Variable-Temperature Powder Neutron Diffraction Study of Ferroelectric Bi4Ti3O12," *Chemistry of Materials,* vol. 11, no. 11, pp. 3359-3364, 1999/11/01 1999, doi: 10.1021/cm991090d.

[11] B. J. Rodriguez, C. Callahan, S. V. Kalinin, and R. Proksch, "Dual-frequency resonance-tracking atomic force microscopy," *Nanotechnology,* vol. 18, no. 47, p. 475504, 2007, doi: 10.1088/0957-4484/18/47/475504.

[12] L. Keeney *et al.*, "Ferroelectric Behavior in Exfoliated 2D Aurivillius Oxide Flakes of Sub-Unit Cell Thickness," *Advanced Electronic Materials,* vol. n/a, no. n/a, p. 1901264, 2020/01/30 2020, doi: 10.1002/aelm.201901264.

[13] C. F. Holder and R. E. Schaak, "Tutorial on Powder X-ray Diffraction for Characterizing Nanoscale Materials," *ACS Nano,* vol. 13, no. 7, pp. 7359-7365, 2019/07/23 2019, doi: 10.1021/acsnano.9b05157.

[14] M. Zurbuchen *et al.*, *Morphology, structure, and nucleation of out-of-phase boundaries (OPBs) in epitaxial films of layered oxides*. 2007, pp. 1439-1471.

[15] Y. Ding, J. S. Liu, J. S. Zhu, and Y. N. Wang, "Stacking faults and their effects on ferroelectric properties in strontium bismuth tantalate," *Journal of Applied Physics,* vol. 91, no. 4, pp. 2255-2261, 2002, doi: 10.1063/1.1431428.

[16] R. A. Armstrong and R. E. Newnham, "Bismuth titanate solid solutions," *Materials Research Bulletin,* vol. 7, no. 10, pp. 1025-1034, 1972/10/01/ 1972, doi: https://doi.org/10.1016/0025-5408(72)90154-7.

[17] R. Shannon, "Revised effective ionic radii and systematic studies of interatomic distances in halides and chalcogenides," *Acta Crystallographica Section A,* vol. 32, no. 5, pp. 751-767, 1976, doi: doi:10.1107/S0567739476001551.

[18] E. Gradauskaite *et al.*, "Robust In-Plane Ferroelectricity in Ultrathin Epitaxial Aurivillius Films," *Advanced Materials Interfaces,* vol. 7, no. 14, p. 2000202, 2020.

[19] S. Bedanta and W. Kleemann, "Supermagnetism," *Journal of Physics D: Applied Physics,* vol. 42, no. 1, p. 013001, 2008.

[20] C. Binns, *Nanomagnetism: fundamentals and applications*. Newnes, 2014.

[21] A. Y. Birenbaum, A. Scaramucci, and C. Ederer, "Magnetic order in four-layered Aurivillus phases," *Physical Review B,* vol. 95, no. 10, 2017, doi: 10.1103/PhysRevB.95.104419.

[22] Ł. Kurzawski and K. Malarz, "Simple Cubic Random-Site Percolation Thresholds for Complex Neighbourhoods," *Reports on Mathematical Physics,* vol. 70, no. 2, pp. 163-169, 2012/10/01/ 2012, doi: https://doi.org/10.1016/S0034-4877(12)60036-6.

[23] J. B. Goodenough, "Theory of the role of covalence in the perovskite-type manganites [La, M (II)] Mn O 3," *Physical Review,* vol. 100, no. 2, p. 564, 1955.

[24] A. Bencan, G. Drazic, H. Ursic, M. Makarovic, M. Komelj, and T. Rojac, "Domain-wall pinning and defect ordering in BiFeO3 probed on the atomic and nanoscale," *Nature Communications,* vol. 11, no. 1, p. 1762, 2020/04/09 2020, doi: 10.1038/s41467-020-15595-0.

[25] T. Rojac *et al.*, "Domain-wall conduction in ferroelectric BiFeO3 controlled by accumulation of charged defects," (in English), *Nature Materials,* vol. 16, no. 3, pp. 322-327, 2017, doi: http://dx.doi.org/10.1038/nmat4799.

[26] X. Y. Mao, W. Wang, and X. B. Chen, "Electrical and magnetic properties of Bi5FeTi3O15 compound prepared by inserting BiFeO3 into Bi4Ti3O12," *Solid State Communications,* vol. 147, no. 5, pp. 186-189, 2008/08/01/ 2008, doi: https://doi.org/10.1016/j.ssc.2008.05.025.

[27] W. Bai *et al.*, "Electrical, magnetic, and optical properties in multiferroic Bi5Ti3FeO15 thin films prepared by a chemical solution deposition route,"

Journal of Applied Physics, vol. 109, no. 6, p. 064901, 2011, doi: 10.1063/1.3553879.

[28] P. G. de Gennes, "Effects of Double Exchange in Magnetic Crystals," *Physical Review,* vol. 118, no. 1, pp. 141-154, 04/01/ 1960, doi: 10.1103/PhysRev.118.141.

[29] G. Catalan and J. F. Scott, "Physics and Applications of Bismuth Ferrite," *Advanced Materials,* vol. 21, no. 24, pp. 2463-2485, 2009/06/26 2009, doi: 10.1002/adma.200802849.

[30] A. Y. Birenbaum and C. Ederer, "Potentially multiferroic Aurivillius phaseBi5FeTi3O15: Cation site preference, electric polarization, and magnetic coupling from first principles," *Physical Review B,* vol. 90, no. 21, 2014, doi: 10.1103/PhysRevB.90.214109.

[31] M. Schmidt *et al.*, "Absence of Evidence ≠ Evidence of Absence: Statistical Analysis of Inclusions in Multiferroic Thin Films," *Scientific Reports,* vol. 4, no. 1, p. 5712, 2014/07/16 2014, doi: 10.1038/srep05712.

[32] A. Faraz *et al.*, "Exploring ferroelectric and magnetic properties of Tb-substituted m = 5 layered Aurivillius phase thin films," *Journal of Applied Physics,* vol. 123, no. 12, p. 124101, 2018/03/28 2018, doi: 10.1063/1.5009986.

[33] N. A. Lomanova, M. I. Morozov, V. L. Ugolkov, and V. V. Gusarov, "Properties of aurivillius phases in the Bi4Ti3O12-BiFeO3 system," *Inorganic Materials,* vol. 42, no. 2, pp. 189-195, 2006, doi: 10.1134/s0020168506020142.

[34] M. Campanini, M. Trassin, C. Ederer, R. Erni, and M. D. Rossell, "Buried in-plane ferroelectric domains in Fe-doped single-crystalline Aurivillius thin films," *ACS Applied Electronic Materials,* vol. 1, no. 6, pp. 1019-1028, 2019.

[35] D. Batuk *et al.*, "Bi3n O9n Homologous Series: Slicing Perovskite Structure with Planar Interfaces Containing Anatase-like Chains."

[36] D. Batuk *et al.*, "Crystal Structure, Defects, Magnetic and Dielectric Properties of the Layered Bi3 n+ 1Ti7Fe3 n–3O9 n+ 11 Perovskite-Anatase Intergrowths," *Inorganic chemistry,* vol. 56, no. 2, pp. 931-942, 2017.

[37] T. Kikuchi, "Stability of layered bismuth compounds in relation to the structural mismatch," *Materials Research Bulletin,* vol. 14, no. 12, pp. 1561-1569, 1979.

Chapter 6

6. Effect of deposition temperature on sequential direct liquid injection chemical vapour deposition (DLI-CVD) of Aurivillius phase materials

6.1. Abstract

A sequential direct liquid injection chemical vapour deposition method was used to deposit a series of Aurivillius phase thin films on epitaxially-matched substrates LSAT and STO. The effect of deposition temperature on the materials was examined. Crystalline Aurivillius phase films were deposited as epitaxial thin films at 710 °C, 690 °C, 670 °C, 650 °C, 630 °C and 610 °C. The crystalline quality was examined by rocking curve XRD analysis. The FWHM of the films deposited at 710 °C were narrower than those deposited at 610 °C, indicating an improved crystallinity at higher deposition temperatures. AFM analysis of the surface morphology indicated the presence of some secondary phases within samples deposited on LSAT substrates but not on the corresponding materials on STO. A further modification of the sequential DLI-CVD recipe consisting of a continuous injection of bismuth precursor accommodating each precursor injection was employed. In this way the cations, titanium, iron and manganese, could be introduced in sequential order to concentrate the magnetic ions to the inner perovskite units without a local deficiency of bismuth. XRD analysis of these materials found that they had narrower FWHM indicating the this method may produce films with fewer dislocations.

6.2. Introduction

Direct liquid injection chemical vapour deposition (DLI-CVD) involves the introduction of pulses of precursor solution with a carrier gas which can either be reactive or inert, which flows over the substrate in the reaction chamber. In previous work from our laboratories [7], the concurrent DLI-CVD method used to synthesise *m* = 5 B6TFMO Aurivillius samples did not deliberately impose layer-by-layer ordering of the material during the deposition process. In Chapter 5, the DLI-CVD method has

been modified to separate the precursor pulses in time, so as to directly mimic the layered structure of the Aurivillius phase and to intentionally place Ti^{4+} cations towards the outer layers and place Fe^{3+} and Mn^{3+} towards the central layers [1]. The method of separating the precursor pulses in time was first proposed by Weber *et al.* [2] and has been used to fabricate HfO_2 [3] and metal-insulator-metal capacitors [4, 5]. Previous work by Deepak *et al*. has used this sequential method to deposit *m* = 3 $Bi_4Ti_3O_{12}$ [1] and $Bi_4Ti_{2.5}Fe_{0.5}O_{12}$ [6] Aurivillius material. By utilising this sequential DLI-CVD method, it was hoped to further direct the location of the magnetic ions towards the inner perovskite blocks to enhance long-range magnetic interactions.

Bismuth volatility is an issue for these materials and deposition at lower temperatures may prevent the loss of bismuth. The diffusion of bismuth through a layered structure often results in crystallographic shear, the formation of out of phase boundary defects and associated secondary phases [7]. There is enhanced bismuth diffusion above 710 °C [8] and recent studies have shown that reducing the deposition temperatures to 710 °C and 700 °C successfully reduced the formation of unwanted secondary phases [9]. Within the present chapter, we examine the effect of deposition temperature on the structural properties of Aurivillius phase thin films formed utilising this sequential method.

The thin films were deposited on epitaxially-matched substrates LSAT and STO and the effects of tensile strain on the physical structure are also investigated. The sequential DLI-CVD recipe was further modified to include a bismuth injection at each step of the deposition recipe (called continuous Bi sequential DLI-CVD). This method was explored as a means to prevent a local deficiency of bismuth during the growth process while also controlling the order of injection of the *B*-site cations.

6.3. Experimental

The BTFMO Aurivillius phase materials were deposited using an Aixtron AIX 200 4/FE AVD system. The precursors were $Bi(thd)_3$, $Ti(O\text{-}iPr)_2(thd)_3$, $Fe(thd)_3$ where thd = 2,2,6,6-tetramethyl-3,5-heptanedionate and O-iPr = iso-propoxide as 0.1 M solutions

in toluene. $Mn(thd)_3$ was prepared as a 0.025 M solution in toluene. The carrier gas was $N_{2(g)}$ and the oxygen source was $O_{2(g)}$. The liquid precursor solutions were vapourised before being introduced into the reaction chamber using the Trijet™ system that forms part of the Aixtron AVD kit. The ratio of precursors used was controlled by varying the opening times and monitoring the flow of precursor solution using flow meters. The single-crystal substrates were placed on a susceptor contained in a quartz reaction chamber which was heated using IR lamps. The reaction chamber was pumped down to ≈ 10 mbar during the deposition process. The substrates used were LSAT ($La_{0.26}Sr_{0.76}Al_{0.61}Ta_{0.37}O_3$ [100]), STO ($SrTiO_3$, [100]) and c-plane sapphire. LSAT and STO were supplied by Crystal GmbH and sapphire by University Wafer. The deposition temperature ranged from 610 °C to 710 °C. The sequential DLI-CVD growth recipe involved 10 pulses of the precursor followed by a 10 second pulse gap before the next injection of precursor. One loop mimicking one half unit cell of the *m* = 5 Aurivillius phase is depicted in figure 1. The loop was repeated 20 times with an additional two injections of Bi precursor at the end to complete the structure. In section 6.4.1 the results of the temperature series deposited using the recipe in figure 1(b) and in section 6.4.2 the results of recipe figure 1(c) are presented.

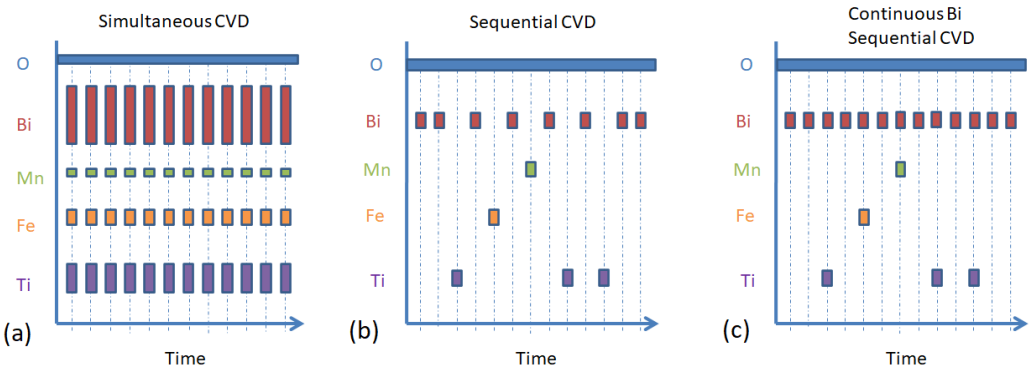

Figure 1: Images depicting the different growth methods, (a) conventional simultaneous DLI-CVD, (b), sequential DLI-CVD and (c) sequential DLI-CVD recipe with additional continuous bismuth flow accompanying each precursor injection.

X-ray diffraction (XRD) analysis was performed using a Panalytical X'pert MRD diffractometer. Parameters included: voltage 45 kV and current 40 mA, scan range between 5 to 40° 2θ, step size 0.001 °/s, Cu Kα radiation λ = 0.1541874 nm. The materials were indexed from a reflection table generated using the VESTA software [10] and the data for the *m* = 4 Aurivillius phase was obtained from Liu *et al*. [11], *m* = 3 from Hervoches and Lightfoot [12] and *m* = 5 from García-Guaderrama *et al*. [13]. Additional XRD was carried out using a Rigaku Smartlab with a 16 kW Cu rotating anode, a 2-bounce Ge monochromator and a Hypix detector. Out-of-plane scans (standard symmetric $\theta/2\theta$ configuration) and rocking curves (varying ω at a fixed 2θ angle) were performed to assess the phase purity and crystalline quality of the samples.

Atomic force microscopy (AFM) was performed using an Asylum Research MFP-3D™ in AC mode with Olympus probes AC240TS (Al reflex coated, 15 nm tip radius, 70 kHz resonant frequency). Additional AFM analysis was performed using a Bruker Dimension Icon instrument in PeakForce tapping mode. Scan rate = 1 Hz and scan angle = 0 °. The AFM probes used were Bruker SCANASYST-AIR probe, Al reflex coated, 2 nm tip radius, 70 kHz resonant frequency.

Piezoresponse force microscopy (PFM) measurements were performed using an Asylum research MFP-3D AFM instrument. The method known as Dual AC resonance tracking PFM (DART-PFM) [14] was used to reduce topographical crosstalk. This was achieved through a feedback system adjusting the drive frequency in response to changes in the amplitude. The probes used were Olympus AC240TM electrilevers (Ti/Pt coated silicon probes, Al reflex coated, 15 nm tip radius, 70 kHz resonant frequency)). Scan rate = 1 Hz and scan angle = 90 °.

Scanning transmission electron microscopy (STEM) analysis was carried out using a Thermo-Fisher Scientific double tilt STEM holder in the Thermo-Fisher Scientific FEI double aberration-corrected monochromated Titan Themis Z at the University of Limerick. The microscope was operated at 300 kV. The imaging mode used was STEM at 146 mm camera length with a 50-µm C2 aperture.

6.4. Results and discussion

6.4.1. Investigations of sequential DLI-CVD over a temperature series

6.4.1.1. XRD analysis

A series of BTFMO samples were deposited at 710 °C, 690 °C, 670 °C, 650 °C, 630 °C and 610 °C on LSAT, STO and sapphire substrates. The deposition process used was a sequential direct liquid injection chemical vapour deposition (DLI-CVD) method that mimicked the *m* = 5 Aurivillius phase material. As discussed in chapter 5, although the recipe mimicked the *m* = 5 phase, the XRD analysis of these materials indexed most closely to the *m* = 4 phase. The XRD analysis of the growth on the LSAT and STO substrates is shown in figure 2 and sapphire in figure S1. The peak reflections of the material deposited on LSAT and STO indexed most closely to the *m* = 4 Aurivillius phase material ($A2_1am$ orthorhombic space group). The calculated nominal stoichiometry of the thin films is presented in Table 1, assuming Bi_5 for an *m* = 4 structure. The nominal stoichiometry is calculated using the ratio of precursors used during the growth process. However, while the materials have been indexed using the *m* = 4 Aurivillius phase as a reference, there is significant peak broadening (table 2) and shift (table 3) from the reference pattern. This indicates the presence of intergrowths of different '*m*' Aurivillius phases such as *m* = 3 or *m* = 5. The formation of these different phases may be in response to the requirement to maintain a balanced charge based on the precursor flow ratios utilised. For instance, with a nominal composition of $Bi_5Ti_{3.16}Fe_{0.68}Mn_{0.16}O_{15}$ and assuming oxidation states of +4, +3 and +3 for Ti, Fe and Mn respectively, this would yield a positive charge of +0.16. On the other hand, for the nominal composition of $Bi_5Ti_{2.6}Fe_{1.23}Mn_{0.17}O_{15}$, this would yield a negative charge of -0.40. Since there should be no net charge on the Aurivillius phase structures, there needs to be a mechanism to compensate for this. One possible compensation mechanism is that the oxidation states can vary, for example, there may be a variable oxidation state for manganese, as was discussed in chapter 4. However, the concentration of Mn in these materials is relatively low and, as seen in table 1, even if all of the Mn was to exist in a +2 or +4 oxidation state it would still

be insufficient on its own to accommodate the unbalanced stoichiometry for many of the materials. This is represented in the table as > Mn^{4+}. A second compensation mechanism that the Aurivillius structures could utilise to respond to charge imbalance is by forming intergrowths of different '*m*' phases. For instance, if the *m* = 4 $Bi_5Ti_{2.6}Fe_{1.23}Mn_{0.17}O_{15}$ structure with a negative charge of -0.40 were to reorganise to an *m* = 5 structure, $Bi_6Ti_{3.25}Fe_{1.54}Mn_{0.21}O_{18}$, the overall charge would be positive +0.25. By accommodating layering between discrete regions of *m* = 5 intergrowths within the *m* = 4 matrix, charge balance could be allowed for. The presence of out of phase boundary (OPB) defects is common in layered Aurivillius phases [15] and OPB defects can occur at the meeting point of two different '*m*' phases. Associated cation (*A*-site or *B*-site ions) or possible anion vacancies (e.g. oxygen anions) at the OPB regions is a third compensation mechanism postulated that would accommodate overall charge balance within the films. These OPB defects would also contribute to the broad peaks observed in the XRD plots. TEM analysis confirms the presence of OPB defects in the 710 °C STO (figure 10) material which is discussed in more detail later.

The thin films deposited on the LSAT and STO substrates clearly show the reflections characteristic of crystalline Aurivillius material. The reflections for the film on the sapphire substrate (figure S1) are consistent with a pyrochlore $Bi_2Ti_2O_7$ which has the reflections 14.6 ° (222) and 29.6 ° (444) (JCPDF 32-0118). This is to be expected at these temperatures as usually a post anneal is required for the crystalline Aurivillius materials to form on sapphire [9, 16]. The LSAT and STO substrates have an epitaxial relationship with the Aurivillius material, whereas the mismatch between the Aurivillius material and the sapphire substrates is much larger. Growth on an epitaxial substrate lowers the energy needed to form the highly ordered Aurivillius structure [15]. To demonstrate this, the pseudo lattice parameter of $Bi_5Ti_{2.5}Fe_1Mn_{0.5}O_{15}$ was calculated as 3.85 Å using the method in [17]. For LSAT a_p = 3.868 Å (+ 0.47 % lattice mismatch) and for STO a_p = 3.905 Å (+ 1.43 % lattice mismatch) (figure 4). However, for sapphire substrates the lattice constant a_p = 4.78 Å which represents a + 19.46 % lattice mismatch.

The excess of bismuth present during the growth run is presented in table 1 also. In previous work by Deepak *et al*., between 68 to 110 % excess bismuth precursor was found to be necessary to produce single phase Aurivillius materials [6]. A large excess of bismuth was a precaution taken due to its volatility during growth. Therefore, the overall formation of the *m* = 4 phase and not the intended *m* = 5 phase in this work may be attributed to an insufficient bismuth excess during the growth process, as well as the requirement for intergrowths of differing '*m*' phases to maintain overall charge balance based on the precursor ratios utilised.

Table 1: Details of nominal sample stoichiometry and bismuth excess.

Sample	*m* = 4	Bi/Ti	%Bi excess	Mn o/s
BTFMO 710°C	$Bi_5Ti_{3.16}Fe_{0.68}Mn_{0.16}O_{15}$	2.09	32%	Mn^{2+}
BTFMO 690°C	$Bi_5Ti_{3.12}Fe_{0.71}Mn_{0.17}O_{15}$	2.08	30%	$Mn^{2.29+}$
BTFMO 670°C	$Bi_5Ti_{2.73}Fe_{1.11}Mn_{0.16}O_{15}$	1.98	8%	> Mn^{4+}
BTFMO 650°C	$Bi_5Ti_{2.71}Fe_{1.12}Mn_{0.17}O_{15}$	1.96	6%	>Mn^{4+}
BTFMO 630°C	$Bi_5Ti_{2.56}Fe_{1.28}Mn_{0.16}O_{15}$	2.15	10%	>Mn^{4+}
BTFMO 610°C	$Bi_5Ti_{2.6}Fe_{1.23}Mn_{0.17}O_{15}$	1.92	0%	>Mn^{4+}

The additional peaks around the (00<u>1</u>0) peak in the STO 610 °C, 630 °C and 650 °C samples indicates superlattice reflections due to a periodic alternating of differing '*m*' phases. The full width half maxima of selected peaks of the material on LSAT are shown in table 2. There is no clear trend in terms of increase/decreasing FWHM through the temperature series. The crystalline quality of the materials may be affected by the variations in stoichiometry as well as the different deposition temperatures used.

In table 3, the peak shift relative to the reference pattern is presented. The (008), (00<u>1</u>6) and (00<u>1</u>8) peaks move from lower to higher 2θ values while the (00<u>1</u>2) shifts from higher to lower 2θ values as the deposition temperature decreases. The crystalline quality of the materials may be affected by the changing stoichiometry as

well as the different deposition temperatures used. Due to run-to-run variability, it is noted that the ratio of Ti to Fe and Mn is generally lower as the temperature series progresses. As a result, there will be differing levels of requirement to compensate for charge balance across the series. Therefore, due to this additional variable it is not possible to attribute the observed peak shift solely to the decrease in deposition temperature.

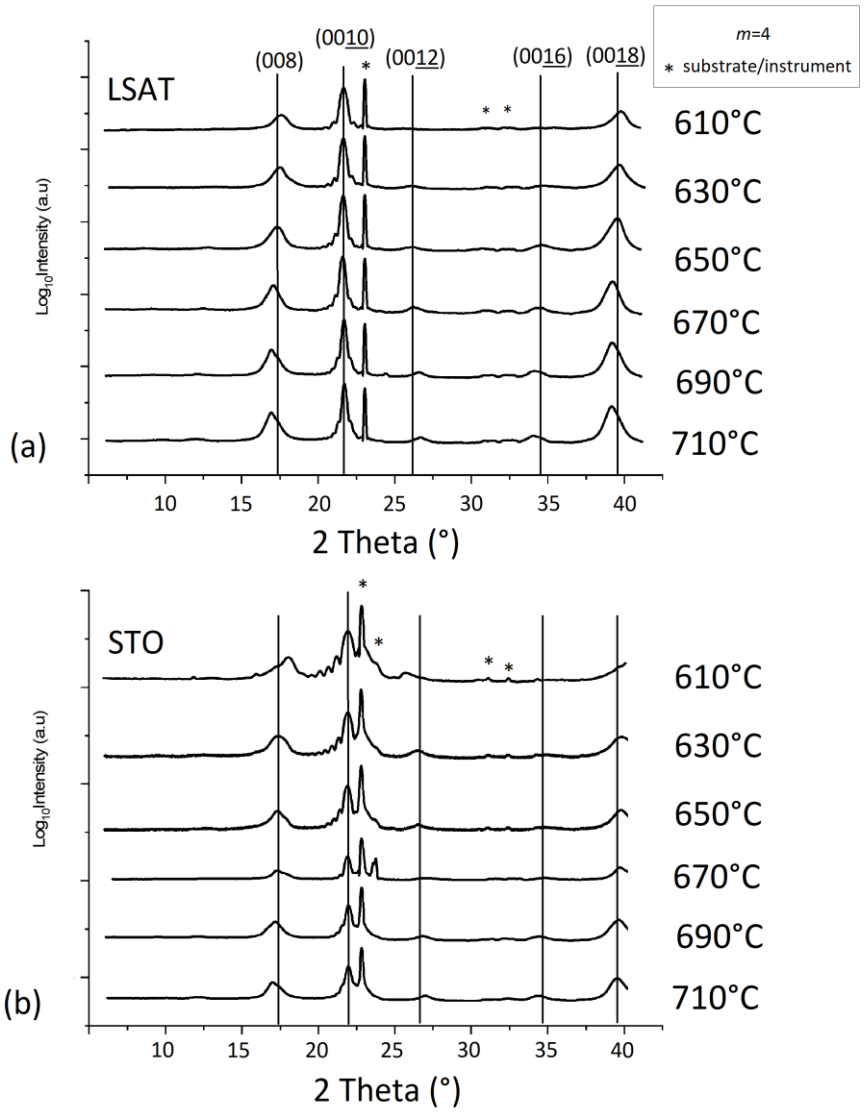

Figure 2: XRD patterns of BTFMO on (a) LSAT and (b) STO as a function of substrate temperature during growth.

Table 2: FWHM of selected peaks of the BTFMO films on LSAT substrates

Peak	710 °C	690 °C	650 °C	610 °C
(008)	0.996 ± 0.053	1.016 ± 0.041	1.108 ± 0.006	0.997 ± 0.037
(00$\underline{12}$)	0.812 ± 0.036	0.725 ± 0.055	1.208 ± 0.027	1.113 ± 0.150
(00$\underline{16}$)	1.163 ± 0.044	1.080 ± 0.017	1.512 ± 0.044	0.941 ± 0.258
(00$\underline{18}$)	1.204 ± 0.027	1.190 ± 0.036	1.214 ± 0.008	1.051 ± 0.020

Table 3: Shift in peak position from the reference pattern of the BTFMO films on LSAT substrates

Peak	710 °C	690 °C	650 °C	610 °C
(008)	-0.253 ° ± 0.068 °	-0.244 ° ± 0.002 °	+0.021 ° ± 0.001 °	+0.304 ° ± 0.001 °
(00$\underline{12}$)	+0.664 ° ± 0.130 °	+0.554 ° ± 0.057 °	+0.060 ° ± 0.004 °	-0.441 ° ± 0.007 °
(00$\underline{16}$)	-0.768 ° ± 0.033 °	-0.699 ° ± 0.035 °	-0.251 ° ± 0.003 °	+0.555 ° ± 0.154 °
(00$\underline{18}$)	-0.224 ° ± 0.006 °	-0.202 ° ± 0.011 °	-0.067 ° ± 0.001 °	+0.261 ° ± 0.001 °

In figure 3, the XRD reflections around the 2θ angle of 17 ° are presented and the peak shift is clearly seen away from the (008) reflection of the *m* = 4 structure. The films with a high Ti to Fe / Mn ratio shift towards the *m* = 3 (006) reflection and those with a low Ti to Fe / Mn ratio shift towards the higher *m* = 5 (00$\underline{10}$) reflection. Individual contributions from the *m* = 3, *m* = 4 and *m* = 5 phases could not be resolved due to similar peak positions for the respective (006), (008) and (00$\underline{10}$) reflections and given the relatively broad nature of the peak.

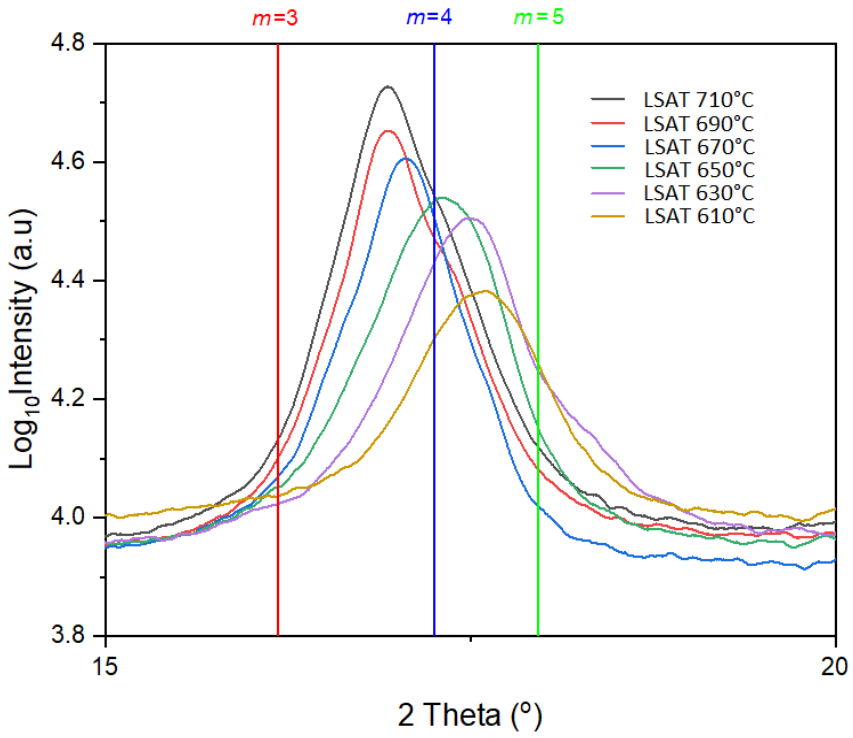

Figure 3: Zoomed-in XRD pattern of the temperature series for B6TFMO on LSAT. The peak shift of the (008) reflection *m* = 3 (006), *m* = 4 (008) and *m* = 5 (00<u>10</u>).

All the XRD peaks for the films deposited on LSAT and STO substrates corresponded to (00*l*) reflections. Therefore, the Lotgering factor for all of these materials was *f* = 1 [18]. As all of the reflections were (00*l*) only the *c*-axis pseudo lattice parameter could be determined using the following relationship between *d* spacing and lattice parameters (6.1),

$$\frac{1}{d^2} = \frac{h^2}{a^2} + \frac{k^2}{b^2} + \frac{l^2}{c^2} \qquad (6.1)$$

The calculated *c*-axis parameter is shown in figure 4. An average value for the (008), (00<u>10</u>), (00<u>12</u>), (00<u>16</u>) and (00<u>18</u>) reflections was used and the error is the standard deviation between the calculated values. There is a relatively large margin of error on these values except interestingly for the 650 °C LSAT and 670 °C STO film (figure 4). The calculated *c*-axis pseudo lattice parameter for the 650 °C film on LSAT is 41.1 Å and that for the STO 670 °C sample is 40.8 Å. The XRD pattern of these materials match closely to the reference *m* = 4 Aurivillius phase pattern. The presence of

different '*m*' phases causes some peaks to shift to higher 2θ values and others to lower 2θ values, thus leads to a large error in the calculated values. The significant error associated with the calculated values prevents an overall trend over the temperature series to be determined. Also, the crystal size broadening effect can contribute to the broadness of the peaks obtained for these materials as the films are quite thin (17-31 nm) [19].

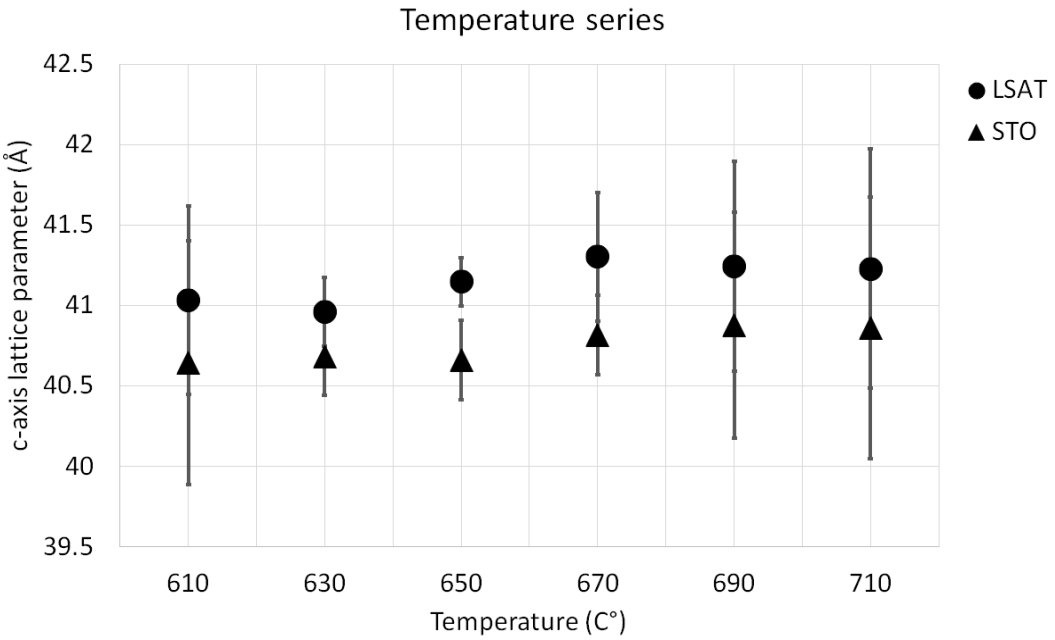

Figure 4: Calculation of the *c*-axis pseudo lattice parameter for BTFMO growth on LSAT and STO as a function of growth temperature.

The theoretical pseudo lattice parameters of the Aurivillius phase thin films were calculated using the stoichiometry given in table 1. The calculation of the pseudo-tetragonal lattice parameter were performed using the following values Bi^{3+} (1.11 Å), Ti^{4+} (0.605 Å), Fe^{3+} (0.645 Å) and Mn^{3+} (0.645 Å) [20]. It was assumed that all Mn was in the 3+ oxidation state. The error bars represent the change in the calculated values when Mn is present in the 2+ or 4+ oxidation state, Mn^{2+} (0.83 Å) and Mn^{4+} (0.53 Å) [20]. As shown in figure 5, the LSAT and STO substrate apply tensile strain to the Aurivillius materials.

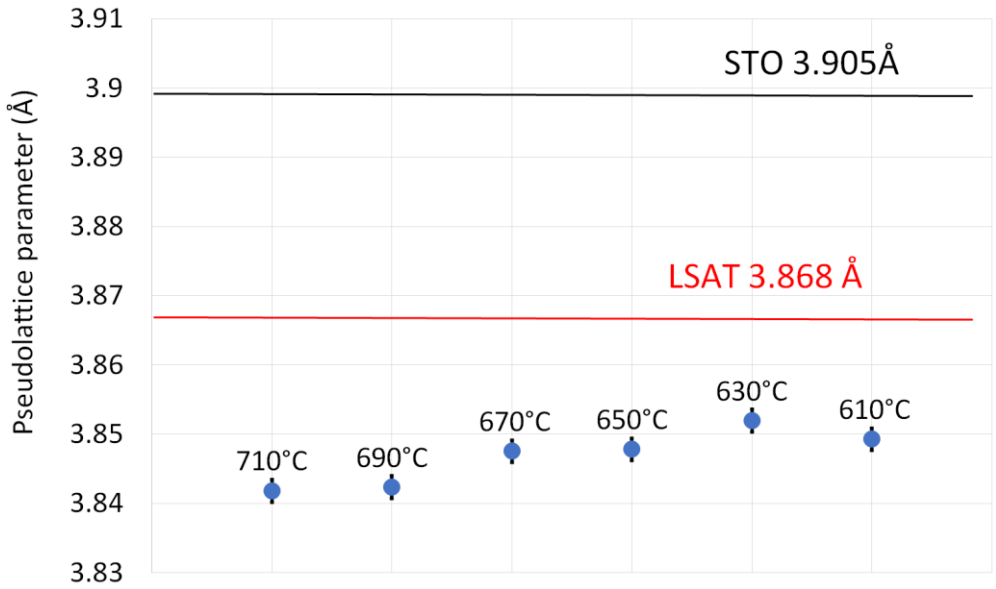

Figure 5: Theoretical pseudo lattice parameters, a_p, of the BTFMO samples, calculated from the stoichiometry of the materials.

The tensile strain applied by the substrates explains the observed shift in the XRD pattern of the films on different substrates in figure 6. The LSAT and STO substrates applies tensile strain which lengthen the *a*/*b*-axis and to maintain the total volume of the crystal lattice, the *c*-axis elongates to compensate. The STO substrate (+ 1.43 % lattice mismatch) applies a greater strain on the Aurivillius material compared with the LSAT substrate (+ 0.47 % lattice mismatch). This is observed in the XRD as the peak positions of the STO materials are consistently shifted higher than the peaks of the Aurivillius materials on LSAT. This is reflected in the calculated *c*-axis parameters for the films in figure 4 where the films on LSAT are consistently higher than for films on the STO substrates.

The *c*-axis pseudo lattice parameters were calculated from the large angle out-of-plane scans (standard symmetric $\theta/2\theta$ configuration) XRD data (figure 6) and are presented in figure S2. The *c*-axis pseudo lattice parameters for materials deposited on LSAT are larger than those for the materials on STO. Note however that the

difference between the 710 °C and 610 °C on the same substrate was not greater than the error associated with the calculation.

In the out-of-plane XRD scans shown in figure 6 it can be seen that the signal to noise ratio of the peaks is higher for the 710 °C samples compared with the 610 °C samples and so more peaks are observed for the materials deposited at 710 °C. This may be attributed to the improved crystalline quality and increased grain size of the 710 °C films but also as seen in TEM analysis (figures 11 and 12), the 710 °C STO film is thicker (≈ 30 nm) than the 610 °C STO film (≈ 17 nm). Again the reflections consist of the (00*l*) reflections and show the film is highly orientated.

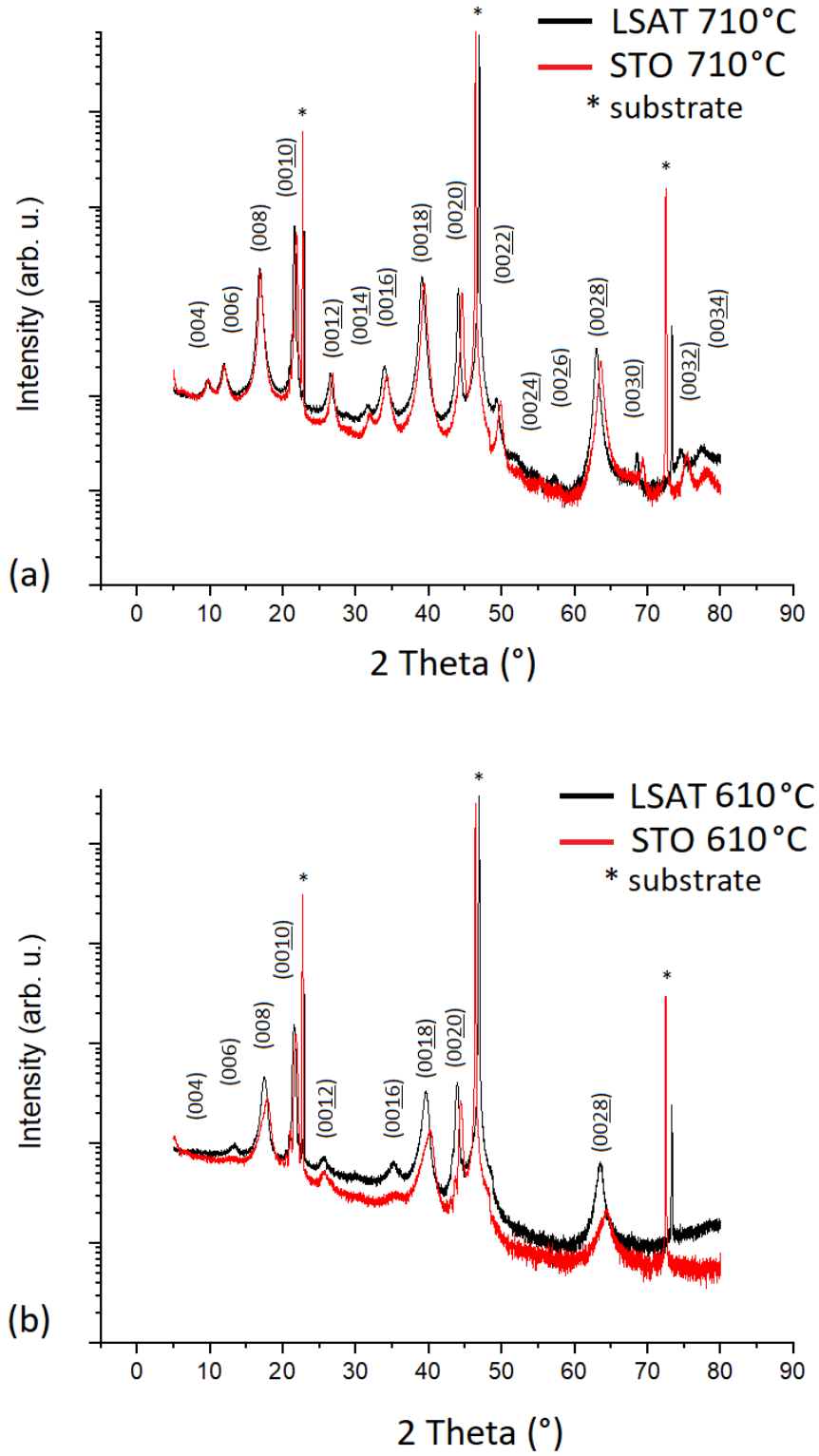

Figure 6: Large angle XRD of BTFMO on (a) LSAT and STO deposited at 710 °C and (b) LSAT and STO deposited at 610 °C.

Measurements of the rocking curve of the Bragg reflections were performed to assess the crystal quality of the films (figure 7). The rocking curves were fitted with a pseudo-Voigt function and the FWHM of the Gaussian (w_G) and Lorentzian (w_L) terms are presented in table 4. The rocking curves are similar for the films on both the LSAT and STO substrates with a broad Lorentzian base and a narrow Gaussian component which indicates the presence of dislocations in the thin films. This is consistent with XRD analysis indicating mixed Aurivillius phases and TEM (figure 11) of the STO 710 °C clearly showing that intergrowths of m = 4 and m = 3 phases are present. The 710 °C deposited films on STO have a larger w_G and smaller w_L than their corresponding films on LSAT. The larger FWHM for the films deposited at 610 °C may indicate that more dislocations are present in the 610 °C films. While it would be expected that higher temperatures would produce better crystalline films, the different chemical composition should also be considered when comparing the 710 °C samples to the 610 °C samples. The w_G FWHM for the LSAT samples deposited at 710 °C is narrower than the STO, due to the compressive strain applied, as observed in previous studies [9].

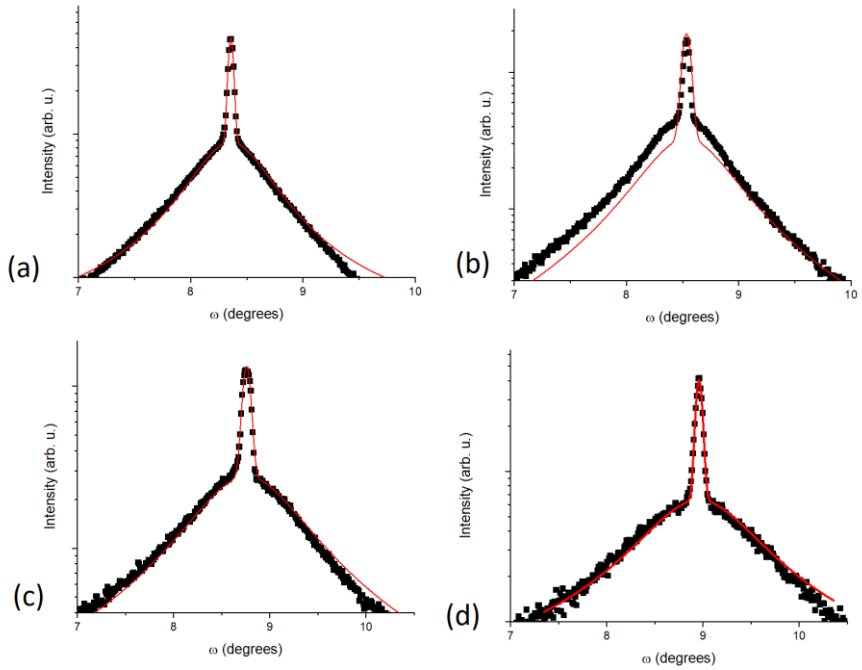

Figure 7: Rocking curve analysis of BTFMO on (a), LSAT 710 °C, (b), STO 710 °C, (c), LSAT 610 °C and (d), STO 610 °C.

Table 4: Comparison of FWHM of the Gaussian (w_G) and Lorentzian (w_L) fits of rocking curves

	LSAT 710 °C	STO 710 °C	LSAT 610 °C	STO 610 °C
w_G	0.053 ± 0.0005	0.070 ± 0.010	0.095 ± 0.001	0.077 ± 0.0006
w_L	0.752 ± 0.013	0.592 ± 0.099	1.213 ± 0.085	1.255 ± 0.038

6.4.1.2. AFM analysis

AFM analysis performed using the Bruker AFM instrument is shown in figures 8 and 9. The narrow radius of the probe tip allows for detailed images to be obtained with resolution as low as 2 nm. In figure 8 the 710 °C, 650 °C and 610 °C samples on LSAT and STO are shown. It should be noted that figure 8 (d) and (f) were imaged after a 10 second gold coat had been applied (to enable previous SEM experiments). This corresponds to a gold coat with a thickness 3-6 nm and as these materials are relatively smooth (RMS roughness ≈ 1 nm) this coat obscures the fine detail of the surface topography.

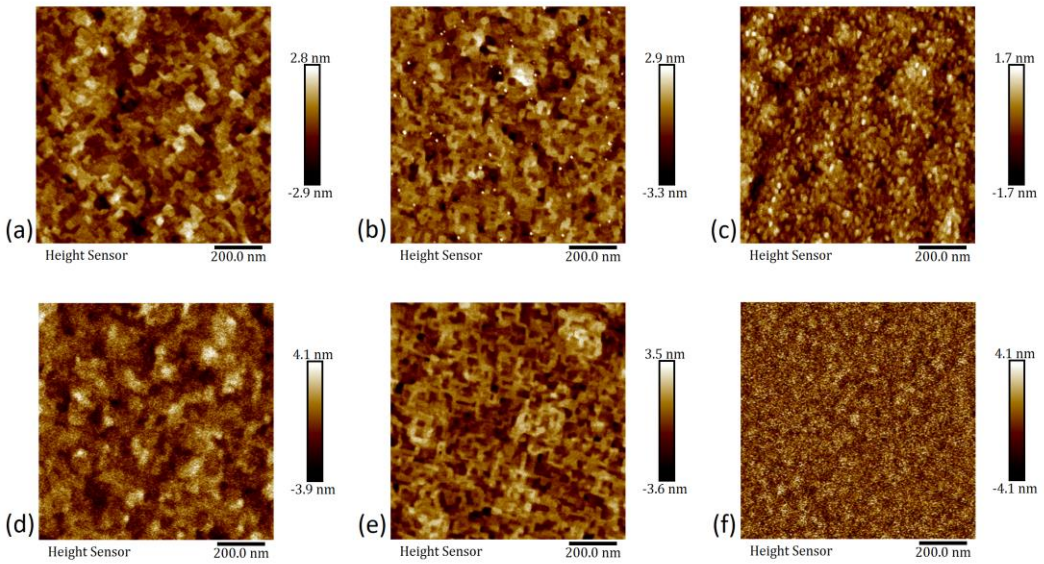

Figure 8: BTFMO films on LSAT (a) 710 °C, (b) 650 °C, (c) 610 °C and STO (d) 710 °C, (e) 650 °C, (f) 610 °C. The BTFMO films on STO 710 °C and STO 610 °C had a 10 s gold coat applied before the AFM analysis.

In figure 9, a comparison of the BTFMO films deposited at 650 °C on LSAT and STO substrates is made. Surface features consisting of small dots are visible on the BTFMO samples on the LSAT substrate but not on the BTFMO films on the STO substrates. These films were deposited during the same growth process and nominally have the same stoichiometry ($Bi_5Ti_{2.71}Fe_{1.12}Mn_{0.17}O_{15}$). As these materials were deposited during the same growth process this may indicate that the strain applied by the substrate may affect the quality of the crystalline films. It is evident then that the substrate is having an effect on segregation of secondary phases within the sample. The secondary phases are likely too dilute to be detected during XRD analysis which has a detection limit of 1-3 vol%. The average diameter of the roughly spherical spots was 10 nm and average surface area was 89 nm^2. This corresponds to the spot occupying just 0.45 % of the imaged area.

A detailed analysis of surface impurities of ultra-thin films of m = 5 $Bi_6Ti_xFe_yMn_zO_{18}$ was undertaken by Keeney *et al.* [9] who identified these as the ferrimagnetic spinel $(Mn,Fe)_3O_4$ (cubic space group *Fd*-3*m*) phase. The occurrence of such magnetic secondary phases would complicate any magnetic measurements of the Aurivillius

materials. For example, the weak ferromagnetic behaviour measured in the $Bi_5Ti_{2.8}Fe_{1.1}Nb_{0.1}O_{15}$ material in chapter 3 of this work could be due to an inclusion of just 0.0095 % vol of the magnetic spinel phase impurities [21]. This highlights the need for thorough phase purity and statistical analysis [22] of materials before any magnetic behaviour can be said to be intrinsic to the Aurivillius phase.

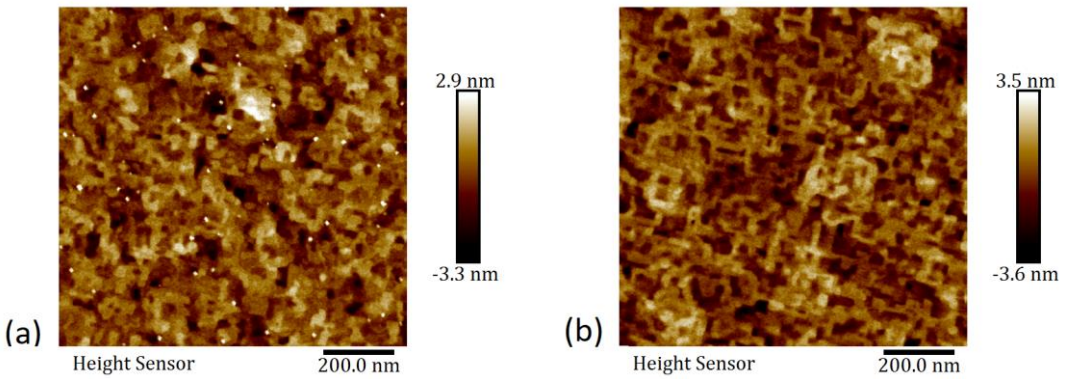

Figure 9: Bruker AFM images of BTFMO on (a) LSAT 650 °C and (b) STO 650 °C.

6.4.1.3. PFM analysis

The ferroelectric properties of the Aurivillius materials originate from a combination of polar distortions and tilts or rotations of the BO_6 octahedra (non-polar structural distortions) [23-26]. The dominant polarisation direction for these materials is along the *a*/*b*-axis [27]. Therefore lateral PFM, which detects the angular torsion of the cantilever as it oscillates was used to examine the in-plane piezoresponse. DART-PFM [14] in the lateral mode was performed on the BTFMO films on LSAT 710 °C and LSAT 610 °C substrates (shown in figure 10). It should be noted that spinel $(Mn,Fe)_3O_4$ inclusions are not ferroelectric and the trace levels within the sample here would not influence the ferroelectric signal. Both samples show similar amplitude and phase response. The domains are much smaller than those observed in Aurivillius samples prepared by chemical solution deposition in chapter 3 and 4. For example, an average domain size in a CSD sample was around 369.6 nm^2 and an average domain size for a sequential DLI-CVD sample was 7.42 nm^2.

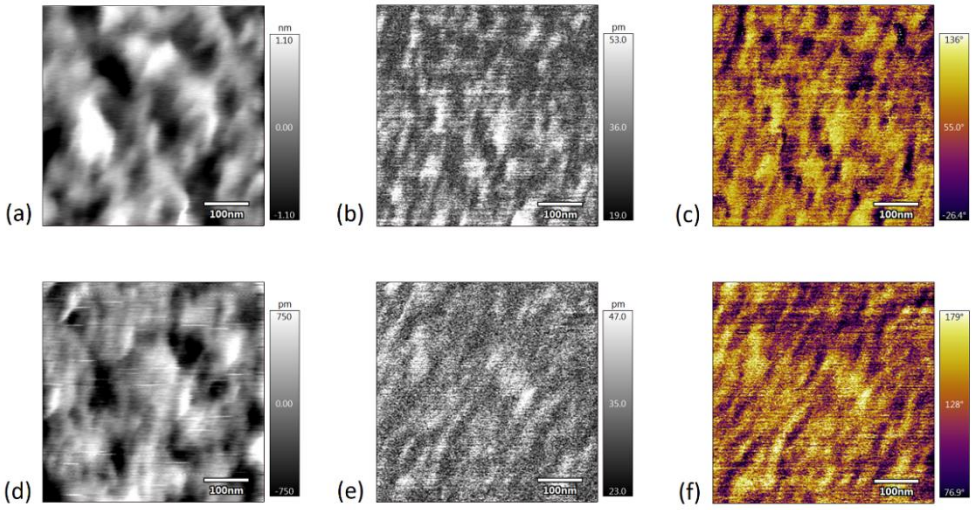

Figure 10: DART PFM of BTFMO on LSAT 710 °C (a) height, (b) amplitude, (c) phase and BTFMO on LSAT 610 °C (d) height, (e) amplitude and (f) phase.

6.4.1.4. TEM analysis

TEM analysis of $Bi_5Ti_{3.16}Fe_{0.68}Mn_{0.16}O_{15}$ on STO substrate (figure 11 (a)) confirms the presence of OPB defects and stacking faults in the sample. The presence of intergrowths of the *m* = 4 and *m* = 3 Aurivillius phase also clearly be seen. As discussed previously, the stoichiometry of this material requires a mechanism to compensate for charge imbalance. Incorporation of different '*m*' phases would help accommodate this imbalance and likely this is the driving force behind the mixed '*m*' phases observed. Also observed are defects in the form of bismuth-deficient interfaces based on anatase-like chains of edge-sharing BO_6 octahedra (circled in yellow in figure 11 (a)), which separate the perovskite blocks. The anatase-like chains, together with the octahedra of the perovskite blocks create "S-shaped tunnels", which are occupied by and stabilised by double columns of lone pair, stereochemically active Bi^{3+} cations. The double Bi columns at the interfaces create a "zig-zag" pattern of Bi atoms between the perovskite blocks [28, 29]. This indicates that the 32 % excess Bi present during the growth process was not sufficient to compensate for bismuth migration during growth and a lager excess would be

beneficial for feature growth processes. Nitin *et al.* found that an excess of 68 % to 110 % was necessary to form single phase *m* = 3 $Bi_4Ti_3O_{12}$ Aurivillius films [1, 6].

To estimate the theoretical thickness of the *c*-axis length of the *m* = 4 BTFMO Aurivillius material the following equation can be used. The can be estimated by equation 6.2 [30];

$$c/2 = f + h \qquad (6.2)$$

where h = *m**p; p is the thickness of the perovskite block (p ≈ 4 Å), *m* is the number of perovskite blocks and f is the thickness of the fluorite $(Bi_2O_2)^{2+}$ interlayer which has an average value of 4.08 Å [31]. Using equation 6.2, the thickness of a BTFMO film with 10 unit cells of *m* = 4 Aurivillius phase would be 40.16 nm.

The vertical thickness of the BTMO thin film on STO deposited at 710 °C is 28 to 31 nm (figure 11). The cross-section lamella prepared for the BTFMO on STO 610 °C sample (figure 12) was too thick to get a clear image of the Aurivillius structure but the vertical thickness of the film was found to be much thinner (≈ 17 nm) than the BTFMO on STO 710 °C sample. It is clear that the films are thinner than a strictly layer by layer growth mechanism. Again this may be due to bismuth deficiency during the growth process, since the presence of perovskite anatase intergrowths (figure 11 (a)) indicates a migration of bismuth away from the film during the deposition process.

In figure 11, 17 half unit cells can be distinguished, if they were all *m* = 4 then the film would be 34.13 nm thick but as there is a mix of *m* = 3 and *m* = 4 the film is only ≈ 30 nm thick. In figure 12, the thickness of 17 nm would correspond to 4 unit cells (or 8 half-unit cells) of the *m* = 4 Aurivillius material.

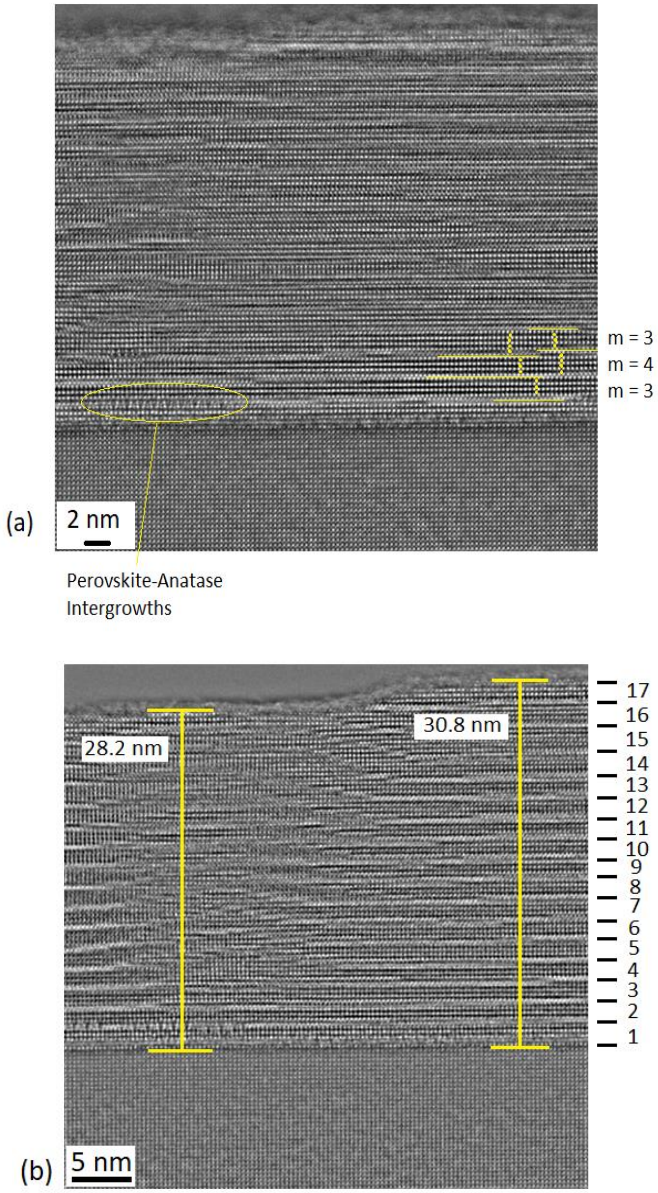

Figure 11: TEM image showing, (a), the mixed phase *m* = 3 and *m* = 4 Aurivillius phase and (b), thickness of the BTFMO thin films materials 710 °C STO substrate.

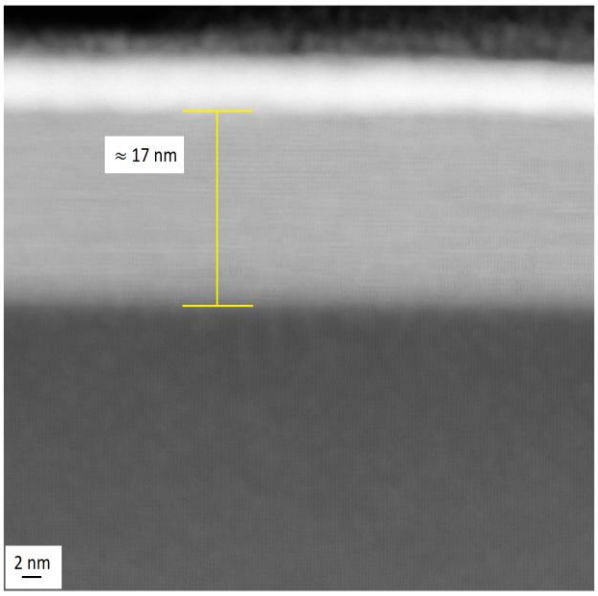

Figure 12: TEM image of thickness of BTFMO on STO 610 °C.

6.4.2. Sequential DLI-CVD recipe with accompanying continuous bismuth injection

A further modification of the sequential DLI-CVD recipe (figure 1 (c)) was developed so that every precursor pulse was accompanied by a continuous bismuth precursor injection. This was to avoid issues pertaining to localised bismuth deficiency that may affect the formation of defects and impurity phases within the Aurivillius samples. The deposition temperature was 710 °C for each growth. The stoichiometry of the continuous Bi (Con Bi) samples are presented in table 5 and the BTFMO 710 °C sample fabricated by the normal sequential DLI-CVD recipe discussed in section 6.3.1 (figure 1(b)) is included for comparison. Due to flow parameters used during the deposition process, sample ConBi 1 unfortunately had a significant shortage of bismuth during the growth process.

Table 5: Details of sample stoichiometry and bismuth excess.

		Bi/Ti	% Bi excess

BTFMO 710 °C	$Bi_5Ti_{3.16}Fe_{0.68}Mn_{0.16}O_{15}$	2.09	32 %
BTFMO Con Bi 1	$Bi_5Ti_{3.03}Fe_{0.83}Mn_{0.14}O_{15}$	1.45	-16 %
BTFMO Con Bi 2	$Bi_5Ti_{2.9}Fe_{0.96}Mn_{0.15}O_{15}$	2.03	22 %

6.4.2.1. XRD analysis of films prepared using continuous bismuth injections

XRD analysis of the $Bi_5Ti_{3.03}Fe_{0.83}Mn_{0.14}O_{15}$ (BTFMO Con Bi 1) material on LSAT and STO is shown in figure 13. The additional peaks seen around the (00<u>1</u>0) peak of the BTMO film on LSAT (figure 13 (a)) indicates superlattice reflections from alternating '*m*' phases such as alternating *m* = 3 and *m* = 4 phases. This was observed previously in the BTFMO on STO 610 °C, 630 °C and 650 °C samples deposited using the normal sequential DLI-CVD recipe (figure 2(b)).

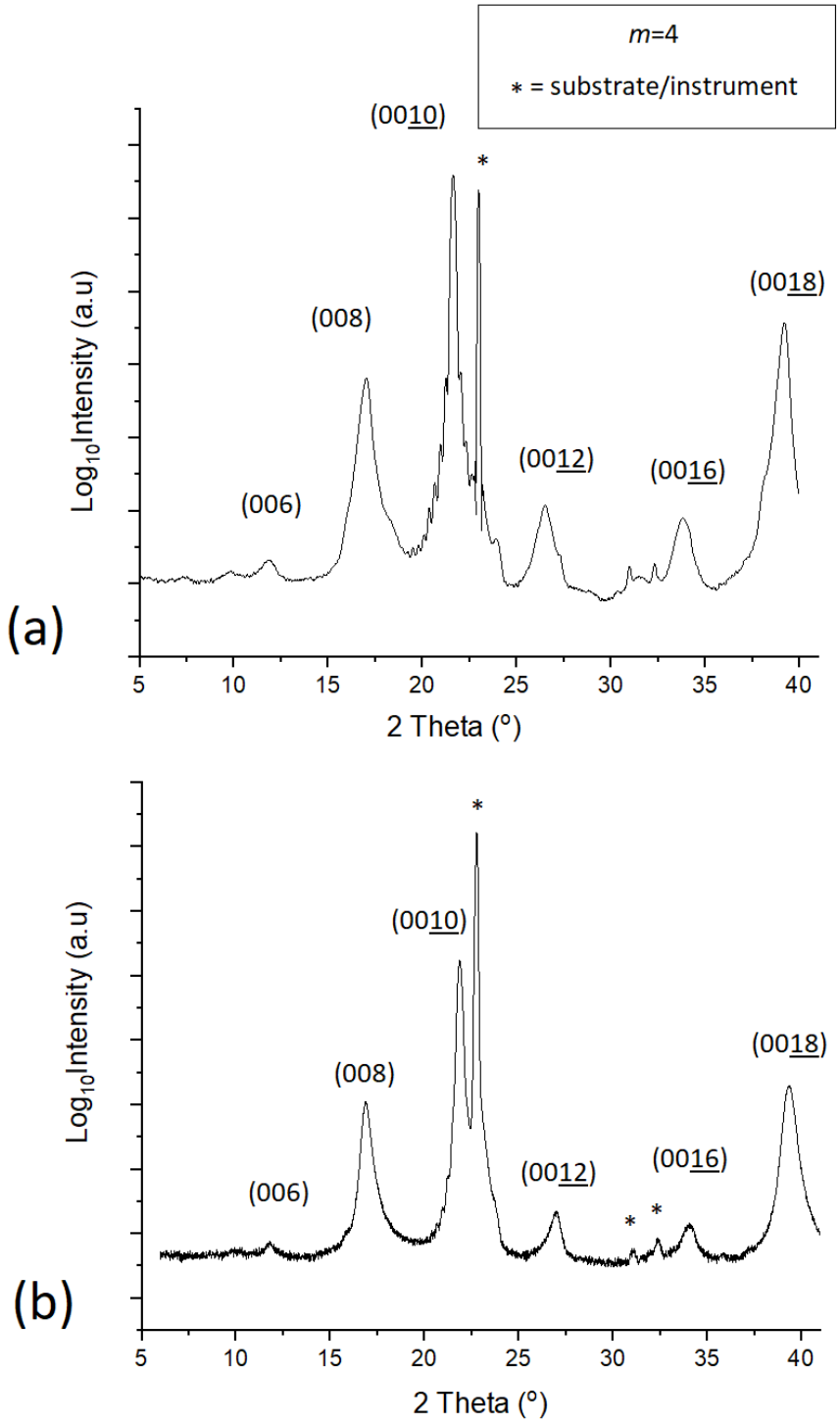

Figure 13: XRD of BTFMO Con Bi 1 sequential DLI-CVD films on (a) LSAT and (b) STO.

In figure 14, XRD analysis of the BTFMO films on STO substrates of ConBi 1, ConBi 2 and 710 °C show that there is no significant difference between these films in term of peak position indicating that the majority of the films correspond to the *m* = 4

Aurivillius phase. However, we know from STEM images, that the BTFMO 710 °C STO material has a mix of *m* = 4 and *m* = 3 phases present, which explains the broader and lower intensity peaks.

Interestingly, for the ConBi 1 growth, which was significantly deficient in bismuth, the XRD analysis shows a similar pattern to both the ConBi 2 and BTFMO 710°C samples indicating the overall formation of the *m* = 4 Aurivillius phase. This result may indicate that the ratio of *B*-site cations has a greater impact on the phase formation than the availability of Bi or that the recipe with continuous bismuth pulses succeeded in providing a sufficient supply of bismuth during the growth process to allow an overall *m* = 4 phase despite the overall shortage. Further studies using this novel sequential DLI-CVD recipe will be necessary to determine its effectiveness in improving the availability of bismuth throughout the growth process.

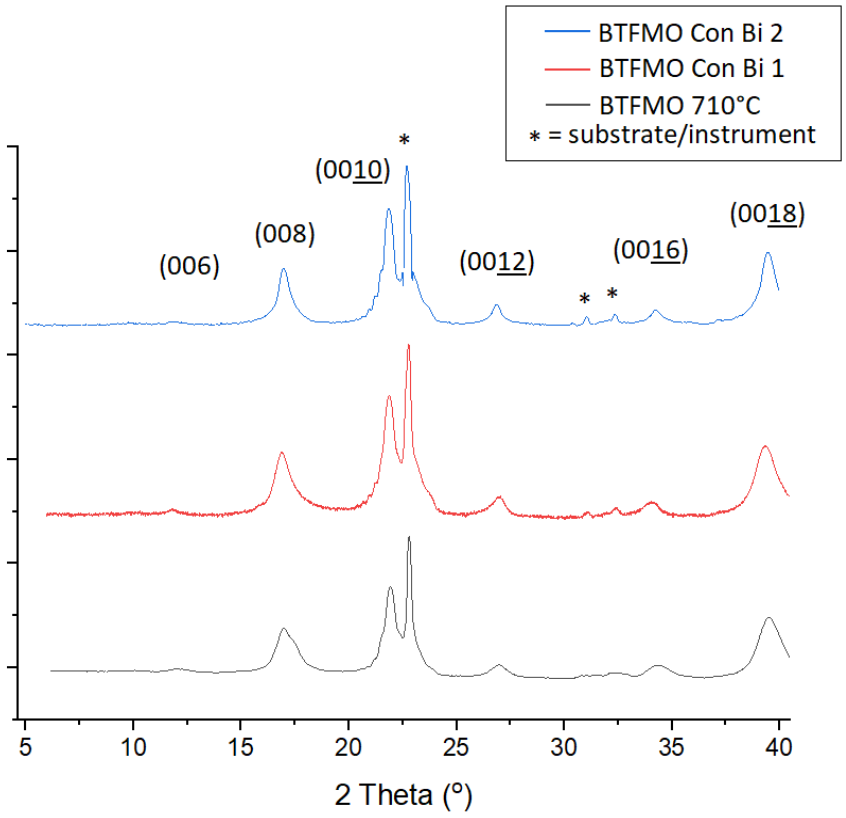

Figure 14: Comparison XRD analysis of, BTFMO 710 °C (black line), BTFMO Con Bi 1 (red line) and BTFMO Con Bi 2 (blue line) on STO substrates.

The FWHM of selected peaks are given in table 6. The FWHM for the ConBi1 and ConBi2 samples are narrower than the FWHM of the BTFMO 710 °C material. This indicates there are fewer dislocations possibly enabled by decreased variation in phases having intergrowths of differing '*m*' numbers or fewer OPB / stacking fault / anatase-type defects. However, the deviation from a charge-balanced stoichiometry may also account for the broad peaks on the 710 °C STO material. As discussed previously, the formation of different *m* phases may occur to accommodate the charge balance where the Ti stoichiometry deviates from a stoichiometric number of 3.

Table 6: FWHM of selected BTFMO peaks on STO substrates

Peak	BTFMO 710 °C	BTFMO ConBi 1	BTFMO ConBi 2
(008)	1.086 ± 0.004	0.868 ± 0.019	0.739 ± 0.026
(0012)	0.845 ± 0.005	0.808 ± 0.039	0.586 ± 0.053
(0016)	1.210 ± 0.014	0.899 ± 0.026	0.675 ± 0.040

6.4.2.2. AFM analysis of films prepared using continuous bismuth injections

AFM images of the ConBi 1 samples from figure 13 are shown in figure 15. The RMS roughness is 740 pm for BTFMO on LSAT and 797 pm for BTFMO on STO. This is comparable to the results of sequential DLI-CVD growth without the constant Bi pulse.

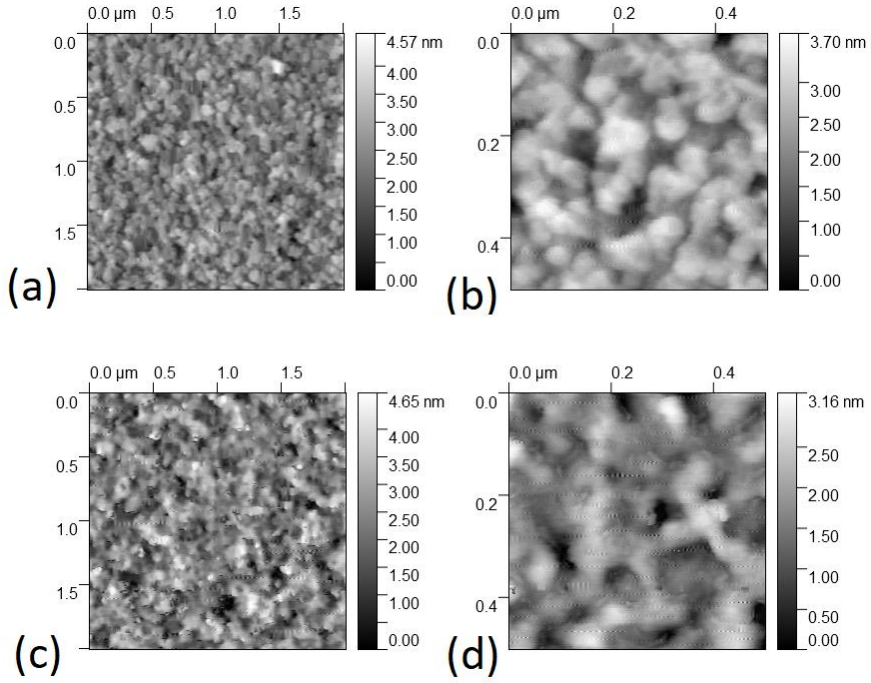

Figure 15: AFM of $Bi_5Ti_{3.03}Fe_{0.83}Mn_{0.14}O_{15}$ Con Bi 1 on LSAT, (a-b) and on STO, (c-d).

6.5. Conclusions

A series of BTFMO Aurivillius phase films were deposited using a sequential DLI-CVD method over a range of temperatures between 710 to 610 °C. Crystalline Aurivillius phase films were formed even at the lowest deposition temperature of 610 °C on the epitaxial substrates LSAT and STO. No Aurivillius phases were formed on sapphire substrates.

The BTFMO films deposited on LSAT and STO matched most closely to the *m* = 4 Aurivillius phase but it can be seen in STEM analysis of the BTFMO on STO 710 °C material that intergrowths of *m* = 3 Aurivillius phases are also present in that sample. The presence of different '*m*' phases causes out of phase boundary (OPB) defects to occur and OPB defects can clearly be observed in STEM images. Additionally, the presence of anatase-type perovskite intergrowths suggests a deficiency of bismuth due to migration during the growth process. The fine microstructure detail could not be determined from the B6TFMO on STO 610 °C sample due to the thickness of the lamella prepared but from XRD analysis the shift in peak position indicated that

mixed *m* = 4 and *m* = 5 phases may be forming. As such, it is not possible to solely attribute the trend in peak shift in the series to the change in temperature, due to the additional variable of changeable stoichiometry throughout the series.

An interesting observation from this study was the formation of secondary phases on the surface of films deposited on LSAT at 650 °C but not on the corresponding BTFMO material on STO. This demonstrates that the strain applied by the substrate may impact segregation of impurity phases and the quality of the films produced.

A novel sequential DLI-CVD recipe was introduced where the sequential recipe was modified to include a continuous bismuth precursor injection at each step to avoid a local deficiency of bismuth during the deposition process. Whereas the formation of anatase-type perovskite intergrowths indicates a deficiency of bismuth during the growth of the 710 °C STO thin film via the first sequential DLI-CVD recipe, XRD analysis indicates that the second, novel DLI-CVD recipe produced samples with fewer dislocations within the film compared with the normal sequential DLI-CVD recipe. However, this may also be attributed to the differences in stoichiometry. Interestingly, a material deposited with a significant shortage of bismuth produced a very similar *m* = 4 material to one with a bismuth excess. This indicates that the ratio of *B*-site cations may have a greater impact on the phase adopted by the Aurivillius material, but much further analysis in this area is needed. Further work will involve the deposition of films with a charge balanced nominal stoichiometry to reliably form single phase Aurivillius thin films.

6.6. Acknowledgements

The authors gratefully acknowledge the support of Science Foundation Ireland Principle Investigator Award Number 15/IA/3015 DEPO-Man, ‘Design, Deposition and Exploitation of Novel Micro and Nano-scale Materials and Devices for Advanced Manufacturing’ and the support of the Royal Society and Science Foundation Ireland (SFI) University Fellowship UF 140263.

6.7. References

[1] N. Deepak, P. F. Zhang, L. Keeney, M. E. Pemble, and R. W. Whatmore, "Atomic vapor deposition of bismuth titanate thin films," *Journal of Applied Physics,* vol. 113, no. 18, p. 187207, 2013.

[2] U. Weber *et al.*, "AVD® technology for deposition of next generation devices," *Microelectronics Reliability,* vol. 45, no. 5-6, pp. 945-948, 2005, doi: 10.1016/j.microrel.2004.11.019.

[3] P. K. Baumann *et al.*, "Innovative Deposition Technology for Advanced Materials," *ECS Transactions,* vol. 28, no. 1, p. 137, 2010.

[4] M. Lukosius *et al.*, "Electrical and Morphological Properties of ALD and AVD Grown Perovskite-Type Dielectrics and Their Stacks for Metal-Insulator-Metal Applications," *ECS Journal of Solid State Science and Technology,* vol. 1, no. 1, pp. N1-N5, 2012, doi: 10.1149/2.023201jss.

[5] M. Lukosius, C. B. Kaynak, S. Kubotsch, T. Blomberg, G. Ruhl, and C. Wenger, "Properties of atomic-vapor and atomic-layer deposited Sr, Ti, and Nb doped Ta2O5 Metal–Insulator–Metal capacitors," *Thin Solid Films,* vol. 520, no. 14, pp. 4576-4579, 2012, doi: 10.1016/j.tsf.2011.10.199.

[6] N. Deepak, P. Carolan, L. Keeney, M. E. Pemble, and R. W. Whatmore, "Tunable nanoscale structural disorder in Aurivillius phase, n= 3 Bi 4 Ti 3 O 12 thin films and their role in the transformation to n= 4, Bi 5 Ti 3 FeO 15 phase," *Journal of Materials Chemistry C,* vol. 3, no. 22, pp. 5727-5732, 2015.

[7] M. Zurbuchen, J. Lettieri, Y. Jia, A. H. Carim, S. K. Streiffer, and D. G. Schlom, "Out-of-phase boundary (OPB) nucleation in layered oxides," *MRS Online Proceedings Library (OPL),* vol. 902, 2005.

[8] G. Palkar, D. Sitharamarao, and A. Dasgupta, "Self-diffusion of bismuth in bismuth oxide," *Transactions of the Faraday Society,* vol. 59, pp. 2634-2638, 1963.

[9] L. Keeney *et al.*, "Ferroelectric Behavior in Exfoliated 2D Aurivillius Oxide Flakes of Sub-Unit Cell Thickness," *Advanced Electronic Materials,* vol. n/a, no. n/a, p. 1901264, 2020/01/30 2020, doi: 10.1002/aelm.201901264.

[10] K. Momma and F. Izumi, "VESTA 3 for three-dimensional visualization of crystal, volumetric and morphology data," *Journal of applied crystallography,* vol. 44, no. 6, pp. 1272-1276, 2011.

[11] X. Liu, L. Xu, Y. Huang, C. Qin, L. Qin, and H. J. Seo, "Improved photochemical properties of Aurivillius Bi 5 Ti 3 FeO 15 with partial substitution of Ti 4+ with Fe 3+," *Ceramics International,* vol. 43, no. 15, pp. 12372-12380, 2017, doi: 10.1016/j.ceramint.2017.06.103.

[12] C. H. Hervoches and P. Lightfoot, "A Variable-Temperature Powder Neutron Diffraction Study of Ferroelectric Bi4Ti3O12," *Chemistry of Materials,* vol. 11, no. 11, pp. 3359-3364, 1999/11/01 1999, doi: 10.1021/cm991090d.

[13] M. García-Guaderrama, L. Fuentes-Montero, A. Rodriguez, and L. Fuentes, "Structural characterization of Bi6Ti3Fe2O18 obtained by molten salt synthesis," *Integrated ferroelectrics,* vol. 83, no. 1, pp. 41-47, 2006.

[14] B. J. Rodriguez, C. Callahan, S. V. Kalinin, and R. Proksch, "Dual-frequency resonance-tracking atomic force microscopy," *Nanotechnology,* vol. 18, no. 47, p. 475504, 2007, doi: 10.1088/0957-4484/18/47/475504.

[15] M. Zurbuchen *et al.*, *Morphology, structure, and nucleation of out-of-phase boundaries (OPBs) in epitaxial films of layered oxides*. 2007, pp. 1439-1471.

[16] A. Faraz *et al.*, "Direct visualization of magnetic-field-induced magnetoelectric switching in multiferroic aurivillius phase thin films," *Journal of the American Ceramic Society,* vol. 100, no. 3, pp. 975-987, 2017, doi: 10.1111/jace.14597.

[17] R. A. Armstrong and R. E. Newnham, "Bismuth titanate solid solutions," *Materials Research Bulletin,* vol. 7, no. 10, pp. 1025-1034, 1972/10/01/ 1972, doi: https://doi.org/10.1016/0025-5408(72)90154-7.

[18] F. K. Lotgering, "Topotactical reactions with ferrimagnetic oxides having hexagonal crystal structures—I," *Journal of Inorganic and Nuclear Chemistry,* vol. 9, no. 2, pp. 113-123, 1959/02/01/ 1959, doi: https://doi.org/10.1016/0022-1902(59)80070-1.

[19] C. F. Holder and R. E. Schaak, "Tutorial on Powder X-ray Diffraction for Characterizing Nanoscale Materials," *ACS Nano,* vol. 13, no. 7, pp. 7359-7365, 2019/07/23 2019, doi: 10.1021/acsnano.9b05157.

[20] R. Shannon, "Revised effective ionic radii and systematic studies of interatomic distances in halides and chalcogenides," *Acta Crystallographica Section A,* vol. 32, no. 5, pp. 751-767, 1976, doi: doi:10.1107/S0567739476001551.

[21] J. C. Halpin, M. Schmidt, T. Maity, M. E. Pemble, and L. Keeney, "Compositional tuning of the Aurivillius phase material Bi5Ti3-2xFe1+ xNbxO15 (0≤ x≤ 0.4) grown by chemical solution deposition and its influence on the structural, magnetic and optical properties of the material," *IEEE Transactions on Ultrasonics, Ferroelectrics, and Frequency Control,* 2020.

[22] M. Schmidt *et al.*, "Absence of Evidence ≠ Evidence of Absence: Statistical Analysis of Inclusions in Multiferroic Thin Films," *Scientific Reports,* vol. 4, no. 1, p. 5712, 2014/07/16 2014, doi: 10.1038/srep05712.

[23] C. H. Hervoches, A. Snedden, R. Riggs, S. H. Kilcoyne, P. Manuel, and P. Lightfoot, "Structural Behavior of the Four-Layer Aurivillius-Phase Ferroelectrics SrBi4Ti4O15 and Bi5Ti3FeO15," *Journal of Solid State Chemistry,* vol. 164, no. 2, pp. 280-291, 2002, doi: 10.1006/jssc.2001.9473.

[24] A. Y. Birenbaum and C. Ederer, "Potentially multiferroic Aurivillius phaseBi5FeTi3O15: Cation site preference, electric polarization, and magnetic coupling from first principles," *Physical Review B,* vol. 90, no. 21, 2014, doi: 10.1103/PhysRevB.90.214109.

[25] Y.-Y. Guo, A. S. Gibbs, J. M. Perez-Mato, and P. Lightfoot, "Unexpected phase transition sequence in the ferroelectric Bi4Ti3O12," *IUCrJ,* vol. 6, no. 3, 2019.

[26] J. Perez-Mato *et al.*, "Competing structural instabilities in the ferroelectric Aurivillius compound Sr Bi 2 Ta 2 O 9," *Physical Review B,* vol. 70, no. 21, p. 214111, 2004.

[27] S. Trolier-McKinstry, "Crystal chemistry of piezoelectric materials," in *Piezoelectric and Acoustic Materials for Transducer Applications*: Springer, 2008, pp. 39-56.

[28] D. Batuk *et al.*, "Bi3n O9n Homologous Series: Slicing Perovskite Structure with Planar Interfaces Containing Anatase-like Chains."

[29] D. Batuk *et al.*, "Crystal Structure, Defects, Magnetic and Dielectric Properties of the Layered Bi3 n+ 1Ti7Fe3 n–3O9 n+ 11 Perovskite-Anatase Intergrowths," *Inorganic chemistry,* vol. 56, no. 2, pp. 931-942, 2017.

[30] N. A. Lomanova, M. I. Morozov, V. L. Ugolkov, and V. V. Gusarov, "Properties of aurivillius phases in the Bi4Ti3O12-BiFeO3 system," *Inorganic Materials,* vol. 42, no. 2, pp. 189-195, 2006, doi: 10.1134/s0020168506020142.

[31] M. Campanini, M. Trassin, C. Ederer, R. Erni, and M. D. Rossell, "Buried in-plane ferroelectric domains in Fe-doped single-crystalline Aurivillius thin films," *ACS Applied Electronic Materials,* vol. 1, no. 6, pp. 1019-1028, 2019.

Chapter 7

7. Conclusions and suggestions for future work

Multiferroic materials potentially offer a host of novel properties that make them an attractive avenue for study. This body of work was centred around the Aurivillius phase materials and an examination of their properties, in particular the structural response to changes in the stoichiometry with the aim of creating multiferroic materials.

Magnetic coupling requires proximity between the magnetic ions. It is therefore adventitious to increase the concentration of magnetic ions in the Aurivillius structure. Common magnetic ions are iron and manganese as in the reported room temperature multiferroic material, $Bi_6Ti_{2.8}Fe_{1.52}Mn_{0.68}O_{18}$ [1], in which the multiferroic behaviour was shown to be intrinsic to the Aurivillius material to a ≥ 99.5 % confidence level [2].

Despite the high levels of research interest, there have only been a few reports of genuine room temperature multiferroics. One cause of this bottleneck is the trade-off between increasing the concentration of magnetic ions and maintaining a phase pure material. Reports about an observed magnetic response originating form very small % vol. levels of secondary phases necessitate caution when reporting on single-phase multiferroic materials [3, 4].

The work presented in this thesis can be broadly divided as an examination of two different approaches to increasing the magnetic behaviour of the Aurivillius materials. The first approach involved increasing the concentration of substituted magnetic ions within the structure and the second involved locally concentrating the magnetic ions within the structure so that they are in closer proximity to enable magnetic coupling interactions. The aim was that increased magnetic ion content and proximity would enable an increase in the magnetic response and increase the likelihood that this magnetic behaviour would persist at room temperature. Computational work has posited that increased magnetic ion content would increase the ferromagnetic Curie temperature (T_c) [5].

The work in chapters 3 and 4 was focused on the first approach of increasing the concentration of magnetic ions in the Aurivillius phase materials. As discussed in chapter 3, aliovalent substitution was used in the $Bi_5Ti_{3-2x}Fe_{1+x}Nb_xO_{15}$ (x = 0, 0.1, 0.2, 0.3 and 0.4) *m* = 4 Aurivillius structure to increase the iron content. The co-substitution of iron and niobium for titanium was an attempt to avoid complications of a net charge in the material. By substituting Fe^{3+}+ Nb^{5+} for $2Ti^{4+}$ a net neutral charge could be nominally maintained. This approach was proposed by Birenbaum *et al.* as a method of increasing the iron content of the material following their computational studies which demonstrated that a higher iron content could induce room temperature magnetic behaviour [5]. Chen *et al.* [6] fabricated a similar series of materials using solid state reaction method but they did not observe robust magnetic ordering predicted by Birenbaum *et al.* [7] even at the higher concentrations of Fe. They do not observe secondary phases from XRD data even at the higher concentration of Fe/Nb [6]. In this work, it was found that secondary phases could be observed in the XRD analysis for samples with x > 0.2. Magnetic measurements of the x = 0.1, $Bi_5Ti_{2.8}Fe_{1.1}Nb_{0.1}O_{15}$ exhibited a weak ferromagnetic response at 2 K, 150 K and 300 K of 2.2, 1.6, 1.5 emu/cm^3 with H_c ~ 40, 36, 34 Oe respectively. Previous work of $Bi_6Ti_{2.8}Fe_{1.52}Mn_{0.68}O_{18}$ materials deposited using a very similar process exhibited a M_R = 0.18 emu/cm^3 [1]. The theoretical concentration of iron atoms over the four available *B*-sites in the $Bi_5Ti_{2.8}Fe_{1.1}Nb_{0.1}O_{15}$ structure was 25 %. This is lower than the percolation threshold of 31 % for strong near neighbour coupling. The origin of the ferromagnetic behaviour may be due to spin canting of antiferromagnetic interactions to yield a weak net magnetic response. Future work should involve a full phase analysis on this material to definitively establish that the magnetic behaviour was intrinsic to the Aurivillius phase.

The work of chapter 4 involved a systematic study of the flexibility of the *m* = 5 Aurivillius phase. Four series of Aurivillius materials with a target composition of $Bi_6Ti_xFe_yMn_zO_{18}$ (x = 3.2- 1.6, y = 1.2- 1.95, z = 0.3- 0.9) (*m* = 5) were fabricated to test the response of the structure to the variation of the *B*-site cations. Long range magnetic ordering benefits from a larger concentration of magnetic ions. However,

there is often a solubility limit for the magnetic ions. It was determined during these investigations that when the occupancy of Ti^{4+} at the *B*-sites fell below 52 %, there was an increasing shift to the *m* = 6 Aurivillius phase. It was proposed that the oxidation of Mn^{3+} to Mn^{4+} was occur when Ti^{4+} was substituted by Fe and Mn which have a nominal valence of +3. Rearrangement of the Aurivillius phase was found to occur above a threshold of 8% nominal Mn^{4+}. Above this, the *m* = 5 structure undergoes a structural rearrangement to the *m* = 6 phase in order to tolerate the additional manganese. It has been proposed that the ionic radii of Mn^{4+} (0.53 Å) is too small to be tolerated in the Aurivillius structure [8]. Previous work with Aurivillius materials has failed to form phase pure structures with Mn^{4+} [9]. The formation of the *m* = 6 phase was observed to occur when the average oxidation state on Mn was above +3.44. The average oxidation state for the stable Aurivillius phase compositions was $Mn^{3.2+}$ for Zurbuchen *et al.* [10] and $Mn^{3.4+}$ for McCabe and Greaves [9]. The presence of Mn^{4+} in Aurivillius multiferroic materials have important implications for the type of magnetic behaviour exhibited. The Mn^{3+} - O - Mn^{4+} and Fe^{3+} - O - Mn^{4+} double exchange mechanism produces ferromagnetic behaviour compared to the superexchange mechanism between Mn^{3+} - O - Mn^{3+} which produces antiferromagnetic behaviour [11, 12]. Future work in this area would include analysis of the magnetic properties of materials where the magnetic ion content above the percolation threshold of 31 % for nearest neighbour interactions [13] and while no obvious secondary impurity phases were observed during XRD analysis a through phase analysis would be performed to determine if the rearrangement to higher '*m*' phase is accompanied by the formation of impurity phases.

The deposition method used for the samples discussed in chapters 3 and 4 was chemical solution deposition (CSD) which has advantages of being a simple and relatively low cost method of fabricating series of Aurivillius materials. Using this method the thin films obtained did not have complete coverage over the sapphire substrate. Unannealed, amorphous films on sapphire substrates showed complete coverage but on annealing, contraction of the film occurred, forming plate like morphology. Continuous thin films would be more suitable for device applications.

So while CSD is a useful deposition method for lab scale exploration of chemical structures, techniques such as direct liquid injection chemical vapour deposition (DLI-CVD) would be more suitable for producing the thin films required for various technological applications. Ultra-thin films of unit cell thickness (< 7 nm) Aurivillius phase materials have been deposited using the DLI-CVD process [14]. DLI-CVD allows precise control of the stoichiometry through control of opening times and monitoring flow meters. Deposition also occurs at higher temperatures and when depositing on epitaxial substrates this eliminates the need for a post anneal step in the fabrication process.

DLI-CVD was the deposition method utilised to produce the samples discussed in chapters 5 and 6 where the second approach to improving the magnetic response in the Aurivillius materials was examined. A conventional DLI-CVD process involves the simultaneous injection of the gaseous precursors into the reaction chamber (simultaneous DLI-CVD). A modification of this recipe called sequential DLI-CVD separates the precursor injections in time. The precursor pulses now enter the reaction chamber in the order that mimics the Aurivillius structure. In this way it was attempted to locally concentrate the Fe and Mn to the inner perovskite units of the Aurivillius material. While the sequential DLI-CVD recipe used mimicked the m = 5 Aurivillius structure, the ratio of precursors during the process favoured the m = 4 stoichiometry and this was the phase that was produced. The materials deposited by this method showed deviations from the reference XRD patterns of the m = 4 Aurivillius phase indicating the presence of other 'm' Aurivillius phases and/or out of phase boundaries.

In chapter 5 this sequential DLI-CVD method was used to fabricate materials with the stoichiometries, $Bi_5Ti_{2.9}Fe_{1.1}O_{15}$ (BTFO) and $Bi_5Ti_{2.8}Fe_{1.1}M_{0.1}O_{15}$ (BTFMO). The deposition was performed at 710 °C and this was sufficient to produce crystalline Aurivillius phases on the LSAT and STO substrates without the need for a post anneal step. This is adventitious as volatilisation of Bi increases above 710 °C [15]. LSAT and STO have an epitaxial relationship to the Aurivillius material. The effect of tensile strain was observed in the XRD analysis of the materials where the peaks of the STO

sample were shifted higher than those of the LSAT samples. This substrate effect was lost in thicker films. Deposition on the sapphire substrate, which has a much larger mis-match between the Aurivillius phase and the substrate, only formed a pyrochlore $Bi_2Ti_2O_7$ phase.

The magnetic behaviour of these materials was examined by SQUID (Superconducting Quantum Interference Device) analysis and a magnetic response was observed for BTFO on STO, BTFMO on LSAT and BTFMO on STO. According to the Goodenough-Kanomori rule, superexchange mechanism between Fe^{3+}- O - Fe^{3+} would be expected to produce antiferromagnetic behaviour. At low temperatures (2 K) spin canting can produce weak ferromagnetic behaviour in antiferromagnetic materials. Double exchange mechanism interactions between Mn^{3+}- O - Mn^{4+} are expected to produce ferromagnetic behaviour. Divergence of the field cooled and zero field cooled lines occurred for BTFMO on LSAT around 250 K and for BTFMO on STO around 280 K. While room temperature magnetic behaviour would be beneficial of practical applications, the presence of a magnetic response with only a concentration of 2.5 % Mn and 27.5 % Fe magnetic ions was encouraging and suggests that the ions are locally concentrated within the structure. Previous work which developed a room temperature multiferroic $Bi_6Ti_{2.8}Fe_{1.52}Mn_{0.68}O_{18}$ material had a concentration of 13 % manganese and a total of 44 % iron and manganese at the *B*-sites [16]. Interestingly the BTFO on LSAT sample did not show long range magnetic ordering while the BTFO on STO did. This may indicate the greater tensile strain applied by the STO substrate may concentrate Fe ions to the inner perovskites and in closer proximity to each other. This effect may also explain why the magnetic moment was higher in the BTFMO on STO sample compared with the BTFMO on LSAT sample (at 20 K, BTFMO on STO M_R = 3.51 emu/cm^3 and BTFMO on LSAT M_R = 1.50 emu/cm^3). Future work with these materials should include electron energy loss spectroscopy (EELS) analysis to determine structural details and the position of ions across the perovskite units. This will demonstrate if the sequential DLI-CVD recipe imposes ordering of the ions in the Aurivillius structure. Other avenues of study

would be the effect of substrate on the partitioning of Ti, Fe and Mn throughout the structure and the oxidation state of the ions, particularly Mn.

Finally, in chapter 6 the effect of deposition temperature was examined for the BTFMO materials deposited using the sequential DLI-CVD method. Aurivillius materials were deposited at 710 °C, 690 °C, 670 °C, 650 °C, 630 °C and 610 °C on LSAT and STO. The volatilisation of bismuth is a concern when fabricating the Aurivillius phases, above 710 °C bismuth is increasingly volatile [15] and diffusion of bismuth can cause crystallographic shear in the layered structure and associated formation of defects and segregation of impurity phases [17]. Decreasing the deposition temperature has been previously reported to reduce the secondary phases in Aurivillius materials [18].

The sequential DLI-CVD method shows promising results for the deposition of Aurivillius materials, as even at low temperatures of 610 °C, crystallised Aurivillius structures were formed on the epitaxial substrates LSAT and STO. The detailed microstructure analysis demonstrated the presence of OPB's and mixed m = 4 and m = 3 Aurivillius phases in the BTFMO on STO 710 °C material. Unfortunately, the fine detail of the BTFMO on STO 610 °C materials could not be determined from TEM analysis of that material. However, from the XRD analysis, it can be seen that the peaks shift in the direction of the higher m = 5 phase as the deposition temperature decreases. In addition, there was also variation in the stoichiometry of the materials throughout the series. This additional variable means that it is not possible to definitely determine that the higher '*m*' phase is produced due to a lower deposition temperature. Instead a similar rearrangement may be occurring as was observed in chapter 5. The materials may be responding to the unbalanced stoichiometry by adopting the higher '*m*' phase. Future work in this area would include a systematic study on the effect of stoichiometry on the materials similar to the study undertaken in chapter 4.

Also discussed in chapter 6 was a further modification of the sequential DLI-CVD recipe to include an injection of the bismuth precursor at each step. This was undertaken to increases the availability of bismuth throughout the growth process. A

deficiency of bismuth is a common concern when fabricating Aurivillius materials and as a precaution an excess of bismuth is used during the fabrication. The materials deposited by this novel method exhibited narrow FWHM which may indicate that there are fewer dislocations in those materials compared to a material fabricated using the sequential DLI-CVD method. However, there was also variation in the stoichiometry of the materials under study and so more thorough analysis of this novel sequential DLI-CVD will form the basis of future work.

Other future work will include targeting the *m* = 5 phase with a larger excess of bismuth (> 30 %) and a stoichiometry that is charge balanced using the sequential DLI-CVD recipe. Increasing the content of Mn within the materials closer to the threshold of percolation of 31 % *B*-site occupation for near neighbour coupling may raise the magnetic response to room temperature levels. From the understanding gained from the work discussed in chapter 4 it is not favourable to lower the Ti content below 52 % without phase rearrangement occurring in those materials. A similar systematic study of materials deposited by DLI-CVD on LSAT and STO to determine the solubility limit of Fe and Mn inclusion should be performed. Further studies of the effect of the substrate on the imposition of strain on the material to potentially further partition the magnetic ions such as iron and manganese to the inner perovskites should be investigated.

In conclusion, the experimental studies performed during this work have advanced the current understanding of the structural behaviour of the Aurivillius phase materials and opened up numerous avenues for future studies. A solution limit of x = 0.1 for the successful incorporation of iron and niobium during the aliovalent substitution of titanium in the *m* = 4 $Bi_5Ti_{3-2x}Fe_{1+x}Mn_xO_{15}$ Aurivillius structure were determined. The structural rearrangement in response to a lowering of the Ti content of the *m* = 5 $Bi_6Ti_3Fe_{1.5}Mn_{0.5}O_{18}$ Aurivillius phase was explored and a threshold of Ti content (52 %) below which structural rearrangement occurs was established. The sequential DLI-CVD method was examined with materials exhibiting magnetic behaviour with a relatively low concentration (2.5 % Mn and 27.5 % Fe) of magnetic ions and crystalline Aurivillius thin films were formed on epitaxial substrates using

deposition temperatures as low as 610 °C. A novel sequential DLI-CVD recipe consisting of a bismuth injection with each precursor step was introduced which appeared to decrease the extent of bismuth migration and associated structural disorder.

7.1. References

[1] L. Keeney *et al.*, "Magnetic Field-Induced Ferroelectric Switching in Multiferroic Aurivillius Phase Thin Films at Room Temperature," *Journal of the American Ceramic Society,* vol. 96, no. 8, pp. 2339-2357, 2013/08/01 2013, doi: 10.1111/jace.12467.

[2] M. Schmidt *et al.*, "Absence of Evidence ≠ Evidence of Absence: Statistical Analysis of Inclusions in Multiferroic Thin Films," *Scientific Reports,* vol. 4, no. 1, p. 5712, 2014/07/16 2014, doi: 10.1038/srep05712.

[3] A. Faraz *et al.*, "Exploring ferroelectric and magnetic properties of Tb-substituted m = 5 layered Aurivillius phase thin films," *Journal of Applied Physics,* vol. 123, no. 12, p. 124101, 2018/03/28 2018, doi: 10.1063/1.5009986.

[4] L. Keeney *et al.*, "Room temperature ferroelectric and magnetic investigations and detailed phase analysis of Aurivillius phase Bi5Ti3Fe0.7Co0.3O15 thin films," *Journal of Applied Physics,* vol. 112, no. 5, p. 052010, 2012, doi: 10.1063/1.4745936.

[5] A. Y. Birenbaum, A. Scaramucci, and C. Ederer, "Magnetic order in four-layered Aurivillus phases," *Physical Review B,* vol. 95, no. 10, 2017, doi: 10.1103/PhysRevB.95.104419.

[6] C. Chen *et al.*, "Effect of Nb and more Fe ions co-doping on the microstructures, magnetic, and piezoelectric properties of Aurivillius Bi5Ti3FeO15 phases," *Journal of Applied Physics,* vol. 120, no. 21, p. 214104, 2016, doi: 10.1063/1.4971256.

[7] A. Y. Birenbaum and C. Ederer, "Potentially multiferroic Aurivillius phaseBi5FeTi3O15: Cation site preference, electric polarization, and magnetic coupling from first principles," *Physical Review B,* vol. 90, no. 21, 2014, doi: 10.1103/PhysRevB.90.214109.

[8] R. A. Armstrong and R. E. Newnham, "Bismuth titanate solid solutions," *Materials Research Bulletin,* vol. 7, no. 10, pp. 1025-1034, 1972/10/01/ 1972, doi: https://doi.org/10.1016/0025-5408(72)90154-7.

[9] E. McCabe and C. Greaves, "Structural and magnetic characterisation of Bi 2 Sr 1.4 La 0.6 Nb 2 MnO 12 and its relationship to “Bi 2 Sr 2 Nb 2 MnO 12”," *Journal of Materials Chemistry,* vol. 15, no. 1, pp. 177-182, 2005.

[10] M. Zurbuchen *et al.*, "Synthesis and characterization of an n= 6 Aurivillius phase incorporating magnetically active manganese, Bi 7 (Mn, Ti) 6 O 21," *Applied Physics Letters,* vol. 91, no. 3, p. 033113, 2007.

[11] J. B. Goodenough, "Theory of the role of covalence in the perovskite-type manganites [La, M (II)] Mn O 3," *Physical Review,* vol. 100, no. 2, p. 564, 1955.

[12] L. W. Martin, Y. H. Chu, and R. Ramesh, "Advances in the growth and characterization of magnetic, ferroelectric, and multiferroic oxide thin films," *Materials Science and Engineering: R: Reports,* vol. 68, no. 4-6, pp. 89-133, 2010, doi: 10.1016/j.mser.2010.03.001.

[13] Ł. Kurzawski and K. Malarz, "Simple Cubic Random-Site Percolation Thresholds for Complex Neighbourhoods," *Reports on Mathematical Physics,* vol. 70, no. 2, pp. 163-169, 2012/10/01/ 2012, doi: https://doi.org/10.1016/S0034-4877(12)60036-6.

[14] L. Keeney, Z. Saghi, M. O’Sullivan, J. Alaria, M. Schmidt, and L. Colfer, "Persistence of ferroelectricity close to unit-cell thickness in structurally disordered Aurivillius phases," *Chemistry of Materials,* vol. 32, no. 24, pp. 10511-10523, 2020.

[15] G. Palkar, D. Sitharamarao, and A. Dasgupta, "Self-diffusion of bismuth in bismuth oxide," *Transactions of the Faraday Society,* vol. 59, pp. 2634-2638, 1963.

[16] A. Faraz *et al.*, "Direct visualization of magnetic-field-induced magnetoelectric switching in multiferroic aurivillius phase thin films," *Journal of the American Ceramic Society,* vol. 100, no. 3, pp. 975-987, 2017, doi: 10.1111/jace.14597.

[17] M. Zurbuchen, J. Lettieri, Y. Jia, A. H. Carim, S. K. Streiffer, and D. G. Schlom, "Out-of-phase boundary (OPB) nucleation in layered oxides," *MRS Online Proceedings Library (OPL),* vol. 902, 2005.

[18] L. Keeney *et al.*, "Ferroelectric Behavior in Exfoliated 2D Aurivillius Oxide Flakes of Sub-Unit Cell Thickness," *Advanced Electronic Materials,* vol. n/a, no. n/a, p. 1901264, 2020/01/30 2020, doi: 10.1002/aelm.201901264.

A.1. Appendix 1- supporting information for chapter 3

Photocatalytic analysis

The photocatalytic analysis of the samples $Bi_5Ti_{2.8}Fe_{1.1}Nb_{0.1}O_{15}$ and $Bi_5Ti_{2.2}Fe_{1.4}Mn_{0.4}O_{15}$ by the degradation of the dye solution (methylene blue in a 0.1 M solution in MilliQ water (18.2 MΩ cm at 25°C)). There was no change to the absorption of light during the analysis indicating that methylene blue was not being reduced.

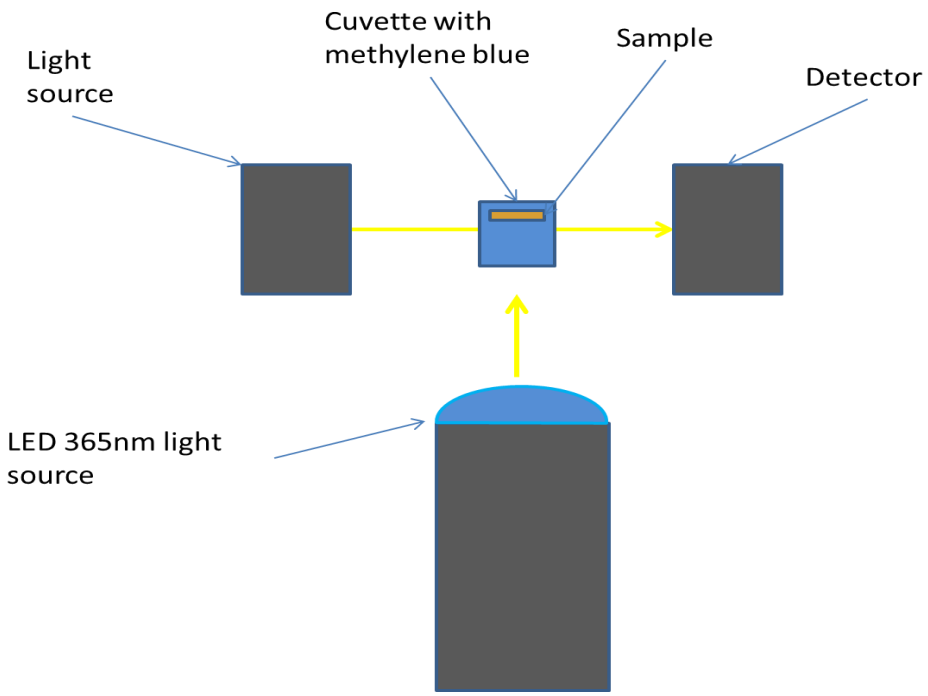

Figure S1: Diagram of the experimental setup for the examination of the photocatalytic behaviour.

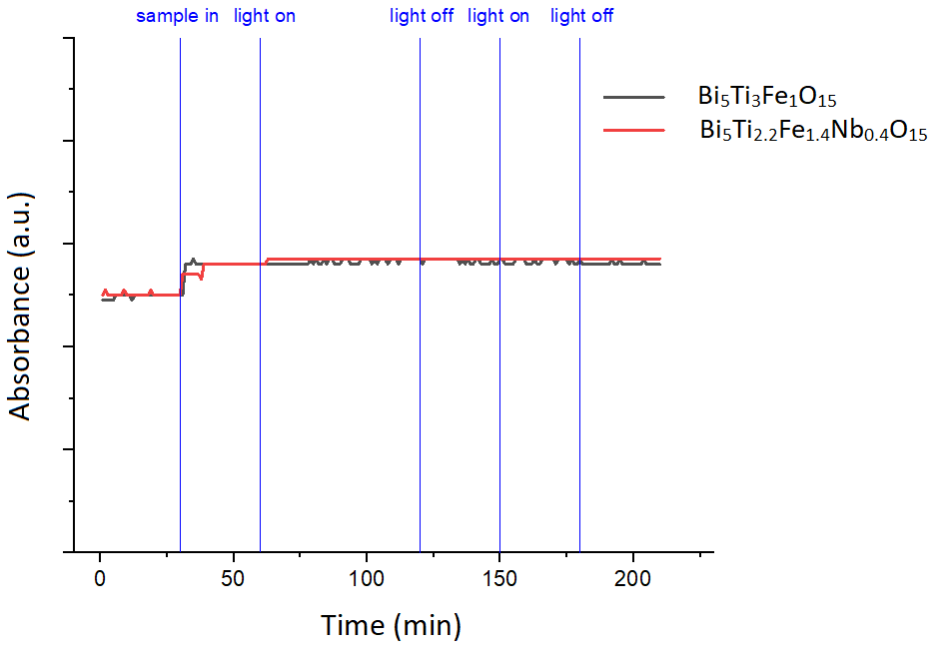

Figure S2: The absorption of light over time, there was no change in absorption

Single frequency PFM

Single frequency PFM measurements of the $Bi_5Ti_{3-2x}Fe_{1+x}Nb_xO_{15}$, where x= 0, 0.2, 0.3 and 0.4.

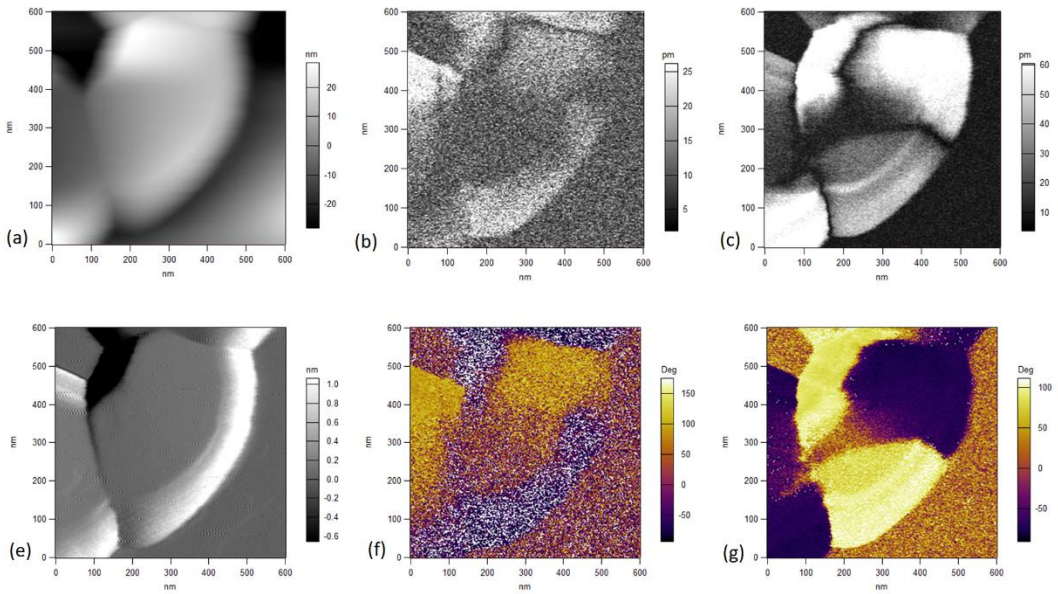

Figure S3: Single frequency PFM measurements of $Bi_5Ti_3Fe_1O_{15}$, (a) height, (b) vertical amplitude, (c) lateral amplitude, (d) vertical deflection, (e) vertical phase and (f) lateral phase.

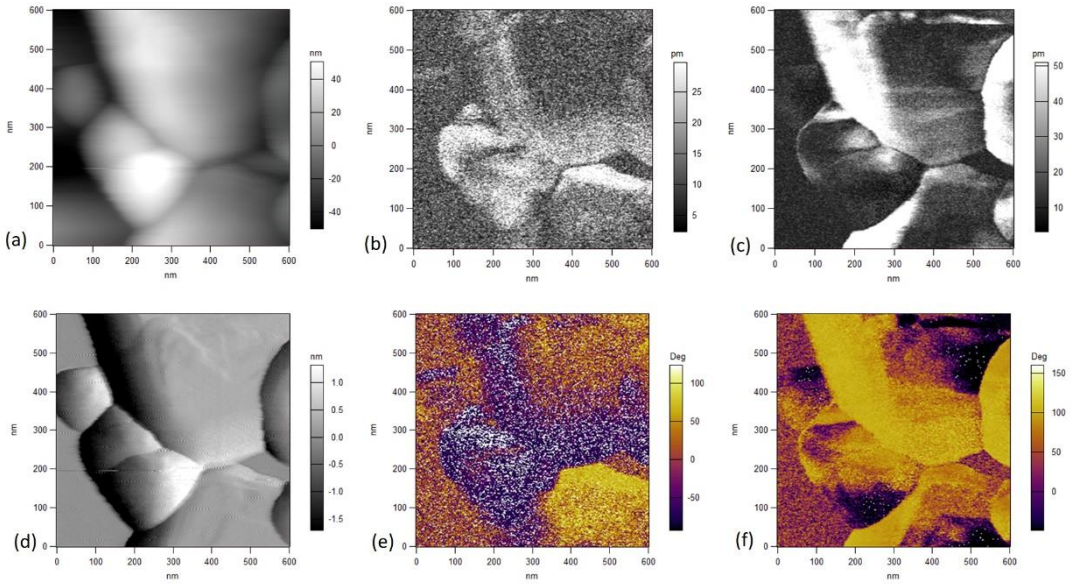

Figure S4: Single frequency PFM measurements of $Bi_5Ti_{2.6}Fe_{1.2}Nb_{0.2}O_{15}$, (a) height, (b) vertical amplitude, (c) lateral amplitude, (d) vertical deflection, (e) vertical phase and (f) lateral phase.

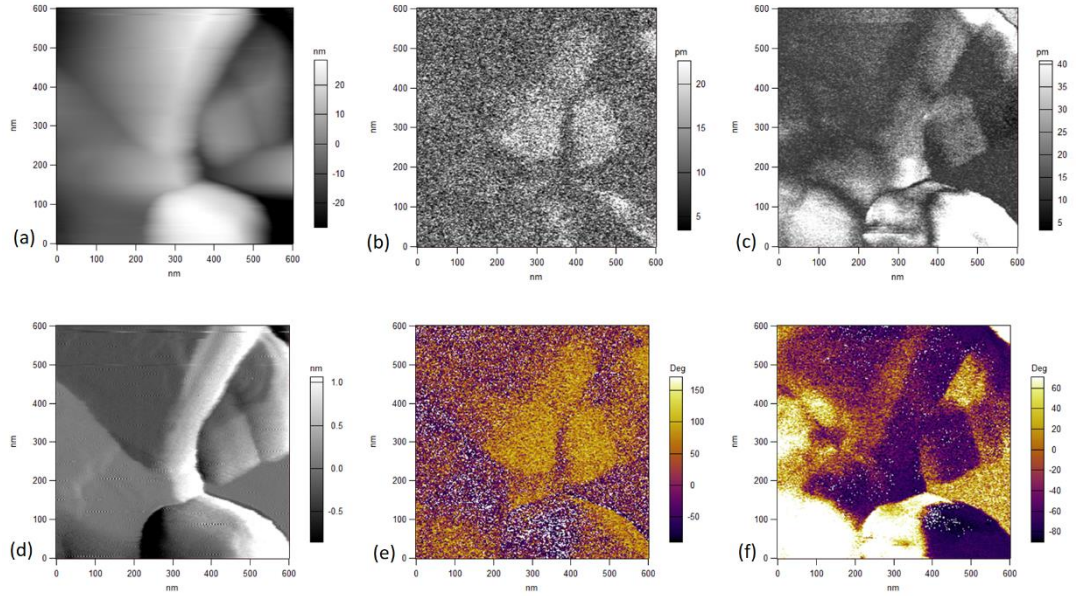

Figure S5: Single frequency PFM measurements of $Bi_5Ti_{2.4}Fe_{1.3}Nb_{0.3}O_{15}$, (a) height, (b) vertical amplitude, (c) lateral amplitude, (d) vertical deflection, (e) vertical phase and (f) lateral phase.

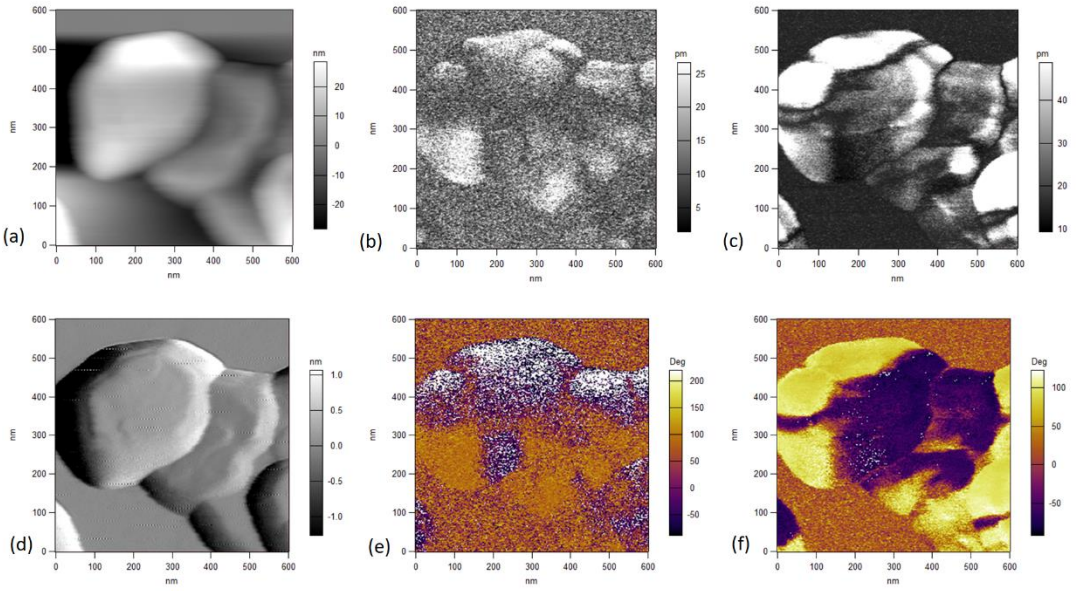

Figure S6: Single frequency PFM measurements of $Bi_5Ti_{2.2}Fe_{1.4}Nb_{0.4}O_{15}$, (a) height, (b) vertical amplitude, (c) lateral amplitude, (d) vertical deflection, (e) vertical phase and (f) lateral phase.

Lateral DART PFM performed on samples under a variable magnetic field

PFM analysis was performed at various magnetic field strengths on the samples $Bi_5Ti_{2.8}Fe_{1.1}Nb_{0.1}O_{15}$ and $Bi_5Ti_{2.2}Fe_{1.4}Mn_{0.4}O_{15}$ The field was increased at 500G intervals to ±2500G. Representative results of this analysis is depicted in figure S7 and S8.

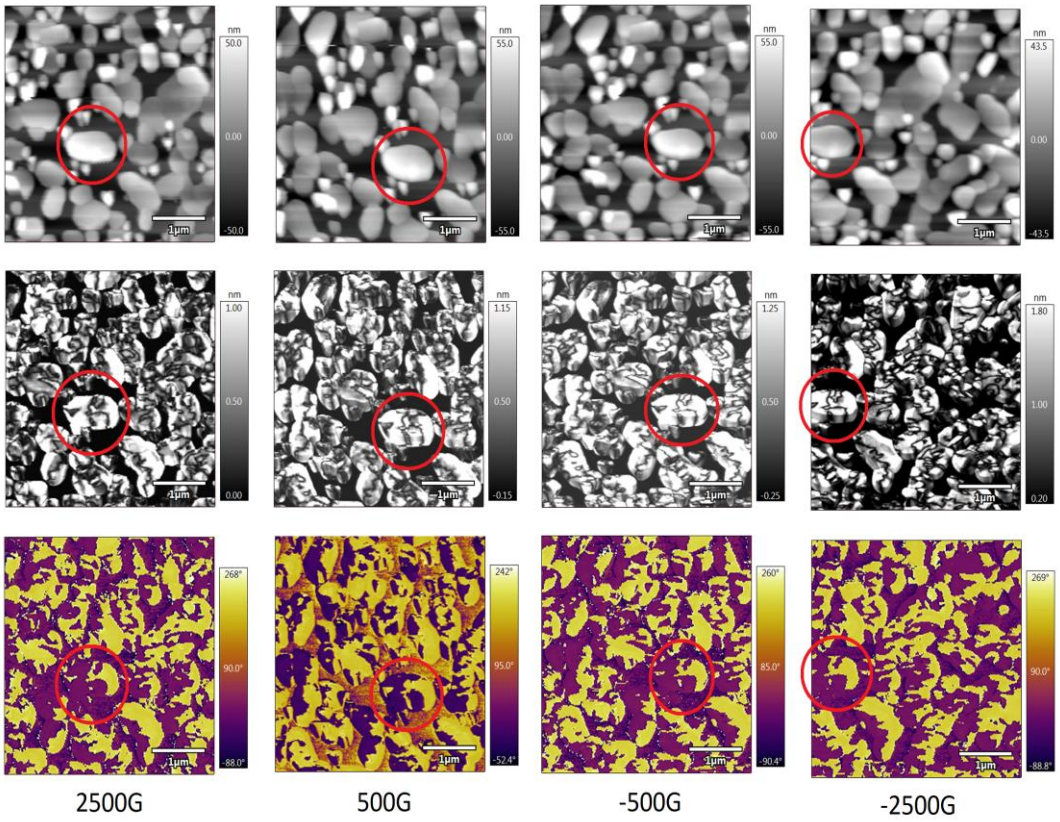

Figure S7: Lateral DART PFM performed under a variable magnetic field $Bi_5Ti_{2.8}Fe_{1.1}Nb_{0.1}O_{15}$.

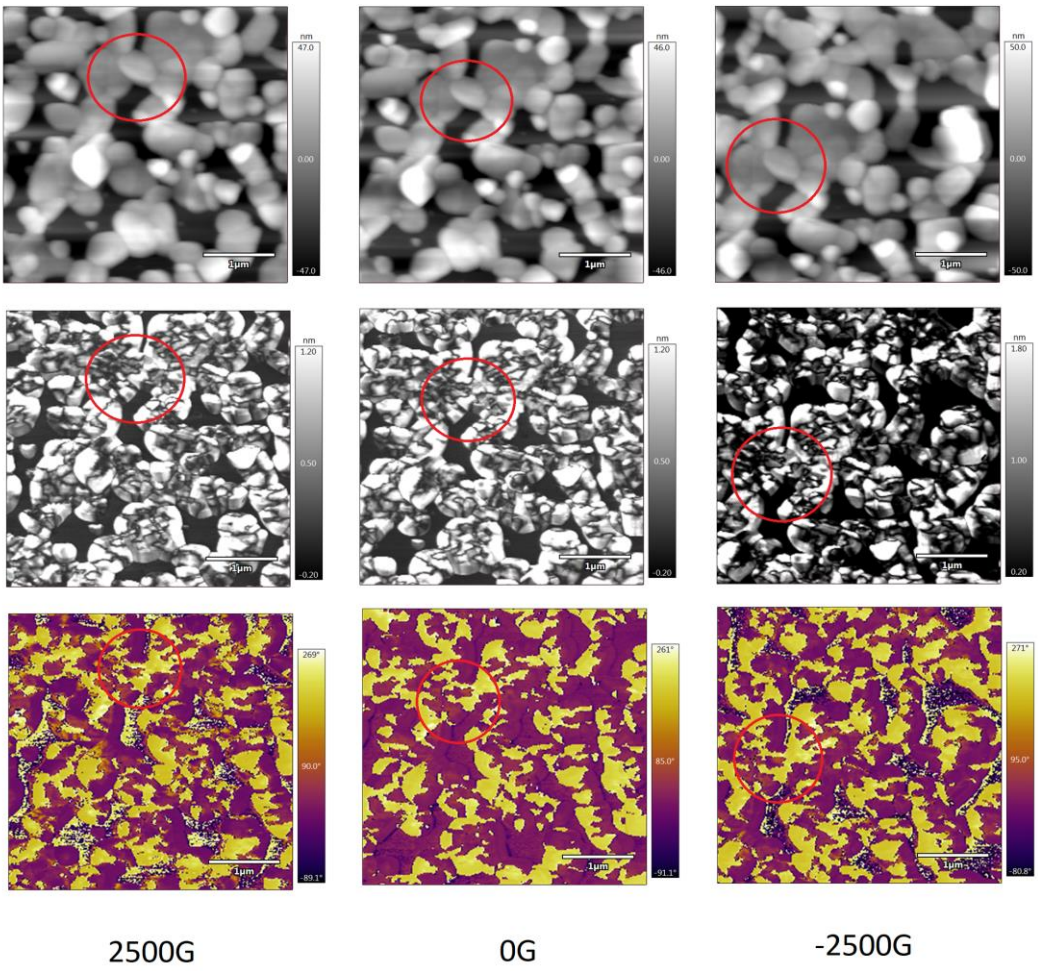

Figure S8: Lateral DART PFM performed under a variable magnetic field $Bi_5Ti_{2.2}Fe_{1.4}Nb_{0.4}O_{15}$.

A.2. Appendix 2- supporting information for chapter 4

Calculation of crystalline quality

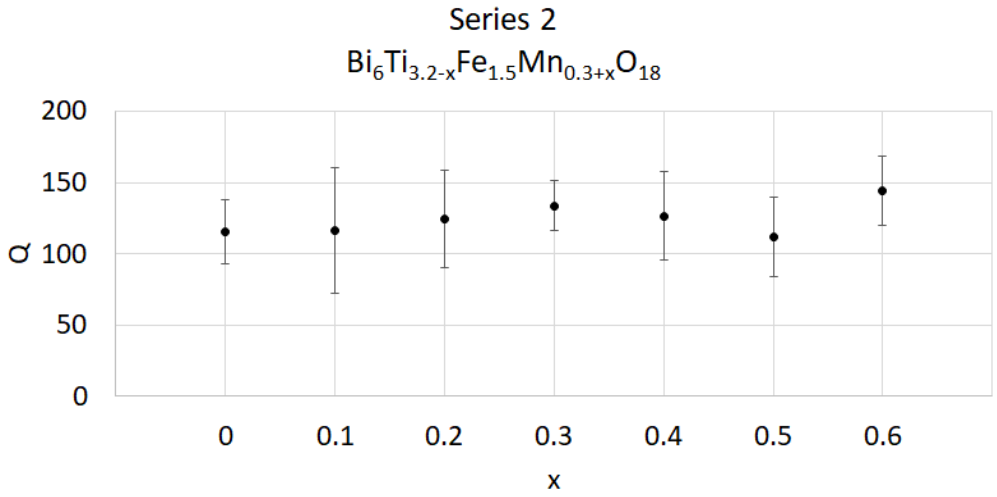

Figure S1: Crystalline quality factor for series 2

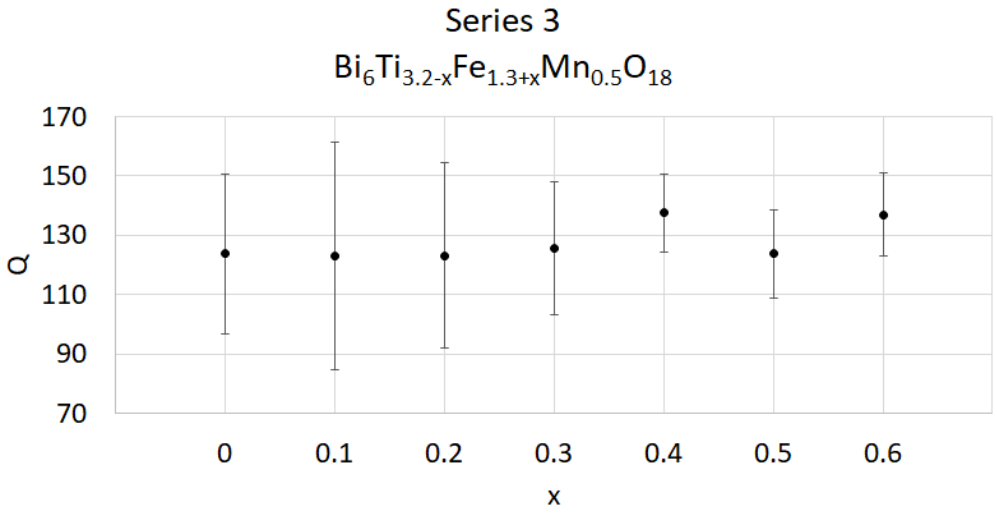

Figure S2: Crystalline quality factor for series 3.

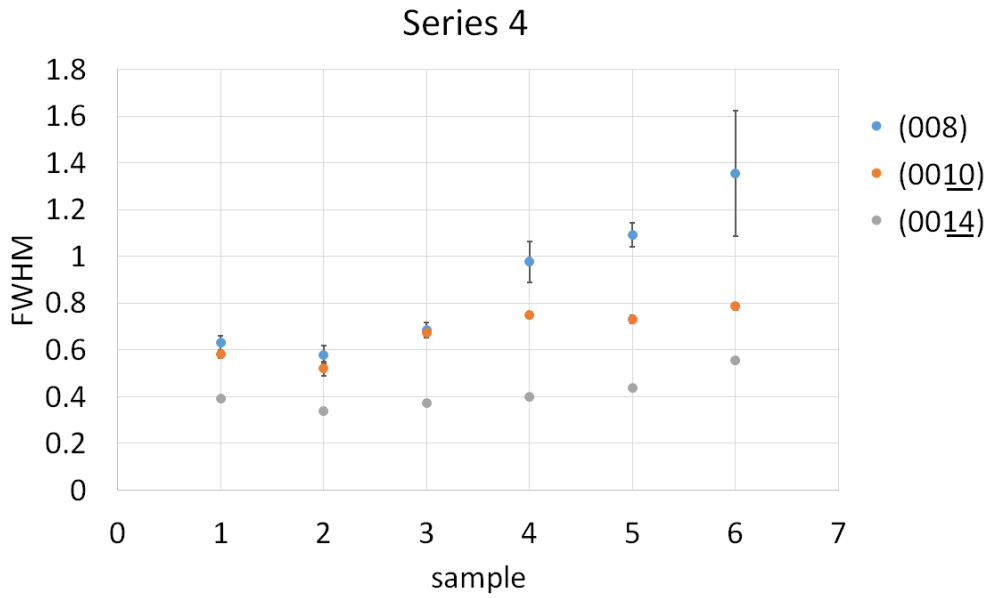

Figure S3: FWHM for series 4 for the (008), (0010) and (0014) reflections.

Pseudo lattice *c*-axis parameter

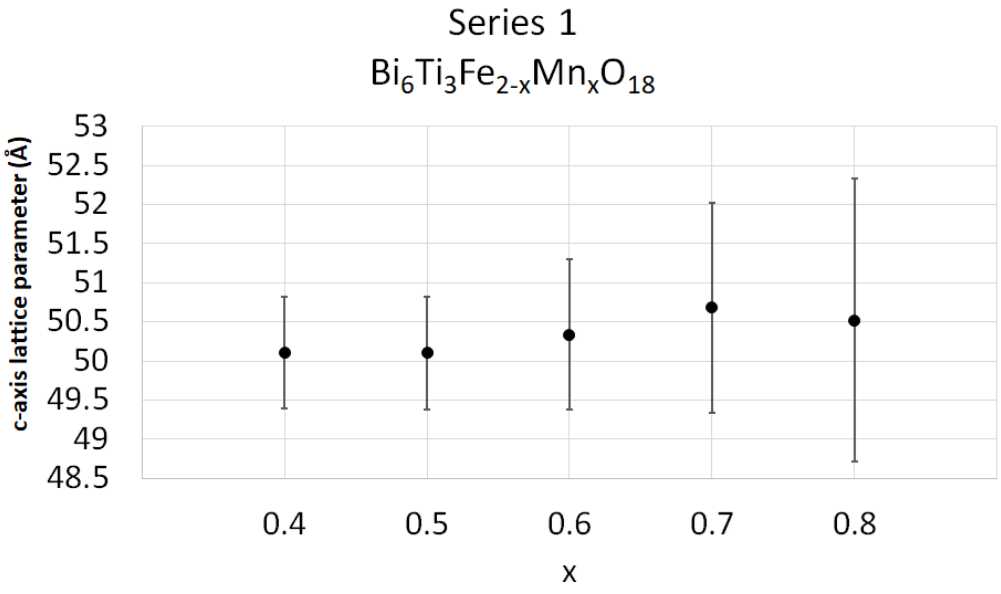

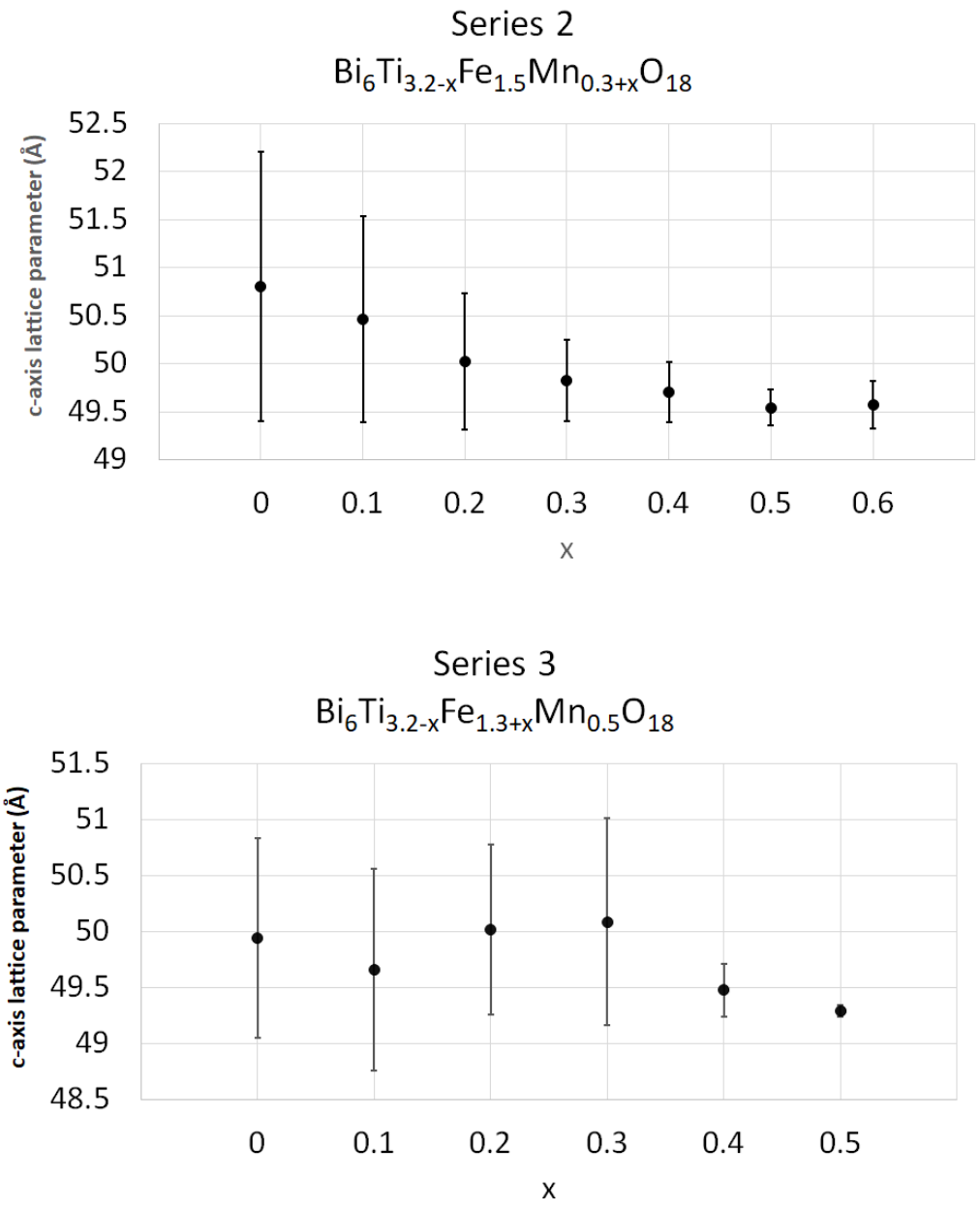

Figure S4: Calculated *c*-axis parameters for series 1,2 and 3.

DART-PFM

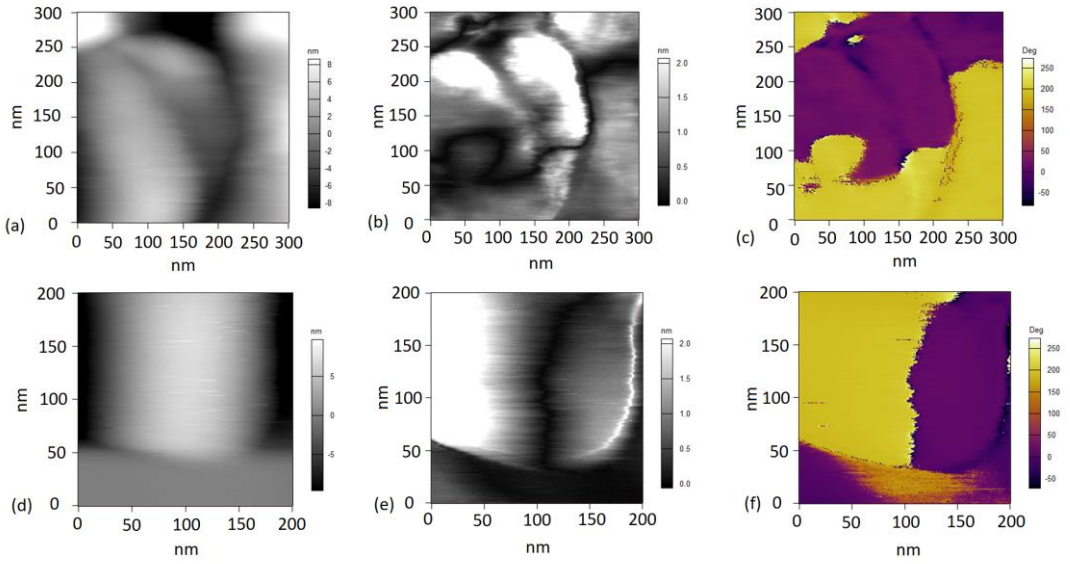

Figure S5: DART-PFM images of two series 1 samples. Height (a), amplitude (b), and phase (c) of $Bi_6Ti_3Fe_{1.6}Mn_{0.4}O_{18}$. Height (d), amplitude (e) and phase (f) of $Bi_6Ti_3Fe_{1.2}Mn_{0.8}O_{18}$.

Calculation of manganese oxidation state

We assume that the decrease in Ti^{4+} is being compensated for by the oxidation of Mn^{3+} to Mn^{4+}. The proportion of Mn^{4+} present is therefore proportional to the concentration necessary to neutralise the net charge on the material. To quantify the amounts of Mn^{3+} and Mn^{4+} the following equation was used,

$$A(3 \times Mn_x) + B(4 \times Mn_x) = Y \qquad \text{(S1)}$$

Where Y = the net charge of Mn^{3+} and Mn^{4+} required to have a net neutral charge, A and B = proportion of Mn in the 3+ and 4+ oxidation state, respectively. Mn_x is the proportion of Mn in the material. A + B = 1 therefore B = 1 - A which gives,

$$A(3 \times\ Mn_x)\ + (1 - A)(4 \times\ Mn_x) = Y \qquad \text{(S2)}$$

For example, the material $Bi_6Ti_{2.4}Fe_{1.92}Mn_{0.68}O_{18}$ has a net charge of -0.7 if Mn is only in the +3 state. Therefore to balance the material it is necessary that the total charge of Mn is 2.95, this is our Y value.

$$A(3 \times\ 0.68)\ + (1 - A)(4 \times\ 0.68) = 2.95 \qquad \text{(S3)}$$

Therefore A is 0.066 and B is 0.933. Converting B to a percentage we get the Mn(IV)% of Mn(IV) 93% shown for the $Bi_6Ti_{2.4}Fe_{1.92}Mn_{0.68}O_{18}$ material in Table 2. The concentrations of the various *B*-site atoms in series four are shown in Table 2. The table is arranged in order of decreasing Ti concentration and samples with an * correspond to the samples shown in figure 10. The appearance of *m* = 6 phase (as observed in the XRD) follows the trend of decreasing Ti concentration. The phase rearrangement observed in this work occurs when the concentration of Fe and Mn at the *B*-site of the perovskite units is above 48%.

Calculation of tolerance factor

The Goldschmidt tolerance factor is a calculated measure of the distortion of the perovskite unit. The distortion of the perovskite is affected by the size of an atoms occupying the perovskite structure [1]. The tolerance factor is given by,

$$t = (r_A + r_O)/\left(\sqrt{2}(r_B + r_O)\right) \qquad \text{(S4)}$$

Where r_A, r_B and r_O refer to the radii of the *A*-site and *B*-site ions and the radius of oxygen respectively. The calculated tolerance factor for series four is depicted in figure S6. This calculation indicates that there is a decrease in tolerance factor as the smaller Ti^{4+} atoms are replaced by the larger Fe^{3+} and Mn^{3+} ions. In table S1 the

sample compositions are given for series 4. The tolerance factor was then calculated using the proportion of Mn^{3+} and Mn^{4+} that were calculated in table 2. This shows that the distortion of the perovskite is lowered with the larger proportion of the smaller Mn^{4+} ion. Ionic radii high spin 6-coordinate ion, Mn^{3+} 0.645Å and Mn^{4+} 0.53Å [2].

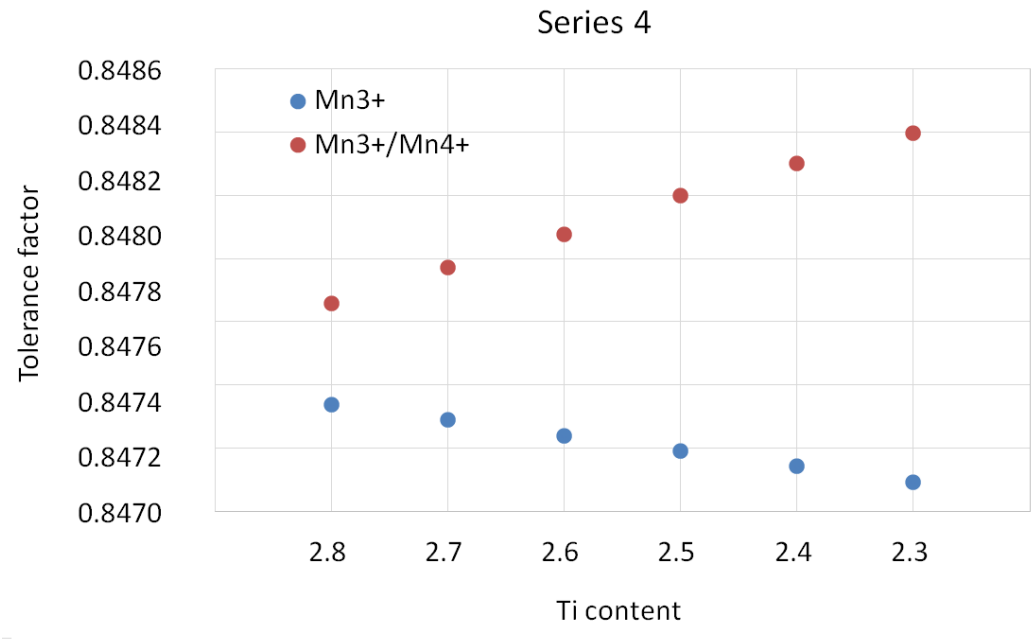

Figure S6: Calculated tolerance factor for series 4 showing a decrease in tolerance factor with decreasing titanium.

Table S1: Series 4 tolerance factor

Sample	Mn^{3+}	Mn^{3+}/Mn^{4+}
$Bi_6Ti_{2.8}Fe_{1.52}Mn_{0.67}O_{18}$	0.8483	0.8491
$Bi_6Ti_{2.7}Fe_{1.62}Mn_{0.68}O_{18}$	0.8482	0.8494
$Bi_6Ti_{2.6}Fe_{1.72}Mn_{0.68}O_{18}$	0.8481	0.8497
$Bi_6Ti_{2.5}Fe_{1.82}Mn_{0.68}O_{18}$	0.8480	0.8500

$Bi_6Ti_{2.4}Fe_{1.92}Mn_{0.68}O_{18}$	0.8479	0.8503
$Bi_6Ti_{2.3}Fe_{1.95}Mn_{0.75}O_{18}$	0.8477	0.8505

References

[1] J. B. Goodenough, "Electronic and ionic transport properties and other physical aspects of perovskites," *Reports on Progress in Physics,* vol. 67, no. 11, pp. 1915-1993, 2004, doi: 10.1088/0034-4885/67/11/r01.

[2] R. Shannon, "Revised effective ionic radii and systematic studies of interatomic distances in halides and chalcogenides," *Acta Crystallographica Section A,* vol. 32, no. 5, pp. 751-767, 1976, doi: doi:10.1107/S0567739476001551.

A.3. Appendix 3- supporting information for chapter 5

Growth recipe instructions for a sequential direct liquid injection chemical vapour deposition process

A section of a typical sequential growth recipe is shown in figure S1. The parameters such as pulse number, frequency and opening times are set by the user along with gas flow volumes. Then one loop of the recipe is defined. This loop process is set to mimic one half unit cell of the *m* = 5 Aurivillius structure. The number of loops is set by the user earlier in the recipe (not shown here). The structure is completed by a final two pulses of bismuth and then the recipe continues through a standard process to return the instrument to stand-by conditions (not shown here).

```
#Prec1

parameter runtime Bi_Pulse_Number = 800;

parameter runtime Bi_Injection_Frequency = 1;

parameter runtime Bi_Injector_OpeningTime = 8.0;


#Prec2

parameter runtime Mn_Pulse_Number = 800;

parameter runtime Mn_Injection_Frequency = 1;

parameter runtime Mn_Injector_OpeningTime = 1.6;


#Prec3

parameter runtime Fe_Pulse_Number = 800;

parameter runtime Fe_Injection_Frequency = 1;

parameter runtime Fe_Injector_OpeningTime = 1.4;


#Prec4

parameter runtime Ti_Pulse_Number = 800;

parameter runtime Ti_Injection_Frequency = 1;

parameter runtime Ti_Injector_OpeningTime = 3.2;


parameter runtime Process_Temperature = 710;

parameter runtime Process_Pressure = 8.5;

parameter runtime Vaporiser_Temperature = 220;


parameter runtime O2_Flow = 1000;

parameter runtime Total_Flow = 3000;

parameter runtime ViewportPurge = 200;
```

```
1 "Start process", begin stat DATA;

loop [Loop_Number]
{
# Start injections
10 Prec1.inj = open; #Bi
5  Prec1.inj = close;

10 Prec1.inj = open; #Bi
5  Prec1.inj = close;

10 Prec4.inj = open; #Ti
5  Prec4.inj = close;

10 Prec1.inj = open; #Bi
5  Prec1.inj = close;

10 Prec3.inj = open; #Fe
5  Prec3.inj = close;

10 Prec1.inj = open; #Bi
5  Prec1.inj = close;

10 Prec2.inj = open; #Mn
5  Prec2.inj = close;

10 Prec1.inj = open; #Bi
5  Prec1.inj = close;

10 Prec4.inj = open; #Ti
5  Prec4.inj = close;

10 Prec1.inj = open; #Bi
5  Prec1.inj = close;

10 Prec4.inj = open; #Ti
5  Prec4.inj = close;

}

# Last 2 Bi injections to finish the structure
10 Prec1.inj = open; #Bi
5  Prec1.inj = close;

10 Prec1.inj = open; #Bi
5  Prec1.inj = close;
```

Figure S1: Reperesentitive growth recipe for the sequential directl liquid injection chemical vapour deposition process

Calculation of crystalline quality

To asses crystalline quality of the materials a modified version of the Scherrer equation [1] was used. This equation is given as,

$$Q = \frac{1}{\beta \cos\theta} \qquad \text{(S1)}$$

Where β is the FWHM (in radians) and θ is the angle of diffraction. An average of the (008), (0012) and (0018) values was taken and the error bars shown represent the standard deviation between the three measurements. As can be seen in figure S3 the error is significantly larger than the variation to the crystalline quality factor. The large error can be accounted for due to the peak shift in the materials. OPBs complicate the XRD patterns and this is reflected in the values used for calculating that crystalline quality factor.

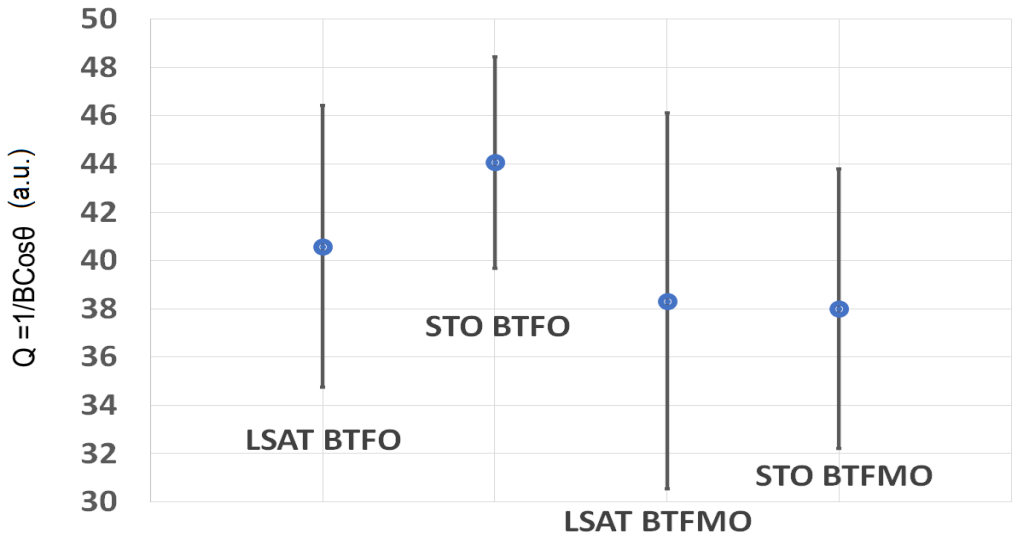

Figure S2: Crystalline quality factor of the full side samples used for magnetic measurements.

Calculation of the *c*-axis pseudo lattice parameter

The pseudo lattice parameters can be calculated using the relationship between the *d*-spacing and orthorhombic crystalline materials using the equation S2;

$$\frac{1}{d^2} = \frac{h^2}{a^2} + \frac{k^2}{b^2} + \frac{l^2}{c^2} \qquad \text{(S2)}$$

Where *hkl* are planes, *abc* are the pseudo lattice parameters and *d* is the interplanar distances of the Bragg condition calculated from the peak position using the following relationship (S3);

$$d = \frac{1.541876}{2\sin\theta} \qquad \text{(S3)}$$

Where θ is the peak position in radians.

As the only reflections obtained from XRD analysis were (00*l*) reflections, it was only possible to calculate the *c*-axis pseudo lattice parameter. The *c*-axis values of the (008), (0010) (0012), (0018) and (0020) reflection were calculated for the BTFO and BTFMO material on LSAT and STO. The standard deviation between those values was used as the error. As can be seen is figure S3 the error introduced from peak shift is substantially greater than the variation in *c*-axis pseudo lattice parameter.

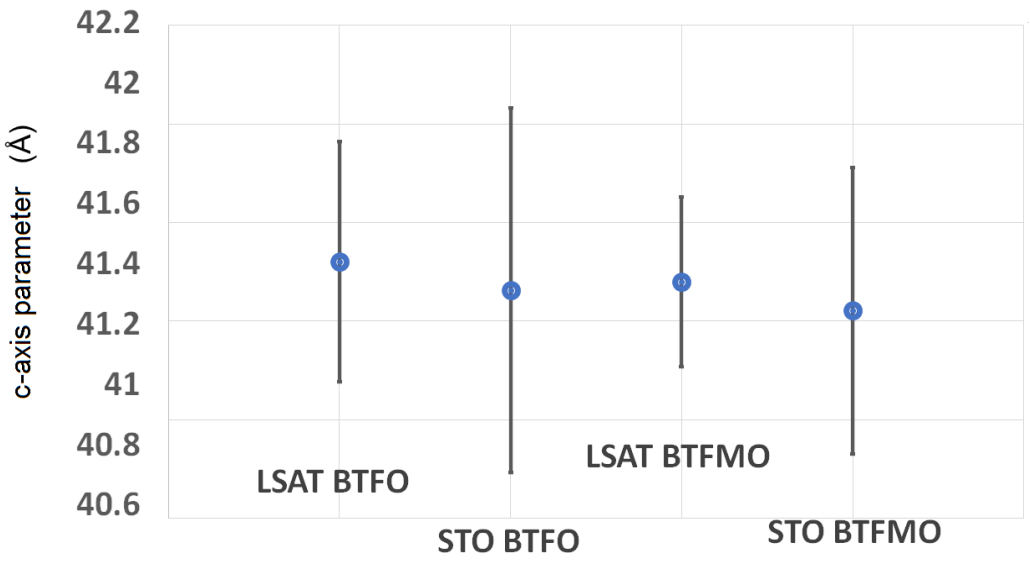

Figure S3: *c*-axis pseudo lattice parameter of BTFO and BTFMO on LSAT and STO.

Effect of sample size on XRD analysis

A comparison between the measurement of a large sample piece to a small sample piece is shown in figure S4. This XRD analysis is of two pieces of the same sample but clearly the smaller piece has additional peaks. It is concluded these are due to interference from the magnets that are used to hold the sample in place during the measurement. This also obscures the reflections from the Aurivillius material around 30° and 35°. The intensity of the peaks is also reduced for the smaller piece. With the exception of the samples shown in figure 5 of the main text, the substrates STO and LSAT used during the CVD process would all be > 0.5 cm^2.

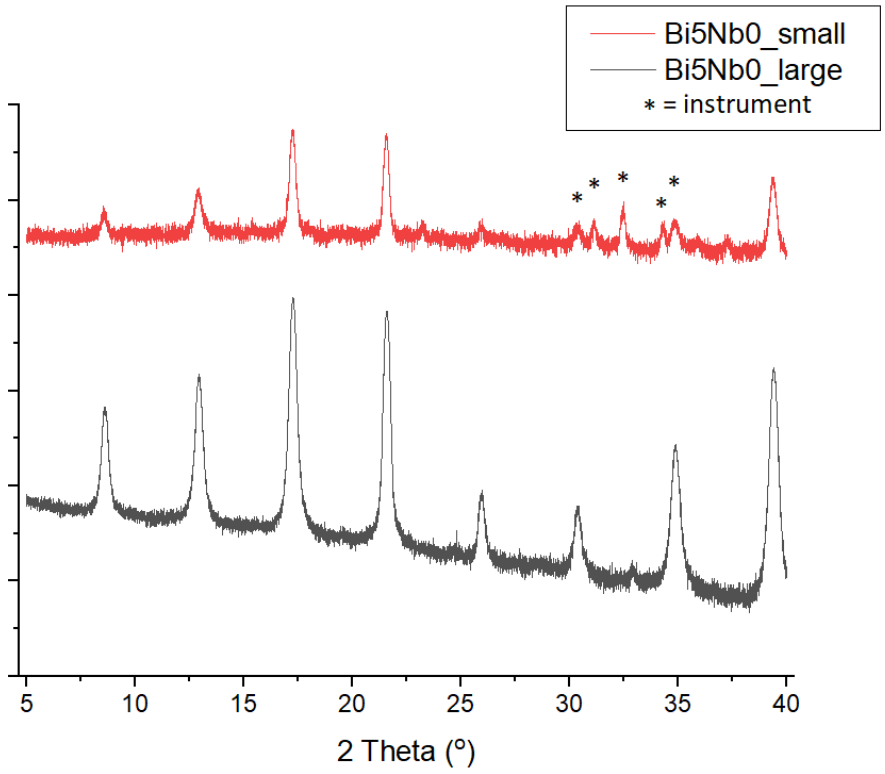

Figure S4: XRD analysis comparing the results obtained from measuring a small piece (< 0.5 cm^2) to a large piece (2.5 cm^2) of the same $Bi_5Ti_3Fe_1O_{15}$ sample deposited by chemical solution deposition on sapphire and annealed at 850 °C.

Analysis of grain size distribution

Using Gwyddion software a watershed algorithm was applied to AFM images of BTFO on LSAT, BTFMO on LSAT, BTFO on STO and BTFMO on STO (figure S5). This dropped

virtual drops of water onto the image which would flow down the steepest path to a local minima. For grain location, the parameters were drop size (1 %), threshold (3 px%) and number of steps (10 steps) and for segmentation the parameters were, number of steps (20 steps) and drop size (1 %) [2]. The same parameters were applied to each image (figure S5). A data process called grain distribution was then applied and the results of the distribution of surface area are presented in figure S6 [2]. The distribution of grain surface area varies between the samples and there is a larger proportion of smaller grains in the BTFMO samples than for the BTFO samples.

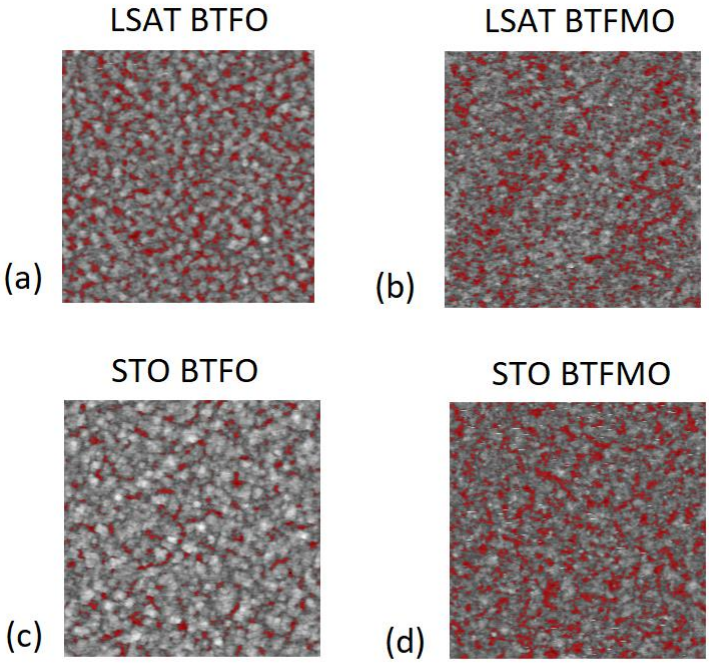

Figure S5: AFM images with watershed algorithm applied

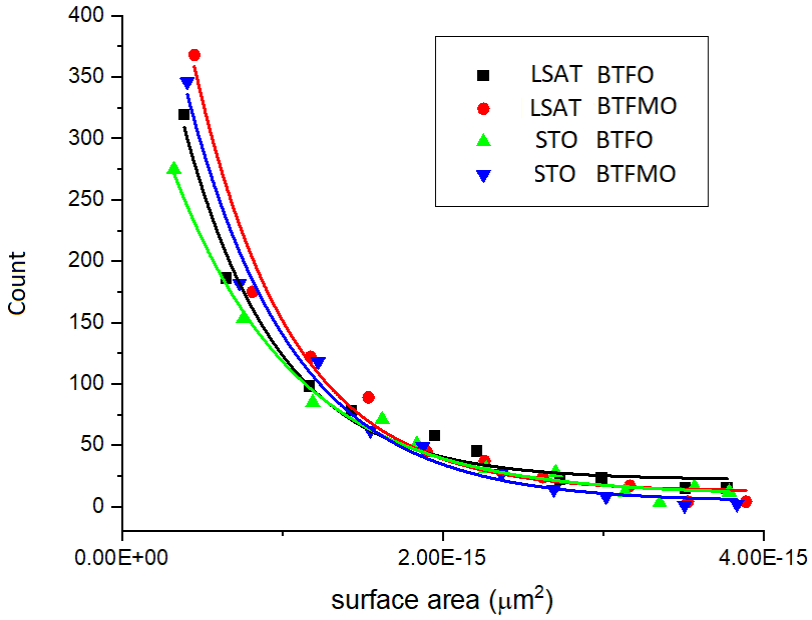

Figure S6: Calculated distribution of surface area of grains from figure S5. For the BTFMO samples there is larger proportion of grains with a smaller surface area (red and blue line) and the BTFO sample have a higher proportion with a larger surface area (black and green line).

Magnetic measurements

The following tables give the values obtained from SQUID magnetic analysis of the BTFO and BTFMO materials on LSAT and STO.

Table S1: BTFMO on LSAT

T (K)	Mr+ (μ emu)	Mr+ (emu/cm³)	Mr- (μ emu)	Mr- (emu/cm³)	Mr (emu)	Mr (emu/cm³)	Hc (Oe)
2	5.29	1.13	-4.92	-0.87	5.11	2.00	19.80
20	4.06	0.86	-3.71	-0.64	3.89	1.50	13.30

100	2.52	0.58	-2.20	-0.34	2.36	0.92	7.50
150	1.84	0.42	-1.19	-1.37	1.51	1.79	4.50
200	1.52	0.37	-0.77	-0.06	1.14	0.43	2.90
250	4.28	0.91	-3.98	-0.71	4.13	1.62	13.00
300	4.28	0.91	-3.98	-0.71	4.13	1.62	13.69

Table S2: BTFO on LSAT

T (K)	Mr+ (μ emu)	Mr+ (emu/cm^3)	Mr- (μ emu)	Mr- (emu/cm^3)	Mr (emu)	Mr (emu/cm^3)	Hc (Oe)
2	4.40	1.14	-4.43	-1.12	4.41	2.26	37.30
5	5.57	1.13	-5.71	-1.10	5.64	2.23	86.40
10	5.93	0.96	-5.95	-0.95	5.94	1.91	147.30
50	4.99	0.87	-5.01	-0.83	5.00	1.70	147.30

Table S3: BTFMO on STO

T (K)	Mr+ (μ emu)	Mr+ (emu/cm^3)	Mr- (μ emu)	Mr- (emu/cm^3)	Mr (emu)	Mr (emu/cm^3)	Hc (Oe)
2	9.91	1.80	-10.35	-1.92	10.13	3.72	140.00
10	9.91	1.80	-10.35	-1.91	10.13	3.71	148.50

20	9.21	1.76	-9.305	-1.75	9.26	3.51	140.00
50	7.71	1.44	-7.681	-1.42	7.69	2.86	104.60

Table S4: BTFO on STO

T (K)	Mr+ (μ emu)	Mr+ (emu/cm^3)	Mr- (μ emu)	Mr- (emu/cm^3)	Mr (emu)	Mr (emu/cm^3)	Hc (Oe)
2	6.69	1.29	-7.29	-1.36	6.99	2.65	348.80
10	6.51	1.25	-6.85	-1.27	6.68	2.52	536.65
20	6.07	1.17	-6.22	-1.18	6.15	2.35	536.65
50	4.82	0.93	-5.61	-0.93	5.21	1.86	425.00
100	3.31	0.63	-3.46	-0.63	3.38	1.26	237.30
150	2.24	0.44	-2.39	-0.43	2.32	0.87	143.30
200	1.70	0.33	-1.86	-0.33	1.78	0.66	96.40
300	1.17	0.25	-1.32	-0.23	1.25	0.48	67.00

References

[1] P. Scherrer, "Nachr Ges wiss goettingen," *Math. Phys.,* vol. 2, pp. 98-100, 1918.

[2] http://gwyddion.net/documentation/user-guide-en/grain-analysis.html (accessed 23-06-2021

A.4. Appendix 4- supporting information for chapter 6

XRD analysis of deposition on sapphire substrates

The XRD analysis of the sequential DLI-CVD deposition on c plane sapphire substrates is presented in figure S1. There are no peaks corresponding to the Aurivillius phase materials. The reflections at 14.6 and 29.6 correspond to the (222) and (444) respectively reflections of pyrochlore $Bi_2Ti_2O_7$ (JCPDF 32-0118).

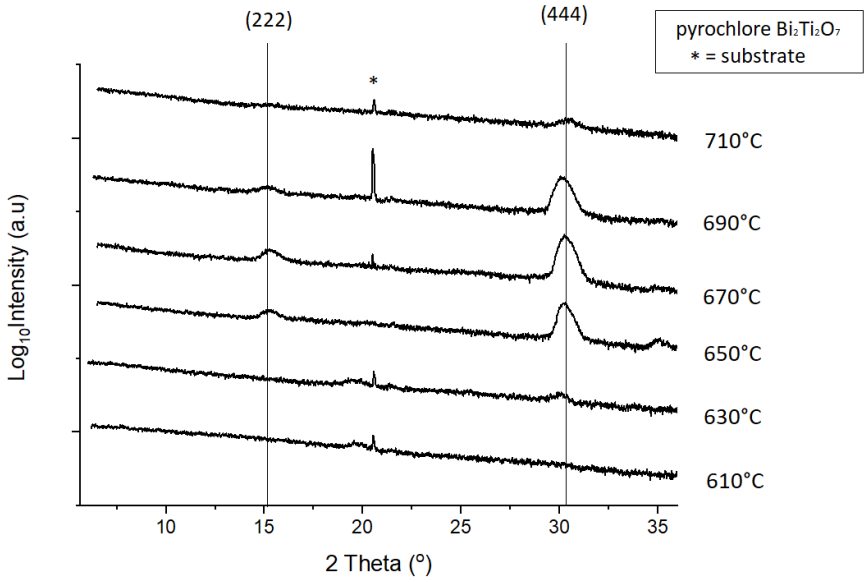

Figure S1: XRD analysis of materials deposited on sapphire substrate.

Calculation of *c*-axis parameter from large angle XRD

The XRD data from the out-of-plane scans (standard symmetric $\theta/2\theta$ configuration) shown in figure 6 of chapter 6 was used to calculated the c-axis parameter of the LSAT 710 °C, LSAT 610 °C, STO 710 °C and STO 610 °C materials. The calculation used all of the identified Aurivillius peaks observed in the data.

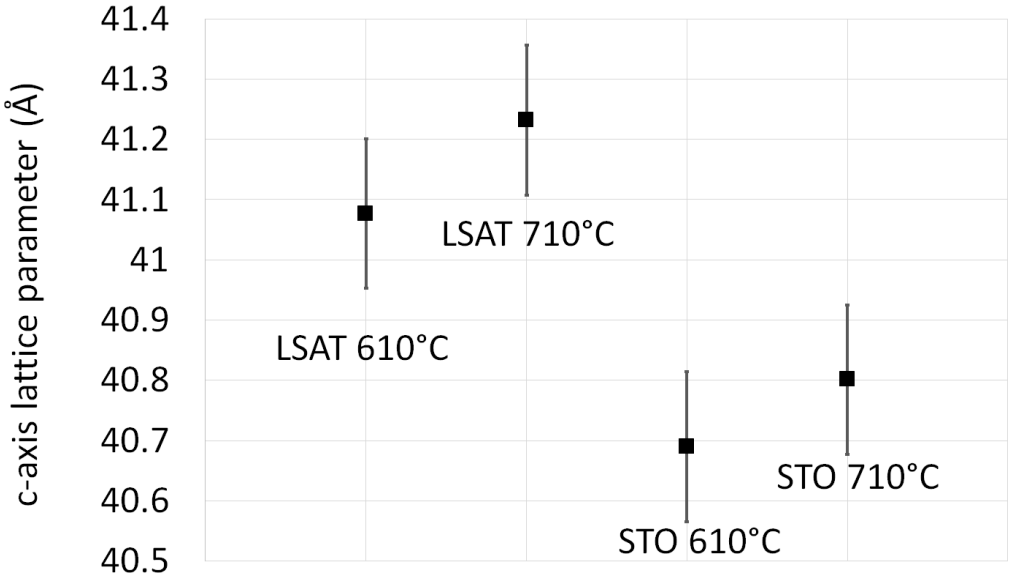

Figure S2: *c*-axis pseudo lattice parameters calculated from the large angle out-of-plane XRD data.